UNIVERSITY OF SÃO PAULO
SÃO CARLOS SCHOOL OF ENGINEERING

Pedro David Bravo-Mosquera

Methodologies for designing, optimizing, and evaluating possible unconventional aircraft configurations for future civil aviation

São Carlos

2022

Pedro David Bravo-Mosquera

Methodologies for designing, optimizing, and evaluating possible unconventional aircraft configurations for future civil aviation

Thesis submitted to the São Carlos School of Engineering - University of São Paulo, in partial fulfillment to the requirements for the Degree of Doctor in Science - Graduate Program in Mechanical Engineering.

Concentration Area: Aeronautics

Supervisor: Prof. Dr. Fernando M. Catalano
Co-supervisor: Prof. Dr. David W. Zingg

VERSÃO CORRIGIDA

São Carlos
2022

Ficha catalográfica elaborada pela Biblioteca Prof. Dr. Sérgio Rodrigues Fontes da EESC/USP com os dados inseridos pelo(a) autor(a).

B826

Bravo-Mosquera, Pedro David
/ Pedro David Bravo-Mosquera; orientador Fernando Martini Catalano; coorientador David W. Zingg. São Carlos, 2022.

Tese (Doutorado) - Programa de Pós-Graduação em Engenharia Mecânica e Área de Concentração em Aeronáutica -- Escola de Engenharia de São Carlos da Universidade de São Paulo, 2022.

1. Box-Wing configuration. 2. Boundary Layer Ingestion. 3. Multidisciplinary Design Optimization. 4. Computational Fluid Dynamics. 5. Wind-tunnel experiments. 6. Aerodynamic Shape Optimization. I. Título.

Eduardo Graziosi Silva - CRB - 8/8907

FOLHA DE JULGAMENTO

Candidato: Engenheiro **PEDRO DAVID BRAVO MOSQUERA.**

Título da tese: “Metodologias para projetar, otimizar e avaliar possíveis configurações de aeronaves não convencionais para o futuro da aviação civil”.

Data da defesa: 13/10/2022.

Comissão Julgadora	**Resultado**
Prof. Titular **Fernando Martini Catalano** **(Orientador)** (Escola de Engenharia de São Carlos – EESC/USP)	Aprovado
Prof. Dr. **Ney Rafael Sêcco** (Instituto Tecnológico de Aeronáutica/ITA)	Aprovado
Prof. Dr. **Odenir de Almeida** (Universidade Federal de Uberlândia/UFU)	Aprovado
Prof. Dr. **João Luiz Filgueiras de Azevedo** (Instituto Tecnológico de Aeronáutica/ITA)	Aprovado
Dr. **Luis Gustavo Trapp** (Empresa Brasileira de Aeronáutica S.A/EMBRAER)	Aprovado

Coordenador do Programa de Pós-Graduação em Engenharia Mecânica:

Prof. Associado **Adriano Almeida Gonçalves Siqueira**

Presidente da Comissão de Pós-Graduação:

Prof. Titular **Murilo Araujo Romero**

Este trabajo es dedicado a mis padres: Hermes y Fabiola, y a mi hermana: Maria Laura; mis pilares.

ACKNOWLEDGMENTS

Thank you God for everything in my life. The good and the bad. Some were blessings and some were lessons.

In engineering and also in life, nothing is achieved by oneself alone, rather it is the result of a supportive group of mentors, family, and friends. First of all, I would like to acknowledge my advisor Prof. Dr. Fernando Martini Catalano for the guidance he has given me throughout my studies at São Carlos School of Engineering - University of São Paulo (EESC-USP). I have benefited immensely from the breadth and depth of his technical experience in experimental aerodynamics.

I would like to express my deepest gratitude to Prof. Dr. David W. Zingg for give me the opportunity to be part of his group at University of Toronto - Institute for Aerospace Studies (UTIAS). His expertise was vital for this thesis and I could not have finished it successfully without his guidance and patience. The experience I gained working with high-fidelity aerodynamic shape optimization is undoubtedly, the biggest goal of this doctoral project.

Special thanks go to the members of my committee, Prof. Dr. Jõao Luiz F. Azevedo, Prof. Dr. Ney Rafael Sêcco, Prof. Dr. Odenir de Almeida, and Dr. Luis Gustavo Trapp, for their time and effort assessing my thesis.

Special thanks to Prof. Dr. Alvaro Martins Abdalla, and Prof. Dr. James Rojas Waterhouse for their important contributions during the evaluation of the work presented hereby. An special recognition goes to Prof. Dr. Hernán Darío Cerón-Muñoz; I wanted to take a moment to express my gratitude for all of his support during my career. Sometimes it seems like you remember my achievements even better than I do myself, so thank you for not only your teamwork and support, but for your vote of confidence.

I gratefully acknowledge the members of the Experimental Aerodynamics Laboratory (LAE) at EESC-USP for their support in setting up and operating the experimental apparatus, specially to Jõao Paulo Eguea and Gabriel Pereira. In addition, I want to thank the laboratory technicians Mr. José Claudio Pinto de Azevedo and Mr. Osnan Ignacio Faria for their help in offering me the resources in running my experimental model. I also acknowledge the input and support provided by the members of the Computational Aerodynamics Group at UTIAS, specially to Dr. Thomas Reist, Dr. Timothy Chau, and Victor Alulema for their invaluable technical guidance and discussions on aerodynamic shape optimization using the Jetstream framework.

My affectionate thanks to Gisele Aparecida Poppi, secretary of the Department of Aeronautical Engineering and Iara Alice de Oliveira, secretary of the Graduate Program

in Mechanical Engineering, who always helped me with paperwork and were present for a good conversation.

In the following lines, I would also like to thank my family and friends who offered moral support and encouragement during this journey:

To my father Hermes Bravo, for teaching me to appreciate the value of work and time. To my mother Fabiola Mosquera, for always being there for me and for believing in me even when I do not believe in myself. To my sister Maria Laura, for being my inspiration to be a better professional and a greater person. You have always stood behind me!

To my entire family. Your constant love and support keep me motivated and confident. My accomplishments and success are because all of you believed in me. I would like to dedicate this thesis to my grandmother Fabi, and the memory of my grandfather, Mauro Mosquera (1949-2018), who is a constant source of inspiration. I hope he would have been proud.

To Paola and my little angel Tinto. I am here because of you. Thanks for your patience, comprehension, love, and unwavering support during this journey. Dra. Paola Ayala-Burbano, you are the best co-author I found to share my life.

To my cousin Guillermo Bravo and his wife Martha Bravo. Thanks for your overwhelming generosity and for taking me in as one of your own.

To Diana Montaño, Sara Jurado, and Juan Arturo. I am truly lucky to have you as my friends (Cunnis).

To my fellows and friends, William Gómez, Andrés Gaviria, Jhonathan Solarte, Fernanda Monteiro, Daniel Garcia, Juan Flores, John Vaca, and Rolando Guzmán. Thanks for providing me inspirations and valuable suggestion during the course of this study.

The author disclosed receipt of the following financial support for the research, authorship, and/or publication of this thesis: This work was supported by the Brazilian Research Agency–CNPq (grants 141950/2017-0 and 203402/2019-7).

São Carlos, SP, Brazil. Pedro David Bravo-Mosquera.

September 19, 2022.

“In design, you are forced to develop unusual solutions to unusual problems.”
Kelly Johnson, ***Kelly: More than My Share of it All.***

"Bravo pueblo de invicta coraza..."
Alberto Quijano Guerrero.

ABSTRACT

BRAVO-MOSQUERA, P. D. **Methodologies for designing, optimizing, and evaluating possible unconventional aircraft configurations for future civil aviation**. 2022. 266p. Ph.D. Thesis - São Carlos School of Engineering, University of São Paulo, São Carlos, 2022.

Due to technological evolution and the development of several environmental aerospace projects, the aeronautical community has been implementing advanced design strategies, aiming to find next-generation configurations that allow mitigating the undesirable impact of aircraft on the environment. Unconventional solutions have attracted the attention of designers, and several aircraft concepts have been proposed in order to achieve ambitious goals. Given the lack of significant design experience with unconventional aircraft, Multidisciplinary Design Optimization (MDO) frameworks enable to understand the impact of various technologies, obtaining reductions in energy use per passenger-kilometer beyond that provided by the configuration itself. In this thesis, multifidelity and multidisciplinary optimization methodologies have been applied towards designing a next-generation commercial airliner, which combines a Box-Wing configuration with Boundary Layer Ingestion (BLI) engines. This project presents four fundamental objectives: (i) To understand the current design issues, methods, and evolving trends of unconventional configurations. This is performed through a compilation of information in the form of a state-of-the-art literature review. (ii) To develop a low-fidelity MDO method to determine the main geometric, aerodynamic, stability, propulsion and performance characteristics of the aircraft, based on its design requirements and constraints. (iii) To carry out Computational Fluid Dynamics (CFD) simulations and wind-tunnel experiments on a scale-model of the aircraft, in order to perform a back-to-back analysis of non-boundary layer ingesting and boundary layer ingesting versions of the aircraft. (iv) To implement a high-fidelity Aerodynamic Shape Optimization method for the Box-Wing concept based on Reynolds-Averaged Navier-Stokes (RANS) equations. The completion of the research effort led to understand the potential benefits of the different technologies implemented on the aircraft at different levels of physical fidelity. Such information is believed to be important in determining whether a Box-wing aircraft powered by a BLI propulsion system can fulfil future aviation demands, providing also interesting and very encouraging results for further development.

Keywords: Box-Wing configuration. Boundary Layer Ingestion. Multidisciplinary Design Optimization. Computational Fluid Dynamics. Wind-tunnel experiments. Aerodynamic Shape Optimization.

RESUMO

BRAVO-MOSQUERA, P. D. **Metodologias para projetar, otimizar e avaliar possíveis configurações de aeronaves não convencionais para o futuro da aviação civil**. 2022. 266p. - São Carlos School of Engineering, University of São Paulo, São Carlos, 2022.

Devido à evolução tecnológica e ao desenvolvimento de diversos projetos aeroespaciais ambientais, a comunidade aeronáutica vem implementando estratégias avançadas de projeto, visando encontrar configurações de próxima geração que permitam mitigar o impacto indesejável dos aviões no ambiente. Soluções não convencionais têm atraído a atenção de projetistas, e vários conceitos de aeronaves têm sido propostos para atingir metas ambiciosas. Dada a falta de experiência em projeto de aeronaves não convencionais, metodologias de otimização de projeto multidisciplinar (MDO) permitem entender o impacto de várias tecnologias, obtendo reduções no consumo de energia por passageiro-quilômetro além daquela proporcionada apenas pela configuração. Nesta tese, metodologias de otimização multifidelidade e multidisciplinar foram aplicadas para projetar uma aeronave comercial de próxima geração, que combina uma configuração Box-Wing com um sistema de propulsão por ingestão de camada limite (BLI). Este projeto tem quatro objetivos fundamentais: (i) Compreender as atuais questões de projeto, metodologias, e tendências em evolução de aeronaves não convencionais. Isto foi realizado através de uma compilação de informação na forma de revisão de literatura. (ii) Desenvolver um método de otimização de projeto multidisciplinar de baixa fidelidade para determinar as principais características geométricas, aerodinâmicas, de estabilidade, propulsão e desempenho da aeronave, com base em seus requisitos de projeto e restrições. (iii) Realizar simulações de dinâmica de fluidos computacional (CFD) e experimentos em túnel de vento usando um modelo a escala da aeronave, a fim de realizar uma análise comparativa entre duas versões da mesma, sendo uma com ingestão de camada limite e outra sem ingestão de camada limite. (iv) Implementar um método de otimização de forma aerodinâmica de alta fidelidade para o conceito Box-Wing baseado nas equações de Reynolds-Averaged Navier-Stokes (RANS). A conclusão do esforço de pesquisa permitiu compreender os benefícios potenciais das diferentes tecnologias implementadas na aeronave em diferentes níveis de fidelidade física. Espera-se que tais dados sejam úteis na interpretação de que uma aeronave Box-wing acoplada a um sistema de propulsão BLI possa atender às demandas da aviação futura, fornecendo também resultados interessantes e muito encorajadores para o desenvolvimento de trabalhos futuros.

Palavras-chave: Configuração Box-Wing. Ingestão de camada limite. Otimização multidisciplinar de projeto. Dinâmica dos Fluidos Computacional. Experimentos em túnel de vento. Otimização de forma aerodinâmica.

LIST OF FIGURES

LIST OF TABLES

LIST OF ABBREVIATIONS AND ACRONYMS

ACARE	Advisory Council for Aeronautics Research in Europe
AIP	Aerodynamic Interface Plane
BLI	Boundary Layer Ingestion
BW	Box-Wing
BWB	Blended Wing Body
CAEP	Committee on Aviation Environmental Protection
CFD	Computational Fluid Dynamics
CG	Center of gravity
CTW	Conventional Tube-and-Wing
DBX	Direction-Based Crossover
DLR	German Aerospace Centre
DOC	Direct Operational Cost
DPLM	Design Payload Mass
DRM	Dynamic Random Mutation
DRO	Design Requirements and Objectives
EIS	Entry into Service
EDF	Electric-Ducted Fan
ERA	Environmentally Responsible Aviation Project
ES	Elitism Strategy
FE	Finite Element
FFD	Free-Form Deformation
FM	Fuel Mass
GA	Genetic Algorithm
GMRES	Generalized minimal residual

HLFC	Hybrid Laminar Flow Control
HWB	Hybrid Wing Body
IATA	International Air Transport Association
ICAO	International Civil Aviation Organization
INTI	Innovative Transport Industry
LFC	Lifting Fuselage Concept
MDO	Multidisciplinary Design Optimization
MFW	Maximum Fuel Weight
MTOW	Maximum Take-Off Weight
MZFW	Maximum Zero Fuel Weight
NACRE	New Aircraft Concepts Research
NASA	National Aeronautics and Space Administration
NLF	Natural Laminar Flow
NPV	Net Present Value, MUSD
NURBS	Non-uniform rational B-splines
OEW	Operational Empty Weight
PSC	Power Saving Coefficient
RANS	Reynolds-Averaged Navier-Stokes
RS	Ranking Selection
SATs	Simultaneous-approximation terms
SBW	Strut-Braced Wing
SBP	Summation-by-parts
SFC	Specific Fuel Consumption
SNOPT	Sparse Nonlinear OPTimizer
SUGAR	Subsonic Ultra Green Aircraft Research
TBW	Truss-Braced Wing

TRL	Technology Readiness Level
TPR	Total Pressure Recovery
VLM	Vortex lattice methods

LIST OF SYMBOLS

$A\!\!\!R$	Aspect Ratio
b	Wingspan $[m]$
$\mathbf{b}^{(m)}$	B-spline volume control points
c_t	Thrust specific fuel consumption
$\bar{c}$	Mean Aerodynamic Chord
C_D	Drag coefficient
C_{D0}	Zero-lift drag coefficient
C_{Di}	Induced drag coefficient
C_{Dwv}	Wave drag coefficient
C_l	Rolling moment coefficient
C_L	Lift coefficient
$C_{L,md}$	Lift coefficient for minimum drag
C_m	Pitching moment coefficient
C_n	Yawing moment coefficient
C_p	Pressure coefficient
C_{pt}	Total pressure coefficient
C_{P_E}	Electrical power coefficient
C_{P_K}	Mechanical flow power coefficient
C_T	Thrust coefficient
C_X	Net streamwise force coefficient
$C_{y\beta}$	Sideslip angle derivative of lateral force
C_Φ	Dissipation coefficient
$\mathcal{C}_e$	Equality constraints
$\mathcal{C}_i$	Inequality constraints

d_{fan}	Model propulsor fan diameter
D	Drag force
DC_θ	Flow distortion index
e	Span efficiency factor
E	Endurance
$f(\mathbf{x})$	Objective function
F_f	Fitness function
F_X	Net streamwise force
g	Vector of constraints
h/b	Height-to-span ratio
H_{cr}	Initial cruise altitude
$\mathcal{J}$	Objective function
k	Drag-due-to-lift factor
L/D	Lift-to-drag ratio
$\dot{m}$	Fuel mass flow rate
M	Mach number
ML/D	Aircraft Mach Lift-to-Drag ratio
$\{\mathcal{M}^{(i)}\}_{i=1}^{m}$	Mesh movement equations
n_{sample}	Measurement sample number
$\hat{n}$	Unit normal vector
$O_D(V)$	Drag measurement voltage output
$O_L(V)$	Lift measurement voltage output
p	Static pressure
p_t	Total pressure
$p_{t\infty}$	Freestream total pressure
p_∞	Freestream static pressure

P_E	Electrical power supplied to propulsors
P_K	Mechanical flow power
P_V	Volumetric flow power
P_{cr}	Pressure at cruise altitude
$\mathbf{q}$	Flow variables
q_∞	Dynamic pressure
r_{fan}	Fan radius
R	Cruise range
$\mathcal{R}$	Flow residual
R_e	Reynolds number
s/b	Stagger-to-span ratio
S	Wing reference area
SM_x	Static Margin
$\mathcal{S}$	Surface of body
t	Wing thickness
t_0	Initial wing thickness
t/c	Airfoil thickness-to-chord ratio
T	Penalty term
T_{EDF}	Thrust generated by the EDFs
T_{max}	Maximum required thrust
T_{req}	Thrust required
T/W	Thrust-to-Weight ratio
u^*, v^*, w^*	Non-dimensional cartesian component of velocity in X,Y and Z direction $(= u/V_\infty, = v/V_\infty, = w/V_\infty)$
$u, v, w\ (rms)$	Velocity fluctuations (Reynolds stress) in X,Y and Z direction
U_{tip}	Fan blade tip speed

$\mathbf{v}$	Design variables
V	Velocity magnitude
$\mathbf{V}$	Velocity vector
$\mathcal{V}$	Fluid control volume
V_j	Mass-averaged outlet velocity
Vol	Wing volume
Vol_t	Wing volume target
V_∞	Freestream speed or Wind tunnel speed
W/S	Wing loading
W_e	Empty weight
W_f	Fuel weight
W_{final}	Final weight
W_i	Weight fraction
W_0	Maximum take-off Weight
$\mathbf{x}$	Vector of design variables
X, Y, Z	Tunnel axes: X is stream-wise direction, Y is vertical direction and Z is span-wise direction

Greek letters

α	Angle of attack
β	Sideslip angle
γ	Isentropic expansion factor
Γ	Dihedral angle
δ	Boundary layer thickness
$\Delta()$	Data correction quantity
Δ_{CG}	Center of gravity offset

η_f	Fan efficiency
η_m	Motor efficiency
η_P	Propulsive efficiency
η_R	Total pressure recovery
θ	Set (chromosome)
λ	Taper ratio
Λ	Sweep angle
ρ	Fluid density
σ_D	Drag measurement standard deviation
σ_L	Lift measurement standard deviation
τ	Twist
$\bar{\bar{\tau}}$	Viscous stress tensor
Φ	Dissipation
Φ_∞	Volumetric dissipation
Ω	Admissible search space
Ω_f	Propulsor fan angular velocity or wheel speed
ω	Weights
ω_x	Streamwise vorticity

Subscript

$_1$	Fore wing
$_2$	Aft wing
$_A$	Airframe
$_{AIP}$	Measured at the AIP
$_{cons}$	Constraint
$_{CG}$	Center of gravity

$_{geo}$	Geometric
$_{i}$	Value at propulsor inlet plane
$_{j}$	Value at propulsor exit plane
$_{J}$	Propulsor jet
$_{perf}$	Performance
$_{s}$	Surface
$_{stab}$	Stability
$_{t}$	Sum of fore and aft wings
$_{v}$	Vortex
$_{w}$	Wake

CONTENTS

1 INTRODUCTION

The aerospace industry is currently experiencing a gradual transition towards more sustainable configurations, which is driven by global warming and climate change concerns, as well as technology saturation of conventional architectures. Such novel configurations represent conceptual design challenges due to the lack of historical information and the need to include optimization algorithms to select a promising concept from a large number of possibilities. Different novel configurations have been proposed as potential candidates for the next-generation aviation. However, the conceptual design of such innovative layouts is a complex task due to the large number of design variables under study. Therefore, to support the development of such novel configurations, new design methodologies are required that go beyond traditional design methods, reducing the risk associated at industrial level.

Although unconventional configurations promise considerable improvements in fuel efficiency over conventional tube-and-wing (CTW) aircraft, their industrial development depends on business and technological risks. Many of these issues can be addressed using Multidisciplinary Design Optimization (MDO) frameworks, reducing the probability of failure and allowing for a better understanding of the benefits over conventional aircraft. MDO tools are organized into different modules that include some of the most important aeronautical technologies at different levels of fidelity. Therefore, specialized computational tools are required to solve the resulting multifidelity multidisciplinary optimization problems, since they often require combining a large design space, comprising both local and global geometric design variables with high-fidelity analyses.

In this thesis, a wide number of optimization and aerodynamic studies were implemented to reduce the risk and uncertainty associated to the viability of different unconventional configurations. Several design and evaluation methodologies were used to find combinations of feasible solutions that, despite variations due to uncertainty factors, produce favourable gains when compared to a conventional baseline. In particular, special attention is given in the design of a Box-Wing (BW) aircraft coupled to a Boundary Layer Ingestion (BLI) propulsion system for the single aisle - medium range and high subsonic transport category. Although these two configurations are not new, the relevance of this research is the integration of these concepts in a single commercial airliner. Considering this scenario, the compilation and integration of computational and experimental data, as well as of the design space in which the unconventional configurations are found, can provide a better understanding of the possible ways to allow sustainable growth of this particular concept.

1.1 Overview of Technologies

1.1.1 Box-Wing Concept

Several studies have shown the potential advantages of BW configurations over CTW aircraft. The key feature of this unconventional layout is the high span efficiency factor, which decreases the induced drag and keeps high values of aerodynamic efficiency at off-design conditions (KROO, 2005). The BW has also exceptional longitudinal stability and stall characteristics, due to its inherent ability to create a pitching moment to restore the state of the aircraft after a perturbation. Furthermore, the lift distribution of the closed-form solution provides a statically indeterminate structure which can reduce the structural weight of the wings (DEMASI; MONEGATO; CAVALLARO, 2016; RUSSO; TOGNACCINI; DEMASI, 2020).

Regardless of such major benefits, many technical issues continue to be investigated to demonstrate the feasibility of this configuration (e.g., aeroelastic behavior of the closed wing system, and center of gravity (CG) excursion due to the weight and location of aircraft components, such as landing gear, engines, fuel system, etc). In particular, the sensitivity of the CG position impacts both control and handling qualities of the BW configuration, requiring a large number of redundant movable surfaces, which increase weight, cost and complexity of integration (CAVALLARO; DEMASI, 2016).

The first conceptual design investigation was reported by Lockheed Martin company, and revealed the BW configuration could reduce approximately 30% of the induced drag over its conventional counterpart (LANGE *et al.*, 1974). The knowledge from this study led to the development of more detailed projects such as PARSIFAL (Prandtlplane architecture for the sustainable improvement of future airplanes), which is funded by the European Union under the Horizon 2020 program. Several articles have been published concerning the design requirements adopted for such an aircraft, including Computational Fluid Dynamics (CFD), stability, emissions, and structural analyzes (FREDIANI *et al.*, 2019; CIPOLLA; SALEM; BACHI, 2019; TASCA *et al.*, 2021; CIPOLLA *et al.*, 2021).

From the point of view of academic projects, many authors have used low-fidelity (SCHIKTANZ, 2011; JEMITOLA, 2012; ZOHLANDT, 2016; KAPAROS *et al.*, 2018), medium fidelity (ANDREWS; PEREZ; WOWK, 2015; ANDREWS; PEREZ, 2018b) and high-fidelity (GAGNON; ZINGG, 2016a; CHAU; ZINGG, 2017) methodologies to compare the aerodynamic benefits of BW configurations against CTW designs. Despite their obvious differences, mainly regarding aerodynamic modeling and optimization algorithms, the studies have offered useful insight into the basic patterns and trade-offs of the large-scale geometric parameters of a BW design. General results have suggested the BW concept is able to reduce the fuel consumption by approximately 5% to 8% compared to CTW designs.

1.1.2 Boundary Layer Ingestion

BLI systems have demonstrated their potential benefits in terms of energy consumption and propulsive efficiency (LV *et al.*, 2016). There are several unconventional aircraft that take advantage of the boundary layer developed along the fuselage, avoiding the integration of pylons and reducing jet dissipation and jet velocity. In this way, the thrust needed to propel the aircraft and therefore, the energy and/or fuel consumption are reduced (PLAS *et al.*, 2007; HENDRICKS, 2018).

The “double bubble" D8 aircraft, which is a realistic configuration developed by NASA, MIT and Aurora Flight Sciences, stands out among the most relevant designs with BLI systems. This unconventional configuration is characterized by a lifting fuselage concept that provides extra lift, low sweep wing which reduces weight, and embedded engines on the rear part of the fuselage. Numerical and experimental investigations have shown its potential benefits to reduce the mechanical flow power by about 8.6% in comparison with podded engines (PANDYA *et al.*, 2014; URANGA *et al.*, 2017).

Propulsive fuselage concepts such as NASA’s STARC-ABL and CENTERLINE use a turboelectric propulsion system with an electrically driven BLI fan mounted on the fuselage tail cone to reduce fuel-burn. This configuration has proven to be the most efficient in terms of power savings against different distributed propulsion concepts (FERNÁNDEZ; SMITH, 2020; SAMUELSSON *et al.*, 2021; SEITZ *et al.*, 2021). High-fidelity simulations based on the NASA’s STARC-ABL concept have shown a fuel-burn reduction by about 12% (GRAY *et al.*, 2018).

Blended Wing Bodies have also demonstrated their increased efficiency over CTW aircraft. They are characterized by a well-suited upper surface that integrates embedded engines, reducing around 15% of fuel consumption (KIM; LIOU, 2013; KIM; LIOU, 2017). Evidently, BLI systems provide a blueprint for achieving future commercial aviation targets while also encouraging advances in engine technology. However, these systems require demanding propulsion-airframe integration designs in order to reduce the influence of distorted flow on the performance of the engines (VALENCIA *et al.*, 2020; MENEGOZZO; BENINI, 2020).

1.2 Research Questions and Objectives

A cutting-edge literature review was conducted at the beginning of this study endeavor in 2017. This analysis showed that:

- Several design methodologies have been implemented to design unconventional configurations, but the results are highly dependent on the physical-model fidelity levels.

- A large number of unconventional configurations are currently being investigated, and subscale prototypes have been manufactured and tested.
- There are studies on the aerodynamic performance of BW concepts, but they are limited to low-fidelity optimization tools and generally lack detail.
- BLI engines are widely researched at experimental level in subsonic regimes, and component sizing methods have been developed.
- Unconventional aircraft configurations are likely to be crucial in minimizing the effect of civil aviation on climate change. Therefore, it is important to address the major design challenges associated with specific unconventional configurations, in order to obtain reliable estimations of the benefits of their energy-efficiency in comparison to the CTW configuration.

This overview serves as the foundation for the following primary research questions:

Which design variables and constraints allow to fully explore the potential of a given unconventional aircraft configuration in an optimization problem?

Which are the minimum fidelity levels required to design unconventional aircraft configurations and evaluate their performance?

Do all important design criteria and design variables have to be taken into account at once during optimization, or may a decoupled approach lead to the same findings at a reduced cost and complexity?

To be able to answer these questions, several objectives must be achieved. These objectives are:

1. To examine and critically evaluate the content of existing research, theories, and evidence about designing unconventional configurations.
2. To develop a MDO tool to capture and enforce the design requirements that are most relevant to the overall sizing of a given unconventional configuration, in this case a box-wing aircraft.
3. To apply a simulation-based methodology for evaluating the aero-propulsive benefits of the BLI and non-BLI versions of the proposed aircraft.
4. To perform subsonic wind-tunnel experiments using a scale model of the proposed aircraft to further evaluate the particular characteristics of the configuration at off-design conditions.

5. To apply aerodynamic shape optimization on the Box-Wing configuration to demonstrate its potential aerodynamic advantage for reducing drag at transonic cruise conditions.

1.3 Thesis Outline

The research project is divided into six chapters, as shown in Fig. 1. This includes the present introductory chapter, where the objectives are defined, and a final chapter where the thesis conclusions are given (Chapter 6). This thesis contributes to the state-of-the-art of new trends in future aircraft development, considering design optimization, numerical simulations and wind tunnel experiments. Chapter 2 then presents a literature review of the most relevant unconventional configurations for future commercial airliners, considering design methodologies, new aerodynamic technologies, and simulation tools of each configuration. The literature review is conducted through an appropriate search protocol to ensure the selection of the most relevant sources. After a brief historical background, progress in the design and development of several unconventional aircraft configurations is presented. Concepts such as Blended/Hybrid Wing Bodies, nonplanar wing designs, next-generation propulsion technologies that are tightly integrated with the airframe, among others, are reviewed. Special attention is given to design methodologies (level-of-fidelity), cruise altitude, aerodynamic performance, and fuel-burn benefits over conventional configurations. The primary contributions of this review are: (i) a detailed survey of the design characteristics of unconventional aircraft for non-specialists, and (ii) a comprehensive review of the literature detailing past and current design trends of such configurations for specialists.

Chapter 3 describes the characteristics of a conceptual-level MDO tool. During the conceptual design of the aircraft, a low-fidelity MDO strategy was developed to identify a set of initial configurations. This process involved a parametric study on the main wing system, in which the aerodynamic performance of each configuration was evaluated in terms of the block-fuel for a given mission profile, while meeting performance and stability constraints. After determining the optimum wing shape, the effect of the integration of new engine technologies was evaluated, and a non-BLI and BLI versions of the aircraft were defined. Several aerodynamic evaluations were carried out on each of the concepts, and CFD simulations allowed to predict the main aerodynamic characteristics of the configurations by simulating real-scale conditions. This process served as a high-fidelity framework to compare the codes developed during preliminary aircraft design optimizations. Following that, a subsonic wind tunnel campaign employing a subscale model was conducted to further investigate the unique characteristics of the proposed configuration, as shown in Chapter 4. Experiments were performed at the Laboratory of Experimental Aerodynamics (LAE) of the Aeronautical Engineering Department at São Carlos School of Engineering -

Figure 1 – General outline of the research presented in this thesis.

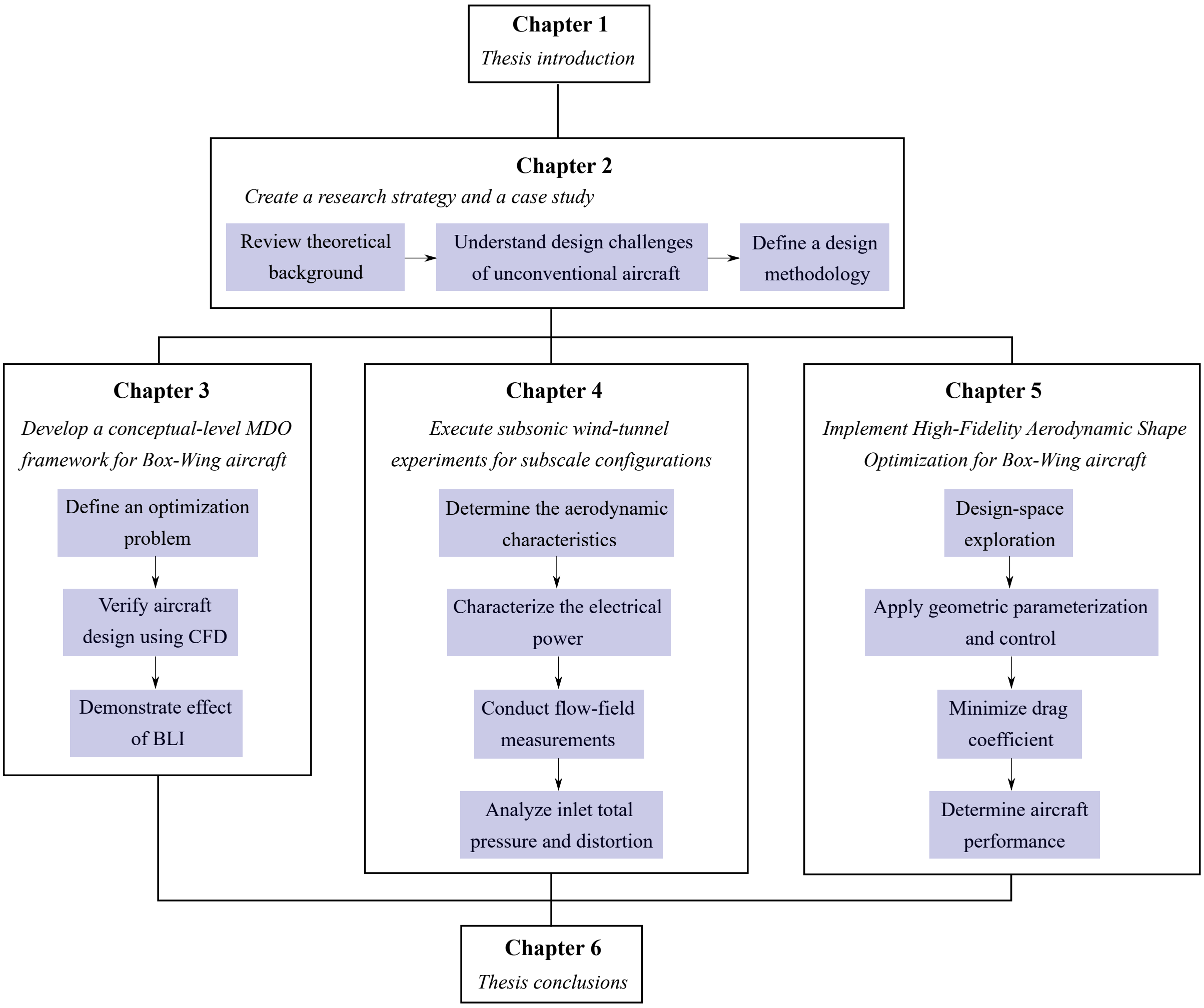

Source: The author

University of São Paulo (EESC-USP). The experiments involved a back-to-back comparison between the non-BLI and BLI configurations in terms of electrical power, flow mapping and total pressure distortion surveys.

Finally, in Chapter 5, a high-fidelity aerodynamic shape optimization method was applied to the aerodynamic design of the box-wing concept, even accounting for wing-fuselage flow interactions. A single-point aerodynamic optimization design explored drag-reduction potential and refined aerodynamic performance. The results presented in this thesis demonstrate the important aerodynamic trade-offs among the drag components generated by the aircraft. The aerodynamic optimization is performed through a framework called Jetstream, that has been developed at the University of Toronto Institute for Aerospace Studies.

2 UNCONVENTIONAL AIRCRAFT FOR CIVIL AVIATION: A REVIEW OF CONCEPTS AND DESIGN METHODOLOGIES

2.1 Introduction

According to the International Air Transport Association (IATA), air traffic tends to double every 15 years with an average growth of 4.4% per annum (OWEN; LEE; LIM, 2010). Despite the current setback caused by the COVID-19 crisis, it is expected that air traffic will recover quickly and resume its normal growth rate (ICAO. . . , 2021). In this context, the aeronautical sector faces a critical environmental challenge in terms of reducing the harmful effects of aircraft emissions on human health and climate change (JOHNSON; GONZALEZ, 2018).

Many countries have recognized the need to address global climate change and have adopted a set of ambitious targets to reduce emissions of carbon dioxide (CO_2) and nitrogen oxides (NO_x) (MACINTOSH; WALLACE, 2009). For instance, the Advisory Council for Aeronautics Research in Europe (ACARE) and the National Aeronautics and Space Administration (NASA) are already targeting these issues in short-term and long-term goals, which are periodically reviewed and updated by Committee on Aviation Environmental Protection (CAEP). For more details refer to the standards reported by Graham, Hall and Morales (2014). Airframe and engine noise also raise similar concerns, and discussions about novel solutions to aeroacoustic problems can be found in Casalino *et al.* (2008), Filippone (2014) and Knobloch *et al.* (2022). Most of these targets require a substantial commitment to research and development of new technologies, i.e., potential future benefits can be achieved if we move away from traditional concepts and introduce new technologies in many fields such as aerodynamics, materials, structures, engines, and systems. No single technology provides the entire solution by itself, but many are complementary and can be combined (ZINGG; GÜLDER, 2018). This multidisciplinary approach has provided a framework for setting standards in the design of new aircraft configurations, while meeting tighter environmental constraints (emissions and noise) (ABBAS; VICENTE; VALERO, 2013).

Based on this context, progress in unconventional configurations has been focused on the minimization of three key design objectives: Direct Operating Cost (DOC), which includes all costs associated with operating and maintaining an aircraft over its entire life cycle, and two main environmental objectives, CO_2 and NO_x emissions (GREEN, 2002; GREEN *et al.*, 2005). DOC is adopted as an economic criteria for aeronautical technology, i.e., the success of a future commercial airliner will depend exclusively on its performance. In contrast, aviation's environmental impacts form due to the combustion of jet fuel in the aircraft engines. The majority of those emissions are carbon dioxide, and water vapor, but there are other remaining emissions such as nitrogen oxides, sulphur oxides, carbon monoxide, hydrocarbons and particulate matter (HILEMAN *et al.*, 2013). The formation of these emissions depends on different factors. For example, CO_2 emissions and water vapor are directly proportional to the amount of fuel-burned, so they are strongly related with aircraft drag and weight. Conversely, NO_x and carbon monoxide depends on the specific mode of operation of the engine, as well as the way these emissions are deposited in the atmosphere, i.e., those emissions per unit of fuel-burned differ among take-off, cruise and approach (MAHASHABDE *et al.*, 2011). The optimization of such objectives has changed the way the aeronautical community foresees aircraft development in the future. Therefore, a significant number of innovative technologies continue to be developed. Several literature revisions summing up challenges, opportunities, and benefits of such technologies have been already published. If readers are interested in any of these technologies, we recommend searching in the following sources: for drag reduction (including viscous drag, wave drag and induced drag) (SCHRAUF, 2005; MAREC, 2001; NEITTAANMÄKI *et al.*, 2004; HEFNER; BUSHNELL, 1977; BUSHNELL, 2003; JOSLIN, 1998b; JOSLIN, 1998a; KRISHNAN; BERTRAM; SEIBEL, 2017); for weight savings (including advanced composites and alloys) (MANGALGIRI, 1999; LEQUEU *et al.*, 2001; SOUTIS, 2005a; YE *et al.*, 2005; SOUTIS, 2005b; TIMMIS *et al.*, 2015; MARINO; SABATINI *et al.*, 2014; ZHANG; CHEN; HU, 2018); for sustainable fuels (including biofuels and liquid-hydrogen) (SEHRA; JR, 2004; KHANDELWAL *et al.*, 2013; KRAMER, 2020; WITHERS *et al.*, 2014; BLAKEY; RYE; WILSON, 2011; RYE; BLAKEY; WILSON, 2010; GUPTA; REHMAN; SARVIYA, 2010; YILMAZ; ATMANLI, 2017; CECERE; GIACOMAZZI; INGENITO, 2014; DAGGETT; HENDRICKS; WALTHER, 2006; DAGGETT *et al.*, 2008); for next-generation propulsion technologies such as open rotors (FARASSAT *et al.*, 2009; GUYNN *et al.*, 2012; STÜRMER; YIN; AKKERMANS, 2014; ZANTE, 2015), distributed propulsion (KIM; PERRY; ANSELL, 2018; GOHARDANI; DOULGERIS; SINGH, 2011; GOHARDANI, 2013; SINGH; NALIANDA, 2014; BIJEWITZ *et al.*, 2017; JANSEN *et al.*, 2017), Boundary Layer Ingestion (BLI) (HENDRICKS, 2018; HABERMANN *et al.*, 2019; MENEGOZZO; BENINI, 2020; DIAMANTIDOU; HOSAIN; KYPRIANIDIS, 2022), and electric/hybrid/turboelectric aircraft (SARLIOGLU; MORRIS, 2015; MADONNA; GIANGRANDE; GALEA, 2018; GNADT *et al.*, 2018; HEPPERLE, 2012; PORNET; ISIKVEREN, 2015; BRELJE; MARTINS, 2018; SAHOO; ZHAO; KYPRIANIDIS, 2020; PELZ; LEISE; MECK, 2021).

Although these technologies have the potential to increase the aircraft efficiency, the challenges of their implementation require extensive research and development efforts towards reducing aircraft emissions, as well as trade-offs between different objectives. As a result, a great number of experiments and simulations are still being developed, in order to assess their overall benefits (JUPP, 2016; HASSAN; MAVRIS, 2019). Despite the efforts to date, there remains considerable uncertainty in terms of the potential fuel-burn, emissions, and noise reductions associated with the various proposed technologies.

Recognized aircraft design companies such as Airbus and Boeing, as well as research institutions and academia (NASA, DLR, ONERA, Bauhaus Luftfahrt, among others) are working on a variety of unconventional configurations. All these concepts aim to increase the ability to transport as much payload over the longest distance with the least amount of required energy or fuel as possible. Although these designs are only promising concepts, they offer a glimpse into the future (SCHMITT, 2001). These configurations provide benefits on two sides: by themselves due to better aerodynamics and/or lighter structures, and partly because they serve as platforms for the integration of new technologies, thus increasing the overall advantages.

This chapter aims to provide a survey of relevant research in next-generation aircraft that can replace current regional, single-aisle, and twin-aisle aircraft. The main objective is to provide a detailed overview of the actual benefits of unconventional configurations over conventional aircraft in the conceptual design stage. We also highlight the importance of the usage of MDO methods to assess different technologies along with conflicting requirements. The reports discussed in this work were identified based on the following methodology. Reports describing performance comparisons (in terms of fuel-burn benefits) between unconventional configurations and conventional tube-and-wing (CTW) aircraft are included. Literature reviews of related topics are also included. Reports based on disciplines (i.e., without any reference to unconventional aircraft design) are excluded. Reports focused on the design of different aircraft categories such as military, general and urban aviation, supersonic transports, and Unmanned Aerial Vehicles, are also excluded. The synthesis of the review process is provided in Appendix A.

The rest of this chapter is organised as follows: a historical background is provided in Section 2.2. A brief description of MDO frameworks that have been used to design unconventional configurations is provided in Section 2.3. Section 2.4 is devoted exclusively to the description and analysis of unconventional configurations, and provides some very rough ranges of estimates of the potential of each configuration. In Section 2.5, there is a discussion of cruise altitude in terms of the challenges it causes as well as its importance to climate change impact. Final considerations are given in Section 2.6. For more detailed information about the review process, the included and excluded reports, as well as selection and rejection criteria, see Appendix A.

2.2 Historical Background

The first flight of the Wright brothers in 1903 and the first flight of Santos-Dumont in 1906, were impressive proofs of concept but still far from suitable for practical use. Nevertheless, these heavier-than-air machines provided the foundation for the development of practical aerial navigation during the pre-war years. At the end of 1910, Glenn Curtis, whose biplane became the first to take-off from the deck of a ship, began to test planes as a platform for weapons. This last achievement marked a design trend for the next 35 years of aviation history, which was dominated by military applications (PETRESCU *et al.*, 2017). Progress in aerodynamics between World Wars I and II centered on the introduction of thick airfoil sections, the development of better flight controls and effective high-lift devices (ANDERSON; JR, 1998). These advances resulted from essential theories such as viscous flow and boundary layer theory by Prandtl, ideal fluid flow by von Karman, flight dynamics by Melvill Jones and compressible fluids by Taylor (DURAND, 2013).

In 1935, Busemann (1971) developed the concept of the wing sweep, which allowed aircraft to fly at higher speeds. The U.S engineers highly appreciated these benefits during World War II, incorporating this technology into new designs. The first two U.S. aircraft with 35° of sweep were both subsonic, the Boeing B-47 bomber and the F-86 Sabre (NELSON; ZINGG, 2004). At that time, Jones (1946) and Jones (1956) gained a critical understanding of the benefits of sweep and promoted its use for high-speed aircraft. Important contributions include swept-wing theory and the supersonic area rule. Based on these developments, large-scale strategic bombing campaigns were launched, fighter escorts introduced and the most versatile airplanes allowed precise attacks on small targets with dive bombers and fighter-bombers (GRANT, 2003).

By the time World War II came to a close, commercial aviation expanded rapidly using mainly ex-military aircraft to transport people and cargo. Companies increased the production of such an aircraft and more than 10000 Douglas C-47 Skytrain, which is a military transport aircraft developed from the civilian Douglas DC-3 airliner, were manufactured and converted for civilian missions (SPEARMAN, 1994). From the introduction of the DC-3 in 1936 to that of the DC-7 in 1956, more than 16000 aircraft were manufactured using mainly a scaling factor of the engine power, wingspan, and fuselage length, resulting in increased speed and payload capacity (FRENKEN; LEYDESDORFF, 2000). For this reason, the DC-3 is one of the most successful aircraft in history. Even today, there are few DC-3's still in service across the world (KELLARI; CRAWLEY; CAMERON, 2018). As the Boeing company had developed innovative and important bombers, revolutionary concepts such as the Boeing 707 and Boeing 727 enabled progress in jet engines and structural design. During the 60s, Boeing produced a wide number of short-haul jet-aircraft designs, and created a new aircraft to replace the 727 on short routes. Thus, the Boeing 737 made its first flight in 1968, and its design features have effectively become a blueprint for most jet airliners that have been manufactured since then (NORTON; OLASON, 1966; BEJAN; CHARLES; LORENTE, 2014). This achievement was boosted by extensive experimental and theoretical work on supercritical wings during the late 70s, such as the ones reported by Whitcomb and Clark (1965) and Whitcomb and Sevier (1960). The success of the Boeing 737 allowed it to stay in service for over half a century with several modifications applied to the fuselage, wings, empennage, and propulsion system (Boeing 737 family)

(SHAW, 1999; MCMASTERS; CUMMINGS, 2002; KELLARI; CRAWLEY; CAMERON, 2017). It is worth noting that other companies such as Airbus, Embraer, Bombardier, etc. have adopted the progress of the CTW aircraft to design and manufacture their own aircraft (HEERDEN; GUENOV; MOLINA-CRISTÓBAL, 2019).

Figure 2 shows the design evolution of commercial aircraft in terms of their measure of progress (technological innovations and more demanding missions) and time. Three main lines composed the conventions on this figure. The first line (dotted line) represents the timeframe line, which is a kind of stair-step progress focused on significant technological breakthroughs that occurred annually, until the launch of the Boeing 787. These breakthroughs include fly-by-wire systems, the use of composite materials, laminar flow control technologies, high Bypass ratio turbofans, among others, which in turn offer improved fuel efficiency, reducing operating costs and emissions. It is observed that the general layout of the CTW aircraft has remained predominantly the same, as this configuration represents a very efficient compromise between aerodynamics and weight, without compromising the safety and comfort of the passengers at high altitudes, i.e., the CTW aircraft is very well understood thanks to years of design, manufacturing and operating experience. That is one of the reasons why the entire fleet of Concorde aircraft was retired on October 2003, i.e., the Concorde deviated from the path traced by successful airplanes that preceded it (BEJAN; CHARLES; LORENTE, 2014). Although Concorde was a great technical achievement, the necessary changes to ensure adequate safety made this aircraft commercially unfeasible which was already at the limit of viability. Only 20 aircraft were manufactured, and fuel cost and ticket prices were always high (NELSON; ZINGG, 2004). Currently, there is a renewed interest in developing civil supersonic transports and supersonic business jets. Some literature reviews described the progress of these concepts, indicating that mitigation of sonic boom intensity is relevant if the vehicles intend to operate over land. There are also important design challenges such as airframe weight and propulsion-airframe integration, which need to be addressed to made these concepts more fuel-efficient and cost-effective (SUN; SMITH, 2017; SMITH, 2007; THIBERT; ARNAL, 2000; KUSUNOSE; MATSUSHIMA; MARUYAMA, 2011).

The second line (dash line) represents a point today, which is the culmination of progress made over the course of approximately 50 years of industrial and academic efforts on the commercial age. After half a century manufacturing the current CTW configuration, concerns about the impact of aviation on climate change require major technologies and investment to satisfy the needs of the vision for sustainable aviation (GRAHAM; HALL; MORALES, 2014). These challenges have a direct impact on the efficiency of air transportation, mainly on aerodynamic, structural and propulsion technologies. In this context, the aeronautical community is aware that current CTW aircraft cannot satisfy these criteria, because there are very small margins for improving, but in contrast, there are very high demands for satisfying. Therefore, major innovations are highly required (black-

Figure 2 – Progress in aircraft design of commercial airliners, from conventional designs to next-generation aircraft.

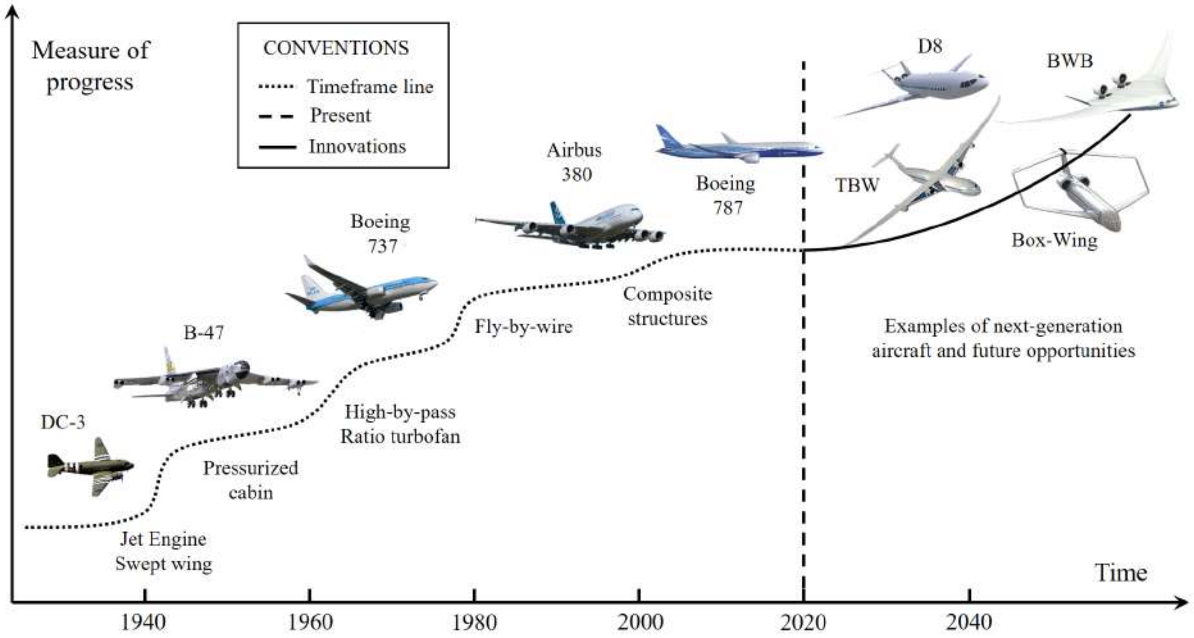

Source: The author

solid line), such as unconventional configurations, since they can provide the necessary improvements in the given timeframe (LANGE, 1988; MCMASTERS; CUMMINGS, 2004). There are many unconventional configurations that offer step-change benefits, some relying on key emerging technologies and/or integration concepts, and some with key barriers to improve. The state of research and development varies for each concept; however, several green aerospace projects (NACRE (FROTA, 2010), ERA (BONET *et al.*, 2011), SUGAR (BRADLEY; DRONEY, 2011a; BRADLEY; DRONEY, 2011b; BRADLEY; DRONEY, 2015a), Clean Sky (BRUNET; AUBRY; LAFAGE, 2015; BROUCKAERT *et al.*, 2018), NASA N+3, N+4 programs (GREITZER *et al.*, 2010; ASHCRAFT *et al.*, 2011), SE^2A (FRIEDRICHS *et al.*, 2022), among others) have identified the technological feasibility of the Blended Wing Body (BWB), Hybrid Wing-Body (HWB), hybrid-electric configurations, the Box-Wing (BW), the Strut-Braced Wing (SBW), the Truss-Braced Wing (TBW), and the Double-Bubble with aft-integrated BLI propulsion. These concepts are further discussed in section 2.4, which are expected to play a major role in reducing global net aviation carbon emissions for the longer-term future (2035 onwards) (CUMPSTY *et al.*, 2017). Figure 3 shows a rendering of some unconventional concepts that have been studied by the aeronautical community.

2.3 Brief Review of MDO Frameworks

The evaluation of unconventional aircraft and their possible technologies is often done for a specific set of requirements, usually due to limitations in terms of experience

Figure 3 – Unconventional aircraft configurations that could be critical for achieving improved fuel efficiency and reduced emissions. A conventional aircraft (centre) is surrounded by concepts for more efficient designs - clockwise from top left: box-wing configuration, strut-braced-wing configuration, lifting-fuselage configuration, and hybrid-wing-body configuration.

Source: Thomas Reist and David Zingg - University of Toronto Institute for Aerospace Studies.

and/or methods that would be needed for an extensive assessment. Therefore, MDO emerged as a way to address the complex design trade-offs in next-generation of aircraft. Several MDO solvers with different levels of complexity and fidelity have been employed in the design synthesis of unconventional configurations, from theoretical/semi-empirical methods to more complex high-fidelity aerostructural design optimization tools. Some authors such as Sobieszczanski-Sobieski and Haftka (1997), Vos *et al.* (2002), Martinez-Val and Perez (2009), Rocca (2012), Martins and Lambe (2013), Martins and Hwang (2013), Papageorgiou *et al.* (2018) and Kenway *et al.* (2019) have presented complete reviews of old and recent advancements in MDO for aeronautic applications.

Based on the above literature revisions, a summary of the level of fidelity, subjects, computational cost and accuracy is given in Fig. 4. The following observations can be made:

- The oldest and therefore the tools with the lowest computational cost are based on semi-empirical and linear methods, which continue to be used due to their ability to generate quick aerodynamic and mass estimations. However, mission output calculations must be re-evaluated at the later stages of the design process, especially for the transonic conditions. Since most low-fidelity methods use discrete variables such as the number of engines, wing position, aspect ratio, CG position, etc., gradient-free optimizers are best suited to explore wide design spaces. Particle Swarm Optimization and Genetic Algorithms are the most well-known methods that are widely used since they are very efficient in finding the global optimum for complex functions. Some examples of MDO frameworks like these are: Initiator (ELMENDORP; VOS; ROCCA, 2014), a preliminary sizing tool for conventional and unconventional aircraft configurations developed by Delft University of technology; PyInit (KARPUK; ELHAM, 2021), a physics-based design tool developed by Technische Universitat Braunschweig; AEROSTATE tool (SALEM *et al.*, 2021b), a conceptual design tool based on a constrained aerodynamic optimization procedure developed at University of Pisa; JPAD code (NICOLOSI *et al.*, 2021), a conceptual design framework for advanced turboprop aircraft developed by University of Naples Federico II; The tool FRIDA (FRamework for Innovative Design in Aeronautics) (IEMMA; VITAGLIANO; CENTRACCHIO, 2017), a multidisciplinary conceptual robust design optimization framework developed by Roma Tre University; and RDS aircraft design software (RAYMER *et al.*, 2011) developed by Conceptual Research Corporation.

- Medium-fidelity methods are more complex than low-fidelity tools. The main difference is the use of non-linear potential or Euler solvers which allow the solution of rotational, non-isentropic shock flows. Thus, they are fairly reliable for predicting wave drag due to their ability to capture the correct position of shock waves. Furthermore, mass estimation methods include elementary physics-based analysis for primary structures, and semi-empirical and statistical methods for secondary structures, thus providing a better accuracy when aerodynamic loads and structural analyzes come up with a coupled design. Some solvers also include 1D approaches for characterizing the propulsion system. In short, these methods provide consistent results to full working precision at very reasonable computational cost. Some examples of MDO and multi-fidelity modeling tools like these are: PrADO (WERNER-WESTPHAL; HEINZE; HORST, 2008), a preliminary aircraft design tool for unconventional aircraft configurations developed by Technische Universitat Braunschweig; SUAVE (LUKACZYK *et al.*, 2015; BOTERO *et al.*, 2016), an open-source environment for future aircraft design developed by Stanford University; TASOPT (DRELA, 2010), a computational tool developed by Massachusetts Institute of Technology which includes noise and emissions constraints into its main MDO environment; EDS (KIRBY; BARROS; MAVRIS, 2009), a physics-based software developed by Georgia Tech capable to estimate fuel-burn, source noise, exhaust emissions, performance, and economic parameters for potential future aircraft designs; FLOPS code (WELLS; HORVATH; MCCULLERS, 2017) developed by NASA to design new aircraft configurations and evaluate the impacts of advanced technologies; GENUS framework (SMITH *et al.*, 2019), a modern computer-based design method which uses a multivariate design optimization environment developed by Cranfield University; and Faber (CHAU; ZINGG, 2021), a low-to-medium fidelity tool developed by University of Toronto.

- Due to advances in high-performance computing, Reynolds-Averaged Navier–Stokes (RANS) simulations and Finite Element (FE) analysis have been successfully applied in aircraft conceptual design studies, particularly in aerodynamic shape optimization and aerostructural design optimization problems (SLOTNICK *et al.*, 2014). These high-fidelity frameworks are able to evaluate large numbers of design variables, design points, and constraints, allowing to sustain the evolutionary improvement of current designs and reducing the risk associated with the development of unconventional configurations. The choice of the optimization algorithm plays a key role when solving this kind of problems, and gradient-based algorithms combined with the adjoint method have demonstrated rapid convergence when controlling a wide range of design variables. The main disadvantage of gradient-based algorithms is that they find a local rather than a global optimum. However, this problem can be mitigated through the use of a gradient-based multi-start algorithm (CHERNUKHIN; ZINGG, 2013; STREUBER; ZINGG, 2021). Some examples of high-fidelity tools that have been used to design unconventional aircraft are: Jetstream code (HICKEN; ZINGG, 2010a; GAGNON; ZINGG, 2015; OSUSKY *et al.*, 2015), a multi-fidelity MDO framework with high-fidelity aerodynamic shape optimization developed by University of Toronto; SU2 (ECONOMON *et al.*, 2015), an open-source tool written by Stanford University in cooperation with the Boeing company to solve multiphysic and optimization problems on the basis of unstructured meshes; OpenMDAO (GRAY *et al.*, 2019), an open code written by NASA in cooperation with University of Michigan to facilitate gradient-based optimization and computation of derivatives. The University of Michigan is also recognized by the MACH-Aero, an open-source high-fidelity framework which uses pyOpt (PEREZ; JANSEN; MARTINS, 2012) to handle large-scale optimization problems, and DAFoam (HE *et al.*, 2020) and ADflow (MADER *et al.*, 2020) for flow simulation and adjoint computation. Further examples include the Onera elsA CFD software (CAMBIER; HEIB; PLOT, 2013), a multi-purpose tool for applied CFD and multi-physics; KADMOS (GENT; ROCCA, 2019), an MDO framework developed by Delft University and supported by the AGILE (Aircraft 3rd Generation MDO for Innovative Collaboration of Heterogeneous Teams of Experts) innovation project (CIAMPA; NAGEL, 2020; CIAMPA *et al.*, 2019); ADEMAO (KARPUK *et al.*, 2022), a multi-fidelity design, analysis, and optimization environment for future transport aircraft developed by Technische Universitat Braunschweig; and various software tools developed by NASA and Boeing (CHRISTOPHER *et al.*, 2020). Specific details of each software are beyond the scope of this review.

It is worth underlining that the estimates of the benefits of new configurations can vary quite a bit depending on the assumptions made and tools used. For example, the SBW concept proposed by Chau and Zingg (2021) assumes current technology levels other than the configuration, involving conceptual-level MDO and high-fidelity aerodynamic

Figure 4 – Hierarchy of MDO solvers with corresponding complexity and computational cost.

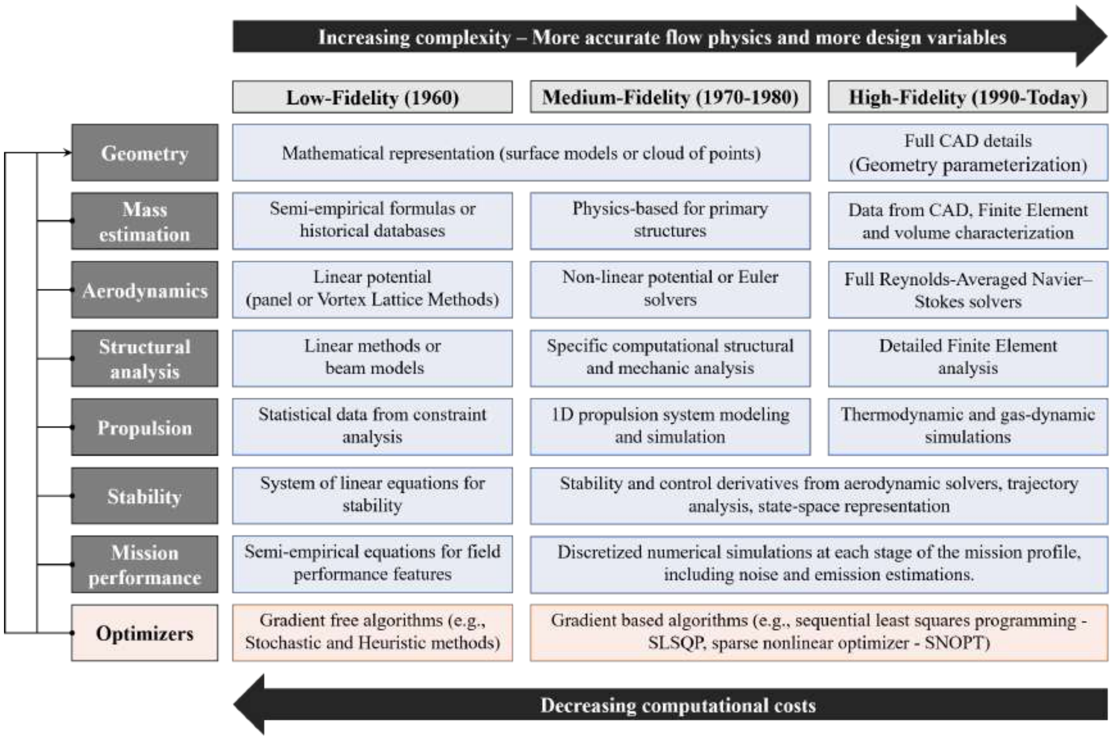

Increasing complexity – More accurate flow physics and more design variables

	Low-Fidelity (1960)	Medium-Fidelity (1970-1980)	High-Fidelity (1990-Today)
Geometry	Mathematical representation (surface models or cloud of points)		Full CAD details (Geometry parameterization)
Mass estimation	Semi-empirical formulas or historical databases	Physics-based for primary structures	Data from CAD, Finite Element and volume characterization
Aerodynamics	Linear potential (panel or Vortex Lattice Methods)	Non-linear potential or Euler solvers	Full Reynolds-Averaged Navier–Stokes solvers
Structural analysis	Linear methods or beam models	Specific computational structural and mechanic analysis	Detailed Finite Element analysis
Propulsion	Statistical data from constraint analysis	1D propulsion system modeling and simulation	Thermodynamic and gas-dynamic simulations
Stability	System of linear equations for stability	Stability and control derivatives from aerodynamic solvers, trajectory analysis, state-space representation	
Mission performance	Semi-empirical equations for field performance features	Discretized numerical simulations at each stage of the mission profile, including noise and emission estimations.	
Optimizers	Gradient free algorithms (e.g., Stochastic and Heuristic methods)	Gradient based algorithms (e.g., sequential least squares programming - SLSQP, sparse nonlinear optimizer - SNOPT)	

Decreasing computational costs

Source: The author. Information taken from Martins and Lambe (2013), Papageorgiou *et al.* (2018) and Kenway *et al.* (2019)

shape optimization to study shock formation and boundary-layer separation within the wing-strut junction; while others, such as the Double-Bubble D8 by Drela (2011), involves various future technologies such BLI, natural laminar flow and a lifting fuselage, although the conceptual design is based on low-to-medium fidelity approaches. In the former case, the benefit of the configuration is calculated in comparison to a CTW using current technology. In the latter case, the benefits come from future technologies, relative to today's aircraft. Furthermore, there is a clear trade-off between the efficiency of the design and the certainty that all requirements will be met when the design is subjected to better analysis methods, i.e., the benefits of the configurations from early conceptual studies to more recent high-fidelity studies have become clearer as the level of fidelity has increased.

2.4 Unconventional Configurations

This section looks at important unconventional aircraft design research that has been done by industry, government entities, and academia. In industry, new aircraft and/or engines are designed to generate income for the manufacturer, which means they have to provide a financial return or benefit for the operator. So they typically minimize a combination of DOC and Net Present Value (NPV), subject to meeting regulations. In this case, fuel consumption comes in through DOC, noise comes in through regulations, and emission reductions come via fuel-burn reductions and a little bit of regulatory pressure (ICAO's new CO_2 standard). Conversely, in academia and research institutes, more flexibility is given on the objective functions and design space, since results with real opportunities for future market is often a limiting factor. In any case, whether a technology is promising or not is ultimately determined by the financial viability and certification studies, rather than the technology's overall potential.

There are several entities worldwide actively involved in next-generation aircraft research, with a number of ideas put forward as a potential successors for the current CTW aircraft. Concepts like the SBW and TBW feature a very high aspect ratio wing, which aim to reduce drag during cruise, while trying to keep the weight as low as possible. The coupling between aerodynamics and structures makes it challenging to design optimal concepts. However, they are based on current fuselage designs, representing a lower cost and risk than other concepts such as the BWB or the Flying-V concept. In particular, the latter concepts target an increase in aerodynamic efficiency. However, a challenge with these concepts is the limited design experience and a larger uncertainty in, for example, structural mass estimation and stability behavior. Consequently, the predicted benefit and the confidence in that prediction must be higher for these concepts in order to justify the risk and investment needed from industry. Similarly, concepts like propulsive fuselage, distributed propulsion, hybrid-electric propulsion, among others, exhibit stronger interactions between the airframe aerodynamics and propulsion system, relative to CTW designs with podded engines, owing to the propulsor-airframe integration. Therefore, it is necessary to consider the challenges in manufacture, certifying the design, but also certifying the design process to ensure safety and integrate these new aircraft with existing airport infrastructure to allow a smooth operation.

Despite these limitations, which also represent an opportunity for future studies, there are potential technologies capable of competing with the current CTW configuration. IATA... (2021) reported the estimated fuel efficiency benefits of such technologies, including the technology readiness level (TRL) classification and the Entry into Service (EIS) (MANKINS, 2009; NAKAMURA; KAJIKAWA; SUZUKI, 2013) (Table 1). Note that some unconventional configurations have the potential to improve fuel efficiency on the order of 30%, but fully-electric or hybrid-electric aircraft are likely to cover a large part of efficiency gains. Therefore, there is a strong desire to improve the efficiency of future aircraft by introducing new technologies and new design concepts.

This chapter highlights the primary characteristics and performance estimates of unconventional configurations that have the potential to meet the most demanding requirements in terms of fuel reduction by enhancing the aerodynamic performance through the implementation of different technologies. However, according to the last independent expert integrated review panel, unconventional configurations are unlikely to be operational before 2037 (CUMPSTY *et al.*, 2017).

2.4.1 Blended/Hybrid Wing Bodies

The BWB concept is one of the most promising unconventional configurations, which provides many different aerodynamic benefits over CTW aircraft. In this design, the shape of the aircraft fuselage is modified so that it can contribute to the generation of lift, i.e. the fuselage and wings are blended together, creating a single lifting body, which offers major reductions in terms of interference drag and wetted area, increasing the aerodynamic efficiency and making available additional space in the cabin to increase passenger and cargo capacity.

The earliest publications about BWB configurations are those by Liebeck (2003), Liebeck (2004), Martinez-Val (2007) and Martínez-Val *et al.* (2010). Liebeck is recognized as one of the pioneers of the BWB configuration. His main contribution was the conceptual design of a double deck BWB that has been extensively studied by using high-fidelity CFD and wind tunnel tests. It is an 800-passenger BWB designed for flying 7000-n mile, which presented a 15% reduction in take-off weight and 27% reduction in fuel-burn per seat mile over a CTW aircraft of equivalent engine and structural (composite) technology for a 2010 entry into service. On the other hand, Martínez-Val reported some of the first conceptual design studies of a BWB configuration for 300 passengers, highlighting its prospects and challenges in subjects such as airport capacity, community noise, air space capacity, and emissions. Besides these significant contributions, Bolsunovsky *et al.* (2001), Okonkwo and Smith (2016) and Zhenli *et al.* (2019) developed complete literature reviews about the progress of the BWB configuration, from historical conceptions and challenges, to future developments and applications. Likewise, Liou, Kim and Liou (2016) summarized the contributions of NASA considering high-fidelity capabilities for designing advanced HWB configurations, specifically on HWBs with embedded engines.

In the past, the BWB design and also the flying wings were mainly conceived for military purposes such as the Northrop B-2 bomber. However, in civil aviation, the BWB configuration has been seen as a typical example of a futuristic aircraft which could enter service over the next few decades. Scientists from NASA, Boeing, Airbus, DLR, among others, have been working on their next generation airliner, testing BWB concepts for future commercial purposes. To explore its aerodynamic capabilities as well as stability and control handling properties, some experimental unmanned subscale concepts, such as the X-48 (shown in Fig. 5), and the MAVERIC concept have been manufactured and tested with a blended-wing design. In case of the X-48, flight tests showed that the aircraft was quieter than expected, and had a better fuel efficiency when flying with a greater payload weight (RISCH *et al.*, 2009). Likewise, the MAVERIC flew for the first time in June 2019, showing the potential to reduce fuel consumption by up-to 20% compared to

Table 1 – List of new technologies (2020-2050). The numbers mentioned below are based on the IATA - Aircraft Technology Roadmap to 2050 for Environmental Improvement[1].

Group	Concept	EIS	TRL	Fuel efficiency benefits
Aerodynamics	Natural Laminar Flow	After 2020	8	5 to 10%
	Hybrid Laminar Flow Control	After 2020	7	10 to 15%
	Variable camber / control surfaces	After 2020	5	5 to 10%
	Spiroid wingtip	After 2020	7	2 to 6%
Propulsion	GE9X	2020	8	10% (GE90-115B)
	Advanced turbofan	2020	8	20% (Trent 700)
	Counter Rotating Fan	After 2020	3	15 to 20%
	Ultrafan	2025	7	25% (Trent 700)
	Ultra-High Bypass Ratio engine	2025	5	5 to 10%
	Boundary layer ingestion[2]	2035	3	10 to 15%
	Hybrid-electric aircraft[3]	2030-40	3	40 to 80%
	Fully-electric aircraft[4,5]	2035-40	2	up to 100%
Systems	Fuel cells	2020	8	1 to 5%
	Electric taxiing system	2021	8	3%
Unconventional configurations	Strut- / Truss-Braced Wings[6]	2030-35	3	30%
	Box-wings[6]	2035-40	3	30%
	Morphing airframe	2040	3	5 to 10%
	Double-bubble aircraft[2,6]	2045	3	30%
	BWB / HWB[7]	2045	3	27 to 50%
Materials/Structures	Lightweight cabin interior	Retrofit		1 to 5%
	Structural health monitoring	Retrofit		1 to 4%
	Advanced materials	Production Upgrade		1 to 3%
	Active load alleviation	Production Upgrade		1 to 5%
	Composite primary structures	Production Upgrade		1 to 3%
	Composite secondary structures	Production Upgrade		$< 1\%$

[1] TRL and EIS are subject to substantial changes due to technological progress and COVID-19 crisis (ICAO..., 2021).
[2] Coupled with distortion tolerant fans.
[3] Depending on battery use.
[4] Primary energy from renewable source.
[5] Only for short range.
[6] With advanced turbofan engines.
[7] With hybrid propulsion.

Source: IATA... (2021)

Figure 5 – X-48B Blended Wing Body.

Source: X-48B (2017). Credits: NASA / Carla Thomas

Figure 6 – Dzyne Technologies' regional-sized BWB design concept.

Source: NASA (2017). Credits: NASA/DZYNE Technologies/Brendan Kennelly

current single-aisle aircraft (MAVERIC, 2020).

So far, the BWB configuration has been studied in many universities, companies, and government labs, mainly developing conceptual designs for different mission profiles. The major different BWB versions are summarised in Tables 2, 3, and 4 and are discussed next. The configurations are arranged by level of fidelity, highlighting the main performance characteristics, as well as fuel-burn benefits over their CTW counterparts. The following observations can be made:

- According to the mission profile, level of fidelity and top-level requirements proposed for each mission, BWB concepts have demonstrated higher ML/D values than existing CTW aircraft, which is mostly in the range of 15 assuming current technology levels (LEE *et al.*, 2001). This variable represents the most important metric for assessing aerodynamic performance, so the high values obtained by each BWB concept can imply a reduction in cruise fuel-burn, which can be translated into DOC savings

Table 2 – Summary of BWB concepts using low-fidelity tools.

References	Range [nm]	Cruise altitude [ft]	No. passengers	Mach number [-]	ML/D [-]	Fuel-burn reduction [%]	Remarks
Wakayama and Kroo (1998)	7500	35000	855	0.85	-	-	Conceptual design studies and cabin layout optimization using both gradient-based and genetic algorithms.
Bradley (2004)	7750	39000	450	0.85	-	-	A sizing methodology for the conceptual design of BWB configurations. The implemented methodology allowed to represent the trade-off between minimum thickness and planform cabin area.
Martinez-Val *et al.* (2007)	5400	45000	300	0.8	-	38	Conceptual design of a C-type flying wing using laminar flow control, vectored thrust, and active stability.
Dommelen and Vos (2014)	6000	36000	400	0.82	22.8	-	This paper reported three different BWB configurations at conceptual design level. Data for BWB with aft-swept wings with aft-mounted engines and winglets doubling as vertical tails.
Okonkwo (2016)	7620	36000	555	0.85	17.3	-	This thesis provides a complete low-fidelity framework for MDO of BWB configurations.
Ammar *et al.* (2017)	2354	35000	200	0.82	18.8	-	Conceptual design of a BWB concept including performance and dynamic stability studies.
Brown and Vos (2018)	3922	35000	250	0.8	17.5	22	Conceptual design methodology for BWB concepts within a semi-automatic design environment. This paper included data for other BWB with different payload requirements.
Centracchio, Rossetti and Iemma (2018)	900	25000	100	0.5	9.5	-	ARTEM BWB - a hybrid electric high-capacity regional BWB aircraft. This project involves the development of efficient models for the aeroacoustic assessment of this class of aircraft.

Source: The author

Table 3 – Summary of BWB concepts using medium-fidelity tools.

References	Range [nm]	Cruise altitude [ft]	No. passengers	Mach number [-]	ML/D [-]	Fuel-burn reduction [%]	Remarks
Ko *et al.* (2003)	7750	36500	478	0.85	25.5	-	This research reported an MDO for a BWB with distributed propulsion. Subsequent works included duct modeling within the optimization algorithm (LEIFSSON *et al.*, 2013).
Daggett *et al.* (2003)	3000	-	468	0.85	-	42	BWB 450-1U airplane. Fuel-burn benefits from BLI and active flow control.
Liebeck (2004)	7000	35000	800	0.85	18.4	27	Conceptual and preliminary design of a BWB configuration. This article discusses potential effects of BWB on air transport. Fuel-burn benefits from equivalent technology levels.
Qin *et al.* (2004)	7500	38000	800	0.85	20.1	-	Aerodynamic considerations of BWB design. The optimized BWB geometry provided an overall drag reduction of 9% against a baseline BWB. This study was limited to aerodynamic and trim considerations.
Hansen *et al.* (2006)	7667	35000	750	0.85	17.8	-	VELA project was created to develop design tools for a very efficient large BWB aircraft concept.
Hileman *et al.* (2010)	4500	45000	335	0.8	20.1	28	SAX-40 concept (Silent Aircraft eXperimental). This aircraft meets the noise requirements relative to the ICAO chapter 4. An MDO framework that assessed the benefit of BLI inlets can be found in (RODRIGUEZ, 2009).
Felder, Kim and Brown (2009) Felder *et al.* (2011)	7500	35000	300	0.8	-	25	The N3-X HWB concept employs turboelectric distributed propulsion which utilizes superconducting electric generators, motors, and transmission lines. Specific details of several disciplines can be found in (KIM; BROWN; FELDER, 2008; BROWN, 2011; ARMSTRONG *et al.*, 2012; BERTON; HALLER, 2014; KIM; LIOU, 2017; KIM; LIOU, 2019).
Kawai (2011)	6000	35000	375	0.8	-	25	Efficient low-noise HWB concepts (N2A and N2B) designed by Boeing. They are expected to offer significant benefits in noise reductions without compromising the fuel-burn. Highlights on duct modeling and BLI optimization can be found in Kim and Liou (2013).
Peifeng *et al.* (2012)	7300	36000	300	0.83	17.4	13	NPU-BWB-300 concept. This research focused on aerodynamic characteristics using equivalent levels of technology. Subsequent studies involved nacelle-airframe integration (ZHENQING *et al.*, 2019).
Nickol (2012)	7500	35000	301	0.84	19.7	6	This study investigated the question of HWB fuel-burn performance as a function of size. Data for a 300-pax Jetliner HWB based on the ERA project; other HWB categories and scaling studies were evaluated.
Nickol and Haller (2016)	6600	35000	216	0.8	24	45.3	Conceptual design and analysis of advanced subsonic commercial transport concepts. Data for a small twin aisle HWB concept; other versions such as very large twin aisle HWB concepts were also evaluated. Fuel-burn benefits relative to a 2005 best-in-class CTW aircraft.
Dorsey and Uranga (2021)	3000	36000	200	0.78	18.9	14.8	This study focused on design space exploration of BWBs. Data for a 200-pax single deck BWB; other categories and double deck BWB configurations were also evaluated.

Source: The author

Table 4 – Summary of BWB concepts using high-fidelity tools.

References	Range [nm]	Cruise altitude [ft]	No. passengers	Mach number [-]	ML/D [-]	Fuel-burn reduction [%]	Remarks
Bradley and Droney (2011a)	3500	35000	154	0.8	-	43	HWB from SUGAR program. This aircraft enables NOx reduction of 28% compared to CTW aircraft.
Lyu and Martins (2014)	7000	35000	800	0.85	18.5	-	High-fidelity aerodynamic optimization of a BWB using a multipoint approach, subjected to trim, static-stability, and root-bending-moment constraints.
Isikveren *et al.* (2015)	4800	41000	340	0.8	21.2	37	HWB with distributed propulsion and ultra-high by-pass rotors. Concept from DisPURSAL Project.
Reist and Zingg (2016)	500	46000	105	0.78	$17.9_{@HWB}$ $18.7_{@LFC}$	-	High-fidelity aerodynamic optimization of an HWB and a narrower version called the lifting fuselage concept (LFC). This work inferred that HWBs with narrow-centerbodies offer superior aerodynamic performance compared with classical BWBs in the regional class.
Prakasha *et al.* (2018a) Prakasha *et al.* (2018b)	4589	43000	450	0.8	-	-	HWB designed by DLR in AGILE-paradigm. This is a long-term project that focuses on BLI and distributed propulsion.
Yang, Page and Smetak (2018) Page, Smetak and Yang (2018)	3600	35000	120	0.8	-	30	Single-aisle airliner disruption with a single-deck BWB (Ascent 1000 BWB from DZYNE Technologies). Fuel-burn benefits from the combination of light structures, and a low drag design.
Reist *et al.* (2019)	2000	36000	100	0.78	16.2	-	Multi-fidelity and multidisciplinary optimization of HWBs with narrow centerbodies, involving stability and control requirements. Data for HWB with fin-equipped; other versions such as winglet-equipped were also evaluated.
Sgueglia (2019)	2750	35000	150	0.78	17.8	13.2	Multidisciplinary optimization of a BWB with distributed electric propulsion. Results have been compared to a conventional A320 aircraft based on the same top level requirements.
Karpuk, Liu and Elham (2020)	8099	35000	300	0.8	27.2	60	Multi-fidelity design of a long-range BWB. This particular concept involved advanced structural design with the integration of active flow control, active load alleviation and boundary layer ingestion with ultra-high bypass ratio turbofan engines.
Gray, Reist and Zingg (2021)	2000	36000	100	0.78	17.8	-	This work is a further exploration of HWBs with narrow-centerbodies including more demanding flight constraints. The optimum result burned 11.2% less fuel than a baseline HWB.

Source: The author

relative to CTW concepts. In particular, the high aerodynamic performance comes from large mean aerodynamic chord and high wetted aspect ratio, although more improvement can be expected by adopting advanced technologies, as in References (MARTINEZ-VAL *et al.*, 2007; DAGGETT *et al.*, 2003; NICKOL; HALLER, 2016; ISIKVEREN *et al.*, 2015; KARPUK; LIU; ELHAM, 2020), whose fuel-burn benefits are remarkable in comparison with CTW aircraft.

- Key technical aspects identified in early studies demonstrated that BWB concepts can reduce noise by shielding the propulsion system, providing an adequate space for installing distributed propulsion or BLI engines (LIEBECK, 2004; RODRIGUEZ, 2009). As a result, multiple MDO formulations, mostly medium-fidelity frameworks, were used to investigate the implications of next-generation propulsion technologies on BWB concepts, as shown in Table 3. In general, the primary benefit of BWBs with BLI is an overall improved system efficiency over podded engines, including reductions in ram and viscous drag, and propulsion integration weight. However, those benefits are largely offset by the engine performance loss from lower total pressure recovery, which increases pressure distortion at the engine fan face, resulting in a further reduction in fan efficiency. Particular concepts such as SAX-40 (HILEMAN *et al.*, 2010), and N3-X (FELDER; KIM; BROWN, 2009) demonstrated that up to a 15% reduction in fuel-burn can be achieved.

- The early studies focused on large capacity (400 to 800 passengers) and long range (up to 6000 nm) BWBs, showing a clear benefit in terms of payload range efficiency and fuel efficiency per seat when compared to conventional reference aircraft. Scaling studies, such as those reported by Nickol et al (NICKOL, 2012; NICKOL; HALLER, 2016), confirmed those findings, demonstrating that typical BWB configurations do not provide enough fuel-burn savings for smaller transport aircraft, because the magnitude of the potential fuel-burn benefit is a function of payload and design range. For example, a 98 passenger configuration burned more fuel (+4%) than a comparable CTW aircraft. Conversely, a 300 passenger configuration burned less fuel (−6%) than its CTW counterpart. A simple geometric analysis shows that the ratio of wetted area to floor area increases as the size of the BWB aircraft decreases, and hence the wetted aspect ratio is reduced for smaller BWBs (REIST; ZINGG, 2015). Therefore, high-fidelity aerodynamic shape optimization has been applied to new regional-class HWBs, as a potential method to obtain suitable drag reductions (REIST; ZINGG, 2016; REIST *et al.*, 2019) (see Table 4). These studies all come to the same result: HWB concepts for regional-class aircraft appear more like a narrow body with a distinct wing, offering a greater level of performance than a blended wing concept. Finally, a more recent effort showed that through design space expansion within a framework encompassing high-fidelity flow physics, the HWB was shown to be more efficient despite being required to satisfy low-speed trim and static margin constraints (GRAY; REIST; ZINGG, 2021).

Based on the above discussion and remarks of each configuration, we can infer that many organizations are seriously considering the BWB/HWB technology as a potential commercial venture. These concepts clearly provide a set of environmental and financial benefits that are appealing to next-generation civil aviation, such as increased cargo capacity at lower fuel-burn, which is critical for airline businesses because any fuel savings will benefit DOC. Nevertheless, several potential issues still require extensive research and development efforts. For example, large cabins imply new operational procedures to satisfy cabin safety requirements, such as new evacuation plans and load paths. Furthermore, passenger comfort problems in a roll maneuver may occur if they are sitting on the farthest sides of the aircraft's central part. Another issue is related to incompatibilities with the existing airport infrastructure, such as gates height and ground facilities. Finally, as the cabin hull is not cylindrical, structural problems may occur due to internal pressurization loads.

Although many of these challenges have been addressed on the DZYNE's Ascent1000 concept (Fig. 6), it involves major technological innovations unproven in any operating aircraft, such as the pivot-piston main-gear required for takeoff rotation, the structural advantages of PRSEUS panel construction, and the T-plug family-oriented manufacturing concept (YANG; PAGE; SMETAK, 2018; PAGE; SMETAK; YANG, 2018). The interactions among these novel technologies, introduced simultaneously, also exponentially increase the risk of innovation. However, we may deduce that DZYNE's Ascent1000 design is the aircraft with the greatest accomplished TRL among others in the same category, providing significant noise reduction, increased safety, increased comfort, and faster gate turns, posing real barriers to entry for a BWB transport.

2.4.2 Box-Wings

The BW configuration is a closed non-planar wing that has been extensively studied since Prandtl invented the "best wing system" in 1924 (PRANDTL, 1924). According to Prandtl, the best wing system is a box-wing that could reach much lower values of induced drag than equivalent monoplanes that have the same wingspan and lift. Such a theoretical foundation introduced the concept, and led to several efforts that have been focused on studying the induced drag problem in non-planar wings and their optimal lift distribution. For example, Kroo (2001) implemented a low-fidelity approach for assessing the aerodynamic properties of non-planar wings, demonstrating that box-wings decrease induced drag by allowing for span efficiencies greater than unity. Later, Frediani and Montanari (2009) studied the box-wing system assuming that the lift is equally distributed on the fore and aft wings, forming a butterfly-shaped distribution on the vertical tip fins.

Figure 7 – Lockheed Martin's box-wing concept for the N+2 study.

Source: Lockheed-Martin-Box-Wing (2017). Credits: NASA/Lockheed Martin

However, Demasi, Monegato and Cavallaro (2017) later showed that the distribution of optimal aerodynamic load/circulation over box-wings does not follow an elliptical law. Indeed, the actual solution has a shape that changes from quasi-elliptical for zero gap between the wings, to a constant distribution when the wings are extremely distant from each other (DEMASI; MONEGATO; CAVALLARO, 2016; DEMASI *et al.*, 2016). Modern computational aerodynamics has provided an additional perspective, demonstrating a strong correlation between numerical results and Prandtl's prediction (HICKEN; ZINGG, 2010b; RUSSO; TOGNACCINI; DEMASI, 2020).

Later conceptual design studies, at different levels of fidelity, have also confirmed Prandlt's hypothesis, concluding that box-wings offer superior performance than conventional wings, without exceeding airport span constraints or deviating dramatically from the CTW concept. Furthermore, recent studies have shown that the structural features of a closed wing system might contribute to a reduction in wing weight (ANDREWS; PEREZ, 2018b; SCARDAONI; MONTEMURRO; PANETTIERI, 2020), increasing reliability on the basis of a deep risk analysis for future development.

Comprehensive reviews about non-planar wing configurations are given by Cavallaro and Demasi (2016), Wolkovitch (1986) and Buttazzo and Frediani (2009). These publications discuss the design challenges and innovations of a variety of non-planar wing configurations, covering different engineering areas such as aerodynamics, structures, aeroelasticity, stability and control. Therefore, current projects have focused on examining the multidisciplinary interaction of those disciplines, in order to improve vehicle and system-level efficiency.

In this context, the first in-depth conceptual investigation was reported by Lange *et al.* (1974), under the NASA contract NAS 1-12413 in cooperation with the Lockheed Martin company. This project intended to improve the aerodynamic performance and enhance the payload capacity of a 400 passenger aircraft. Several configurations were explored and studies concerned both aerodynamic and structural aspects. Parametric studies revealed the optimum sweep combination for minimum drag is 45^o forward-wing sweep and -30^o aft-wing sweep. This arrangement provided a 30% lower induced drag than its CTW counterpart while retaining longitudinal stability constraints. The rest of the project was devoted to meet flutter criteria, which revealed that symmetric and antisymmetric modes occur below the required flutter speed. A more recent update of this project is the box-wing concept for the NASA ERA N+2 studies (Fig. 7). In this particular case, the aircraft features Hybrid Laminar Flow Control (HLFC), an advanced turbofan engine, and a fully composite structure (LOCKHEED-MARTIN-BOX-WING, 2017). Even with proven technology, this configuration requires further optimization, in order to find the best compromise among the entire characteristics of the aircraft.

Following this effort, a large number of research projects are still being explored, demonstrating that the deployment of the BW concept as a next-generation aircraft can provide a long-term solution to the growing demand of air passengers in the future decades. In particular, the University of Pisa is developing the research project called PARSIFAL (Prandtlplane architecture for the sustainable improvement of future airplanes), which is funded by the European Union under the Horizon 2020 program and intends to enter service in the 2030s (Fig. 8). Frediani, Cipolla and Rizzo (2012) presented the PrandtlPlane configuration in a review paper, summarizing motivations, possible applications, and experience gained in more than a decade of studies on the topic. The experience gained in PARSIFAL contributed to the conceptual development of BW aircraft of various categories, such as business jets and hybrid electric regional aircraft. Some of the main challenges along with general possible solutions were reported by Salem *et al.* (2021a). A large effort was the development of the IDINTOS project. This configuration is an ultralight amphibious PrandtlPlane, which was designed and manufactured as a technology demonstrator in order to study the advantages of a box-wing design over conventional configurations. The main technical data can be found in (FREDIANI; CIPOLLA; OLIVIERO, 2015; CIPOLLA *et al.*, 2016). In this study, two main advantages have been observed. First, the fore wing stalls first so that the aft wing introduces a significant negative pitching moment that keeps the aircraft away from the stall conditions. Furthermore, since the two wings are placed at a considerable distance from the center of gravity, the pitch damping moment is higher than in a conventional aircraft; thus, the longitudinal stability is improved. Such features along with various ongoing research activities have enabled other design perspectives, such as future urban air mobility configurations (DIAZ; YOON; THEODORE, 2018; KONING *et al.*, 2018).

Major design studies by academia and research centers are listed in Table 5, and Table 6. Different levels of fidelity, as well as payload and range capabilities are highlighted, and the concepts are discussed next:

Table 5 – Summary of Box-Wing concepts using low-fidelity tools.

References	Range [nm]	Cruise altitude [ft]	No. passengers	Mach number [-]	ML/D [-]	Fuel-burn reduction [%]	Remarks
Lange *et al.* (1974)	5500	37000	400	0.95	-	-	"Interim" configuration of the transonic Box-Wing studied at Lockheed in the 1970s. The results showed that a transonic biplane may have the same gross weight and superior fuel efficiency than a conventional reference.
Khan (2010)	3100	37000	189	0.78	18.6	-	The BW configuration reduced the induced drag by about 18% compared to CTW aircraft.
Schiktanz (2011)	1550	42300	150	0.78	15.9	9	Conceptual design of a BW aircraft using semi-empirical approaches. This research looked into a variety of subjects, with a focus on the flying qualities of the aircraft.
Jemitola (2012)	4000	36000	270	0.79	17.1	7	Conceptual design of a BW aircraft. An empirical equation for the mass estimation of the fore and aft wings was derived (JEMITOLA; MONTERZINO; FIELDING, 2013).
Beccasio, Tesconi and Frediani (2012)	2500	29000	250	0.75	12.3	-	Conceptual design of a BW aircraft powered by liquid hydrogen. The optimum aspect ratio and cruise altitude were determined as a trade-off between high performance and low environmental effects.
Zohlandt (2016)	2160	37000	144	0.78	14.1	8	Conceptual design of high subsonic Prandtlplanes. Data for single aisle - medium range aircraft; other categories were evaluated.
Garcia-Benitez *et al.* (2016)	6000	35000	250	0.82	18.5	-	Conceptual design of a non-planar wing concept. The best configuration increased range by about 17% compared to a CTW aircraft.
Kaparos *et al.* (2018)	2160	35000	180	0.78	-	-	Conceptual design of a BW aircraft using semi-empirical approaches and some CFD analysis for validation.
Bravo-Mosquera, Cerón-Muñoz and Catalano (2019)	1000	41010	160	0.78	14.2	10	Conceptual-level MDO of a BW aircraft coupled to a BLI system. Wind-tunnel experiments and high-fidelity optimization studies continue to be developed.

Source: The author

Table 6 – Summary of Box-Wing concepts using medium-fidelity and high-fidelity tools.

References	Range [nm]	Cruise altitude [ft]	No. passengers	Mach number [-]	ML/D [-]	Fuel-burn reduction [%]	Remarks
Salam and Bil (2016)	1000	35000	150	0.7	-	5	Multidisciplinary analysis of a BW aircraft using low-fidelity aerodynamics and a finite-element method for structural analysis.
Andrews and Perez (2018b)	1540	37000	86	0.74	12.6	1.2	Multidisciplinary analysis of regional-jet BW aircraft. Novel models for predicting static longitudinal stability and structural weight were developed (ANDREWS; PEREZ; WOWK, 2015; ANDREWS; PEREZ, 2018a).
Frediani *et al.* (2019)	2160	36000	320	0.79	16.2	20	PARSIFAL (Prandtlplane Architecture for the Sustainable Improvement of Future Airplanes). Results of this investigation demonstrated an increase in payload capability of 66% and a reduction in fuel consumption per passenger km up to 22%, in comparison with a conventional reference. The authors have also reported aerodynamic optimization (CARINI *et al.*, 2020), performance (CIPOLLA *et al.*, 2020), stability (CIPOLLA; SALEM; BACHI, 2019), structural (CIPOLLA *et al.*, 2021), and emissions (TASCA *et al.*, 2021) analyses.
Ciampa *et al.* (2019)	1943	36000	150	0.78	-	5.5	BW concept from AGILE project. The study focuses on the impact of the fuel trim system on the stability and control qualities of the vehicle.
Gagnon and Zingg (2016a)	500	36000	100	0.78	-	-	Aerodynamic trade-offs of a BW concept using an Euler-based approach. Induced drag was reduced by 43% compared to its CTW counterpart. This study did not include wing-body flow interactions.
Chau and Zingg (2017)	600	36000	100	0.78	13.9	7.6	RANS-based aerodynamic shape optimization of a regional-class BW concept.

Source: The author

Figure 8 – PrandtlPlane from PARSIFAL project.

Source: Salem *et al.* (2021b). Credits: Pisa University

- Overall, low-fidelity BW designs (Table 5) showed a lower induced drag, and a lower fuselage weight due to distributed bending loads than their CTW counterparts. Some minor differences were evidenced depending on the aircraft category. For example, for single-aisle - medium-range missions, the authors found fuel-burn benefits by about 7% considering a maximum payload. However, more significant gains are obtained by a long-range mission aircraft, where the low induced drag can produce a 10% saving on fuel-burn. This fact demonstrated that high-payload BW aircraft can handle existing airport constraints such as take-off and landing lengths, as well as wingspan limitations imposed by gate restrictions. Despite these exciting findings, some of these studies lack an effective optimization method and thus need more comprehensive research to achieve more reliable estimates of the potential benefits of this configuration.

- More recently, multidisciplinary studies of BW configurations allowed a deeper understanding of the trends leading to a reduction in fuel consumption for transport aircraft (Table 6). The main results demonstrated that the BW aircraft achieves a higher lift-to-drag ratio (L/D) at cruise, indicating superior performance in terms of cruise fuel burn over CTW aircraft. However, estimating the wing mass has been a significant challenge, and different methods have been used to obtain an acceptable level of accuracy, ranging from semi-empirical relations based on statistical data (JEMITOLA; MONTERZINO; FIELDING, 2013), beam finite element models (ANDREWS; PEREZ, 2018b), and structural surrogate models (CIPOLLA *et al.*, 2021). Although the BW can have a lower span than a CTW aircraft designed for the same mission, it can require a larger planform area if the fuel is stored in the wings, increasing the skin-friction drag, and wing weight (ANDREWS; PEREZ, 2018b). This gives the CTW aircraft an advantage over BW designs in terms of operational empty weight and maximum takeoff weight, reducing fuel consumption in take-off and climb. The distribution of fuel in the wings presents a design challenge. A potential solution is to hold a large volume of fuel inside the fuselage; however, this still requires extensive research efforts and introduces certification challenges. Finally, these BW concepts share specific design characteristics such as a rear installation of the engines and fuselage-mounted main landing gear, which increase fuselage weight, as well as cost and integration complexity.

- There are a few works focused on high-fidelity optimization of BW concepts (GAGNON; ZINGG, 2016a; CHAU; ZINGG, 2017). Such works provided a more detailed perspective about its benefits in terms of the geometric arrangement. For example, the area allocation between the fore and aft wings provides a unique capability to the BW to redistribute its optimal lift distribution. Since the two wings are placed at a considerable distance from the center of gravity, the pitch damping moment is higher than in a CTW aircraft; thus, trim and other design constraints can be satisfied without performance reduction. Such studies focused solely on the wing geometry, therefore, more detailed information about the actual performance of a BW concept can be obtained if the fuselage is included in the aerodynamic optimization. This subject is being analyzed on the INTI aircraft (BRAVO-MOSQUERA; CERÓN-MUÑOZ; CATALANO, 2019); results will be reported in future publications.

Although the practical benefits of the BW configuration can only be proved in a detailed design study, the concepts reviewed in this chapter demonstrated the potential for fuel-burn reduction and the importance of adopting a multidisciplinary design approach. In this regard, many areas require further studies. For example, through the viewpoint of flight dynamics, unconventional control surfaces may cause a more complex dynamic behavior. Therefore, CFD and/or wind-tunnel experiments are required to evaluate the dynamic derivatives, since empirical methods do not provide accurate results. Even though there is a recent study about the mission performance of a BW aircraft in low-speed conditions (SALEM *et al.*, 2020), high-lift devices still require high-fidelity analysis, in order to evaluate the actual behavior on the different flight phases of a transport mission.

Moreover, the aft wing of the BW configuration may suffer different types of aeroelastic instabilities, such as divergence due to its negative sweep angle (NANGIA; PALMER; TILMANN, 2003), and flutter, in which a dual-fin assembly is the most promising solution (FREDIANI; CIPOLLA; RIZZO, 2012). Some efforts have studied challenges and opportunities associated with dynamic aeroelasticity and the structural nonlinearities on the Prandtlplane aircraft (CAVALLARO *et al.*, 2015; BOMBARDIERI *et al.*, 2021). The authors demonstrated that its particular distribution of stiffness, along with its dual-fin configuration, prevents physical instability. The relevance of considering the vehicle's elasticity while evaluating its flying qualities is further highlighted by the authors. It is important to note, however, that the dual-fin configuration increases the structural weight and may be prone to shock formation and interference drag. Thus, their viability remains a challenge in a full-scale concept. As such, aerostructural optimization can provide a more detailed understanding of the effects of structures on weight and the entire aerodynamic performance. Finally, further research on the BW aircraft's manufacture is necessary, in order for industry to take on the development cost and risk of this configuration.

2.4.3 Strut- and Truss-Braced Wings

Since 1950, the SBW configuration has been studied to evaluate its feasibility and potential features. The SBW configuration enables a substantial span increase, even reducing the structural weight, thereby decreasing induced drag to yield a net fuel-burn benefit. The idea of using an SBW for a long-range transonic transport aircraft was first proposed by Pfenninger at Northrop from 1950 to 1980 (PFENNINGER, 1954). Other pioneering SBW studies were performed at NASA and Lockheed (SMITH *et al.*, 1981; TURRIZIANI *et al.*, 1980), demonstrating that SBW concepts with high aspect ratio wings can improve cruise range when compared to a same baseline concept.

Likewise, the TBW emerged due to the potential benefits of the SBW. The main difference is that TBW concepts have a strut and jury members connecting the strut and the main wing, enabling the aspect ratio to be further increased. However, longer wings are subject to flutter, so trusses are used to alleviate this phenomena. Such a configuration needs a significantly larger design space, since truss members require additional design variables to account for the size and shape of each member in the truss. In this context, the two primary implications of SBW and TBW concepts are flutter and shock waves in junction regions and in the "channel" formed by the strut. Buckling is also a design challenge for the SBW, since the strut is compressed during negative load conditions, and the inboard wing segment is compressed during positive load conditions, resulting in increased weight penalties (CHAU; ZINGG, 2021). This is generally true for all joined wing systems, including box-wings, which are statically indeterminate structures. It is important to note that the main challenges in terms of aerodynamic and structural nonlinearities represent a design opportunity, since detailed design and certification require more accurate procedures (CAVALLARO; DEMASI, 2016).

Grasmeyer (1999) investigated the benefits of SBW concepts over advanced CTW aircraft. The optimum configuration showed a 15% reduction in takeoff gross weight, a 29% reduction in fuel weight, a 28% improvement in L/D ratio, and a 41% increase in seat-miles per gallon. Since this work, several MDO methods have been developed to study the design characteristics of SBW and TWB configurations. Table 7, Table 8, and Table 9 summarise major design studies by academia and research entities arranged by level of fidelity. The main design and performance characteristics are presented and discussed as follows:

- The most important outcomes showed the advantage of strut and simple truss configurations over CTW cantilever aircraft in terms of fuel-burn. The high wingspan

Table 7 – Summary of SBW and TBW concepts using low-fidelity tools.

References	Range [nm]	Cruise altitude [ft]	No. passengers	Mach number [-]	ML/D [-]	Fuel-burn reduction [%]	Remarks
Grasmeyer (1999)	7380	39432	305	0.85	23.3	29	MDO of several SBW concepts, including advanced technologies such as Natural Laminar Flow (NLF) and relaxed static stability to increase performance. Fuel-burn benefits over a 1995 technology aircraft.
Gundlach *et al.* (2000)	7500	42300	325	0.85	21.6	13.6	Conceptual design of an SBW concept focused on takeoff gross weight reduction. Data for fuselage-mounted engines, and performance benefits given for a 2010 service entry date aircraft.
Gur *et al.* (2010)	7730	$47000_{@SBW}$ $48000_{@TBW}$	305	0.85	$21.2_{@SBW}$ $21.2_{@TBW}$	$3.9_{@SBW}$ $8.8_{@TBW}$	Single objective optimizations of SBW and TBW concepts at different levels of technology. Three objective functions were studied: minimum takeoff gross weight, minimum fuel consumption, and maximum L/D ratio. Data for minimum-fuel objective and current technology levels.
Gur *et al.* (2011)	7730	48000	305	0.85	$22.8_{@SBW}$ $27.9_{@\frac{TBW}{1-jury}}$ $29.4_{@\frac{TBW}{2-jury}}$	$8.6_{@SBW}$ $18.1_{@\frac{TBW}{1-jury}}$ $19.8_{@\frac{TBW}{2-jury}}$	MDO of SBW and TBW concepts assuming aggressive laminar flow on wings, fuselage, and fairing. Fuel-burn benefits are given for three distinct configurations at the same level of technology of a CTW counterpart.
Gur, Schetz and Mason (2011)	7730	48000	305	0.85	$31_{@0.01}$ $36.5_{@0.5}$ $38.2_{@0.75}$	- - -	MDO of TBW concepts (2-jury). This work focused on several drag-reduction technologies into the optimization loop such as fuselage relaminarization, surface riblets, tailless arrangements, and Goldschmied propulsion apparatus.
Hosseini *et al.* (2020)	1240	20000	72	0.5	9.6	9.6	Conceptual design of a TBW concept for regional missions. This work involves medium fidelity aerodynamics and low order mass estimation methods.

Source: The author

Table 8 – Summary of SBW and TBW concepts using medium-fidelity tools.

References	Range [nm]	Cruise altitude [ft]	No. passengers	Mach number [-]	ML/D [-]	Fuel-burn reduction [%]	Remarks
Gern *et al.* (2001)	7500	42300	325	0.85	25.1	12.2	MDO of an SBW using a refined aerodynamic module by using CFD simulations and a structural module to evaluate the aerodynamic loads. Data for fuselage-mounted engines and minimum fuel weight objective; other categories, objective functions and engine location were evaluated.
Meadows *et al.* (2012)	3115	$45700_{@SBW}$ $48800_{@TBW}$	162	0.78	$28_{@SBW}$ $30.3_{@TBW}$	$8.5_{@SBW}$ $9.2_{@TBW}$	MDO of SBW and TBW concepts. This work focused on engine installation (wing and fuselage) assuming advanced aerodynamic technology levels. Fuel-burn benefits are given for wing-mounted engines at the same level of technology of a CTW counterpart.
Chakraborty *et al.* (2015)	3500	45000	154	0.7	-	-	MDO of SBW and TBW concepts (1-jury) using NLF technologies. The TBW with NLF on wing upper and lower surface (70%) was transferred to Boeing Company for further detailed analysis (SUGAR TBW concept).
Mallik *et al.* (2015)	7730	48000	305	0.85	23.1	6	MDO of TBW concepts considering the effects of flutter. Data for minimum-fuel objective and advanced aerodynamic technology levels over CTW aircraft with same technology.
Ma, Karpuk and Elham (2022)	3400	33000	186	0.78	18.3	23.1	Conceptual design of different SBW concepts with advanced airframe technologies and materials. A comparative study over twin-fuselage concepts is also discussed in this article. Data for medium-range mission, and performance benefits compared to A320neo aircraft.

Source: The author

Table 9 – Summary of SBW and TBW concepts using high-fidelity tools.

References	Range [nm]	Cruise altitude [ft]	No. passengers	Mach number [-]	ML/D [-]	Fuel-burn reduction [%]	Remarks
Carrier *et al.* (2012)	3000	39000	150	0.75	-	5.7	MDO of the Albatros project carried out by ONERA. The SBW concept increased the wing aspect ratio while decreasing sweep angle and airfoil thickness, resulting in laminar flow across a significant portion of the wing surface. High-fidelity aerodynamic and structural analyses can be found in (CARRIER *et al.*, 2022)
Bradley, Droney and Allen (2015)	900	40800	154	0.72	18.1	56	SUGAR High (765-095) concept - a high aspect ratio SBW design with 2030s advanced technologies (primarily to wing weight, propulsion, and aerodynamics). Fuel efficiency relative to current CTW.
Bradley and Droney (2015b)	900	42000	154	0.72	17.9	63.4	SUGAR Volt (765-096) concept - a similar layout to the SUGAR High that has been resized to accommodate modular battery packages and a hybrid gas turbine electric propulsion system. Fuel/energy efficiency relative to current CTW.
Droney *et al.* (2020)	900	40000	154	0.74	19.4	57	Sugar High (765-095 Rev-J) - a transonic TBW variant. Higher-order tools were used to create this concept, which was then tested in a wind tunnel. Fuel-burn benefits compared to a CTW with technology levels representative of the 2008 single-aisle fleet.
Gagnon and Zingg (2016b)	550	34500	100	0.78	-	-	High-fidelity optimization of several unconventional concepts using an Euler-based approach. The SBW showed a drag reduction by about 40% compared to a conventional reference.
Moerland *et al.* (2017)	1700	42093	154	0.72	19.1	32	SBW carried out by DLR applying collaborative design. The concept includes open rotors as novel propulsion technology and NLF.
Torrigiani *et al.* (2018)	1890	36000	90	0.78	-	0.87	SBW from AGILE project. This aircraft included board system design and cost assessment, proving that when several systems are included in the design space, only a minimal improvement over the conventional reference can be achieved.
Secco and Martins (2019)	-	30000	-	0.72	14.9	-	RANS-Based aerodynamic shape optimization of an SBW concept. Total drag reduction by about 14.7%.
Maldonado *et al.* (2020)	-	40000	-	0.74	16.7	-	Computational analysis of a TBW concept using unstructured and structured grids. Experimental campaign findings were compared to computational aerodynamic data.
Chau and Zingg (2021)	500	44670	104	0.78	16.4	7.6	Conceptual-level MDO and aerodynamic optimization of an SBW concept using a RANS-based approach. Performance benefits are given assuming 2020 technology levels.

Source: The author

of these concepts, which can be vulnerable to aeroelastic phenomena, posed significant structural and aerodynamic uncertainties in the early studies. However, most recent medium fidelity frameworks expanded their capabilities by considering the extent of laminar flow on the wings, fuselage relaminarization, structural characteristics, the influence of supercritical airfoils on the wing-strut intersection and the effects of flutter (Table 8).

- SBW and TBW concepts demonstrated higher ML/D values than CTW counterparts. This is an anticipated outcome, since these concepts have higher aspect ratio wings and are designed to operate at higher cruise altitudes than conventional aircraft. Furthermore, the studies reported different design approaches in terms of objective functions, design constraints and technological feasibility. For example, some aircraft used a set of aerodynamic considerations for reducing skin-friction drag such as fuselage relaminarization, surface riblets, and tailless arrangements, which increased the ML/D values substantially. Conversely, some aircraft are constrained by the effects of flutter, and also penalized by interference drag. Therefore, there is a discrepancy in the stated values. The authors agree that such configurations presented optimistic ML/D values, as a result of the inclusion of aggressive technologies. However, due to current technological limitations, these statistics cannot be regarded as realistic, requiring further research efforts.

- A few efforts have looked into aerodynamic shape optimization to study the aerodynamic interactions between SBW surfaces (e.g., reduction of shocks and separation in the wing-strut junction). Gagnon and Zingg (2016b) performed an Euler-based aerodynamic shape optimization on several unconventional configurations (see Fig. 9), enabling comparison of four distinct configurations. The authors designed and optimized a BW, a C-tip BWB, and an SBW concept for the same regional mission (similar to the Bombardier CRJ-1000) and subjected to the same problem formulation. The SBW configuration obtained the least amount of drag (-40.3%) relative to an equivalently optimized CTW, followed by the C-tip BWB (-36.2%), and finally the BW (-34.1%). Such results demonstrated the high potential of the SBW configuration relative to other unconventional configurations. Nevertheless, RANS-based optimization is needed to increase the confidence in these comparisons. Recent efforts, however, have demonstrated that aerodynamic shape optimization is effective in eliminating shocks at the wing-strut junction using a RANS-based approach. In particular, Secco and Martins (2019) at low Mach numbers using the PADRI SBW geometry (BIELER *et al.*, 2018), and Chau and Zingg (2021) at more conventional transonic Mach numbers (regional-class aircraft).

In addition to such important progress on the development of SBW and TBW configurations, there is also remarkable progress on aero and structural characteristics

Figure 9 – Regional transports, dimensions in meters.

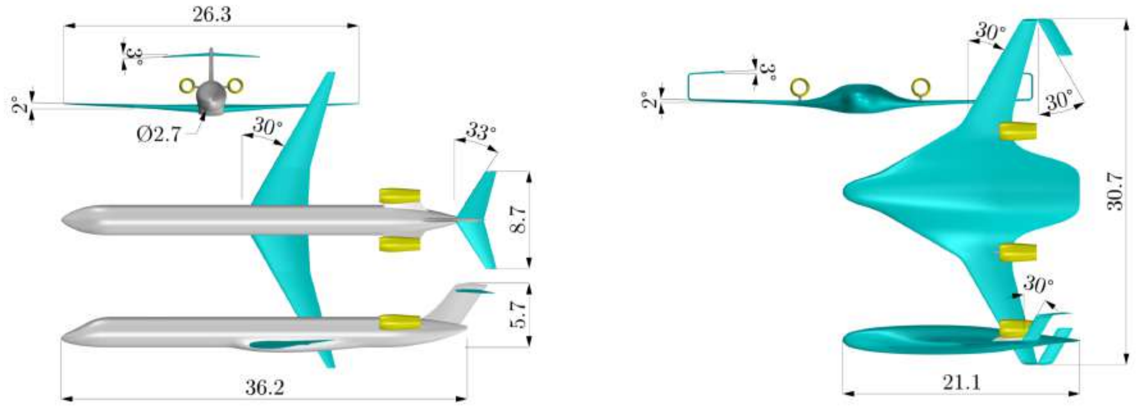

(a) Baseline conventional aircraft.

(b) C-tip BWB aircraft.

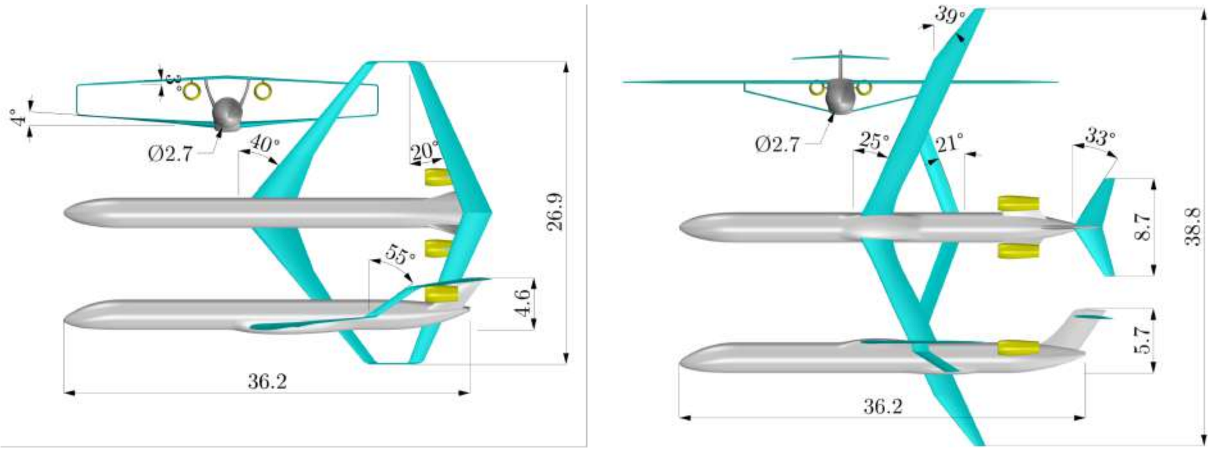

(c) Box-wing aircraft.

(d) Strut-braced wing aircraft.

Source: Gagnon and Zingg (2014)

that has been in continuous development since 2008 in the SUGAR program under NASA and Boeing sponsorship (BRADLEY; DRONEY, 2011a; BRADLEY; DRONEY, 2011b; BRADLEY; DRONEY, 2015a). During phase I, researchers selected baselines and advanced configurations, conducted performance analyses, and measured noise and emissions. Additional technologies such as liquefied natural gas, hydrogen, fuel cell hybrids, BLI propulsion, unducted fans, and advanced propellers were evaluated in phase II. Phases III and IV focus on improving the maturity of CFD models and experimental campaigns in order to facilitate industry adoption of transonic TBW technology, i.e., the objective is to identify remaining technical and certification challenges, and develop a roadmap for the continued systematic reduction in risk (HARRISON *et al.*, 2020). An aircraft example from SUGAR program is the SUGAR Volt (Fig. 10), that has been optimized under several aeroelastic constraints before being validated in high-speed wind tunnel tests. This particular concept also involves critical technologies such as hybrid electric propulsion, and high rate composite manufacturing, promoting a radical fuel-burn reduction of 63.4% compared to a 2020 in production aircraft, thus demonstrating that a high ML/D and

Figure 10 – SUGAR Volt aircraft.

Source: SUGAR… (2017). Credits: NASA/The Boeing Company

lighter materials enable much greater range for a given battery energy density, as stated by Bushnell (2018).

As described in this section, many studies have been conducted to explore the potential of SBW and TBW in a multidisciplinary way. The following aspects illustrate the main advantages of such configurations: (i) the strut provides a bending load alleviation to the wing, allowing for a decreased thickness to chord ratio, and consequently, a reduction of wing weight and lower transonic wave drag. (ii) the truss allows for higher aspect ratios, providing a significant reduction in induced drag. This condition also allows for smaller wing sweep, which can provide natural laminar flow over conventional transonic wings, reducing viscous drag. Given the large wingspan of both concepts, folding wingtips are mandatory in order to meet the gate constraints of the airports.

Regarding the structural and aeroelastic characteristics of these configurations, the best flutter performance for SBW occurred when the wing and strut had the same sweep angle, whereas the TBW provided the best flutter performance using a swept-forward strut, reducing both the natural frequencies and flutter speed (BHATIA; KAPANIA; HAFTKA, 2012). Cost-benefit analyses are needed to determine the feasibility of using active flutter-suppression mechanisms, as current technologies may add weight, impacting on the gross take-off weight or the fuel-burn (JONSSON *et al.*, 2019). In conclusion, both the SBW and TBW concepts are promising innovative designs for next-generation airliners, with the highest TLR among other unconventional configurations.

2.4.4 Advanced Propulsion Concepts

Airframe-propulsion integration is considered one of the most important aspects in aircraft design, since the Specific Fuel Consumption has a direct impact on the DOC of a new aircraft. The most conventional way to reduce the Specific Fuel Consumption is increasing the bypass ratio, which improves the propulsive efficiency, and compensates the thrust loss by increasing the mass flow rate. However, the integration of high bypass ratio engines using pylons results in a large wetted area and heavier structures, increasing fuel-burn (EARLY, 2000). As a result, most novel propulsion concepts integrate the engines in alternative positions, providing drag and acoustic benefits (BIJEWITZ *et al.*, 2016). For example, distributed propulsion, BLI propulsion, and electrified propulsion are projected to maximize vehicle benefits by coupling propulsion and wing aerodynamics. These advanced technologies have enabled engineers to design new types of aircraft that will serve new roles in the future.

There are appropriate reviews summarizing the most important developments in terms of aircraft propulsion technology. For example, Gohardani, Doulgeris and Singh (2011) and Gohardani (2013) reported complete literature revisions of design challenges of distributed propulsion technology and its potential application on next-generation commercial aircraft. Conventional and alternative configurations were extensively reviewed, highlighting the potential application of distributed propulsion using podded and BLI technologies on BWB and HWB configurations. Other literature reviews involving BLI modeling and its effects on aircraft design were presented by Hendricks (2018), Habermann *et al.* (2019), Menegozzo and Benini (2020) and Diamantidou, Hosain and Kyprianidis (2022).

More than 70 all-electric conceptual, experimental, and commercial aircraft along with progress in battery technology were reviewed by Gnadt *et al.* (2018). In this case, the performance of such aircraft was compared to advanced fuel-powered CTW aircraft at the same design range. Performance limitations of full-electric aircraft are presented by Hepperle (2012), where a variety of propulsion systems were investigated with a focus on energy and battery storage systems. Recently, Brelje and Martins (2018) reported an overview of electrical components and electric propulsion architectures. The authors reviewed existing commercial products, demonstrators, and conceptual design studies, in order to provide a list of potential benefits and disadvantages of electric propulsion for future high-fidelity multidisciplinary design of electric aircraft.

Although many studies have been well summarized and discussed in previous reviews, this section summarizes the unconventional concepts that have been designed with revolutionary propulsion technologies for commercial aviation. Some of them are already described in the previous sections due to their synergy with innovative airframes. Table 10, Table 11, and Table 12 list other design studies by academia and government entities, arranged by the type of propulsion system, showing the product between Mach number and lift-to-drag ratio (ML/D) at cruise, as well as fuel/energy benefits over conventional configurations. Each of the configurations involve multiple technologies, with different payload and range capabilities and are discussed next:

Table 10 – Summary of Boundary Layer Ingestion concepts.

References	Range [nm]	Cruise altitude [ft]	No. passengers	Mach number [-]	ML/D [-]	Fuel-burn reduction [%]	Remarks
Drela (2011)	3000	39000	180	0.72	16.8	33	Double Bubble with Aft-integrated BLI propulsion (D8). CFD simulations and wind tunnel experiments have been carried out on this concept (HALL; LIEU, 2021; URANGA *et al.*, 2017).
Singh *et al.* (2014)	4800	41000	340	0.8	21.8	8.9	Conceptual design of propulsive fuselage concept from DisPURSAL project. Propulsion system was sized using parametric models for integrated aircraft.
Wiart *et al.* (2015)	3000	37000	180	0.82	17.2	-	NOVA concept from ONERA including side-mounted BLI engines. RANS simulations coupled with an actuator disk evaluated the propulsion-airframe integration characteristics.
Bijewitz *et al.* (2016)	4800	41000	340	0.8	24.7	9.4	MDO of propulsive fuselage concept from DisPURSAL project. The propulsion system was modelled using CFD and gas turbine performance estimates.
Welstead and Felder (2016)	3500	38500	154	0.72	16.5	12	NASA's STARC-ABL aircraft. A turboelectric propulsion system with an electrically driven BLI mounted on the fuselage tail cone. Fuel-burn benefits relative to an advanced conventional reference. High-fidelity optimizations can be found in Gray *et al.* (2018), Gray and Martins (2019), Gray *et al.* (2020), Yildirim *et al.* (2021), Yildirim *et al.* (2022).
Seitz *et al.* (2021)	6500	41000	340	0.82	17.0	11.3	Proof of concept study of Centreline concept with propulsive fuselage by Bauhaus Luftfahrt. Fuel-burn benefits relative to an advanced conventional reference.
Samuelsson *et al.* (2021)	3500	37000	180	0.8	19.6	7.8	Propulsive Fuselage with turbo-electric propulsion and advanced technologies (NLF on nacelles, variable camber and high aspect ratio wings).
Ahuja and Mavris (2021)	3450	35000	180	0.78	-	-	This study focused on aero-propulsive coupling during the conceptual design of top-mounted and side-mounted BLI configurations.
Karpuk and Elham (2021)	2000	35000	200	0.78	17.2	43.6	This aircraft combines the benefits of forward swept wing, active load alleviation and BLI technologies in a multi-fidelity approach. This concept reduces fuel-burn by 43.6% compared to a conventional aircraft with 2020 technology.
Secchi *et al.* (2021)	1500	35000	84	0.75	10.7	7	Regional aircraft with a BLI electric engine at the fuselage tail cone. This study implemented parametric variations of the thrust split ratio and electric fan pressure ratio.

Source: The author

Table 11 – Summary of open rotor concepts and new turboprop aircraft.

References	Range [nm]	Cruise altitude [ft]	No. passengers	Mach number [-]	ML/D [-]	Fuel-burn reduction [%]	Remarks
Guynn *et al.* (2009)	3060	35000	162	0.72	-	24	This paper describes assessments of an open rotor aircraft. The open rotor aircraft is predicted to have 24% lower fuel-burn than a 1990s reference baseline aircraft.
Larsson, nstedt and Kyprianidis (2011)	3000	35000	150	0.73	-	15	Multidisciplinary conceptual design of an open rotor configuration using low-fidelity tools. Fuel-burn benefits relative to a 2020 technology conventional aircraft.
Raymer *et al.* (2011)	2774	30000	180	0.8	20	60	Advanced transport aircraft concept including tandem open rotors and NLF wings. Fuel-burn benefits relative to a 2010 technology conventional aircraft.
Guynn *et al.* (2011)	3250	35000	150	0.72	15.4	30	Medium-fidelity conceptual design of an open rotor concept. Fuel consumption reduction relative to 1990s technology.
Perullo *et al.* (2013)	-	35000	-	0.8	-	29	Advanced open rotor performance modeling for multidisciplinary optimization evaluations. Fuel consumption reduction relative to a modern baseline.
Gern (2013)	6500	35000	244	0.8	-	-	Conceptual design of an HWB including open rotors. This concept was subjected to both low- and high-fidelity structural investigations.
Dorsey and Uranga (2020)	4000	37000	200	0.78	13.75	-	Design exploration of open rotor concepts. Data for a wing-mounted open rotor using medium-fidelity tools; other categories and engine location were evaluated.
Nicolosi *et al.* (2021)	1600	37000	130	0.68	12.7	17.2	Low-fidelity MDO of large turboprop aircraft. Data for a three lifting surface concept with rear-mounted engines.

Source: The author

Table 12 – Summary of electric fixed-wing aircraft concepts.

References	Range [nm]	Cruise altitude [ft]	No. passengers	Mach number [-]	ML/D [-]	Fuel-burn reduction [%]	Remarks
Hornung *et al.* (2013)	900	34000	190	0.75	15.5	-	C-wing concept with super-conducting electric engines.
Strack *et al.* (2017)	800	23000	70	0.41	9.6	4	Conceptual design study of hybrid electric turboprop aircraft configurations. Data for a parallel hybrid architecture with a high aspect ratio wing, electrically driven propellers at the wingtip and reduced vertical tailplane. Fuel-burn benefits relative to an advanced EIS 2035 turboprop without hybrid electric propulsion.
Voskuijl *et al.* (2018)	825	25000	70	-	-	28	Design of hybrid electric regional turboprop aircraft. All the analyses are based on relatively low fidelity methods. Fuel-burn benefits relative to a fuel-powered conventional aircraft. This comes at the cost of a larger and heavier aircraft.
Schmollgruber *et al.* (2019)	1200	33000	150	0.78	14.9	8.5	DRAGON concept from ONERA using multidisciplinary low-fidelity aerodynamics. The aircraft includes a hybrid electric distributed propulsion system.
Schiltgen and Freeman (2019)	900	35000	150	0.78	16.9	11	ECO-150-300 concept. A distributed electric propulsion concept subjected to an extensive CFD study for external and internal aerodynamic performance.
Hoogreef *et al.* (2019)	800	33000	150	0.78	-	10	Conceptual design of 35 hybrid-electric aircraft. Data for a boosted turbofan parallel hybrid concept. Comparison over conventional turbofan aircraft.
Vries, Brown and Vos (2019)	825	18000	72	0.41	7.5	-	This study presented a low-order MDO environment that can capture the unique features of serial/parallel hybrid-electric aircraft. Data for partial-turboelectric powertrain with distributed propulsion. This concept consumes 3% more energy than a conventional configuration.
Sgueglia *et al.* (2020)	1500	40000	150	0.78	14.4	-	High-fidelity MDO of a hybrid-aircraft concept with distributed electric ducted fans.
Vries and Vos (2022)	1500	36000	75	0.6	-	5	This study presented an aerodynamic evaluation of an over-the-wing distributed-propulsion for hybrid-electric transport aircraft. Comparison over conventional twin-turboprop reference for the 2035 timeframe.
Jansen *et al.* (2022)	750	37000	180	0.78	-	26.8	The SUSAN Electrofan Variant 3. A ducted turbofan propulsor concept which includes a gearbox to improve propulsive efficiency. Fuel-burn benefits compared to a CTW with technology levels representative of the 2005 single-aisle fleet. More details of several disciplines can be found in (CHAU; KENWAY; KIRIS, 2022; MACHADO *et al.*, 2022).

Source: The author

Figure 11 – Revolutionary BLI concepts.

(a) The Double Bubble D8.

(b) NASA's STARC-ABL concept.

Source: Aurora. . . (2017). Credits: NASA/MIT/Aurora Flight Sciences
Source: SUGAR. . . (2017). Credits: ASAB Projects

- The concepts described in Table 10 show how the benefits of boundary layer ingesting and distributed propulsion systems can minimize the fuel-burn by improving propulsive efficiency. However, such configurations are exposed to flow distortion arising from airframe separation, causing pressure losses, vibration, and noise. Therefore, the integration of distortion tolerant fan blades is mandatory, in order to operate at their maximum design performance. It is worth clarifying that the methods used to evaluate the benefit of boundary layer ingestion differ among the referenced studies. For example, the older studies were limited to 1D propulsion system modeling and simulation, whereas some of the most recent studies involve numerical simulations to account for complex flow interactions, such as fully coupled body force models. In this context, the prediction of the potential gains of BLI in aircraft design requires propulsor models that accurately estimate upstream interaction of the fan with the non-uniform inlet flow. Figure 11 shows a rendering of innovative propulsion technologies explored by different research institutions. The Double Bubble D8 concept (Fig. 11a) integrates potential technologies such as a lifting fuselage, BLI engines, a low-sweep wing that contributes to a lighter structure, and a lower cruise speed (Mach 0.72) than typical commercial aircraft (Mach 0.78). This concept provides a 30% fuel-burn benefit relative to a conventional aircraft with 2010 technology (URANGA *et al.*, 2017). The NASA STARC-ABL concept (Fig. 11b) integrates turboelectric propulsion with an electrically driven BLI mounted on the fuselage tail cone, providing a 12% fuel-burn benefit over conventional aircraft with advanced aerodynamic technologies for entry into services in 2035 (WELSTEAD; FELDER, 2016).

- Open rotors in the single-aisle category (shown in Table 11) have demonstrated high propulsive efficiency, approximately on the order of 86%, at 0.72 Mach, allowing for a 30% reduction in fuel-burn over conventional turbofan engines (STÜRMER; YIN; AKKERMANS, 2014). The high propulsive efficiency is a function of the difference between the jet velocity and the ambient velocity, i.e., open rotors have the capacity to accelerate a large mass flow rate, increasing the effective bypass ratio to more than 30:1 (ZANTE, 2015). Despite significant progress on these concepts, important challenges require further research efforts in terms of propulsion airframe integration, noise and weight penalties, and certification issues.

- Table 12 summarises aircraft concepts incorporating electric or hybrid-electric engines with various types of integration. The implications of using electric or hybrid power architectures, i.e., concepts that combine different power sources such as gas turbines, advanced batteries, or liquid hydrogen fuels, dictate innovative approaches and can significantly reduce emissions from commercial aircraft. However, the main disadvantage is their restricted range, which is determined by the amount of batteries they can carry. The battery use itself brings challenges such as the weight on board, which reduces payload capabilities, and its specific energy, which reduces the operating capabilities (HALL *et al.*, 2019). For that reason, full-electric propulsion is currently being implemented in general aviation, urban air taxis, and commuter aircraft, which require less demanding requirements (EPSTEIN; O'FLARITY, 2019). In contrast, hybrid-electric systems and turbo-electric systems are well-suited for application on distributed propulsion architectures for civil aviation. Nevertheless, in terms of aircraft performance, research into realistic aircraft systems integration and implementation is currently at a low TRL. Simplified models to forecast the performance of those concepts are widely available, but a detailed and accurate portrayal of the interaction between the propulsive system and the airframe is essential, as the two parts work in synergy. Indeed, the benefits of distributed propulsion concepts have been shown to be affected by structures, vibrations, and acoustics problems, given the unsteady nature of the flow interactions. Therefore, the implementation of high-fidelity aerodynamic shape optimization can provide a better understanding of such time-dependent problems (CHAUHAN; MARTINS, 2021). Finally, there are challenges for airport infrastructure and ground operations arising from aircraft concepts using alternative sources of energy (SCHMIDT *et al.*, 2016; TRAINELLI *et al.*, 2021).

To conclude this section, the latest efforts to develop hydrogen-powered commercial aircraft are mentioned. According to Khandelwal *et al.* (2013), hydrogen stores three and a half times more energy than kerosene per unit weight, which undoubtedly represents an advantage compared to traditional aviation fuels. However, it presents an energy density three times lower than that of kerosene per unit volume. Therefore, the main issue is the volume needed on board to transport the same amount of energy as conventional fuels. As a result, very large tanks are required, particularly because the hydrogen must be stored as a cryogenic fluid at -423°F (KRAMER, 2020). That is why hydrogen-powered aircraft consider cryogenic hydrogen deposits in the fuselage, rather than in the wings. This influences the shape of the aircraft, and therefore the aerodynamics. Brelje and Martins (2021) explored the aerostructural wing optimization for a hydrogen fuel cell aircraft. The findings indicate that storing compressed hydrogen in the wing root of a single-aisle transport aircraft could be a viable option at conceptual design level. However, due to the weight and volumetric capacity of compressed hydrogen storage tanks, it is unlikely to be used on transcontinental routes.

Rompokos *et al.* (2021), and Druot *et al.* (2022) presented several unconventional configurations using external and internal hydrogen tanks. Whatever the case, there are obvious trade-offs between external aerodynamics and the issue of integrating very big tanks within the airframe, which could affect payload volume and fuel capacity, or both. The BWB is thought to be a feasible solution for this idea, although other potential configurations are Twin Tail-Boom and Tail-Tank concepts.

Airbus' efforts in developing hydrogen-powered aircraft must be highlighted. Three concepts were recently presented in the framework of French public support for the aviation sector in the COVID-19 crisis: a BWB aircraft for up to 200 passengers, range of 2000 nm, and hybrid hydrogen turbofan engines; a regional aircraft for up to 100 passengers, range of 1000 nm, and hybrid hydrogen turboprop engines; a single-aisle aircraft for 120-200 passengers, range of 2000 nm, and hybrid hydrogen turbofan engines. All of them capable of a Mach 0.78 cruise speed (RAO; YIN; WERIJ, 2020; HUETE; PILIDIS, 2021).

Despite such an important contributions on new propulsion technologies for modern and unconventional configurations, it is required the evaluation of economic variables such as DOC, NPV, and direct maintenance cost, to quantify the actual economic benefits for airliners, and justify the cost and risk of such configurations.

2.4.5 Other Configurations

This section includes other unconventional configurations that have been investigated recently. The following cited configurations involve an original layout with reduced fuel-burn when compared to their CTW counterparts. Since there are major difference among these concepts, a precise classification was not made in this chapter.

- Throughout aviation history, forward-swept wing concepts have been tested to improve aircraft performance in transonic and supersonic flight. The implementation in military aviation demonstrated a reduction in compressibility effects at transonic speeds and greater lift at low speeds (ZHANG *et al.*, 2013). However, earlier studies evidenced several aeroelastic problems such as divergence, flutter, buffeting, among others (SPACHT, 1980). Composite materials and new additive manufacturing techniques can mitigate those problems, enabling also lightweight structures, a substantial increase in strength ratio, and reduction in maintenance cost (SOUTIS, 2005a; ZHANG; CHEN; HU, 2018).

For this reason, there is recent progress on forward-swept wing concepts for commercial aviation due to the synergy between active load control and natural laminar flow, which can yield to significant gains in terms of fuel and cost (XU; KROO, 2014). Iwanizki *et al.* (2020) presents an overview of several forward-swept wing concepts investigated in the European Clean Sky 2 and ONERA-DLR projects. This paper showed that forward-swept wing concepts enable NLF at high Reynolds numbers, which reduce friction drag by delaying the onset of turbulent flow. The combination of forward-swept wing, NLF, and composite materials can offer fuel savings by about 18% compared to an improved conventional configuration with a backward-swept composite wing.

Two configurations stand out within this group: the LamAiR concept (KRUSE; WUNDERLICH; HEINRICH, 2012; WUNDERLICH *et al.*, 2017) designed with a forward-swept NLF wing, smart droop nose leading edge high-lift device, and carbon fiber reinforced polymer wing; and its successor the TuLam concept (SEITZ; HÜBNER; RISSE, 2020) designed with similar characteristics of the LamAir concept, but adding HLFC systems. Both studies followed a high-fidelity MDO process, obtaining an overall aerodynamic performance at cruise (ML/D) equal to 14.9 and 16 respectively, at design cruise Mach of 0.78.

- Twin-fuselage concept has also been proposed as an alternative commercial airliner. Some early designs demonstrated a substantial increase in aspect ratio while reducing the bending moment in the wing root sections. As a result, this configuration provides an operational empty weight reduction without compromising payload capacity (MOORE; MADDALON, 1982). This advantage has enabled engineers to include additional technologies in the design space of this concept such as HLFC and active load alleviation, offering additional fuel-burn benefits (MA; ELHAM, 2021). This particular concept was designed using a multi-fidelity approach involving low-fidelity aerodynamics and a semi-analytical equation for wing mass calculation. The results show that twin-fuselage concepts combined with advanced aerodynamic and structural technologies provide an aerodynamic performance (ML/D) equal to 18.33 at cruise Mach of 0.78, which can reduce fuel-burn by roughly 30% over the current conventional configurations. However, high-fidelity studies are required to evaluate the benefits of this concept.

  Design challenges of twin-fuselage concepts include a significant more wetted area than single-fuselage concepts of equivalent capacity, so friction drag can be higher than conventional aircraft. In addition, twin fuselage are prone to produce interference drag penalties. Other issues include roll stability requiring larger rolling moments, so ailerons must be larger or placed farther away from the centerline, which increase the weight of system and operational items. On the other hand, operational challenges involve current airport infrastructure requiring wider runways due to the arrangement of the landing gears. In addition, the high aspect ratio wings are not able to operate on current airport gate-box limits. This problem can be solved in a similar way to truss-braced wing concepts, which require folding wing tips, however this adds wing weight (CHIESA; SCIUVA; MAGGIORE, 2000).

- The Flying V concept (Fig 12) presents an innovative tailless airframe, whose wings act as passenger cabin, fuel tanks, and cargo haul. Such an arrangement provides a lower aerodynamic drag than CTW aircraft, since the wetted area is reduced, so that reduces the friction drag, and the effective wingspan is increased, lowering lift-induced drag. Fuel-burn benefits reach to 20% over a comparable CTW aircraft, providing and overall aerodynamic performance at cruise (ML/D) equal to 20.14 at Mach 0.85. This concept has also demonstrated a reduction in empty weight as well as lower noise inside the cabin (FAGGIANO *et al.*, 2017). High-fidelity aerodynamic studies, including CFD and wind-tunnel experiments, have determined the ideal engine location as well as the arrangement of control surfaces on this concept (PASCUAL; VOS, 2020; PALERMO; VOS, 2020).

  Despite the fact that conceptual studies have shown cost-effective fuel-burn advantages over the CTW arrangement, this concept presents a number of potential issues that need to be investigated further, such as the overhaul of cabin interiors to improve the overall flying experience, and the fact that fuel tanks are located on the same level as the passengers cabin, creating potential risk in case of incidents. The flight envelope also needs to be improved in order to minimise the rate at which the aircraft manoeuvres while maintaining flying safety. The high angle of attack needed during take off and landing could also put passengers in an uncomfortable position, especially if the seats are at an angle to the direction of flight. Staggered seats might be a solution for a V-shaped aircraft, but evacuation plans and more detailed designs are needed (VINK *et al.*, 2020).

2.4.6 Other Technologies

Up to this point, the literature reviewed for this paper focused on describing the main design characteristics, design methodologies, and potential fuel burn reduction offered by several unconventional configurations. This section discusses other potential technologies that significantly improve aircraft performance and reduce aircraft fuel consumption. According to Bushnell (2021), there are available and emerging technologies that reduce aircraft operating costs and emissions, through simultaneous optimization of ML/D, acoustics, and weight. For example, natural laminar flow uses a careful geometric

Figure 12 – Flying V concept.

Source: Flying-V (2021). Credits: TUDelft

design to delay laminar-turbulent transition passively, whereas hybrid laminar flow control techniques delay transition with the help of suction through slots or small holes. The use of natural laminar flow is more suitable for smaller aircraft such as regional or commuter categories, due to their relatively low Reynolds numbers and potentially lower Mach numbers enabling reduced wing sweep angles. SBW and TBW concepts can also take advantage of such technology, since the use of external trusses reduces the wing weight, allowing the wing to be thinner than those of conventional aircraft, reducing wave drag and enabling reduced sweep and thus crossflow instabilities. On the other hand, aircraft with higher Reynolds numbers and sweep angles, such as twin-aisle aircraft, require active laminar flow control. The use of these systems often imposes operational penalties because of the additional weight or system complexity that, along with significant operational challenges, have restricted their use in transport aircraft (SCHRAUF, 2005). In contrast to SBW and TBW aircraft, the high sweep angles typical of BWBs are better suited to hybrid laminar flow control (KRISHNAN; BERTRAM; SEIBEL, 2017).

Other viscous drag reduction technologies include: riblets, which have been studied to evaluate their performance on several TBW configurations (GUR; SCHETZ; MASON, 2011); plasma actuators, which have demonstrated an increase in the lift-to-drag ratio when applied on swept wings, as well as noise reduction benefits when applied in high-lift devices (SILVA *et al.*, 2020); and morphing wings (CUMPSTY *et al.*, 2017), including variable camber concepts using existing control surfaces (RECKZEH, 2014). In case of induced drag, the use of wing-tip devices such as blended winglets, Whitcomb winglets and sharp-ranked winglets, provide an effective aspect ratio improvement without great span increase (BUSHNELL, 2003). From there, several wing-tip extensions have been proposed, presenting interesting aerodynamic and control implications, such as the C-wing concept, tip sails, spiroid tips and even morphing winglets (DEMASI *et al.*, 2022; BARBARINO *et al.*, 2011; EGUEA; SILVA; CATALANO, 2020; EGUEA; BRAVO-MOSQUERA; CATALANO, 2021).

In terms of weight reduction approaches, advanced composites have been used to reduce the aircraft structural weight. Their lightweight and substantial strength ratio enhance aircraft performance and reduce maintenance costs. Other benefits include reduction of parts, reduction of scraps, improvement of fatigue life and improvement of corrosion resistance (TIMMIS *et al.*, 2015). According to Soutis (2005b), an empty weight reduction can be achieved by using developments in the following areas: advanced metallic technologies, advanced composite technologies and optimized local design. In case of metallic technologies, new alloys with specific properties are being developed. For example, a lower density has been obtained by aluminum-lithium alloys and higher permissible stress alloys. In addition, the use of fiber/metal laminates and metal laminates structures often saves some mass. For composite materials technologies, different lay-ups obtained through optimization techniques may result in high-strength fibers with improved matrix properties (MARINO; SABATINI *et al.*, 2014). New composite sandwich panels with truss-like cores have the potential to take the place of metallic panels (ZHANG; CHEN; HU, 2018). Finally, potential improvements through optimized local design can be obtained, such as the use deployable chutes for refused takeoff instead of heavy brakes, and new additive manufacturing processes that allow to obtain more precise geometries, as well as greater emphasis on the material properties of the components (BUSHNELL, 2021).

2.5 Discussion

As noted in the previous section, several unconventional aircraft have been designed towards the next-generation airliner. All those studies showed improvements in fuel-burn compared to equivalent conventional aircraft. We may deduce that progress in this field has been aided by both the growth of new technologies and the introduction of more robust design algorithms. However, there has been no inquiry into how far such configurations will actually operate from their optimum flight condition. Therefore, this section explores further into the importance of the findings presented in Section 2.4, in terms of the overall aerodynamic performance at cruise and the optimum cruise altitude, since both have a relevance on the climate change impact.

In this context, the Breguet equation (Eq. 2.1) has been used to identify major technological drivers for unconventional aircraft at cruise phase (TORENBEEK, 1997).

$$R = E\ .\ V = \frac{V}{c_t}\frac{L}{D} Ln\left[\frac{W_i}{W_{i+1}}\right] \tag{2.1}$$

where R and E are the cruise range and endurance, respectively, V is the flight velocity, c_t is the thrust specific fuel consumption, L/D is the lift-to-drag ratio or aerodynamic efficiency, and W_i is the weight of the aircraft at the end of the mission segment i. From Eq.

2.1, it can be assumed that engines run at a constant overall efficiency corresponding to a constant specific fuel consumption, so the aircraft operate in an idealized manner in cruise, i.e., lift is equal to weight ($L = W$), whereas thrust is equal to drag ($T = D$). Therefore, for a given range, payload and Mach number, the drag reduction determines the condition for optimal lift-to-drag ratio, resulting in minimum thrust and hence minimum fuel-burn. The mathematical formulation to relate these forces is obtained from the equilibrium equations of the static movement of the aircraft,

$$W = L = q_\infty S C_L \tag{2.2}$$

$$T = D = q_\infty S C_D \tag{2.3}$$

where S is the wing reference area, q_∞ is the freestream dynamic pressure, given by ($q_\infty = \gamma P_{cr} M^2/2$), γ is the isentropic expansion factor, and P_{cr} is pressure at cruise altitude. Dividing the Eq. (2.3) by the Eq. (2.2) is obtained the linear estimation of the required thrust (T_R) (Eq. 2.4):

$$T_R = \frac{W}{C_L/C_D} \tag{2.4}$$

Thus, the condition for maximum lift-to-drag for a given Mach number, resulting in minimum drag (md) and hence minimum thrust, is defined by the lift coefficient $C_{L,md}$. As fuel is burned during cruise, the aircraft weight decreases, so the dynamic pressure is also reduced in order to keep the lift coefficient at its optimum value (for maximum lift-to-drag and/or minimum drag). Therefore, for a given cruise Mach number, the optimum pressure at cruise altitude must decrease throughout the flight trajectory, corresponding to an increase in true altitude. Arranging Eq. 2.2 to determine the pressure at cruise altitude,

$$P_{cr} = \frac{2}{\gamma}\frac{W/S}{M^2 C_L} \tag{2.5}$$

where W/S represents the wing loading at a given Mach number and flight altitude. Alternatively, if there is only one drag polar, the aircraft has a constant maximum lift-to-drag ratio defined by $C_L = C_{L,md}$. The parabolic drag polar equation is given by Eq. 2.6:

$$C_D = C_{D0} + C_{Di} \tag{2.6}$$

where C_{D0} represents the zero-lift drag (i.e., skin friction drag, interference drag, form drag, plus the effects of compressibility on drag), and C_{Di} represent the induced drag, which is given by Eq. 2.7:

$$C_{Di} = kC_L^2 \tag{2.7}$$

where k is the drag-due-to-lift factor, given by Eq. 2.8:

$$k = \frac{dC_D}{dC_L^2} \equiv \frac{1}{\pi Æe} \tag{2.8}$$

where $Æ$ is the wing aspect ratio, and e is the span efficiency factor. The conditions for minimum drag at a given Mach number are obtained by deriving

$$\frac{d(C_L/C_D)}{dC_L} = \frac{C_{D0} + kC_L^2 - C_L(2kC_L)}{(C_{D0} + kC_L^2)^2} \tag{2.9}$$

setting the factors equal to zero, we obtain

$$C_{L,md} = \sqrt{\frac{C_{D0}}{k}} = \sqrt{C_{D0}\pi Æe} \tag{2.10}$$

$$C_{D,md} = 2C_{D0} \tag{2.11}$$

$$\left(\frac{L}{D}\right)_{md} = \frac{1}{2\sqrt{C_{D0}k}} \tag{2.12}$$

Eq. 2.5 and Eq. 2.10 can be rearranged as:

$$P_{cr} = \frac{2}{\gamma}\frac{W/S}{M^2\sqrt{C_{D0}\pi Æe}} \tag{2.13}$$

From Eq. 2.13, we may conclude that most unconventional configurations presented in Section 2.4 (at a given Mach number, and own zero-lift drag values), must fly at a higher altitudes than conventional airliners, to benefit from their specific design features. For example, BWBs and HWBs are characterized by their large reference area, i.e., low wing loading (W/S), implying that higher lift-to-drag ratios can be achieved at higher altitudes, i.e., cruising at lower static pressure. This statement is also valid for SBW and TBW concepts, whose potential fuel-burn benefits come from their high $Æ$ values. So, the higher $Æ$ the lower pressure at cruise altitude. The same for BW concepts, which are characterized by their high e values, which also depend on the height-to-span ratio (h/b) of the box-wing layout. So, the higher e the lower pressure at cruise altitude.

However, there are significant concerns about the net global warming consequences by flying at higher cruise altitudes, such as the nitrogen oxides and carbon dioxide depositions, and the formation of water vapor and contrails near the ozone layer (HILEMAN *et al.*, 2013; MAHASHABDE *et al.*, 2011). In particular, these latter spread into high-level thin cirrus clouds, which change the thermal infrared radiation, enhancing global warming (JOHNSON; GONZALEZ, 2018). For this reason, it is recommended to investigate the trade-offs between environmental objective functions such as minimum CO_2 and minimum NO_x, along with minimum DOC or minimum fuel-burn, in order to find a balance between aviation emissions and the high financial and technical risk associated to the development of a new unconventional aircraft.

It should be noted that the present formulation can be analogous to the Breguet equation for all-electric or hybrid-electric aircraft, assuming specific energy from batteries (pack density) and performance parameters properly (GNADT *et al.*, 2018; HEPPERLE, 2012). However, in this case, the optimum flight speed and altitude are restricted by the ratio of power generated by an electric engine in a hybrid aircraft to the total power consumed by the aircraft (i.e., degree of hybridization), as well as the risk of electrical arcing at high altitude. More details about the optimal flight conditions for a hybrid-electric aircraft were described by Pornet and Isikveren (2015).

2.6 Final Considerations

Next-generation civil transport aircraft must have greatly reduced environmental impact while remaining economically viable, meeting the many constraints associated with the air transportation system, and maintaining the necessary level of safety. While the conventional configuration has served well over many decades, it is an open question whether it will remain the optimal solution in the future. Considerable research has been conducted to develop and investigate unconventional aircraft configurations which have the potential to displace the conventional configuration as a result of their potential improvements in environmental and economic performance. A review of this research has been presented here with the objective of providing the reader with a summary of the benefits, challenges, and trade-offs associated with the various concepts currently under consideration.

Given the paucity of design experience with unconventional aircraft configurations, virtually all of the studies described rely on some sort of physics-based design tools, ranging from simple and fast conceptual design methodologies through multidisciplinary optimization frameworks where the aerodynamics discipline is based on the numerical solution of the Reynolds-averaged Navier–Stokes equations. The purpose of the studies reviewed is generally twofold. First the authors seek to develop solutions to the design challenges faced by the unconventional configuration under study and to develop a preliminary model of such an aircraft. This model is then used to provide a performance estimate of the novel configuration relative to a conventional tube-and-wing aircraft designed and evaluated consistently for the same mission. The development of accurate estimates of such performance benefits is crucial to enabling industry to make informed decisions on whether to commercialize a given configuration. The credibility of performance estimates for unconventional aircraft configurations depends on both the number of disciplines included in the design as well as the level of fidelity of the analysis. Both of these have steadily evolved over the years such that the relative performance of several unconventional configurations is now moderately well understood, although there remains work to be done to determine which configuration should be selected for a given aircraft class.

The studies discussed make various assumptions with respect to technology levels, which can make direct comparisons difficult. Some studies assume next-generation technologies in all aspects, such as engines. It is then critical to compare with a tube-and-wing that is also equipped with next-generation technologies. Other studies assume current technologies and can therefore be compared with today's most efficient aircraft in order to assess the benefit of the configuration alone. A disadvantage of this latter approach is that the aircraft developed will not be representative of the aircraft that could eventually be built, which will be equipped with next-generation engines, for example. A major advantage, however, is that this approach reduces the guesswork associated with new technologies in terms of their viability and effectiveness, hence providing a credible estimate of the impact of the configuration on its own, although this may not be possible when several new technologies are tightly integrated. In any case, it is important for the reader to be careful to have a clear understanding on the technology assumptions made in making an assessment of a particular concept.

In evaluating unconventional aircraft configurations, benefits and risks must be weighed against one another. For example, the TBW/SBW and BW have reduced risk relative to an HWB because they can use existing fuselage technology. Another important consideration is the trade-off between competing priorities, such as fuel efficiency, climate change impact, and noise. A clear understanding of how these are to be prioritized will be needed in order to choose the most promising configuration. Finally, the optimal configuration may be different for different aircraft classes, and the benefits of unconventional configurations depend on the aircraft class.

Aviation must reduce its environmental impact as quickly as possible. Adding advanced technologies to the conventional configuration can be accomplished in a fairly short time frame and should be aggressively pursued. Based on the studies presented, it appears that a strut-braced-wing configuration could be brought to market in the medium term and could provide significant benefits in the single-aisle and regional classes. The hybrid wing-body, on the other hand, may offer a better solution in the long term, especially for large long-range aircraft. Given the urgency of the environmental challenge, unconventional aircraft configurations with both medium and long term potential should be pursued, with academia and government continuing to pave the way until the cost and risk can be reduced to the point where one or more unconventional configurations can be commercialized.

2.7 Dissemination

The following article has been published as a result of this chapter:

- BRAVO-MOSQUERA, P; CATALANO, F; ZINGG, D. Unconventional Aircraft for Civil Aviation: A Review of Concepts and Design Methodologies. **Progress in Aerospace Science**, v. 131, p. 100813, 2022. (BRAVO-MOSQUERA; CATALANO; ZINGG, 2022).

3 DESIGN, AERODYNAMIC ANALYSIS AND OPTIMIZATION OF A NEXT-GENERATION COMMERCIAL AIRLINER

3.1 Introduction

Unconventional configurations and innovative propulsion technologies have been continuously developed for reducing both fuel-burn and global net carbon emissions. This chapter describes an advanced civil transport aircraft designed from the combination of a Box-Wing configuration with a Boundary Layer Ingestion (BLI) propulsion system. A conceptual-level Multidisciplinary Design Optimization strategy provided the main aerodynamic and performance characteristics of the aircraft, based on appropriate design requirements, variables and constraints. For direct performance comparison against a conventional aircraft, a single-point objective function based on minimum block fuel was evaluated by means of low-fidelity aircraft models. Subsequently, a back-to-back Computational Fluid Dynamics assessment of non-BLI and BLI versions of the aircraft was performed. Two major analyses comprised the aerodynamic evaluation: (i) quantification of the BLI benefit using the power balance method, (ii) performance evaluation of the propulsor inlet in terms of the total pressure recovery and the distortion index. The conceptual design results showed the box-wing configuration provided major fuel-burn savings compared to its conventional counterpart. On the other hand, the BLI version reduced engine power requirements at cruise in comparison to the non-BLI version, but decreased the total pressure recovery, resulting in more distortion at the aerodynamic interface plane. The main contribution of this study lies on the potential benefits of such an original unconventional configuration, whose technologies increased aerodynamic performance, which reduced fuel consumption and hence carbon emissions.

The remainder of the chapter offers a systematic description and detailed specifications for the INTI aircraft design and simulation methodologies. Section 3.2 describes the methodologies for the conceptual design stage and single-objective optimization problems based on the initial mission requirements; Section 3.3 is devoted to an aerodynamic evaluation based on Computational Fluid Dynamic (CFD) simulations; Section 3.4 discusses the results; Section 3.5 presents the key findings and suggests some future research. Appendix B details the multidisciplinary problem variables, their bounds, and optimum values, whereas Appendix C presents specific details of the conceptual-level MDO modules implemented in **Paerom**.

3.2 Conceptual-Level MDO

Four different aircraft geometries (Fig. 13) have been designed by the Department of Aeronautical Engineering, at the São Carlos School of Engineering - University of

São Paulo (EESC - USP) in the last few years with a particular emphasis on engine integration: a conventional tube-and-wing based on Airbus A320neo (A320. . . , 2005) (Fig. 13a); an unpowered configuration composed by a conventional fuselage, a BW layout and a single vertical tail (Fig. 13b); a BW layout with podded engines (non-BLI) (Fig. 13c); and a BW layout with semi-buried engines (BLI) (Fig. 13d). Note the wings and forward-fuselage geometries are identical for all BW configurations. The unpowered and non-BLI configurations have the same rear fuselage, except for the engine pods. The fuselage length of all models is the same as that of the reference conventional aircraft.

In order to evaluate the potential fuel-burn reductions offered by the INTI aircraft, an in-house conceptual-level MDO framework is used (**Paerom**). This is a Matlab-based tool programmed by several low-fidelity modules supported by a set of top-level requirements and sensitivity analyses. The tool is structured in a modular fashion such that the analysis consists of subroutines representing different disciplines, which are summarized as follows: design requirements, aerodynamic, weight, packaging and center of gravity, stability, propulsion, and performance.

Figure 13 – General view of the designed configurations.

(a) Conventional reference.

(b) Unpowered configuration.

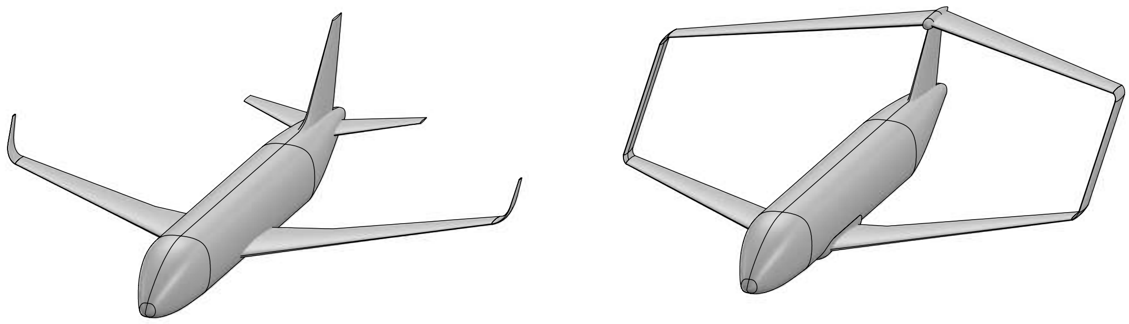

(c) Non-BLI configuration.

(d) BLI configuration.

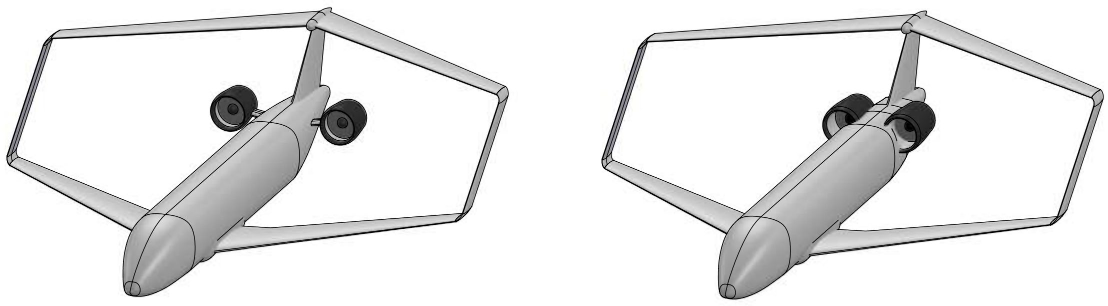

Source: The author

The most general structure of the interconnection of these modules is shown in Fig. 14, with evidence of involved user inputs and outputs. The complete MDO workflow setup is detailed as follows:

1. Aircraft initialization: specifies the input file (initial geometry and design requirements).
2. Mission specification: specifies details of the mission profile.
3. Optimization setup: enables the user to set up the objective function, variable inputs and design space (see subsection 3.2.2 for more details).
4. Aerodynamic modeling: creates an aerodynamic database (including stability derivatives) with low-fidelity tools. The aerodynamic database is extended through high-fidelity aerodynamic analyses performed offline.
5. Weight estimation: primary and secondary masses are calculated using a semi-empirical approach.
6. Propulsion modeling: calculates the engine dimensions and some other performance metrics.
7. Center of gravity: calculates weight and balance of aircraft components.
8. Stability: performs static stability calculations guaranteeing longitudinal constraints. Lateral-directional stability analysis is performed offline.
9. Performance modeling: computes the overall aircraft performance, simulates the mission profile, and updates the block fuel.

The modules are the essential elements of any conceptual level aircraft design. Each module has its own variables and constraints in order to perform low-fidelity analysis in full design space. For more details on the design modules, see Appendix C. Earlier versions of the conceptual design tool involved the development of Unmanned Aerial Vehicles (BRAVO-MOSQUERA *et al.*, 2017), agricultural aircraft (BRAVO-MOSQUERA *et al.*, 2018), fighter aircraft (BRAVO-MOSQUERA *et al.*, 2019), and commuter aircraft (BRAVO-MOSQUERA *et al.*, 2022c). The tool validation is given in Appendix C.0.9. In what follows, a brief description of each module is provided.

3.2.1 Design Requirements and Assumptions

Design Requirements and Objectives (DRO) are defined assuming current technology levels, except for the BLI modeling (IATA. . . , 2021). The optimization problems focused on the design of a single-aisle medium-range aircraft, since this category represents the dominating cabin layout for more than 70% of worldwide operated flights (KIRACI; AKAN, 2020). Fig. 15 illustrates a typical airliner mission profile, and Table 13 summarizes the top-level requirements of the current design space.

Figure 14 – Paerom software environment (conceptual-level MDO).

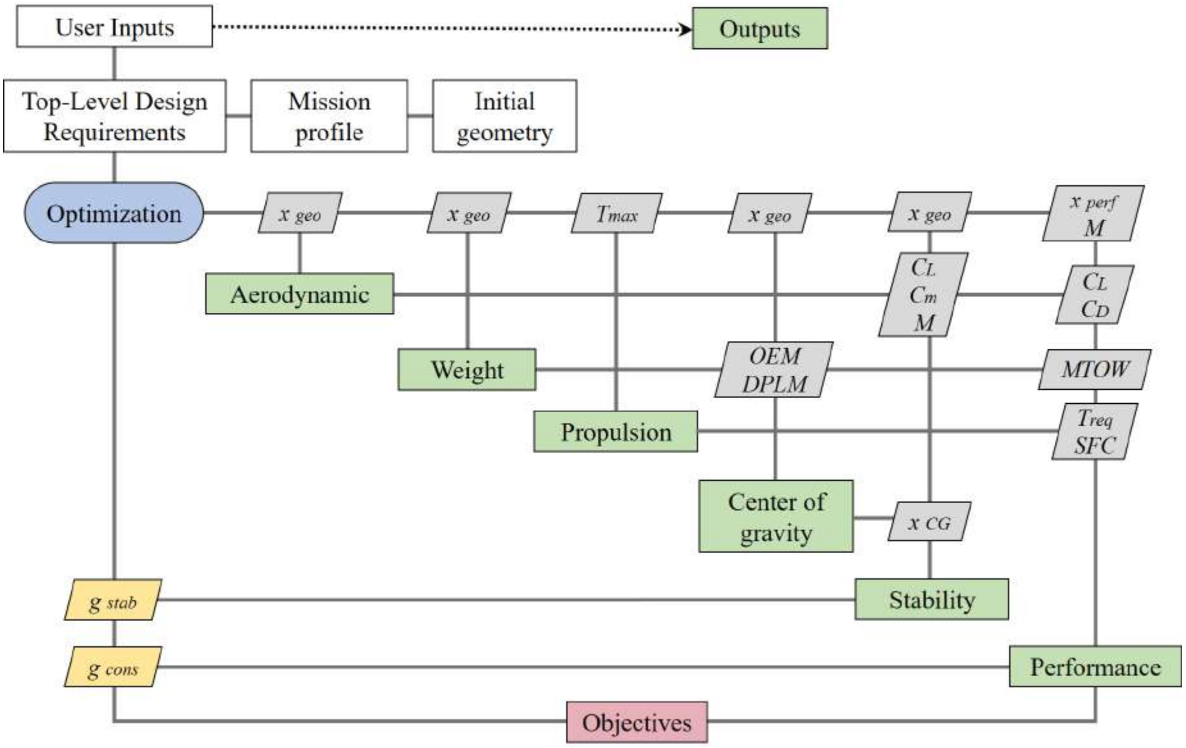

Source: The author

Figure 15 – Mission profile including the flight phases as treated within the performance module in conceptual-Level MDO.

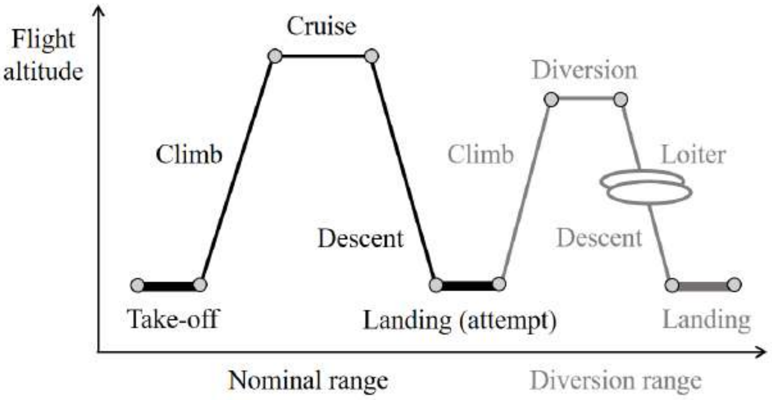

Source: The author

Sizing and propulsion requirements determined the specific non-conventional characteristics of the INTI aircraft. For example, a single vertical tail configuration is mandatory for the combination of the BW layout with a BLI propulsion system, since a dual fin solution may lead to heavier structural weight on the rear part of the fuselage and an increase in parasite drag, interference drag, and shock formation. This sizing requirement diverges from that proposed by Frediani and Montanari (2009), who suggested a twin vertical tail to solve the aeroelastic problems of Lockheed Martin's BW design (LANGE *et al.*, 1974). Nonetheless, due to current advanced materials and new manufacturing

Table 13 – INTI aircraft top-level design requirements.

Performance	**Sizing and propulsion**
Passengers = 165	Box-wing layout
Design payload mass $[kg]$ = 16335	Single vertical tail
Maximum payload mass $[kg]$ = 19500	Rear-mounted engines
Conventional range $[km]$ = 4000	Non-BLI and BLI version
Nominal range $[km]$ = 1852	High bypass ratio turbofans
Diversion range $[km]$ = 805	Conventional nose gear
Diversion altitude $[m]$ = 4512	Fuselage-mounted main landing gear
Loiter time $[min]$ = 30	
Cruise Mach [-] = 0.78	
Initial rate of climb $[m/s]$ = 12.5	
Rate at top-of-climb $[m/s]$ = 1.52	
Rate of descent $[m/s]$ = 9.5	

Source: The author

techniques, the single vertical tail solution can reduce wetted area, shock formation, and empty weight, while still providing stability and control benefits (CAVALLARO; DEMASI, 2016).

The location of the engines was primarily motivated by the CG envelope and longitudinal stability constraints. Thus, the engines are positioned at the rear of the fuselage and behind the CG. This mounting location provides less yaw in case of asymmetric thrust and reduces noise within the cabin because the exhaust is located behind the passengers (MATTINGLY; HEISER; PRATT, 2002). From this approach, two potential propulsion-airframe integration concepts were investigated: a conventional assembly using pylons on the aft fuselage side (referred to as the Non-BLI version), and a non-conventional assembly that ingests the boundary layer created along the fuselage (referred to as the BLI version). It should be noted that the INTI aircraft was designed considering current high bypass ratio engines. Therefore, new engine technologies such as all-electric and hybrid-electric engines were not considered in the design space. Finally, the location of the nose gear and main landing gear was mainly driven by the manipulation of the longitudinal CG position, and based on the landing gear position of reference BW configurations (FREDIANI *et al.*, 2019; ANDREWS; PEREZ, 2018b). In particular, a fuselage-mounted main landing gear is used, whereas the nose gear is a conventional one, providing enough clearance of the aircraft wings and nacelles with the runway.

3.2.2 Optimization Problem

3.2.2.1 Objective Function

A design optimization problem is described as the process of search for a particular objective function (measure of merit) under given design variables and constraints. Conceptual-level MDO studies on the CTW and BW concept involved single-point optimization problems. In particular, the objective is to minimize the block fuel over the nominal range mission. The block fuel objective accounts for a large portion of the direct operating cost and correlates to lower emissions (SKOWRON *et al.*, 2020). Therefore, the use of such an approach is extremely interesting since new technologies are included in the design space. It should be noted that block fuel also depends on fuel cost, which, although it is a purely economic factor, plays a decisive role (KEHAYAS, 2007).

3.2.2.2 Design Constraints

Most of the design constraints are imposed on the performance requirements of the aircraft (Table 13). However, additional constraints such as static margin at the cruise point based on CG position and available wing fuel volume are also treated during the optimization process. The constraints were added to the objective function as penalty terms. Table 14 summarizes the design constraints for this specific case study.

Table 14 – Design constraints.

Constraint	**Value**	**Description**	**CTW**	**BW**
Longitudinal stability	$-dC_m/dC_{L\alpha} > 0.05$	Aircraft static margin (SM_x) of 5%.	-	✓
Wingspan	$b \leq 36\ m$	Wingspan limited by Code C airport gate constraints (BRADLEY; DRONEY, 2015a).	✓	✓
Fuselage length	$37.57\ m$	Constrains the fuselage length based on the reference conventional aircraft.	✓	✓
Tip chord	$1.6\ m$	Constrains the tip chord to prevent the optimizer from decreasing wing taper significantly, or making unreliable vertical tip chord.	-	✓
Initial cruise altitude	$\geq 10500\ m$	Constrains the initial cruise altitude from MTOW.	✓	-
Available wing fuel volume	≥ Required fuel volume	Constrains the fuel tank capacity based on the maximum fuel mass.	✓	✓

Source: The author

Table 15 – Design variables for CTW concept.

Geometric Variables (x_{geo})	**Lower bound**	**Upper bound**
Aspect Ratio [-]	9	12
Wing sweep angle [DEG]	20°	30°
Wing taper ratio [-]	0.2	0.6
Wing section thickness-to-chord ratio (x2) [-]	0.08	0.16
Performance variables (x_{perf})		
Wing area [m^2]	120	130
Maximum required thrust (per engine) [kN]	110	125

Source: The author

3.2.2.3 Design Variables

Design variables of CTW and BW configurations contain the operational and geometric parameters listed in Table 15, and Table 16, respectively. The lower and upper bounds were selected to be as wide as possible, while still being representative of a typical conceptual design phase.

For the CTW concept, seven design variables have been used to focus on the performance of the configuration itself. Note that the the stability constraint is not accounted as the horizontal tail was not specifically modelled in the optimization loop. However, the tail surfaces (horizontal and vertical) were sized using the shortcut technique based on the tail volume coefficient approach (TORENBEEK, 2013). In contrast, for the BW concept, the stability constraint was active since the fore and aft wings were treated as the main wing and horizontal tail, respectively. Fig. 16 shows the parametric study that defined the geometric design variables for the BW concept.

Table 16 – Design variables for BW concept.

Geometric Variables (x_{geo})	**Lower bound**	**Upper bound**
Aspect Ratio [-]	5	8
Height-to-span ratio [-]	0.1	0.4
Stagger-to-span ratio [-]	0.5	1.5
Fore wing leading edge station[2] [-]	0.2	0.4
Wing taper ratio (x2) [-]	0.2	0.6
Wing section thickness-to-chord ratio (x4) [-]	0.08	0.16
Weight and balance variables (x_{CG})		
Center of gravity offset ($\Delta_{CG}/\bar{c}$) [-]	-2	2
Nose gear axial location[1,2] [-]	0.05	0.15
Main gear axial location[1,2] [-]	0.5	0.7
Propulsion station[1,2,3] [-]	0.7	0.8
Performance variables (x_{perf})		
Initial cruise altitude [m]	11000	13000
Wing area[4] [m^2]	120	180
Wing area ratio [-]	0.5	0.6
Maximum required thrust (per engine) [kN]	110	125

[1] Based on center of gravity limits between the fore and aft wings ($\Delta_{CG}/\bar{c}$).
[2] Normalized by fuselage length.
[3] For Non-BLI and BLI configurations.
[4] Portion inside the fuselage included.

Source: The author

Different aspect ratios were evaluated and restricted by the maximum wingspan for the BW concept. The height-to-span ratio (h/b) relates the wingspan and the height of the BW concept, i.e., the height between fore [1] and aft [2] wings, whereas the stagger-to-span ratio ($2s/b$) relates the distance between the quarter chord point of the fore and aft wings and the wingspan. For the BW case, sweep values (Λ) are determined by the stagger variation so that the fore wing has an aft-swept and the aft wing has a forward-swept

Figure 16 – Geometric design variables of the box-wing system.

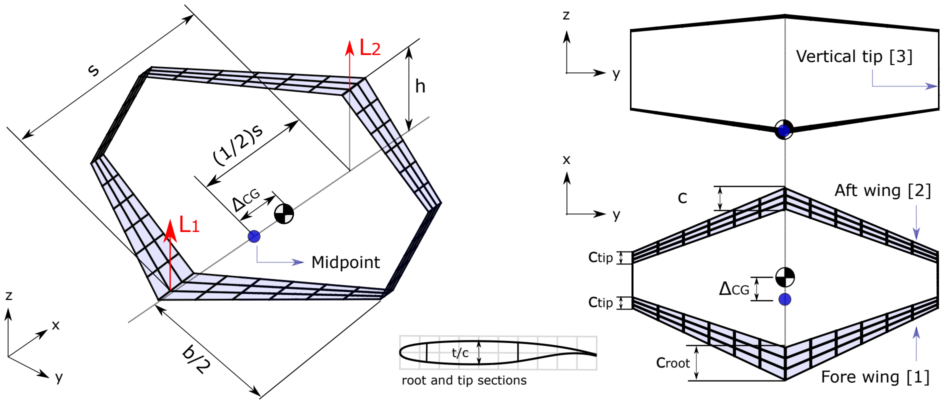

Source: The author

while keeping their tips aligned, i.e., the vertical tip fin [3] has zero cant angle. Since the sweep angle has a significant impact on weight and cost, the limits of the stagger-to-span ratio can only reflect the historical trend of jet transport wing sweep angles. Conversely, sweep values for the CTW case were defined by prescribed bounds.

Previous studies on BW concepts have shown the Lift-to-Drag (L/D) ratio improves when height-to-span and stagger-to-span ratios increase (DEMASI; MONEGATO; CAVALLARO, 2016; ANDREWS; PEREZ, 2018b; CHAU; ZINGG, 2017). Therefore, the fore wing leading edge station was chosen as a design variable, enabling the BW concept to be compatible with both the fuselage length of the reference aircraft and the current airport infrastructure. Moreover, its bounds prevent the optimizer from achieving unreliable aerodynamic values. Taper ratios (λ) of the fore and aft wings are design variables based on initial chords imposed as geometric inputs. Airfoil thickness-to-chord (t/c) ratio design variables were included at the root and the tip of the dual-wing system, and their optimum values were limited to ensure the maximum usable fuel.

On the other hand, a study of the available balance range determined the forward and aft CG limits to meet stability requirements for the BW concept. The center of gravity offset (Δ_{CG}) was adjusted in function of the mean aerodynamic chord ($\bar{c}$) of the combined wings and the midpoint between the aerodynamic centers of the dual-wing system. The sensitivity of this interval was assessed at the beginning and the end of the cruise phase, whose bounds represent a constraint for the operational CG range during the optimization. As a frame of reference, a negative offset represents a forward displacement of the CG based on the midpoint. Landing gear and propulsion system were assumed to be connected to the fuselage. Therefore, three design variables controlled their longitudinal position along the aircraft. The landing gear was treated as a point mass item, i.e., its position was determined by the weight of nose and main gear within the center of gravity offset limits. The weight of the propulsion group was also considered in the excursion of the CG, bearing in mind the optimized configurations have fixed BW layout (aircraft trimmed). This indicates that the difference in CG range between non-BLI and BLI configurations has no influence on the net streamwise force, and thus the BLI advantage at cruise.

Finally, performance variables involved initial cruise altitude (H_{cr}) in order to obtain an optimal L/D for cruise range, as well as wing reference area (S) and maximum thrust (T_{max}) which are related to the aircraft sizing. The wing area ratio (S_1/S_t) variable is for the BW concept, which determines the area of each lifting surface, where S_t is the total planform area.

3.2.2.4 Genetic Algorithm Optimizer

A Genetic Algorithm (GA) optimization is proposed to solve single-point optimization problems. GAs are well-known stochastic methods that emulate natural evolution, and their application in aircraft conceptual design leads to satisfactory results when low-fidelity solvers and limited call functions are used (RAYMER, 2002). Basically, a GA modifies a population of individual solutions on a regular basis, i.e., at each step, the GA selects promising individuals from an initial population (parents) and uses them to produce the offspring of the next generation. Therefore, the next generation is obtained through a repeated use of genetic operators, i.e., selection, crossover, mutation, and elitism (WHITLEY, 1994). The combination of these parameters is necessary to obtain an optimal solution within the constraints imposed in the problem (BINITHA; SATHYA *et al.*, 2012). In **Paerom**, the optimization is performed by **ga** function from Matlab, which is a global optimization toolbox that can handle both nonlinear inequality constraints and linear equality constraints. Details on the optimization module are provided in Appendix C.0.8.

The constrained optimization problem considered in this chapter is formulated as follows:

$$\begin{aligned} \text{min} \quad & f(\mathbf{x}) \\ \text{subject to} \quad & \begin{cases} g_{in}(\mathbf{x}) \leq 0, in = 1, 2, ..., IN \\ g_{eq}(\mathbf{x}) = 0, eq = 1, 2, ..., EQ \end{cases} \\ \text{with respect to} \quad & \mathbf{x} = [x_1, x_2, ..., x_n] \in \Omega \end{aligned} \tag{3.1}$$

where $f(\mathbf{x})$ represents the objective function (min $block - fuel$), $\mathbf{x}$ is the vector of design variables in the admissible search space (Ω), and $g_{in} \leq 0$ and $g_{eq} = 0$ are inequality and equality constraints, respectively. Based on the above formulation, the constraints were taken into consideration by penalizing the fitness value using a weighted quadratic loss function derived from a vector of constraints, which is given by Eq. 3.2 (COELLO, 2002):

$$T = \omega_{in} \sum_{in=1}^{IN} g_{in}^{*}(\mathbf{x}) + \omega_{eq} \sum_{eq=1}^{EQ} g_{eq}^{*}(\mathbf{x})^{2} \tag{3.2}$$

where T is the penalty term, g_{in}^{*} and g_{eq}^{*} are indication functions to account for the violations of the inequality and equality constraints, and ω_{in} and ω_{eq} are weights applied to the penalty term, in this case ($\omega_{1 \to n} = 10$). The penalty factors are normally set to positive constants that are large enough to amplify the penalty function for infeasible solutions (YENIAY, 2005). Figure 17 depicts the optimization that solves the constrained optimization problems formulated in Eq. 5.1, where the evolutionary operators (RS, DBX, DRM, and ES) are integrated in the GA module to emulate a specific evolutionary process.

Figure 17 – The genetic algorithm flow chart.

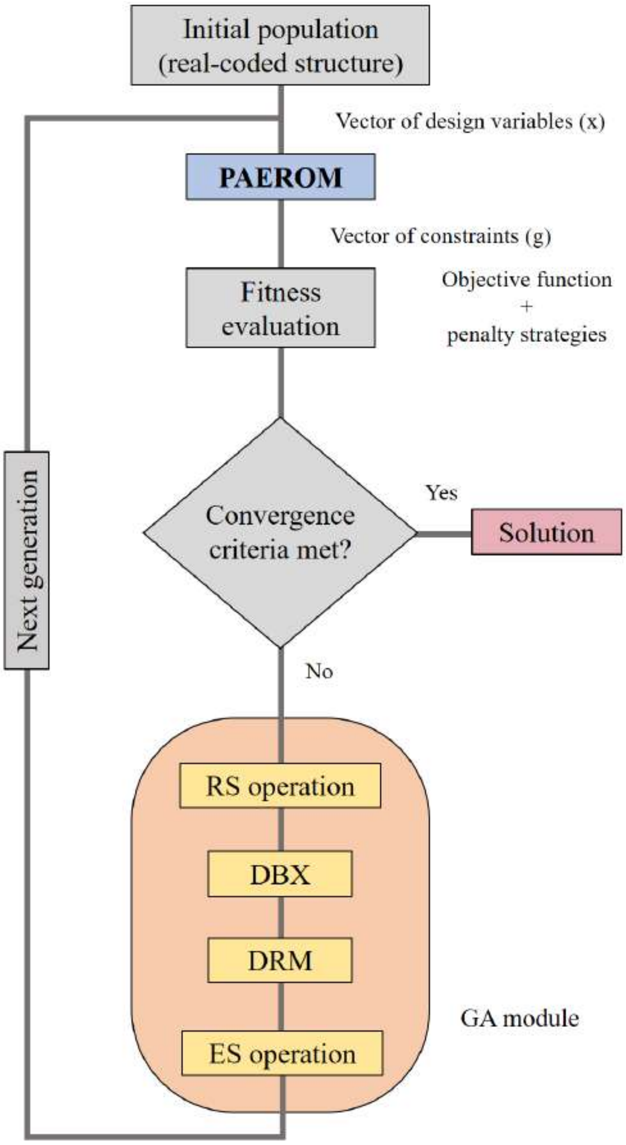

Source: The author

The algorithm begins by creating a first population using a randomly real-coded technique with a number of individuals. This coding structure is conceptually closest to the real design space, and reduces the string length required in binary-encoding (COELLO, 2002). As the problem is continuous, the real-encoded GA is generally more efficient than a binary-encoded GA (MARTINS; NING, 2021). Once the design space is defined in terms of a set of real-number genes, an initial population, represented by Eq. 3.3, is generated:

$$\theta = [x_1, x_2, ..., x_n] \tag{3.3}$$

where θ is a solution set (chromosome) of the optimization problem and x_i is called a gene, $i \in n$ and $n = \{1, 2, ..., n\}$. The allowable parameter space for θ is defined by Eq. 3.4:

$$\Omega = \{\theta \ \in \ \Re^n \mid x_{1,min} \leq x_1 \leq x_{1,max}, \ x_{2,min} \leq x_2 \leq x_{2,max}, ..., x_{n,min} \leq x_n \leq x_{n,max}\} \tag{3.4}$$

In this way, it is generated a random initial population, whose fitness value is designated to each individual running **Paerom**. The fitness function (F_f) is the result of the sum between the objective function and the penalty term ($F_f = f(\mathbf{x}) + T$). This fitness scaling avoids the dominance of the population by exceptional individuals on the first generations, which could lead to an early convergence. The main operators behind the GA are presented in the following items:

- Selection process - the first operation required for the establishment of the next-generation. After a first fitness evaluation, the Ranking Selection (RS) operator eliminates chromosomes of low fitness and replaces them with the top ranked ones for the production of new offspring. The overall number of chromosomes in the population is kept constant, thus significantly improving the average fitness.

- Crossover operator - new individuals are generated in this process through the exchange of characteristics from the previous selected chromosomes. The GA setup implemented a Direction-Based Crossover (DBX) operator that uses the fitness rating information sorted by the RS operator to separate the population into two groups (based on fitness levels), forming each pair of parents to produce two candidate offspring. From this classification, a string of random variables chosen from the interval (0, 1] is then implemented. If such string is greater than the specified probability threshold, the DBX generates a crossover direction based on the information from each paired gene, thus improving the effectiveness of gene recombination. This method can generate non-null and effective crossing routes, increasing the chances of finding the global optimum in the optimization problem.

- Mutation operator - mutation is a process that randomly changes the gene of a chromosome towards avoiding early convergence to a suboptimal solution. The GA setup implemented a Dynamic Random Mutation (DRM) operator that determines a new value for a gene by combining a random perturbation vector chosen within the (0, 1] interval with an updated mutation step size. The operator increases the variability of the mutation rate, so that the searching process reduces the chance of falling in a local optimum.

- Elitism strategy - a strategy implemented due to the continuous population size towards retaining the best solution to be used in the next generation. The GA setup used a substitution operator, which compares each offspring chromosome to its parent chromosome individually. The chromosome of highest fitness is elected the survivor.

- Stopping criteria and applicability of the GA - an independence study defined the GA parameters for the optimization problems. The following setups provided a fair performance comparison base: an initial population was randomly created in the search space; crossover probability = 0.80; mutation probability = 0.1; elitism = 1%. These values are recommended to contain all the information and parameter combination (CHUANG; CHEN; HWANG, 2016; CHUANG; CHEN; HWANG, 2015). The applicability of this GA strategy has been validated on conceptual designs of transport aircraft with a reduced level of fidelity (SINGH; SHARMA; VAIBHAV, 2016; SINGH, 2018).

Table 17 shows a summary of the results for five comparative GAs, including population size, maximum number of generations, and best and average values for the block fuel objective function. The GA-1, GA-2, and GA-3 are unable to find any feasible solution within 150 generations. Conversely, the GA-4 setup performs satisfactorily to find a best solution to the true optimum at the lowest computational cost. Each experiment consisted of 20000 fitness evaluations, as a result of a population of 100 individuals run for 200 generations. The GA module was applied in an Intel Core i7 processor, 2.6 GHz with 16 Gb RAM. The single processor run time of each experiment was about 9 hours per run.

The corresponding convergence history of block fuel minimization (best and average individual versus generation) for CTW and BW aircraft are given in Fig. 18. For the best individuals, the GA converged to minimum values after about 100 iterations. The average individuals showed several oscillations because the random mutation process caused the reproduction of individuals with low-fitness values. However, a clear convergence to an optimum value can be observed on all computations.

3.2.3 Aerodynamic Module

Paerom includes an in-house aerodynamic module, whose outputs are used to calculate the parameters of subsequent modules. The aerodynamic module quantifies the

Table 17 – Numerical setup for different parameter combination of GAs[1].

Proposed GA	Population size	Number of generations	Optimized $f(\mathbf{x})$ Best	Average
GA-1	50	100	8412.2	8674.2
GA-2	50	150	8396.4	8573.2
GA-3	100	150	8178.7	8294.5
GA-4	**100**	**200**	**7886.7**	**7886.7**
GA-5	150	300	7886.7	7886.7

[1] Data for block fuel optimization of BW concept (given in $[kg]$).

Source: The author

Figure 18 – Best and average individuals versus generation (block fuel minimization, units of objective function in $[kg]$).

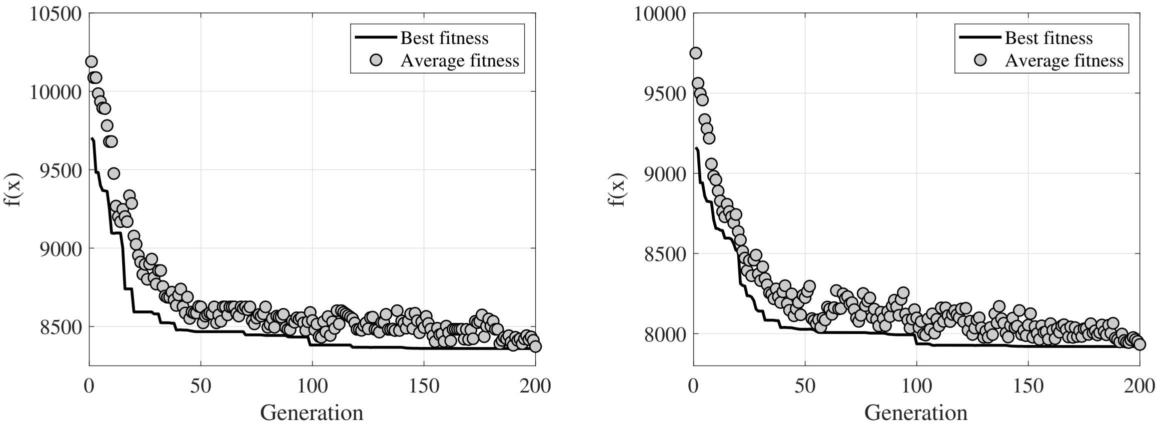
(a) CTW optimization. (b) BW optimization.

Source: The author

zero-lift drag (i.e., skin-friction drag, form drag, interference drag) of wings, fuselage, tails, pylons, nacelles, embedded engines, as well as induced drag, trim drag and wave drag from the wing system. Zero-lift drag (C_{D0}) calculation is based on the wetted area (S_{wet}) using predictions of skin-friction models and form-factor estimates, as suggested by Raymer (RAYMER, 2012). In the case of the induced drag, calculations are obtained using a Vortex Lattice Method (VLM) code, where the singularity element is the vortex line solution of the incompressible potential flow equation ($V = \nabla\phi$), while the imposed boundary condition is that of non-penetrating flow on the surface of the wing panels. The induced drag (C_{Di}) is then calculated in a plane located at an infinite distance downstream the configuration, which is perpendicular to the wake (Trefftz plane). It is possible to use a simpler method, in which an elliptical lift distribution over the fore and aft wings is assumed, and the induced drag calculated from a simple VLM method is converted from this optimal 'Biplane' to a 'Box-wing' based on Prandtl's original relationships (FREDIANI; MONTANARI, 2009). Trim drag is also accounted for the double-wing system, as the lift distribution of both wings affects the CG envelope and the downwash angle. Transonic effects (wave drag, C_{Dwv}) are considered using simple sweep theory to

Figure 19 – Aerodynamic model showing trailing vortex filaments on the box-wing.

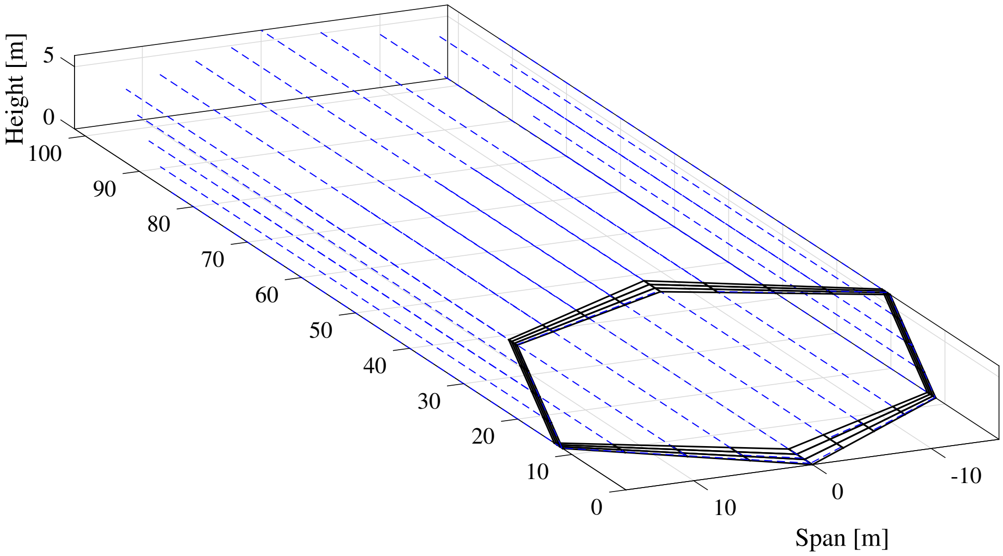

Source: The author

account for sweep and the Korn equation (GUR; MASON; SCHETZ, 2010). Finally, a set of supercritical airfoils was chosen and a performance database was created by means of rapid two-dimensional CFD analyses, varying Mach number, altitude and angle of attack (BRAVO-MOSQUERA; CERÓN-MUÑOZ; CATALANO, 2019). The selection criteria was based on adequate lift-to-drag ratio and internal volume at the expense of small wave-drag penalties. Among the selected airfoils, those best adapted to the operational and stability requirements were chosen in a cost-benefit analysis. A typical wing aerodynamic model using this method is shown in Fig. 19, which shows the wing surface discretization and trailing vortex filaments. For more details on the aerodynamic approximations used in **Paerom**, see Appendix C.0.2

3.2.4 Weight Module

Paerom evaluates the Maximum Take-Off Weight (MTOW) by breaking down into Operational Empty Weight (OEW), Design Payload Mass (DPLM), and Fuel Mass (FM) for the specified mission profile. OEW depends on aircraft geometry, propulsion system, structural layout, materials properties, aircraft systems and operational items. Semi-empirical prediction formulas were used to compute the CTW's fuselage and wing weights (TORENBEEK, 2013). For the BW concept, the mass of the fuselage is calculated by semi-analytical methods for novel aircraft, considering penalties from pressurization, engines and landing gear mounted on fuselage, and nonstructural mass components like windows and doors (TORENBEEK, 2013). In addition, the method considered a weight fraction saving (7.5%) due to bending loads provided by the closed wing system (OLIVEIRO, 2015). The fore and aft wing masses were calculated by a semi-empirical equation derived from finite element methods and regression analysis based on an idealized wing box cross-section geometry (JEMITOLA; MONTERZINO; FIELDING, 2013). This method accounts for wing-box skin, stringers, spar caps and webs with equivalent flat panels. The static load case associated to $+2.5g$ was considered as sizing condition, and the dive speed was obtained from the aircraft envelope. The other factors needed to use this formula are design variables imposed in the optimization problem. The applicability of this methodology demonstrated very accurate results when compared to structural surrogate models (equivalent to 1% of the total mass of the two wings), providing a high-level of confidence for conceptual design purposes (CIPOLLA *et al.*, 2021). Finally, to account for the mass of two vertical fins, a fixed fraction (4%) of the dual-wing system mass is considered from higher fidelity structural analysis of box-wing concepts (CANTO *et al.*, 2012).

First-order mass estimate equations calculated the mass of secondary elements such as high-lift devices and control surfaces, as well as single vertical tail, systems and operational items, and landing gear (TORENBEEK, 2013). The main gear is assumed to have two main struts each with two tires, whereas the nose gear has one strut and two tires. The current conceptual design does not look into the specifics of main landing gear integration and the resulting belly fairing. DPLM is obtained from the aircraft design requirements. Therefore, passengers are located in a typical single aisle fuselage, and baggage is located at conventional cargo bay. FM is calculated by estimating the fuel consumption for each flight segment of the nominal mission profile, where each segment is associated with a mass fraction (RAYMER, 2012). More details of FM calculation are given in subsection 3.2.8, whereas details on the weight module and analysis approach are provided in Appendix C.0.3.

3.2.5 Propulsion Module

The propulsion-airframe integration of a new aircraft is one of the most important aspects for reductions in fuel-burn, emissions, and noise. The main purpose of the propulsion module is to calculate the engine dimensions (nacelle length and diameter) and mass based on a rubber-engine model (MATTINGLY; HEISER; PRATT, 2002). Pratt & Whitney PW1000G was used as the reference engine and the data sheet values are included in Table 18.

Table 18 – Pratt & Whitney PW1000G engine reference values. Source EASA (PW1100G-JM. . . , 2019).

Specification	**PW1000G**
Dry mass $[kg]$	2857.6
Length [m]	3.4
Fan diameter [m]	2.06
Bypass ratio [-]	12.5:1
Static Thrust $[kN]$	110–160

Source: The author

The design of non-BLI and BLI configurations was based on the engine dimensions and the optimum values of the design variables. Close-up views of the propulsion station of both configurations are depicted in Fig. 20. Non-BLI configuration (Fig. 20a) has nacelles mounted on symmetrical pylons, which are tilted upward (about 10 degrees) in order to avoid the ingestion of the local downwash produced by the fore wing. BLI configuration (Fig. 20b) obtained benefits from both the propulsive efficiency inherent to BLI, and the reduced wetted area of nacelles and the mass of pylons, decreasing fuel-burn. The nacelle geometries were designed under off-design conditions, using the ultra-short nacelle design strategy for low fan pressure ratio engines (PETERS *et al.*, 2015). The inlet duct was designed to couple with a rear semi-buried engine (about 40% of burying) in order to ingest a portion of the airframe boundary layer and part of the free stream flow ($h/\delta > 1$, where h is the height of the ingested streamtube, and δ is the fuselage boundary layer thickness). The boundary layer thickness was computed by the momentum equation assuming an ideal 1-D model for a flat plate in a turbulent flow. For additional information, please refer to Goldberg *et al.* (2017), and the equations provided in Appendix C.0.4.

Figure 20 – Close-up view of the propulsion integration versions on the INTI aircraft, dimensions in meters.

(a) Non-BLI schematic.

(b) BLI schematic (inflow situation).

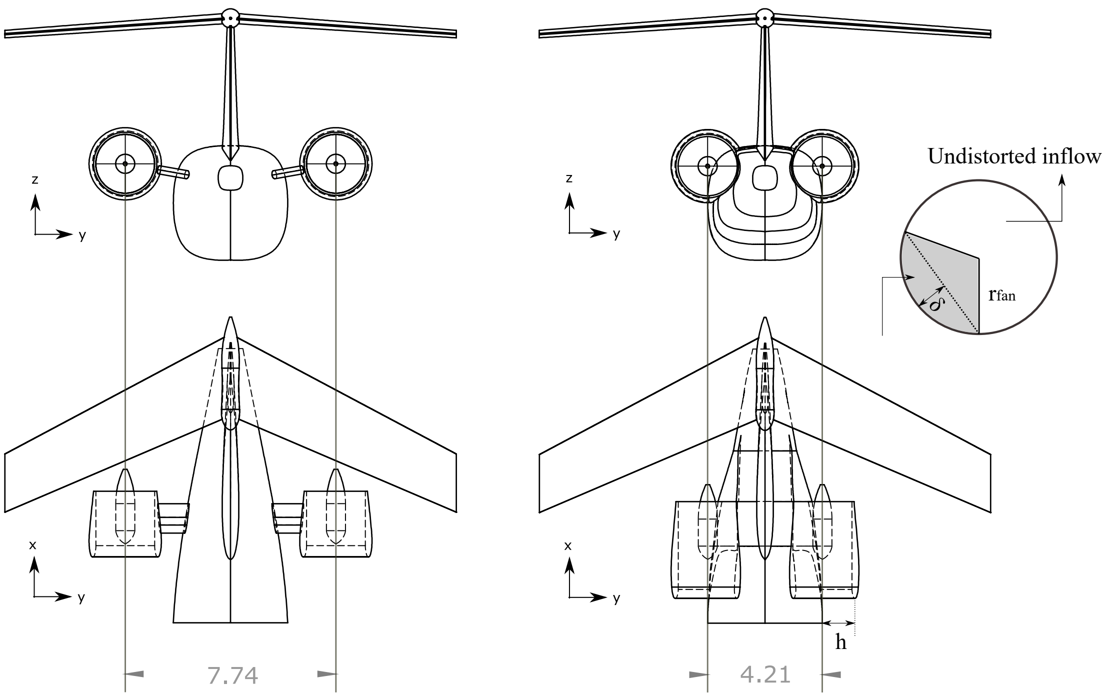

Source: The author

3.2.6 Center of Gravity

After the collection of the masses values, a weight and balance analysis assesses whether the current design is satisfactory or whether components must be relocated for achieving the desired CG range for static margin. Iterations with aerodynamic, weight and stability modules determined the optimum CG offset regarding the selected datum line and limits of specific design variables.

For illustrative purposes, Fig. 21 shows the geometry of the BW aircraft used in the multidisciplinary optimization with its respective CG position. Elevators, trailing edge flaps and ailerons are located at outboard stations of both wings, whose dimensions are based on advanced aircraft designs (TORENBEEK, 2013). It should be noted that high-lift devices and control surfaces were designed at off-design conditions, so they are treated as point masses attached to the wings during the optimization loop. Fuel tanks are located in the fore and aft wings, as well as inside the fuselage where the wing box passes through. The fuel tanks are sized as a simple wing box structure, according to the optimum thickness-to-chord distribution of the dual-wing system, and the available wing surface. Both fuel tanks are assumed to distribute the same amount of fuel throughout the mission. No additional fuel storage (e.g., a cargo bay fuel tank) is considered in the current optimization process due to certification challenges. For more details on the center of gravity module, see Appendix C.0.5.

Figure 21 – Configuration and center of gravity (example of the non-BLI version).

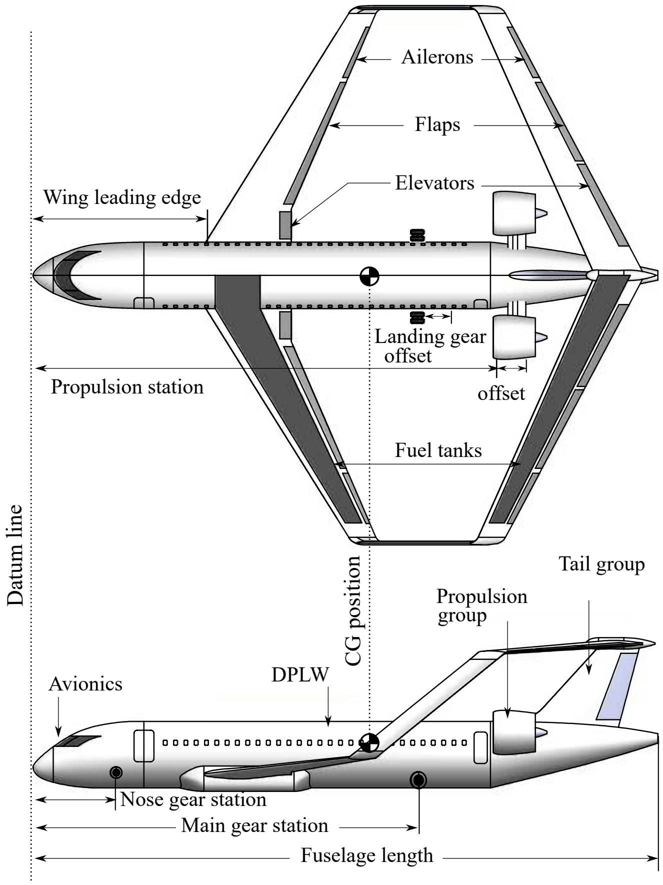

Source: The author

3.2.7 Stability Module

The optimization problem involved design constraints on longitudinal flying qualities at cruise. Therefore, the study of forces and moments acting on the BW system was a major aspect in determining the best design. The development of the stability module was based on a preliminary stability analysis from PARSIFAL project (CIPOLLA; SALEM; BACHI, 2019). Longitudinal stability determined the static margin (SM_x) and neutral point referred to the leading edge of the mean aerodynamic chord and the permissible CG travel. The minimum acceptable static margin of 5% is imposed in the optimization problem, since designs with a static margin lower than zero are longitudinally unstable. The balance of forces and moments of a dual-wing system evaluated the pitching moment induced by each wing, whereas the stability derivatives were derived from the DATCOM method (WILLIAMS; VUKELICH, 1979). The lift-curve slope of the wing-body junction is accounted by using Torenbeeks' equation (TORENBEEK, 2013). The final result is the desired force stability derivatives with respect to angle of attack. Interference factors due to the fuselage, downwash ratio and aft wing were also considered to calibrate the longitudinal model.

On the other hand, lateral-directional stability was evaluated at off-design condition. In particular, the sideslip angle derivative of lateral force ($C_{y\beta}$) was determined by the product among the single vertical tail surface, the lift-slope of the vertical tail derived from lifting line results, and the sidewash parameter calculated by semi-empirical correlations. Note that Prandtl-Glauert corrects the incompressible lift coefficient for the Mach number effects. Once obtained $C_{y\beta}$, the roll moment ($C_{l\beta}$) and yaw moment ($C_{n\beta}$) derivatives were evaluated from the definition of vertical and horizontal distances between the vertical surface aerodynamic centre and aircraft CG. As a result, the dihedral angles (Γ) of the fore and aft wings were 4° and $-2°$, respectively. Details on the stability module can be found in Appendix C.0.6.

3.2.8 Performance Module

Paerom evaluated the performance of the INTI aircraft based on block fuel calculations and discretization of the mission profile. Warm-up, taxi, take-off, and landing segments were estimated using fixed fuel fractions for jet transport given by Raymer (2012). These values are accurate for CTW configurations and may differ for the BW concept, however, they are necessary to compare the mission profiles of the two configurations. The climb segment was analyzed for a specified initial climb altitude at maximum calibrated airspeed, until the initial cruise altitude is reached. Lastly, phases such as cruise, descent, and loiter are discretized in function of range and endurance using the Breguet equation (TORENBEEK, 2013). Once the fuel fractions are determined, they are multiplied together to find the ratio of the aircraft weight at the end of the total mission. This ratio is used to calculate the total fuel burn for a given mission profile. The methods used for calculating each of these contributions are presented in Appendix C.0.7.

3.3 CFD-based Approach

A CFD-based approach is developed to correlate the applicability of the conceptual-level MDO presented above. CFD simulations are divided into two main stages, both at cruise condition. The first stage deals with the computational analysis of the unpowered configuration (i.e., without engines). Such simulations analyzed the flow behavior on the aircraft in order to compare the **Paerom** low-fidelity aerodynamic module. The second stage evaluated the performance of the propulsion integrated models in a high-fidelity environment (offline optimization loop). The goal of this study was to quantify the aerodynamic benefits of the BLI configuration, comparing its performance with the non-BLI configuration. Therefore, both configurations used the same fan diameter and nozzle area. The performance evaluation was carried out following the power balance framework reported by Drela (DRELA, 2009), and also assessing the performance of the inlet in terms of the total pressure recovery and the distortion index. The computations were carried out using **ANSYS-FLUENT**, solving Reynolds Averaged Navier-Stokes (RANS) equations (MATSSON, 2020). A second-order finite volume is selected to solve the Reynolds stress tensor by using the two equation $\kappa - \omega$ SST (Shear Stress Transport) model. This turbulence model is one of the most commonly used models to capture the effect of turbulent flow conditions, demonstrating superior performance for complex boundary layer flows under adverse pressure gradients and separations (MENTER; KUNTZ; LANGTRY, 2003).

3.3.1 Grid Generation

The main computational domain (Fig. 22) was discretized using conventional meshing algorithms. The domain was divided into three computational subdomains (or control volumes) located in critical regions where the flow has more complex behaviors. This approach increases the data accuracy while keeping a conservative idea about the time consumption in the simulations. For instance, around the aircraft was created one control volume with more refined meshes, extending it to the models' back in order to capture the physics involved in the wake with more precision.

Unstructured, tetrahedral elements were implemented throughout the fluid domain, in order to simplify the meshing procedure and model complex geometries. Near the outer wall boundaries, a structured inflation mesh was applied to enhance the resolution within the boundary layer at the fluid-solid interfaces. Table 19 summarizes the details of the final mesh for all configurations.

A mesh independence analysis was performed to achieve the best precision in

Figure 22 – Computational domain and boundary conditions (BLI version depicted).

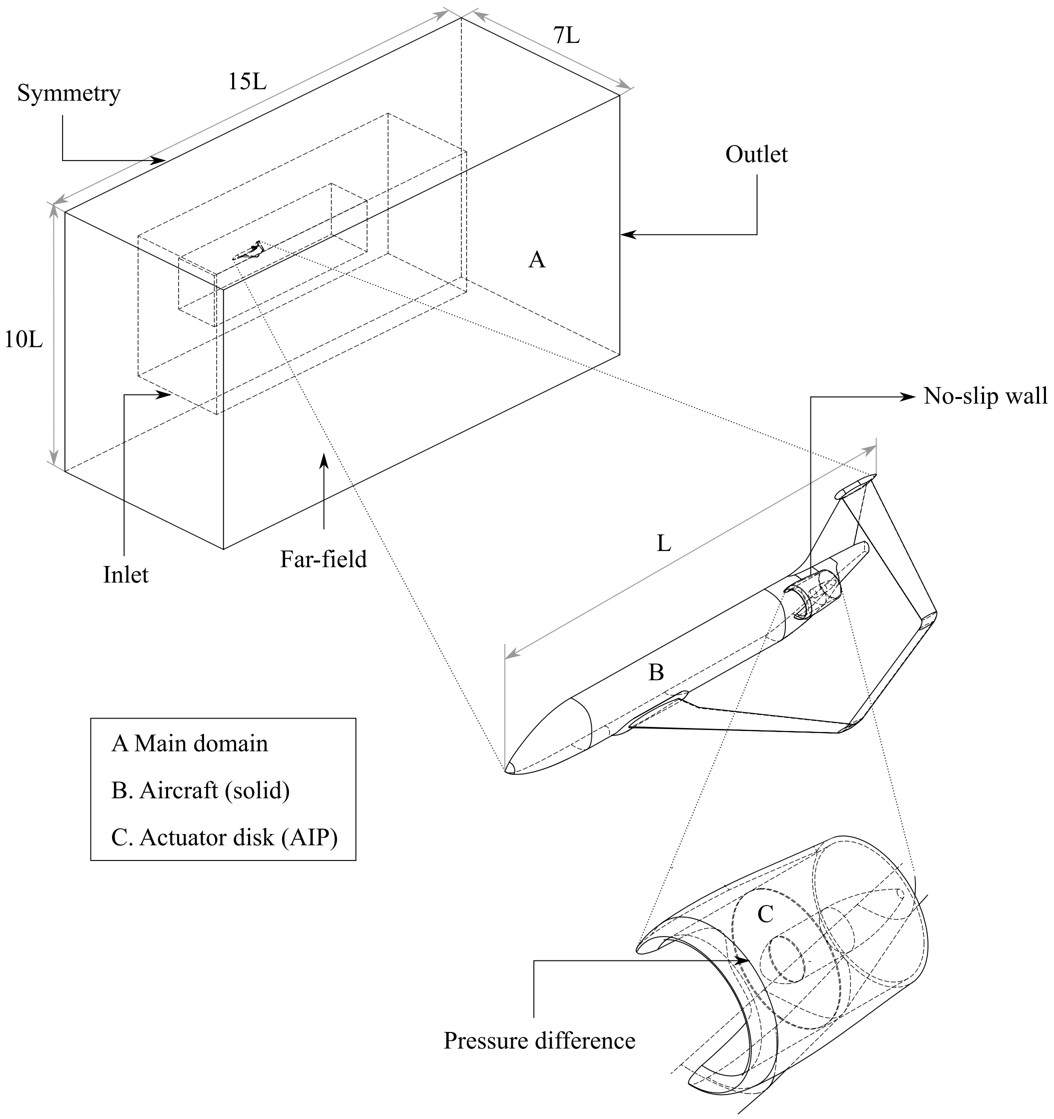

Source: The author

Table 19 – Computational mesh parameters.

Method	Unstructured Tetrahedrons
Body sizing	0.8 m
Face sizing	7×10^{-2} m
Inflation, y+	1.0
Wall spacing	6.1×10^{-6} m
Inflation, number of layers	20
Inflation, growth rate	1.2

Source: The author

the results without compromising the simulation time. Five grids were established with different mesh refinement levels, as shown in the Table 20. The refinement level 5 was defined as the benchmark in this study. The levels 1, 2 and 3 had less number of elements, lowering computational cost. However, the drag coefficient (C_D) remained divergent from the reference values. Thus, the refinement level 4 was implemented on each simulation. From this number of cells, there is no divergence in the variables under evaluation, and the time of each simulation is decreased, ensuring that the results are reliable. The final computational grid of the unpowered configuration is shown in Fig. 23, whereas close-up views of the grids on the powered concepts are displayed in Fig. 24.

Table 20 – Independence mesh analysis for the unpowered configuration.

Refinement level	Number of elements	Simulation time[1]	C_D [-]	Δ [%] C_D
Level 1	6.75×10^6	15h 04min	0.0312	12.51
Level 2	11.04×10^6	21h 47min	0.0301	9.32
Level 3	14.89×10^6	29h 41min	0.0285	4.21
Level 4	18.48×10^6	**35h 57min**	**0.0274**	**0.36**
Level 5	23.14×10^6	45h 37min	0.0273	-

[1] Using an Intel Core i7 processor, 3.2 GHz with 24 Gb RAM (in a parallel fashion).

Source: The author

Figure 23 – Computational mesh on the surface (left) and close-up view of the fuselage (right) of the unpowered configuration.

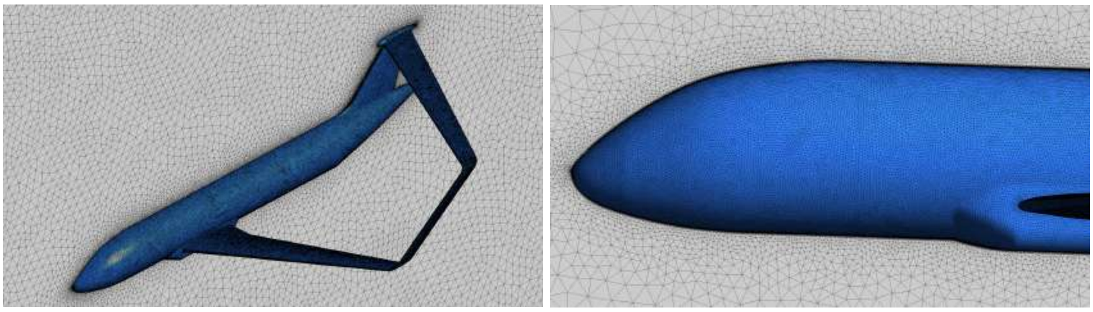

Source: The author

Figure 24 – Close-up views of surface meshes. Non-BLI (left) and BLI (right).

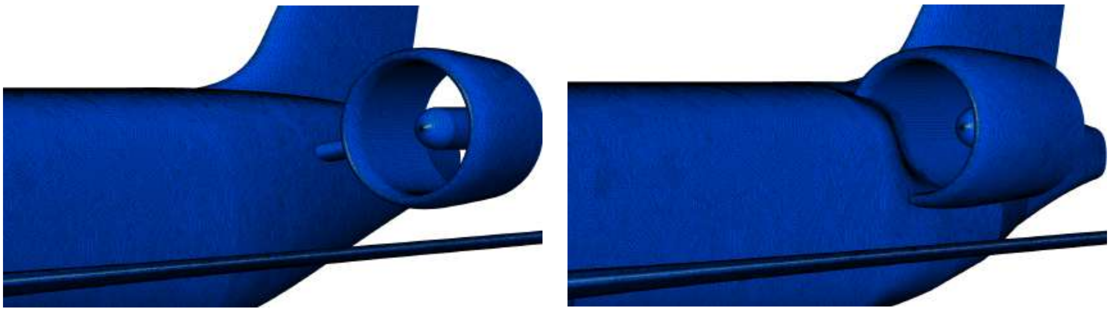

Source: The author

3.3.2 Boundary Conditions

The computational domain (A) as well as the imposed boundary conditions for the BLI version of the INTI aircraft are shown in Fig. 22. The dimensions of the main domain are based on the aircraft length (L). The flow-field solution was initialized at all grid points using the freestream flow conditions. The outlet condition was imposed with no pressure gradient. No-slip and adiabatic wall conditions were imposed on the wall surfaces (B). The propulsor fan was modeled as an actuator disk (no tangential component of induced flow) inside the nacelle (C), which was considered as the Aerodynamic Interface Plane

(AIP) to compute the analysis. For cruise condition, four distinct pressure differential values were imposed across the actuator disk in order to simulate the thrust force. The following calibration function was considered in CFD simulations: $T_{req} = \Delta_p \cdot \pi r_{fan}^2$, where Δ_p is the required pressure difference, and πr_{fan}^2 is the area of the actuator disk (WALSH; FLETCHER, 2004). The non-BLI and BLI actuator disks are set with the same static pressure difference, so the propulsor performance is determined from the merit of the model to preserve the boundary layer history and the resulting differences in mass flow. This boundary condition allowed for a lower computational cost when compared to a completely unsteady approach for fan modeling. Even without such a detailed analysis, actuators disks have been used on several unconventional concepts for preliminary estimates of the BLI benefits (PANDYA *et al.*, 2014; WIART *et al.*, 2015; BLUMENTHAL *et al.*, 2018). Finally, cartesian velocity components were considered as initial conditions. The advection scheme and turbulence numerics were discretized using high resolution terms. The convergence control was set to reach 1000 iterations for the unpowered case, and 5000 iterations for the powered configurations, both with a residual target equal to 1×10^{-5}.

3.4 Results and Discussions

The results have been separated into three sections for the sake of comparison and clarity. Section 3.4.1 shows low-fidelity optimization results of the CTW and BW concepts, in order to better understand the key characteristics of the optimal designs with respect to the objective function evaluated. The optimized BW concept is also compared to other BW concepts available in the literature. Section 3.4.2 presents a more detailed aerodynamic comparison between the CTW and BW concepts by CFD simulations. Section 3.4.3 summarizes the results from the CFD evaluation of propulsion integrated models on the BW concept.

3.4.1 Comparison of CTW and BW Using Low-Fidelity Results

Optimized designs were obtained using conceptual-level MDO for the specified mission. Severe constraints such as the available fuel volume, maximum wingspan, fuselage length, and nominal range were highly penalized, causing the fitness value to be set to zero, so these constraints were fully satisfied by the optimum solutions. Other performance constraints, such as the minimum top-of-climb thrust, which is dependent on both the optimum cruise altitude and the appropriate rate of climb, may be slightly violated; however, for most performance constraints, increasing wing area and/or engine thrust was the simplest manner to address a constraint violation.

The results of the conceptual-level MDO are presented in Table 21. Note that the optimum BW concept has 29.4% more wing area than the optimum CTW aircraft. This is because the block fuel objective function tends to reduce drag, so the wings of the BW

Table 21 – Conceptual-level MDO results[1].

Parameter	**CTW**	**BW**
Reference M.A.C [m]	3.56	2.55
Wingspan [m]	35.94	32.2
Wing area [m^2] -	123.37	174.90
Aspect Ratio [-] - fore/aft	10.47	10.01/14.24
Wetted Aspect Ratio [-]	1.60	1.29
Wingspan efficiency [-]	1.0	1.46
Mach number [-]	0.78	0.78
Cruise altitude [m]	11200	12500
Reynolds number [$\times 10^6$]	23.13	16.57
Cruise L/D [-]	17.7	19.3
Cruise C_L [-]	0.59	0.51
Cruise C_D [-]	0.0334	0.0264
Cruise C_{D0} [-]	0.0210	0.0186
Cruise C_{Di} [-]	0.0107	0.0075
Cruise C_{Dwv} [-]	0.0017	0.0003
Cruise drag [N]	37928.0	35075.4
Block Fuel [kg]	8367.4	7886.7
T_{max} [kN] (per engine)	119.54	121.62
Cruise SFC [$g/kN/s$]	0.53	0.53
MTOW [kg]	77334.3	78978.8
OEW [kg]	43240.1	44982.1
Total Wing [kg]	8636.1	9990.4
Fore wing [kg]	-	5095.1
Aft wing [kg]	-	4495.6
Tip fin [kg]	-	399.6
Fuselage [kg]	8047.5	8247.8
Vertical tail [kg]	483.7	746.0
Horizontal tail [kg]	839.8	-
Landing gear [kg]	2967.3	3160.5
Propulsion[2] [kg]	8930.8	8946.9
Systems [kg]	11064.1	11646.9
Operational items [kg]	2273.4	2273.4
W/S [Kg/m^2]	634.9	457.2
T/W ratio [-]	0.309	0.310

[1] Aerodynamic data obtained from cruise condition, and operating data for nominal range plus diversion range.

[2] Includes bare engines, nacelles, and pylons.

Source: The author

become longer (higher Æ) and thinner (lower t/c ratios) than the CTW, reducing the induced drag and the wave drag, respectively. However, due to the available fuel volume constraint, a larger wing area is necessary, resulting in a higher OEW, which affects the MTOW, and a higher wetted area, which reduces the overall wetted aspect ratio. In this context, there is a clear trade-off between the available fuel volume constraint and the need to reduce drag for the specified objective function and mission requirements.

Such an increase in wing area reduced the wing loading (W/S) of the BW compared to the CTW, ensuring that a sufficient amount of lift can be generated for take-off conditions. However, since the wing area ratio variable bound is active during the optimization process, the fore wing is more loaded than the aft wing due to longitudinal stability constraints, i.e., the wing loading of the fore wing represents a compromise between the search for higher L/D ratios and the need to satisfy other constraints. These results are consistent with those of other researchers, who agree that the lift characteristics of the fore wing determine the majority of the BW performance, including stall characteristics, cruise Mach number, and the downwash effect on the aft wing (FREDIANI *et al.*, 2019; ANDREWS; PEREZ, 2018b).

As per the results, and based on the above discussion, the OEW of the BW is 3.87% higher than the CTW. The mass breakdown of the configurations can be used to explain this result. Note that the wing mass of the BW is 13.55% higher than the CTW. Such an increase is related to the larger wing area, as well as additional mass components due to the distribution of secondary elements like control surfaces and trailing edge movable surfaces. The BW layout itself also had a considerable impact on the vertical tail mass (about 35.15%).

Despite benefiting from the distributed bending loads created by the double-wing design, the BW fuselage mass is 2.42% higher than the CTW. This is due to the effects of the fuselage-mounted landing gear and propulsion system point masses, as well as the cabin pressurization loads caused by flying at higher cruise altitudes. Moreover, having two fully separate fuel tanks increased the weight of the fuel system and made integration more difficult. Therefore, there is a system mass penalty of about 5.0%.

The aerodynamic data obtained from the respective cruise condition determined the overall performance benefits of the BW over the CTW. Since the initial cruise altitude is allowed to vary during the optimization process, the BW achieved a more favorable balance between zero-lift drag and lift-dependent drag at higher cruise altitudes due to its relatively high $A\!\!\!R$ of each wing and low W/S. That is the reason why the BW concept for block fuel minimization cruises at higher altitudes than the CTW, keeping the lift coefficient at its optimum value for minimum drag. This way, the BW resulted in a considerable aerodynamic efficiency improvement at cruise (about 8.2%) for the optimal drag-altitude combination.

Overall, the optimum BW is 5.7% more fuel efficient than the optimum CTW for nominal range. The benefits of the BW concept can be understood from two main points of view. For example, when looking at a single wing of the BW configuration, high aspect ratio wings are responsible for the induced drag reduction of the whole BW system. Consequently, the span efficiency (e) of a single wing is about the same as that of the CTW concept. On the other hand, when looking at the whole double-wing system, the total aspect ratio of the BW concept is reduced ($A\!\!\!R = 5.92$). In this case, the span efficiency ($e = 1.46$) is responsible by the induced drag reduction which depends on both the height-to-span ratio and the stagger-to-span ratio. These variables relate the geometric height and streamwise separation, as well as the sweep angles and wetted area, so they also have an effect on the zero-lift drag. Their optimal values, when combined with higher cruise altitudes, have a direct impact on the optimal cruise C_L, which holds the cruise drag at its lowest value to achieve a higher aerodynamic efficiency and thus reduce fuel consumption during the flight.

After accounting for all mass components, the BW is 2.05% heavier than the CTW. Despite the higher MTOW, the optimum BW reduced W/S and kept T/W without exceeding the restrictions imposed on the problem. This means that the BW has a suitable trade-off between low and high speed aerodynamic performances. In particular, the propulsion system was sized by the top-of-climb thrust constraint, requiring an increase in the maximum takeoff thrust parameter, but reducing thrust once the aircraft has reached the desired cruise altitude.

Based on the loads distribution and integration difficulty found in this conceptual research for the BW concept, weight and cost are the primary figures of merit that need to be considered in preliminary design studies. A minimum weight concept might represent a design with lowest development and production costs due to structural mass reduction, but the highest operating cost due to fuel consumption and maintenance. In contrast, the current minimum block fuel design exhibited larger wing dimensions at a substantial penalty in terms of OEW (roughly 4% compared to the CTW concept), which might represent a significant increase in production cost from the manufacturer's perspective. It is expected that the customer operational expenses would be lower due to the fuel efficiency of the BW concept, however, this design ended up requiring a higher level of thrust, increasing the cost related to engines as well. Therefore, the aircraft unit price should be higher to provide a financial return to the manufacturer. It should be noted that the net price of an aircraft also depends on the market opportunities and the life cycle costs (TORENBEEK, 2013). A detailed presentation is beyond the scope of this conceptual design study.

Finally, as a matter of discussion, Table 22 shows a comparative analysis of the optimal BW design against aircraft available in the literature. In this case, the fuel mass is calculated in function of the conventional range of the mission profile and assuming the maximum payload mass. For comparative reasons, the wing area values of all listed concepts include the part inside the fuselage. The information taken from unclassified data is subjected to different levels of fidelity. The optimum BW concept (min fuel) demonstrated a close correlation with other BW concepts. Note that there is a fair agreement when looking at the L/D ratio, empty weight ($OEW/MTOW$), and fuel weight ($FM/MTOW$) fractions, despite the differences in the methods used to calculate wing mass. This performance comparison provides interesting design rules that can be used in future conceptual design initiatives. In particular, comparison against box-wings in the single-aisle category showed the most interesting outcomes. For example, concepts such as the ones reported by Schiktanz (2011), Zohlandt (2016), Kaparos *et al.* (2018) evidenced a lower wing area than the optimum BW concept reported in this chapter. As expected, such concepts have a lower MTOW, which might represent a lower fuel consumption in take-off and climb phases. However, due to the limited fuel tank volume inside the wings, additional fuel needs to be stored in containers inside the fuselage, making fuel distribution a design challenge owing to certification requirements. In contrast, the aircraft reported by Binante *et al.* (2020) has a similar wing area than the optimum BW, guaranteeing the fuel is allocated inside the wings, although it has a lower span. In this case, both configurations have a similar overall performance; however, the difference in aerodynamic efficiency can be attributed to the fact that the optimum BW operates at higher cruise altitudes.

Even though there are large margins of improvement in the next design phases, the optimum BW concept exhibited promising results when compared to its recognized competitors. In this context, it can be concluded that the methods applied here are valid for practical engineering purposes at conceptual design level. The list of all design variables, ranges, and optimum values for CTW and BW configurations can be found in Appendix B (Table 37).

3.4.2 Comparison of CTW and BW Using CFD Simulations

Once obtained the optimum configurations, CFD simulations compared the conceptual-level MDO, and evaluated the external aerodynamic characteristics of the unpowered BW concept in a high-fidelity environment. CAD tools were used to create the models for the CFD simulations. Figure 25 shows the main dimensions of the optimum configurations. Note that the vertical tip fin connects the fore and aft wings at the wingtips, using a pair of blended transitions that help to minimize interference drag. In addition, a belly fairing was designed to reduce form drag and interference drag between the fuselage and wings. Note that the belly fairing design was quite simply re-used.

Figure 25 – Geometry comparison of conventional tube-and-wing (winglet designed offline) and box-wing configurations, dimensions in meters.

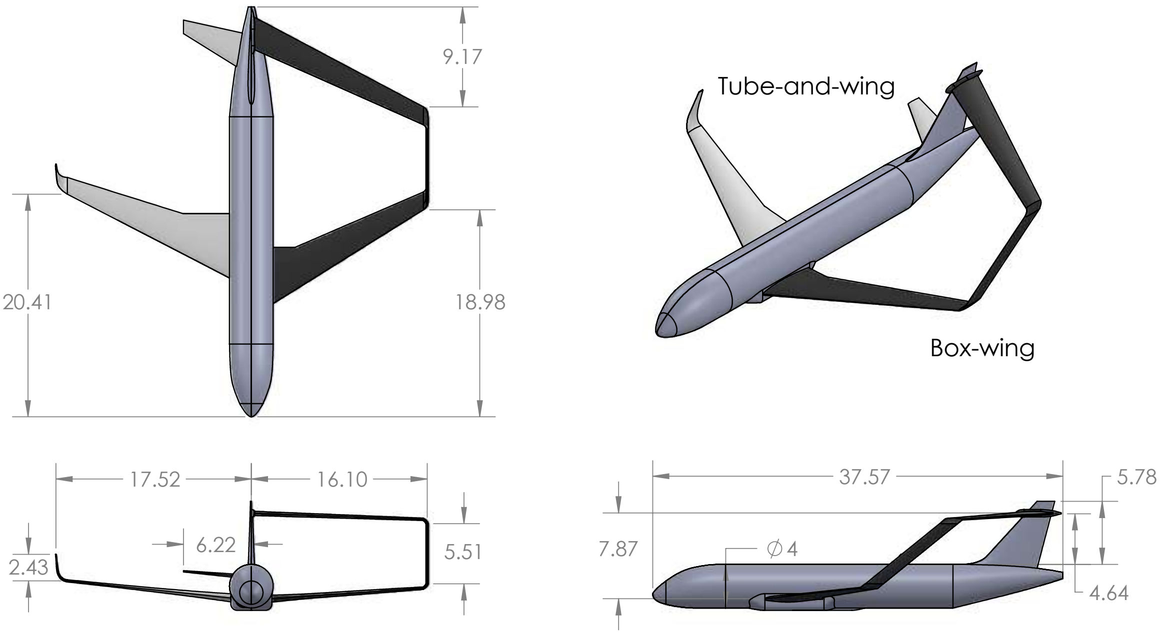

Source: The author

Table 22 – Comparative analysis and design validation through databases.

Box-Wing	**min fuel**	Salem *et al.* (2021a)	Binante *et al.* (2020)	Schiktanz (2011)	Jemitola (2012)	Zohlandt (2016)	Kaparos *et al.* (2018)	Andrews and Perez (2018b)
Wingspan $[m]$	32.2	36.0	28.8	34.0	37.6	31.2	30	22.17
Wing area[1] $[m^2]$	174.9	247.7	175.1	122.0	224.0	157.0	105	104.0
Aspect Ratio [-]	5.92	5.23	4.73	9.47	6.31	6.25	8.57	4.72
Height-to-span ratio [-]	0.244	0.220	-	0.220	0.220	0.194	-	0.250
Mach number [-]	0.78	0.79	0.79	0.76	0.80	0.78	0.78	0.74
Cruise altitude $[m]$	12500	11000	11000	12750	11000	11278	10668	11278
Cruise L/D [-]	19.3	21.6	18.5	20.4	21.3	18.0	-	17.4
Design range $[km]$	4000	5000	5180	2870	7408	4000	4000	2849
MTOW $[kg]$	78978	125126	78130	73500	126670	77510	69800	40100
OEW $[kg]$	44982	68866	43360	41333	68200	43620	-	24259
DPLM $[kg]$	19500	29260	17670	20000	32000	19500	16800	9595
FM $[kg]$	14496	27000	17100	15400	44000	14390	13927	6245
T_{max} $[kN]$ (per engine)	121.6	208.6	-	-	254	120.5	-	68.6
T/W [-]	0.31	0.33	-	-	0.408	0.316	-	0.348
W/S $[Kg/m^2]$	457.2	505.1	446.2	602.4	565.4	493.6	664.7	385.5
$OEW/MTOW$ [-]	0.569	0.550	0.554	0.562	0.538	0.562	-	0.604
$FM/MTOW$ [-]	0.183	0.215	0.218	0.209	0.252	0.185	0.199	0.155

[1] Portion inside the fuselage included.

Source: The author

Lift and drag coefficients were compared for the optimized BW and CTW concepts at cruise condition. Later on, the aircraft L/D values were used in the Breguet equation to update the block fuel over cruise, and the low-fidelity performance calculations of the other flight phases (warm-up, taxi, take-off, climb, descent, landing), were added to obtain the total block fuel. These results are summarized in Table 23. The difference between low-fidelity and high-fidelity results lies mainly, above all, in the CFD accuracy to model turbulent layers and their interactions with shock waves (i.e., the solution is closer to the real flow). However, low-fidelity results had acceptable error rates (about 6%), suggesting a high-degree of reliability for conceptual design purposes. In sum, the BW concept reduced block fuel by 4.6% as compared to its CTW equivalent.

Table 23 – CFD correlation with conceptual-level MDO

	CTW concept				**BW concept**			
Parameter	C_L [-]	C_D [-]	L/D [-]	Block fuel [kg]	C_L [-]	C_D [-]	L/D [-]	Block fuel [kg]
Low-Fidelity	0.59	0.0334	17.7	8367.4	0.51	0.0264	19.3	7886.7
High-Fidelity[1]	0.59	0.0344	17.1	8425.1	0.51	0.0281	18.1	8035.1
Δ [%]	-	-	3.38	0.68	-	-	6.21	1.84

[1] Includes a 2.6% zero-lift drag contribution from nacelle and pylon (estimated by low-fidelity aerodynamics).

Source: The author

CFD simulations allowed for the extraction of additional information from the pressure distribution on the optimized concepts. The wing geometries were generated by the cross-section (supercritical airfoils) between each wing segment, and their optimum geometric variables. In both cases, the angle of attack relative to the x axis (i.e., to the fuselage) is fixed at 3°. Figure 26 shows the pressure coefficient contours over the upper surfaces of the optimized concepts, as well as four pressure coefficient C_p plots at 25, 50, 75, and 100% chord, respectively. There are no significant differences on the C_p distribution near the root section, although the tube-and-wing has a thicker root airfoil, so the pressure distribution regions rise slightly, resulting in an increase in lift. The most significant differences can be seen at the outboard wing sections ($2y/b = 50\%$ and 75%), where the fore wing controlled the impact of wave drag due to a higher sweep angle along the span and lower cross-section thickness. However, some critical areas in terms of shock formation were identified close to the junction between the fore wing and the blended transition, causing a transonic drag increase that was unfavourable. In conclusion, the optimum concepts present a trade-off between reducing induced drag and avoiding strong shock waves. Such results allowed to identify the most critical design parameters in transonic conditions and the potential strategies to improve the aerodynamic design of a BW concept in cruise.

3.4.3 CFD Evaluation of Propulsion Integrated Models

In this section, the findings of the inlet/airframe integration analysis are presented and discussed, including a direct assessment of the BLI benefit, as well as the total pressure recovery and distortion index at the engine face.

Figure 26 – Surface pressure coefficient contours.

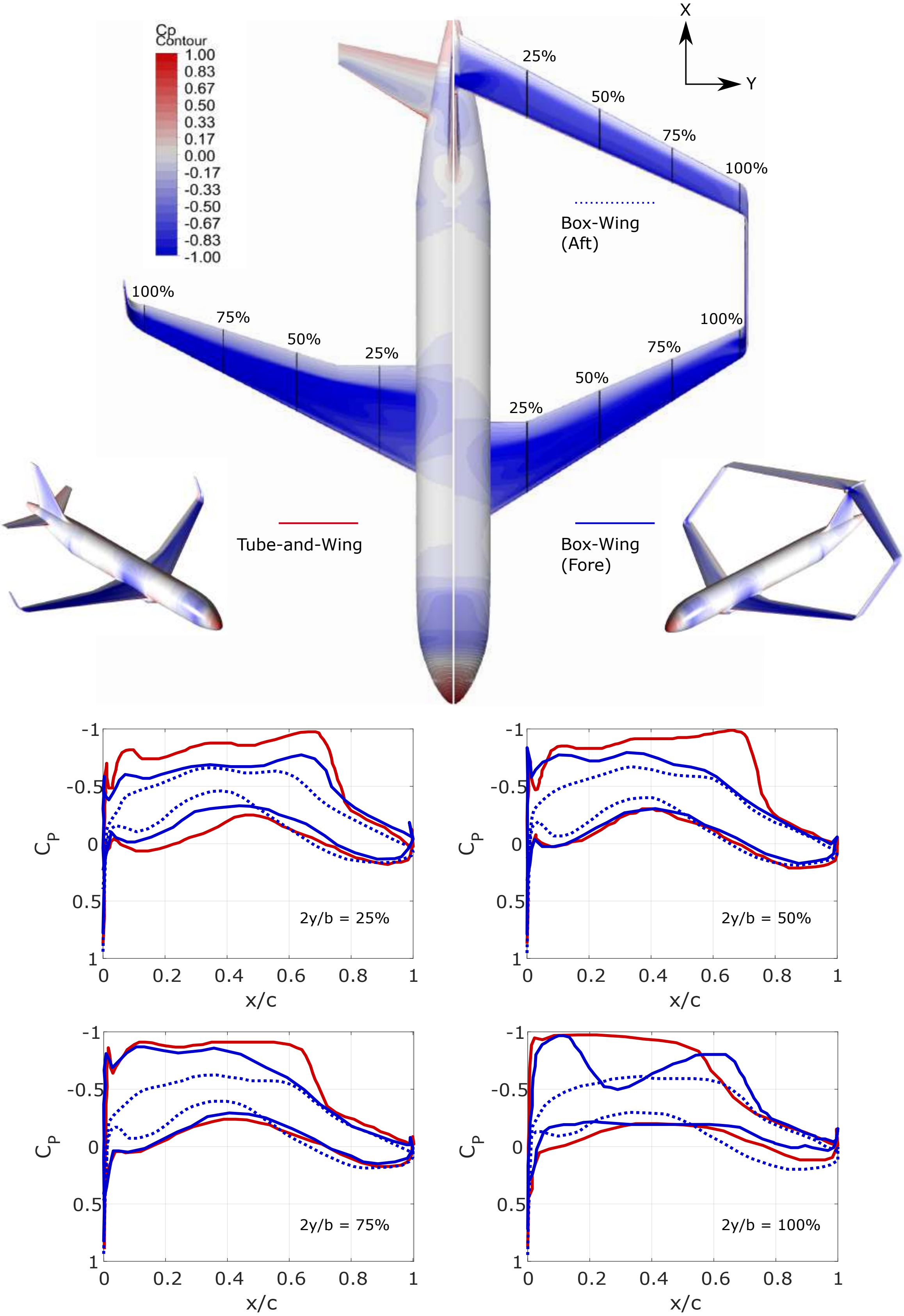

Source: The author

3.4.3.1 Power Balance Method

According to Drela (2009), the total power consumed by the aircraft is the product of the net streamwise force (zero at cruise condition) and the freestream velocity ($F_X V_\infty$), as in Eq. 3.5:

$$F_X V_\infty = \Phi_\infty - P_K - P_V \tag{3.5}$$

where P_V is the volumetric flow power throughout the control volume (Eq. 3.6), P_K is the mechanical flow power taken over the inlet and exit planes of the propulsor (Eq. 3.7), and Φ_∞ is the volumetric dissipation throughout the control volume (Eq. 3.8).

$$P_V \equiv \iiint (p - p_\infty)\, \nabla \cdot \mathbf{V}\; d\mathcal{V} \tag{3.6}$$

$$P_K \equiv \oiint \left[p_\infty - p + \frac{1}{2}\rho \left(V_\infty^2 - V^2\right)\right] \mathbf{V} \cdot \hat{n}\; d\mathcal{S} \tag{3.7}$$

$$\Phi_\infty \equiv \iiint \left(\bar{\bar{\tau}} \cdot \nabla\right) \cdot \mathbf{V}\; d\mathcal{V} = \Phi_J + \Phi_A \tag{3.8}$$

where p is static pressure, p_∞ is freestream static pressure, $\mathbf{V}$ is the velocity vector, $\mathcal{V}$ is the fluid control volume surrounding body, ρ is fluid density, V_∞ is the freestream speed, V is the velocity magnitude, $\hat{n}$ is the unit normal vector to the fan face, $\mathcal{S}$ is the surface of body, including propulsor inlet and outlet surfaces, and $\bar{\bar{\tau}}$ is the viscous stress tensor. The variables on the right-hand side of Eq. 3.8 are viscous dissipation terms, in the propulsor jet (Eq. 3.9), and over the airframe (Eq. 3.10), respectively:

$$\Phi_J = \frac{1}{2}\dot{m}\left(V_j - V_\infty\right)^2 \tag{3.9}$$

$$\Phi_A = \Phi_s + \Phi_w + \Phi_v \tag{3.10}$$

where $\dot{m}$ is the mass flow in the propulsor, V_j is the mass-averaged velocity in the exit plane of the duct, and Φ_s, Φ_w, and Φ_v are viscous dissipation terms on the airframe surface, in the airframe wake, and from the induced losses (vortex) of the wings, respectively.

According to Eq. 3.5, P_K is associated to a reduction in either Φ_∞ or P_V, if F_X is constrained to be zero for all configurations at cruise condition. P_V is relatively small, particularly in cases where transport aircraft are involved (BLUMENTHAL *et al.*, 2018), so it was neglected for the current analysis. Thus, the reduction of P_K is directly related to the account of all viscous dissipation terms, Φ_∞. Since both configurations have the same BW layout, vertical tail, and most of the fuselage shape, the presence or absence of

BLI had no significant effects on vortex dissipation. Therefore, the actual BLI benefits are attributed to lower dissipation in both the propulsor jet and airframe wake, due to the merging of these wake quantities (HALL *et al.*, 2017). To explain the power balance approach bearing in mind the aforementioned assumptions, Eq. 3.5 and Eq. 3.8 can be rearranged in Eq. 3.11.

$$P_K + \Phi_J = \Phi_A - F_X V_\infty \tag{3.11}$$

In this context, when the net streamwise force is constrained to be zero, the power added to the flow by the propulsor (P_K) balances lost of power due to dissipation in the wake, i.e., the savings from Φ_J generally dictate savings from Φ_w. Therefore, the benefit of BLI is derived from reducing the power dissipation in the flowfield by reducing streamwise velocities and kinetic energy losses due to the boundary layer on the fuselage, producing a low-momentum wake downstream the configuration (BLUMENTHAL *et al.*, 2018).

The most appropriate definition to evaluate the propulsive efficiency (η_P) in terms of power and dissipation is given by Eq. 3.12:

$$\eta_P = \frac{P_K - \Phi_J}{P_K} \tag{3.12}$$

which for the BLI configuration must be higher than for the non-BLI configuration, since the BLI propulsion system uses the work already done by the airframe drag, i.e., a higher η_P for BLI concepts is due to a decrease in jet dissipation, Φ_J, required to impart a given thrust, $\dot{m}(V_j - V_i)$, since V_i and therefore V_j are reduced. Finally, the aerodynamic BLI benefit is calculated via the Power Saving Coefficient (PSC), which in terms of mechanical flow power is given by Eq. 3.13:

$$PSC \equiv \frac{(P_K)_{non-BLI} \ - \ (P_K)_{BLI}}{(P_K)_{non-BLI}} = 1 - \frac{(P_K)_{BLI}}{(P_K)_{non-BLI}} \tag{3.13}$$

The overall benefit of the BLI configuration over the non-BLI configuration is presented in Fig. 27. As a matter of fact, the mechanical flow power and the net streamwise force are given in non-dimensional forms, thus:

$$C_{P_k} \equiv \frac{P_K}{q_\infty V_\infty S} \tag{3.14}$$

$$C_X \equiv \frac{F_X}{q_\infty S} \equiv C_T - C_D \tag{3.15}$$

The mechanical flow power coefficient (C_{P_K}) values were calculated from Eq. 3.7, using numerical integration over a control volume containing the propulsor, specifically one

Figure 27 – Net streamwise force coefficient versus Mechanical flow power coefficient for both non-BLI and BLI configurations (cruise altitude = 12500 m, Mach number = 0.78, angle of attack = 3°).

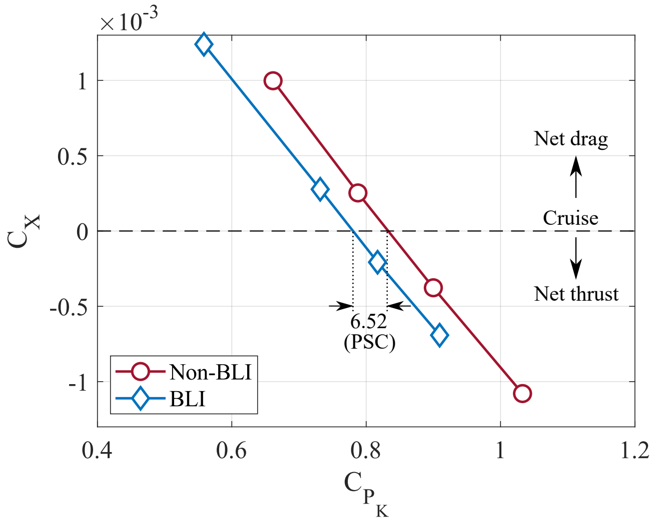

Source: The author

constrained by the inflow and outflow planes. The net streamwise force coefficient (C_X) was calculated as the thrust coefficient (C_T) minus the drag coefficient (C_D); where the thrust force is determined by adding the forces acting on the inlet and exit planes of the actuator disk, which are also in the streamwise direction. A linear interpolation was used to obtain C_{P_K} at the desired cruise point of ($C_X = 0$). The BLI configuration is shown to require approximately 6.52% less propulsive power relative to the non-BLI configuration. For this particular interpolation, Table 24 provides other quantities of interest from the evaluated configurations. The non-BLI configuration had more airframe dissipation than the BLI configuration due to the podded engines, which increased both interference and viscous drag. These findings are consistent with the higher propulsive efficiency of the BLI configuration compared to the non-BLI configuration, as lower inflow velocities and thus lower jet dissipation are obtained. Therefore, the INTI aircraft may benefit from a substantial reduction in fuel consumption using BLI engines.

Table 24 – Summary of CFD results for propulsion integrated models at cruise.

Parameter	C_D [-]	C_{Φ_J} [-]	C_{P_K} [-]	η_P [-]	$\frac{(P_K)_{BLI}}{(P_K)_{non-BLI}}$ [-]	PSC [-]
Unpowered	0.0274	-	-	-	-	-
Non-BLI	0.0285	0.203	0.828	0.758	1	0
BLI	0.0279	0.161	0.774	0.792	0.935	6.52

Source: The author

Figure 28 shows the total pressure ratio maps on each version of the INTI aircraft. The cutting planes are located at $x/c = 20\ m$ from the reference axis (datum line), where c is the chord length and x is the free-stream velocity axis. By comparing the non-BLI configuration (Fig. 28b) against the unpowered configuration (Fig. 28a), the presence of pylons and nacelles increased the wasted kinetic energy of the aircraft, which has been previously confirmed by a higher airframe dissipation (body viscous drag). On the other hand, note that a low-momentum wake is presented downstream the BLI configuration (Fig. 28c), as a result of adding propulsive momentum to the wake generated by the airframe. Therefore, it was proved that the difference in wasted kinetic energy, at equivalent net streamwise force, is a critical parameter for determining the actual BLI benefits, as the power dissipation in the overall flow-field is reduced.

3.4.3.2 Total Pressure Recovery and Distortion Index

The total pressure recovery (η_R), is the ratio of the average total pressure at the AIP ($p_{t_{AIP}}$) to the freestream total pressure ($p_{t\infty}$), based on eq. 3.16. This performance variable evaluated the pressure losses associated with the boundary layer on the inlet surface, i.e., the flow separations in the duct at cruise condition.

$$\eta_R = \frac{p_{t_{AIP}}}{p_{t\infty}} \tag{3.16}$$

On the other hand, the flow distortion index (DC_θ) evaluated the uniformity of the circumferential total pressure distribution at the AIP (eq. 4.10).

$$DC_\theta = \frac{p_{t_{AIP}} - p_\theta}{q_{AIP}} \tag{3.17}$$

where p_θ is the mean total pressure on a 60° sector that has the lowest mean recovery, and q_{AIP} is the mean dynamic pressure calculated by $q_{AIP} = \rho V_{AIP}^2/2$.

Figure 44 shows the Mach number contours (left) and total pressure contours (right) for the non-BLI and BLI configurations respectively. As can be observed, the non-BLI configuration (Fig. 29a) is characterized by a clean and uniform airflow inside the inlet. Hence, there is a higher total pressure recovery, and lower distortion at the AIP (see Table 25). The Mach contour of the non-BLI configuration also evidenced a clear aerodynamic interference between the fuselage and the nacelle, causing separation on the pylons and increasing the drag acting on the nacelle surfaces, thus the propulsor efficiency is reduced. Conversely, the BLI configuration (Fig. 29b) depicted areas of total pressure losses, which increased the thickness of the boundary layer (higher distortion), decreasing the velocity of the airflow inside the duct. The lower the airflow velocity, the lower the ram drag, which explains the improvement in propulsive efficiency.

Table 25 – Internal flow quality factors.

Parameter	η_R [-]	DC_θ [-]
Non-BLI	0.995	0.002
BLI	0.918	0.101

Source: The author

Figure 28 – Contours of total pressure ratio at the wake (cut plane $x/c = 20\ m$).

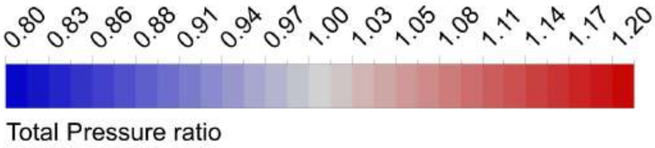

(a) Unpowered configuration.

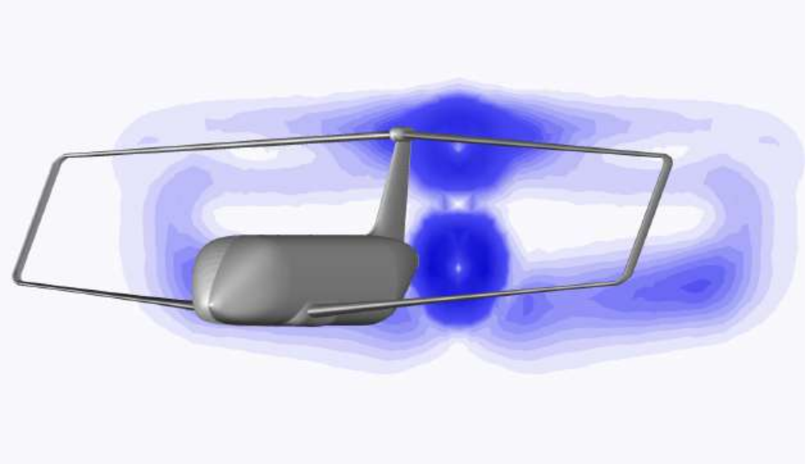

(b) Non-BLI configuration.

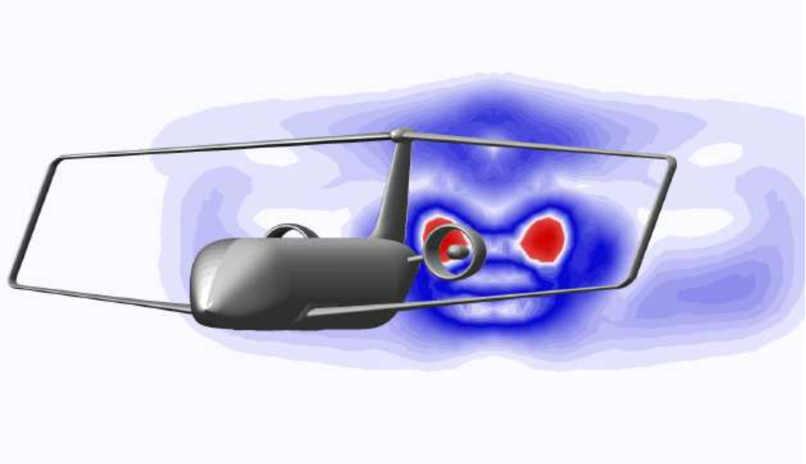

(c) BLI configuration.

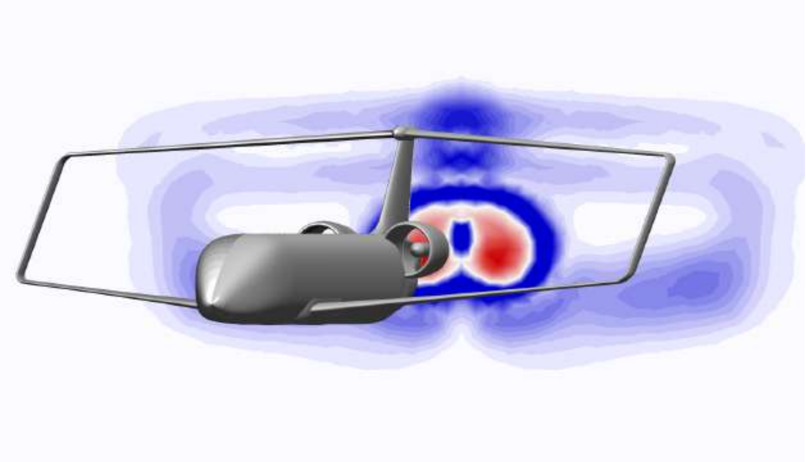

Source: The author

Figure 29 – Mach number contour (left) and Total Pressure Recovery contour (right) of the INTI aircraft, plane located at the AIP.

(a) Non-BLI version.

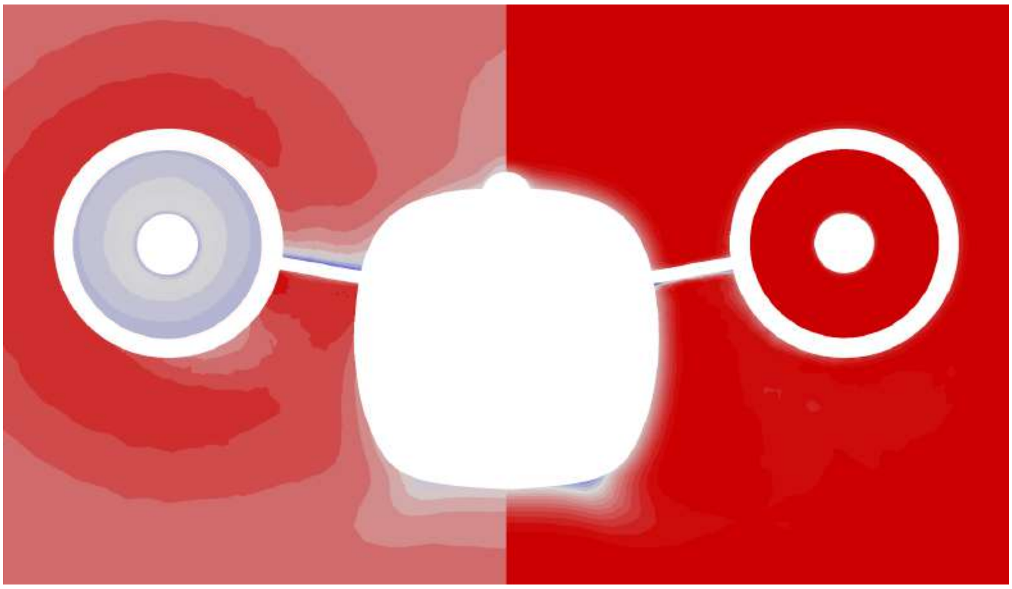

(b) BLI version.

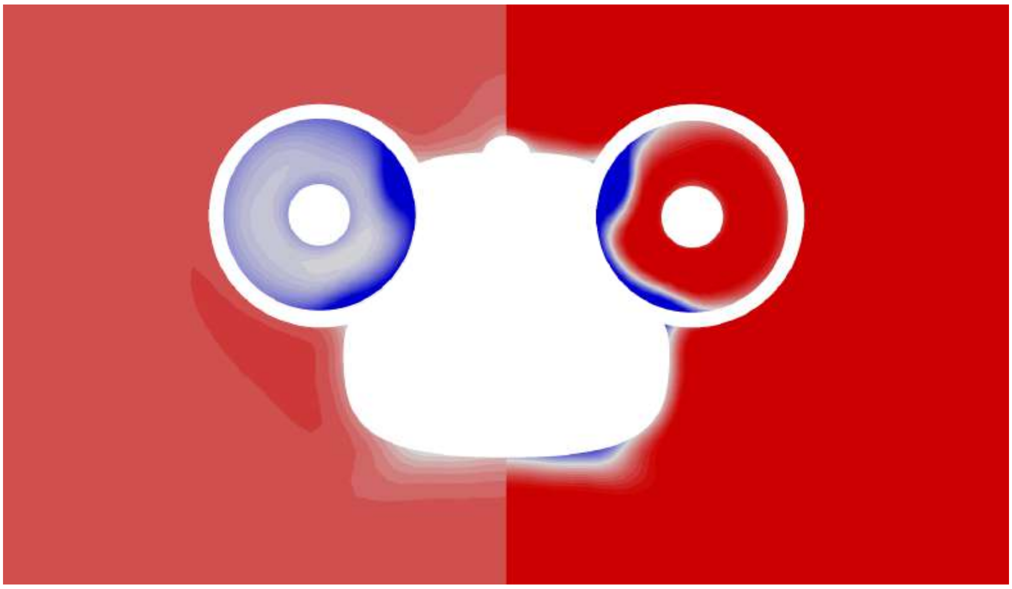

Source: The author

Figure 30 – INTI aircraft, BLI version at the end of the conceptual-level MDO (landing gear belly fairing designed at off-design condition).

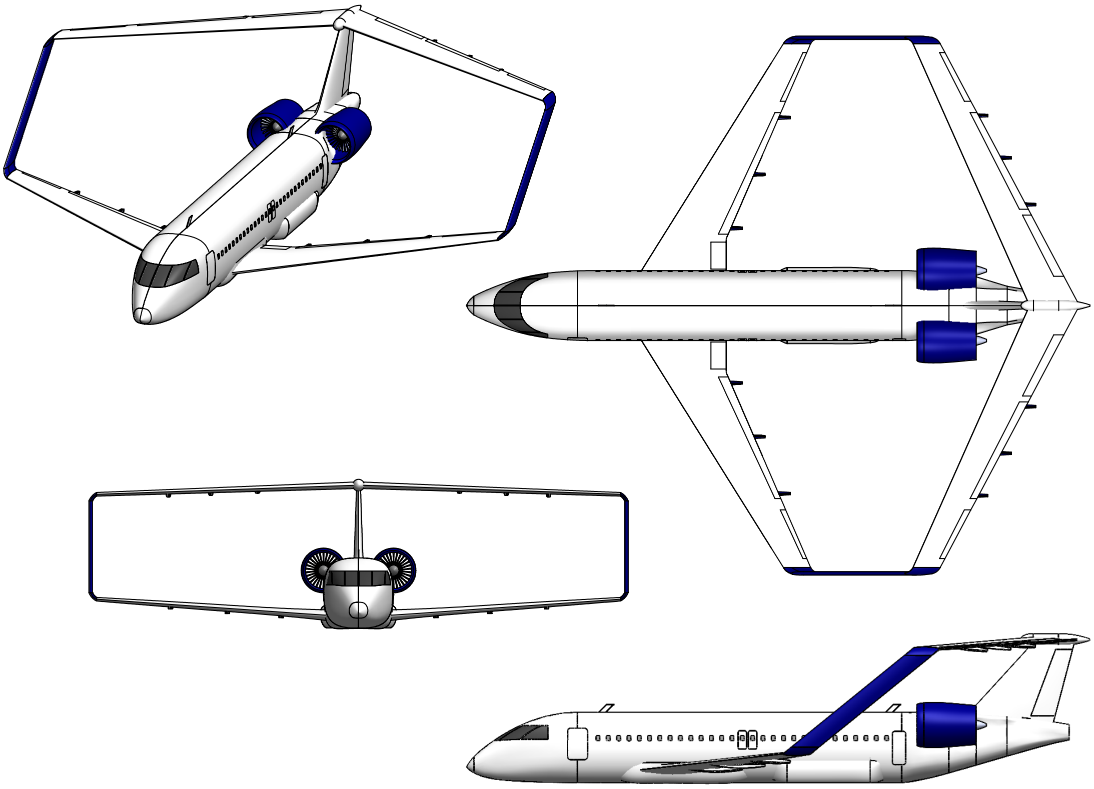

Source: The author

It should be noted that the potential benefit of a BLI system is likely to be affected by the fan performance due to the high distortion inside the duct. Therefore, distortion tolerant fans are needed to preserve the propulsive efficiency along the mission. After an extensive MDO process and high-fidelity CFD simulations, the results demonstrated that the integration of aerodynamics and propulsion is crucial for achieving the fuel-burn reductions desired in next-generation airliners. Figure 30 shows a 3D representation of the INTI aircraft (BLI version) at the end of the conceptual design phase.

3.5 Summary of Key Findings

This chapter described the conceptual-level MDO and computational assessment of a next-generation commercial airliner, in the single-aisle medium range category. Aircraft design optimizations focused on the box-wing layout at a given mission profile and design constraints, whereas CFD simulations focused on the integration of the propulsion system. The following statements summarize the most important outcomes:

- A set of single-objective optimizations have been applied to study the advantages of a BW aircraft over a CTW, based on specific levels of physical fidelity. According to the optimization results, although the MTOW of BW is higher than MTOW of CTW, a considerable amount of fuel was saved due to the flight at higher altitudes obtaining more optimal L/D values. It is interesting to note that high aerodynamic efficiency does not always lead to the most cost-effective aircraft, since the BW has a larger wing area, which increase the OEW and decreases the effect of induced drag reduction. So far, the results have shown that the BW concept can minimize fuel consumption when compared to conventional aircraft.

- The real-coded evolutionary algorithm proved effective in defining the design space in terms of geometric variables with no binary-to-real number conversions, making the algorithm convergence faster. On the other hand, the proposed GA operators demonstrated a feasible convergence to an optimum value, in which, only the best individuals are reproduced from one generation to the next. As far as the constraints implementation is concerned, the penalty function indicated that all requirements were entirely satisfied, proving that the GA is a very efficient optimization algorithm for aircraft conceptual design studies at low-fidelity levels.

- CFD simulations were carried out to compare the aerodynamic results from the conceptual-level MDO of INTI aircraft, providing more details about the optimal box-wing layout. However, the trends presented in this paper can be improved by using high-fidelity aerostructural optimization. In addition, for a more realistic design, it is recommended to include multiple flight conditions in the optimization loop such as take-off and approach.

- The performance of the INTI aircraft can be improved by tightly integrating the propulsion system and the airframe, according to the back-to-back comparison of non-BLI and BLI models. The BLI concept promoted power savings of 6.52% at cruise, which, combined with the box-wing layout, led to 12% system-level fuel-burn savings. Such results were achieved with the use of an actuator disk as a propulsor model, which is commonly adopted in those problems for generating quick estimations. However, the implementation of a more advanced propulsor model (e.g., body force) is recommended for a more reliable CFD simulation, mainly regarding inlet-fan interactions for distorted inflow conditions. Finally, subsonic wind-tunnel experiments complemented the results presented in this chapter, and the main findings are given in Chapter 4.

3.6 Dissemination

The following articles have been published as a result of this chapter:

- BRAVO-MOSQUERA, P; CERÓN-MUÑOZ, H; CATALANO, F. Design, Aerodynamic Analysis and Optimization of a Next-Generation Commercial Airliner, **Journal of the Brazilian Society of Mechanical Sciences and Engineering**, v. 44, p. 609, 2022. (BRAVO-MOSQUERA; CERÓN-MUÑOZ; CATALANO, 2022).
- BRAVO-MOSQUERA, P; CERÓN-MUÑOZ, H; CATALANO, F. Design and Computational Analysis of a Closed Non-Planar Wing Aircraft Coupled to a Boundary Layer Ingestion Propulsion System. In: **AIAA Propulsion and Energy 2019 Forum**. [S.l.: s.n.], 2019. p. 3850 (BRAVO-MOSQUERA; CERÓN-MUÑOZ; CATALANO, 2019).

4 EXPERIMENTAL INVESTIGATION OF A NEXT-GENERATION COMMERCIAL AIRLINER WITH BOUNDARY LAYER INGESTION

4.1 Introduction

Different interpretations of the physics involved in BLI are represented by several methodologies. In terms of computational analyses, the most significant aspect is to represent inlet distortion concerns using propulsor models that accurately capture both flow physics and implementations, such as pressure rise, losses resulting from the fan blades and ducts, and the inlet-fan interactions for distorted inflow conditions (BRAVO-MOSQUERA; CATALANO; ZINGG, 2022). Therefore, actuator disk methods, inlet/outlet boundary conditions, and body force models are currently being applied to evaluate the aerodynamic flow through BLI propulsors (HALL; LIEU, 2021). Earlier investigations of unconventional aircraft with BLI have considered one or two of these important flow simulation methods. A thorough review of previous work on numerical modeling of BLI propulsion is given by Menegozzo and Benini (2020).

Conversely, when dealing with experimental analyzes, there are implementation constraints, owing to sub-scale conditions such as wall and model support interference, as well as a potentially lower Reynolds number than full-scale free flight conditions. Despite these limitations, several studies have been undertaken on this topic, using evidence from numerical simulation and wind tunnel tests to improve knowledge and provide additional insight into BLI. For example, Carter *et al.* (2006) conducted an experimental study focused on determining the potential of highly integrated propulsion systems using BLI inlets on a BWB concept. This study determined the potential benefits of using active flow control with BLI inlets since the combination of both technologies reduces the inlet distortion and prevents flow separation which results in reduced ram and viscous drag. The results also showed a benefit up to a 10% reduction in fuel burned in comparison with pylon-mounted engines on the same configuration.

For the D8 transport aircraft, experimental assessments indicated power savings due to BLI on the order of 6% to 8% for a zero net streamwise force, which simulates cruise condition (URANGA *et al.*, 2017; HALL *et al.*, 2017; URANGA *et al.*, 2018). These investigations focused on a back-to-back comparison using a BLI and a non-BLI concept to compare their performance. The two powered models (1:11 scale) were tested at the NASA Langley subsonic wind tunnel at speeds of 31.3 and 37.5 m/s, corresponding to Reynolds numbers based on model reference chord of 5.7×10^5 and 6.8×10^5, respectively. Since the power balance method was used as the theoretical framework to determine the benefit of BLI, Reynolds number impacts are minimal and low-speed results can be scaled to actual flight Reynolds numbers (DRELA, 2009).

More recently, experimental investigations have been focused on axisymmetric fuselage concepts with an integrated BLI fan, also known as Propulsive Fuselage Concepts (CORTE *et al.*, 2021; CORTE *et al.*, 2022). The geometry of the aft fuselage section of the scale model is based on the PFC configuration proposed within the CENTRELINE project. The propulsor size was scaled to reach the same ratio between the fan diameter and the fuselage momentum thickness at the fan location, guaranteeing similarity between wind-tunnel results and full-scale aircraft. These studies characterized the flowfield around the BLI propulsor and evaluated the aerodynamic forces and moments in different flight conditions. The authors found that a PFC can generate a power saving of about 5% through an ideal BLI propulsor for an axial equilibrium condition and Reynolds number based on the wing mean chord of around 4.6×10^5.

As can be seen from literature, previous experimental studies have demonstrated the benefits of BLI, employing a large variety of geometries and electrical propulsors. The power balance method has been used as theoretical framework to evaluate those tightly integrated propulsion concepts. The primary benefit of this method is that it accounts for all power losses on the aircraft, including propulsive losses from the power plant and surface boundary layer momentum losses from the airframe (DRELA, 2009). Therefore, the power balance method approach was applied in this study, along with conventional thrust-drag calculations to account for the impacts of BLI using the power balance terminology.

This chapter focused on the aerodynamic behavior of the particular characteristics of the INTI aircraft using subsonic wind tunnel experiments. The analyses provide a much better understanding of the systems involved in this configuration, such as the BW layout, which reduces the induced drag, and the quantification of the BLI parameters using flow surveys at specific motor power inputs. The experimental aerodynamic measurements were conducted on a scale-model of the INTI aircraft using a non-BLI version, i.e., with nacelles assembled on pylons, and a BLI version with rear semi-buried engines. Aerodynamic forces at various angles of attack, power sweeps, wake mapping, and total pressure rake measurements demonstrated the relative contribution of each configuration to overall aircraft performance.

The outline of this chapter is as follows: the experimental set-up, analyses, and procedures are detailed and discussed in Section 4.2. This section describes the wind tunnel facility, as well as the test conditions, the metrics used in the experimental procedures, and the measurement uncertainty and repeatability. Section 4.3 reports preliminary results at the simulated sub-scale conditions with non-BLI compared to the BLI configuration. The chapter concludes with a summary of the most important findings and discussions of future work (Section 4.4). Finally, Appendix D, Appendix E, Appendix F, Appendix G, Appendix I, and Appendix H, present more details of the experimental campaign, including the test matrix, calibration of the pitch-strut system, model breakdown, calibration of aerodynamic forces, calibration of the 7-hole pitot probe, and the uncertainty analysis, respectively.

4.2 Experimental Set-up

4.2.1 Wind-Tunnel Facility

Experimental measurements were conducted in the LAE-1 wind tunnel at the São Carlos School of Engineering - University of São Paulo. The test section has a rectangular cross-section of 3.0 m length, 1.3 m height and 1.7 m width. The wind tunnel has an eight-blade fan that is powered by a 110 HP electric motor and can provide speeds of up to 40 m/s in the test section. A recent update for aeroacoustic measurements decreased the turbulence levels from the original 0.25% to 0.21%. More information about the wind tunnel is reported by Catalano (2004), Santana *et al.* (2014), and Almeida, Catalano and Pereira (2021). Figure 31 shows a schematic of the model inside the tunnel. It is coupled to a pitch-strut system near the fore wing's quarter chord, which controls both angle of attack and model height. The system is basically composed by a strut, a threaded bar ($NC4-32$), and a step motor ($KTC-5034-349-K$). The pitch-strut system was calibrated by verifying the relation between the number of steps taken by the motor and the angle of attack of the model (see Appendix E). The step motor provides a static torque of 1.86 $N.m$, step in angle of 1.8° with a precision of 5%, and continuous power of 25 W. The model is positioned vertically so that while the angle of attack changes, a reference point at the fore wing root remains in the center of the tunnel. The uncertainty on model position within the test section (Y and Z directions) is ± 1 cm.

Note that at zero angle of attack, the 1:28 scale INTI model results in a wind-tunnel blockage of approximately 2.39%. The interaction effects between the boundary layer of the wind-tunnel walls and the model were corrected by using Computational Fluid Dynamics (CFD) simulations. In this case, the corrections were applied to relate a confined flow field to an equivalent free stream flow field, so two Reynolds Averaged Navier-Stokes (RANS) simulations were run: one in the tunnel and one in free air, both using a no-slip boundary condition on the walls of the computational domains (HANTRAIS-GERVOIS; PIAT; HANTRAIS, 2012). Such an approach allowed to correct the wake blockage and angle of attack due to walls interference.

4.2.2 Tested Configurations

A scale model (1:28) of the INTI aircraft was designed for investigating the aerodynamic benefits of boundary layer ingestion. Three models were needed for the wind-tunnel tests: (i) an unpowered configuration, which was used to measure the main aerodynamic characteristics of the airframe. The schematic in Fig. 32a illustrates the main model dimensions and the conventional tail used by the non-BLI and BLI configurations

Figure 31 – Schematic views (side and front) of the INTI model in the test section of LAE-1 wind tunnel, dimensions in meters.

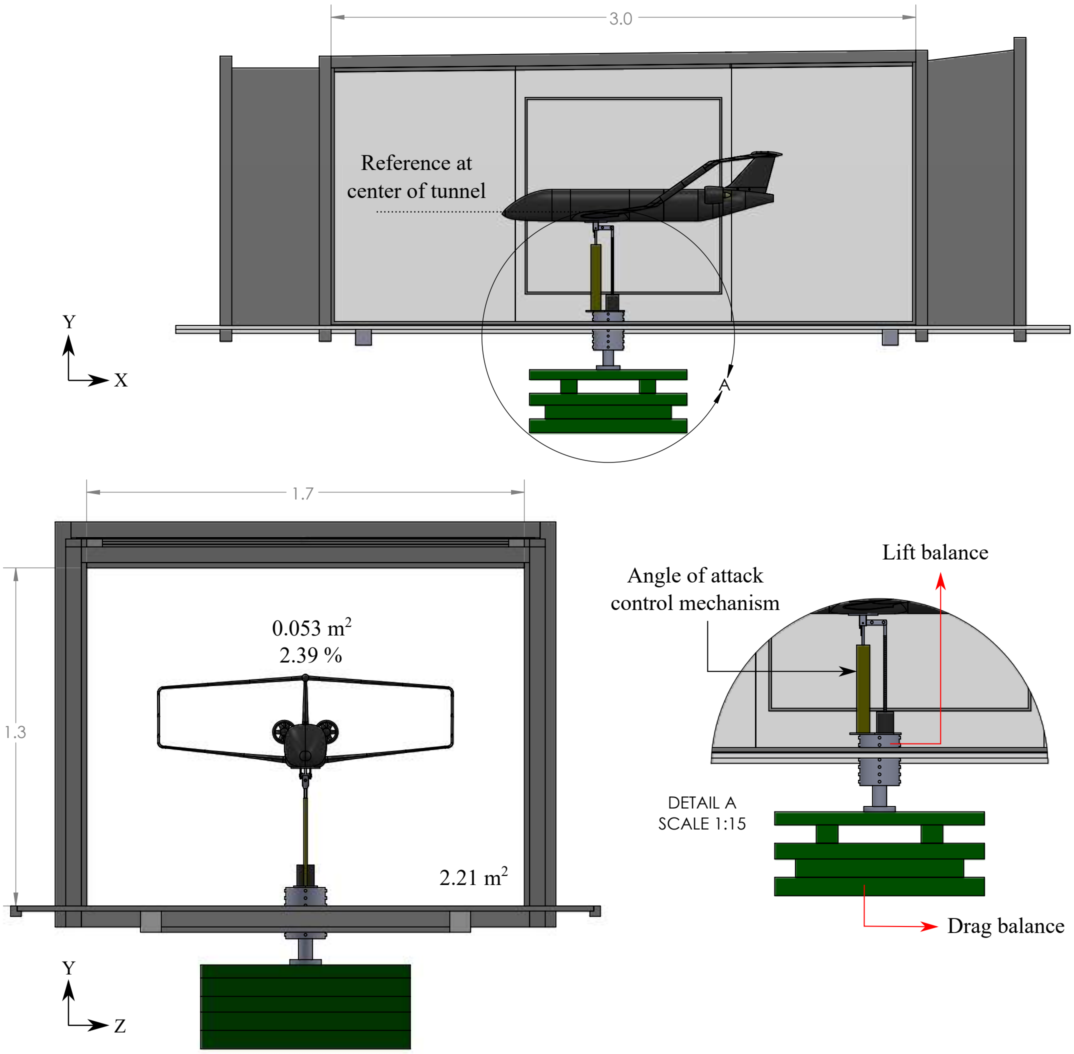

Source: The author

with no pylons nor propulsors. Technical views and details of the electric fan used in the wind tunnel campaign are shown in Fig. 32b. (*ii*) the non-BLI configuration, shown in Fig. 33a, which has podded engines with axisymmetric nacelles that are assembled on pylons at the rear part of the aircraft for ingesting clean airflow. (*iii*) the BLI configuration, shown in Fig. 33b, which is designed with rear semi-buried engines in order to capture a relatively large part of the boundary layer developed over the fuselage.

The airfoils of the BW model differ from the full-scale configuration due to the subsonic nature of wind-tunnel tests. This is important to provide adequate behavior at relatively low test Reynolds numbers. In this context, two methods were used to find a match between experimental and full-scale aircraft performance. The first was to ensure lift coefficient equivalency by employing proper airfoils, and the second was to force boundary layer transition by using trip strips on all model surfaces (wings, fuselage, tail,

Figure 32 – Details of the unpowered model and electric fan equipping the wind-tunnel powered models, dimensions in millimeters.

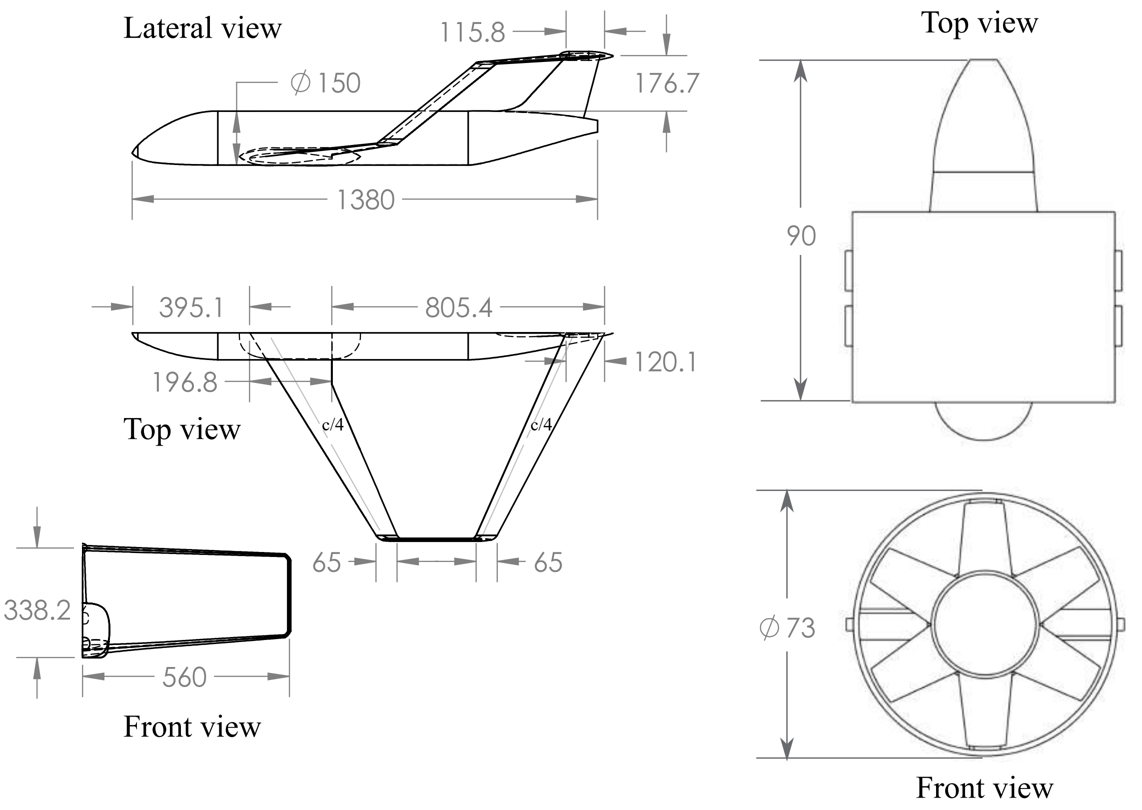

(a) Technical views of the wind-tunnel unpowered model.

(b) Drawings of EDF for powered configurations.

Source: The author

and propulsor nacelles). The thickness and position of the trip strips were established by ensuring that the drag coefficient increased uniformly as tunnel speed decreased, as recommended by (BARLOW; RAE; POPE, 1999). This method ensured the presence of fully turbulent boundary layers on the model at some representative condition. A 3 mm wide and 0.08 mm thick strip (grit size) was placed over the complete aircraft model. For the closed-wing system, trip strips were located at $x/c = 0.05$ on its suction side, and on its pressure side at $x/c = 0.10$. For fuselage and nacelles, the trip strips were located at 5-10% of the body length. This ensures the development of fully turbulent boundary layers during the experimental campaign. For more detailed information about the experimental model breakdown, see Appendix F.

The models were created using additive manufacturing techniques. A total of 48 pieces conformed the mockups, and carbon fiber beams reinforced the closed-wing structure. The pieces were assembled manually, meeting manufacturing tolerances based on the Computer-Aided Design (CAD) process. The aerodynamic surfaces were then treated and painted for ensuring a smooth surface finish. Note that the non-BLI, BLI, and unpowered models share the same physical components, except for the removable tail cone. The connections between these components were adjustable, with the parts clamped together with set screws.

The model instrumentation includes 13 static pressure taps distributed inside the duct of the BLI configuration. Both non-BLI and BLI models are powered by two QF2827-2300KV Brushless Motors (6 blades), a commercial Electric Ducted Fan (EDF), typically used for R/C models. The central duct has an outer diameter of 70 mm and total length of 58 mm. The fan's nominal voltage is 8 - 22 VDC and the maximum electrical current allowed is 50 A. The maximum thrust of each fan is 16.77 N at 30000 RPM. The EDFs were controlled by a Readytosky 50A (ESC) and powered by a RSP-3000-48 power supply. The motor shaft rotational speed was determined using an optical tachometer that uses a laser light to accurately measure the speed in RPM. The speed controllers were located inside the fuselage of the model, requiring about 5 meters of wire length between the ESC and the power supply. Finally, the propulsor power was varied by setting the fan wheel speed using a SIKAF RC Servo speed controller. Some important values of the scaled models are presented in Table 26.

Figure 33 – INTI models: CAD rendering of mockups, and photographs of the wind-tunnel setup assembled in the test section of the LAE-1 subsonic wind tunnel (scale 1:28).

(a) Non-BLI model configuration.

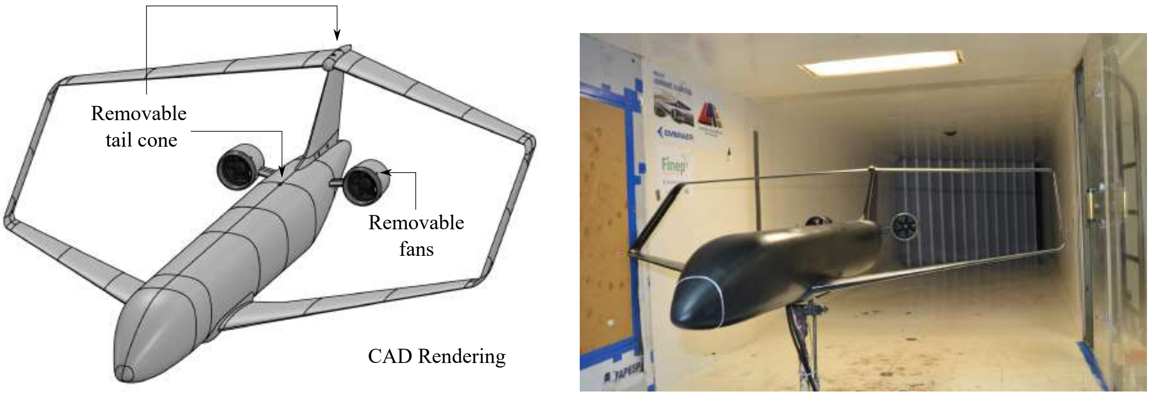

(b) BLI model configuration.

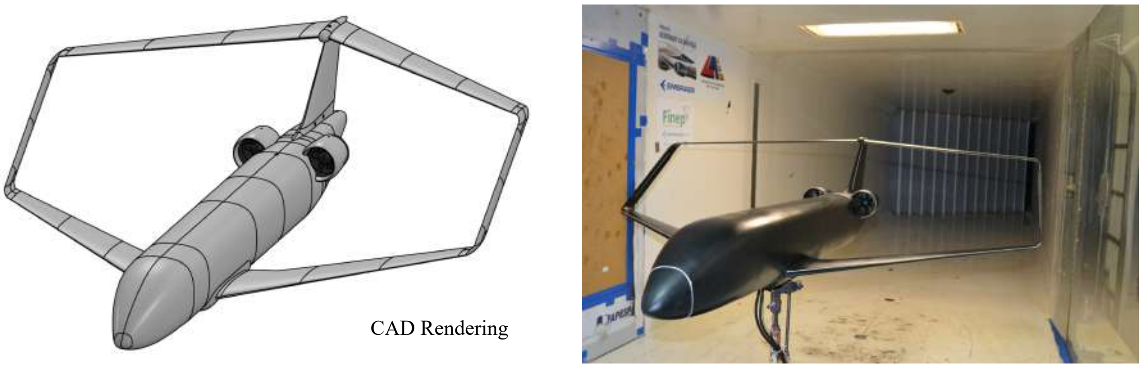

Source: The author

Table 26 – Reference dimensions of the 1:28 INTI models.

Dimension	Value
Reference area $[m^2]$	0.25
Reference chord $[mm]$	160
Wingspan $[mm]$	1120
Length $[mm]$	1380
Outer diameter of fan $[mm]$	73

Source: The author

Table 27 – Non-dimensional flow parameters for different tests.

Freestream velocity $[m/s]$	Dynamic pressure $[Pa]$	Mach number [-]	Reynolds number [-]
27.0	410.9	0.080	2.72×10^5
30.0	507.3	0.089	3.02×10^5

Source: The author

4.2.3 Test Conditions

The LAE-1 wind tunnel was operated at velocities of about 27 m/s and 30 m/s, which correspond to Reynolds numbers based on the reference chord length of 2.72×10^5 and 3.02×10^5, respectively. These velocities were carefully determined after testing the propulsor thermal and model structural capabilities. The latter was generally the limiting constraint. At the beginning of each test, atmospheric conditions were monitored in order to establish non-dimensional parameters. A calibrated mercury barometer with a 1 $mmHg$ precision measured the atmospheric pressure. A thermocouple measured the temperature inside the wind tunnel. Relative humidity was measured by a hygrometer and was then used to determine the air density. Dynamic pressure was measured by a pitot-static probe located at the test section, which is connected to a micro-manometer (TSI Model 8705 DEP-CALC; uncertainty of ± 0.1 Pa). The model was installed on the pitch-strut system and remained there until the test campaign was completed. Changes of the tail cone and instrumentation of the fans were undertaken insitu. The reference quantities of the tunnel operating conditions are listed in Table 27, whereas the propulsor non-dimensional fan wheel speeds implemented during the tests are given in Table 28.

The ratio between the fan blade tip speed and the tunnel speed (U_{tip}/V_{∞}) is used to assess the effect of the propulsors on the flow features, where the fan blade tip speed is defined by Eq. 4.1:

$$U_{tip} = \Omega_f \frac{d_{fan}}{2} \tag{4.1}$$

where Ω_f is the fan wheel speed, and d_{fan} is the model propulsor fan diameter, equal to 73 mm.

Table 28 – Propulsor dimensional and non-dimensional wheel speeds

Ω [RPM]		9000	10300	15500	18200	20400
U_{tip}/V_{∞} [-] at	$V_{\infty} \approx 27.0\ m/s$	1.33	1.44	2.17	2.55	2.86
	$V_{\infty} \approx 30.0\ m/s$	1.20	1.30	1.96	2.30	2.58

Source: The author

4.2.4 Data Collection

Four main types of runs were performed. See Appendix D to check the test matrix for each type of experiment:

1. Force measurements (Lift and Drag) were taken for the unpowered, non-BLI, and BLI configurations, in order to quantify their aerodynamic behavior at several angles of attack (α). In this case, the engines were easily disassembled from the nacelle to obtain through-flow nacelle conditions. This approach allowed for the analysis of pure geometry effects. To provide some form of experimental validation, the wind tunnel results for the unpowered configuration were compared to CFD simulations. The angles of attack measured ranged from $\alpha = -4°$ to $12°$ in $1°$ steps.

2. Electrical power (P_E) measurements were performed for the powered configurations, i.e., with the engines assembled on the non-BLI and BLI models. The objective of this experiment was to determine the electrical power coefficient, along with the net streamwise force (F_X) for a range of fan wheel speeds, fixed angle of attack, and fixed tunnel velocity. A set of fan wheel speeds were defined, and force and power readings were recorded. The product between the voltage input to the ESC (v) and the current from the power supply (i) determined the electrical power supplied to propulsors ($P_E = vi$).

3. Flow field measurements were conducted for both powered and unpowered models. The goal here was to determine the variation of axial flow velocity (u^*) between configurations in a transversal plane; therefore, aerodynamic measurements are presented by considering the streamwise velocity contours, and flow mapping for selected fan wheel speeds, fixed angle of attack, and fixed tunnel velocity. In particular, for powered configurations, the flow surveys were conducted at power levels that bracket zero net streamwise force.

4. Inlet pressure distortion measurements were carried out on the models with the fan uninstalled, in order to evaluate the dependence of the distortion on the INTI airframe at various points in the flight envelop, and to establish differences in the distortion level between a non-BLI and a BLI configuration. In this case, total pressure rake surveys were conducted at fixed tunnel velocity, and angles of attack ranged from $0° < \alpha < 8°$ in $1°$ steps.

Finally, polyester mini-tuft flow visualization is used to assess the flow on the aerodynamic surfaces of the models at specific flow conditions. Mini-tufts were attached to the wind tunnel models to characterize separation points and recirculation zones.

4.2.5 Measurement Techniques

4.2.5.1 Aerodynamic Forces

The aerodynamic forces acting on the models were measured by a two component balance, as illustrated in detail A of Fig. 31. The drag balance was built in the Laboratory of Experimental Aerodynamics at EESC-USP. Conversely, a second balance measured the lift force which is composed by two strain gauges placed on flexures stiffeners forming a Wheatstone bridge. More details of the lift balance and angle of attack control mechanism can be found in (CERÓN-MUÑOZ, 2009), whereas previous aerodynamic results using the current balance scheme can be found in (CERÓN-MUÑOZ; CATALANO, 2010; CERÓN-MUÑOZ *et al.*, 2016). The signals are recorded by a data NI AT-M10-16X acquisition sheet of 500 Hz sample frequency. Prior to the experiments, the aerodynamic balances were calibrated by loading known weights in order to create a linear voltage-force ratio (see Appendix G). The complete scheme has, at maximum loading, measurement accuracy of ±0.7%; therefore, for lift, drag, and angle of attack, the accuracies are $\pm 0.8\ N$, $\pm 0.18\ N$, and 0.2°, respectively (see Appendix I).

The net streamwise force can be defined as the difference between the drag and thrust (URANGA *et al.*, 2017), being positive in downstream direction. In its non-dimensional form, the net streamwise force coefficient (C_X) is expressed by:

$$C_X = \frac{T_{EDF} - D}{q_\infty S} = C_T - C_D \tag{4.2}$$

where T_{EDF} is the thrust generated by the EDFs, D is the drag of the model, q_∞ is the freestream (tunnel) dynamic pressure, S is the wing reference area, C_T is the thrust coefficient, and C_D is the drag coefficient. In this case, the experiment was carried out in search of a zero net streamwise force, which is calculated using the load cell of the drag balance, measuring the difference between the propulsor's gross thrust and the model's drag. The pitch-strut system drag was subtracted from the model's drag to determine the main aerodynamic characteristics of the aircraft. This process involved a simple approach to evaluate the tare (direct drag of the support), in which the forces on the pitch-strut system (i.e, removing the model) are measured at different tunnel speeds, and the drag generated by the support is corrected in function of the tunnel dynamic pressure using regression statistical analysis (BARLOW; RAE; POPE, 1999) (see Appendix G).

To determine the primary aerodynamic coefficients, the wind tunnel data of the unpowered configuration is compared to CFD simulations. In this case, the geometry of the model was discretized using **ANSYS** meshing. The atmospheric conditions of the experimental setup were adjusted to the computational setup. Two computational domains with different sizes were considered: a small one to simulate the confined flow of the wind tunnel, and a large one to simulate free air conditions. The drag difference between these simulations was subtracted to the drag of the wind tunnel model to account for wall effects. An unstructured tetrahedral mesh was used in all the simulations, as shown in Fig 34a. Grid density is regulated near the aerodynamic surfaces to increase the grid's resolution in that region. The dimension of the cells in the refinement area is limited to 0.02 m. The surface meshes included structured cells (prism) in order to capture the boundary layer effects with adequate precision. The near wall treatment was adjusted in terms of the total thickness, with 20 sub-layers and a growth rate of 1.2. The boundary layer refinement kept the dimensionless wall distance value (y+) close to 1.0. The Figs. 34b and 34c show close-up views on the surface meshes. The generated mesh of the large domain features a total of 6.32 million nodes.

Figure 34 – Mesh structure for unpowered configuration.

(a) Mesh global view.

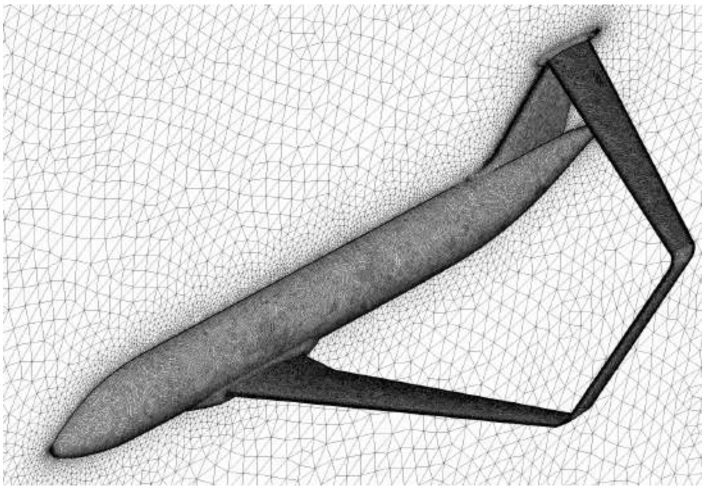

(b) Close-up view for wing-fuselage intersection.

(c) Close-up view of boundary layer prism on wing.

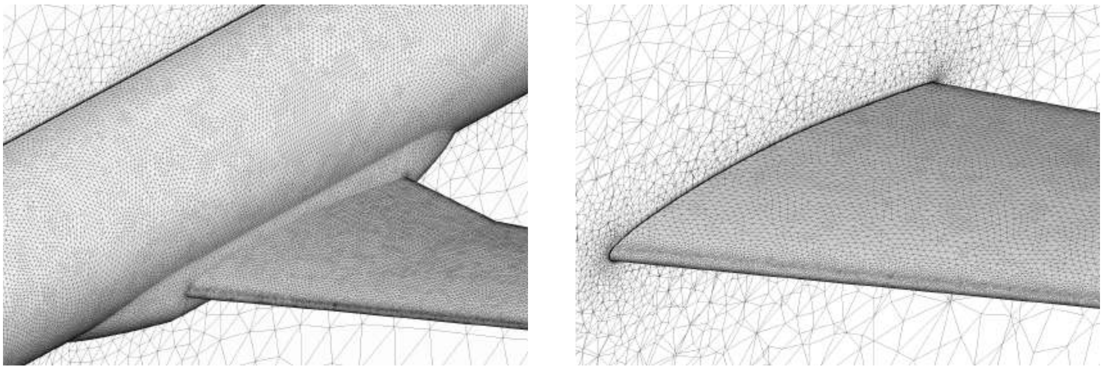

Source: The author

The inlet velocity is set to 30 m/s whereas turbulent intensity is set to 0.21%

based on wind tunnel turbulence level (SANTANA *et al.*, 2014). On the symmetry plane of the domain, symmetric boundary condition is applied, while the model surfaces are treated as no-slip walls. The outlet surface of the domain is modeled as a pressure outlet. Steady simulations using the SST turbulence model are carried out for the CFD analysis. Second-order schemes are used for all the flow, i.e., the advection terms and turbulence numeric were discretized using a high resolution scheme. The convergence control was set to reach 600 iterations, with a residual target equal to 1×10^{-5}.

4.2.5.2 Application of the Power Balance Equation

The main equation of the power balance method is derived in this section. The power balance method is a solution presented by Drela (2009) to evaluate the performance of highly coupled systems. Basically, this method focuses on a mechanical power and kinetic energy analysis, instead of focusing on momentum equation analysis. For a control volume which fully envelopes the propulsor, and assuming a low speed, the only input power term in the power balance equation is the mechanical flow power (P_K), which is calculated by:

$$P_K \equiv \oiint (p_{t\infty} - p_t)\, \mathbf{V} \cdot \hat{n}\; d\mathcal{S} \tag{4.3}$$

where p_t and $\mathbf{V}$ represent the flow stagnation pressure and the local velocity vector, respectively, $\hat{n}$ is the normal vector which points into the propulsor, and $d\mathcal{S}$ is the surface differential. According to Uranga *et al.* (2017), the mechanical flow power can be measured with two different methods, i.e., the direct and indirect method. The direct method consists of surveying the propulsor inflow and outflow planes with flow measurement techniques (e.g., PIV, 5-hole probe, or rotating P_t-rake system). The indirect method, on the other hand, determines the mechanical flow power from the measured electrical power supplied to the motor, combined with the fan efficiency (η_f) and motor efficiency (η_m). Such quantities can be non-dimensionalized as follow:

$$C_{P_K} \equiv \frac{P_K}{q_\infty V_\infty S} \tag{4.4}$$

$$C_{P_E} \equiv \frac{P_E}{q_\infty V_\infty S} \tag{4.5}$$

$$C_{P_K} = \eta_f \eta_m C_{P_E} \tag{4.6}$$

The BLI benefit is given by the Power Saving Coefficient (PSC), where the objective is to obtain the required power to achieve a zero net-streamwise force:

$$PSC \equiv \frac{(C_{P_K})_{non-BLI} \; - \; (C_{P_K})_{BLI}}{(C_{P_K})_{non-BLI}} \tag{4.7}$$

In these experiments, it was assumed that the fan and motor efficiencies do not differ considerably between the BLI and non-BLI configurations for the same operating point. Indeed, initial motor characterization indicated the motor operates close to its maximum efficiency, i.e., > 71% (data from EDF's data sheet). Such an approach is considered a surrogate to evaluate the flow power, since the electrical power can be directly measured during the wind tunnel tests (URANGA *et al.*, 2014). Therefore, it is assumed that the BLI benefit can be computed as:

$$PSC \equiv \frac{(C_{P_E})_{non-BLI} \; - \; (C_{P_E})_{BLI}}{(C_{P_E})_{non-BLI}} \tag{4.8}$$

Note that the assumption of maintaining constant efficiencies for the BLI benefit leads to higher uncertainty. In this case, the uncertainty in the BLI benefit is found to be ±2.5% (see Appendix I).

4.2.5.3 Flow Mapping

Flow-field measurements were performed using a L-shape 7-hole probe (AeroProbe® system). It is composed by a conventional cylindrical body (stainless steel 3.2 mm diameter) with seven holes at its tip. The probe is adequate for wind tunnel testing since its tip is directly in the airflow, and the probe is attached to the side so that the data obtained is not disrupted. The probe allows for highly accurate measurements of flow vector magnitude and direction, as well as static and total pressure. The acceptance angle is up to ±30° with an error rate lower than ±1°. The velocity error is lower than ±1% and can have up to 500 discrete aerodynamic calibration points per speed (AEROPROBE. . . , 2018). The calibration of the 7-hole probe was done using a neural network trained with input data from ±30°, 1-degree precision in Y and Z direction, and RMS-error of 0.1 m/s (see Appendix H).

A three-axis traverse system (DANTEC® traverse system) was used to move the sensors in a specified grid for obtaining the wake characteristics. The system moved the probe in three directions at micrometer accuracy. In particular, each axis movement has 0.0125 mm accuracy, and was operated by serial communication. The traverse system was fixed at approximately 50 mm away from the fuselage tail cone, where a rectangular transversal plane was used to measure the flow pattern of the propulsor jet. With the center of the fan diameter as a reference, the grid of the rectangular transversal plane was set from 150 mm to -80 mm with a 5 mm spacing in the lateral direction, and from -50 mm to 90 mm with a 5 mm spacing in the vertical direction. The data average was calculated using 500 samples from 5 seg measurements. The probe was traversed through

Figure 35 – Grid dimensions for wake mapping with 7-Hole Pitot probe, dimensions in millimeters.

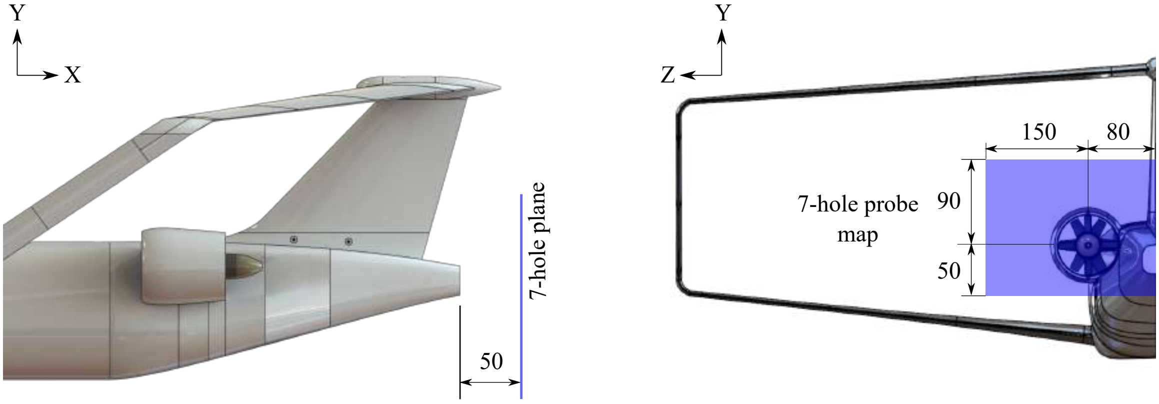

Source: The author

Figure 36 – Overview of the wake mapping experiment in the test-section.

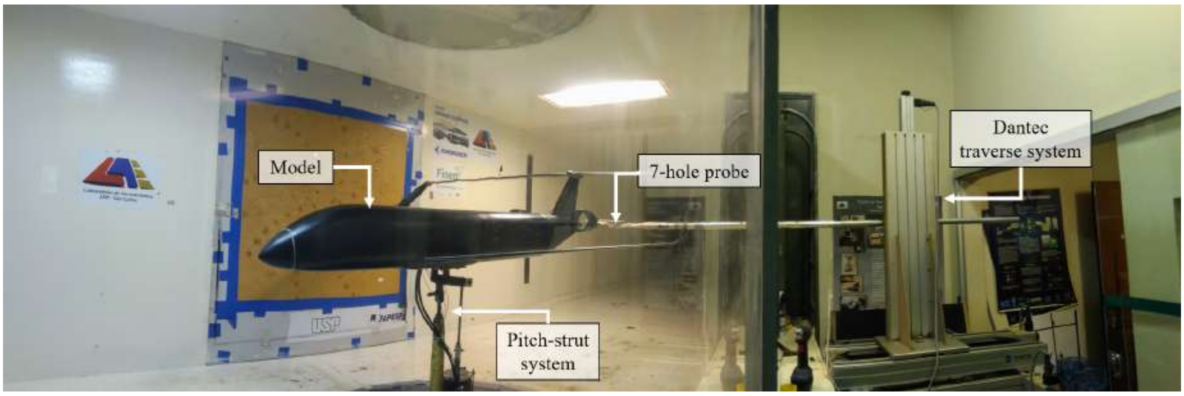

Source: The author

the same grid points in space, and time-averaged values for all three velocity components (u^*, v^*, w^*) and velocity fluctuations (u_{rms}, v_{rms}, w_{rms}) are obtained at each point. Thus, the in-plane velocity vectors (v^* and w^*) are used to calculate streamwise vorticity (ω_x). The dimensions of the grid planes for the wake mapping are shown in Fig. 35, whereas the complete wake mapping experiment, mounted on the wind tunnel test section is shown in Fig. 36.

4.2.5.4 Steady Total Pressure Distribution and Distortion Analysis

The inlet efficiency was evaluated through the total pressure coefficient (Eq. 4.9) and the distortion index (Eq. 4.10), as follow:

$$C_{p_t} = \frac{p_t - p_{t_\infty}}{q_\infty} \tag{4.9}$$

$$DC_\theta = \frac{p_{t_{AIP}} - p_\theta}{q_{AIP}} \tag{4.10}$$

Figure 37 – Total pressure rakes installed on the wind-tunnel models.

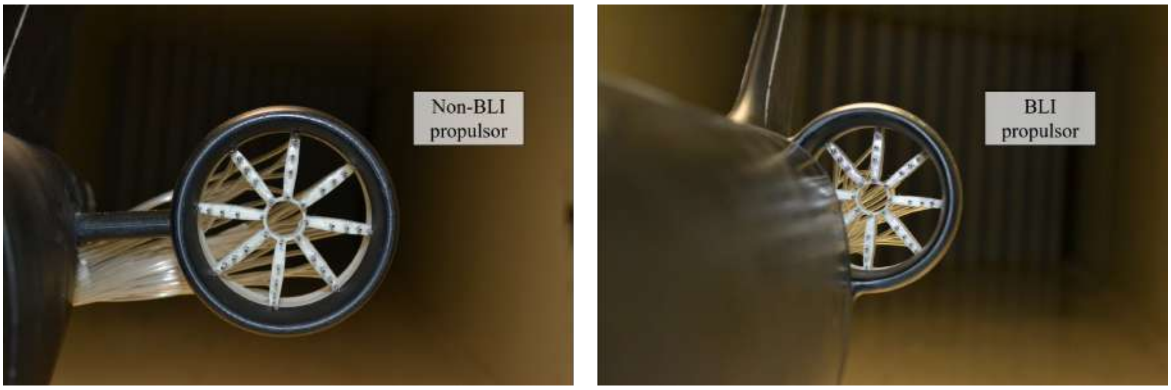

Source: The author

where $p_{t_{AIP}}$ is the average total pressure value in the survey plane (360°), p_θ is the minimum average total pressure value in a sector of 60°, and q_{AIP} is the mean dynamic pressure calculated by $q_{AIP} = \rho V_{AIP}^2/2$. The goal of these tests was to look inside the engine inlet duct and study if there is a significant difference in overall pressure across the Aerodynamic Interface Plane (AIP) between the configurations. The total pressure distribution at the AIP was measured with a total pressure rake with an outer diameter of 70.5 mm. The rake was located in a plane perpendicular to the freestream velocity direction, as shown in Fig. 37.

The rake is characterized by 40 total pressure probes, distributed in 8 circumferential locations with 25° of circumferential spacing, and 5 radial locations. For each configuration and condition, the pressure data were recorded through a pressure scanner (Scanivalve® DS4-48) for a period of 5 seg and averaged over this period (the pressure rating is 0.01 to 100 psi). The Scanivalve has an electro-mechanical pressure multiplexer which allows to read and transmit several input signals sequentially thanks to a solenoid. The position transmitter (encoder) electrically indicates the port being measured, and a solenoid stepper drive provides sequential connection of ports to 48 transducers. The signal conditioner gain was set to the full scale pressure range of the transducer, i.e., for 5 V (20mA) output (SCANIVALVE..., 1975). The freestream static and total pressures were measured simultaneously with a Pitot static probe positioned at the test section's inlet and acquired using the same pressure scanner. In this way, possible changes in the freestream conditions owing to temperature or velocity drifts were accounted for. The uncertainty of the measure was 1% for each type of run (see Appendix I).

4.2.6 Measurement Uncertainty

All measurements are susceptible to some degree of uncertainty. Therefore, measurements were carried out with extreme caution in order to avoid random and systematic errors that arise in any experimental measurement situation. In this study, several types of experimental uncertainties were examined, along with some methods of error and data analysis that can be used in subsequent experiments. The uncertainty in tunnel operating conditions was obtained from the precision of the tunnel instrumentation. This way, the same magnitude and sign of experimental uncertainty are obtained when the measurement is repeated several times.

The uncertainty of BLI measurements depended on the electrical power uncertainty and measured net streamwise force. The instrument precision of electrical power was calculated by error propagation of voltage and current, with the 1.1% precision error in the monitor of the power supply. These instrumentation uncertainties were propagated to the quantities of interest, assuming that all uncertainties are statistically independent (BARLOW; RAE; POPE, 1999), as follows:

$$\delta R = \left[\left(\frac{\partial R}{\partial x_1} \delta x_1 \right)^2 + \left(\frac{\partial R}{\partial x_2} \delta x_2 \right)^2 + \left(\frac{\partial R}{\partial x_3} \delta x_3 \right)^2 + ... + \left(\frac{\partial R}{\partial x_n} \delta x_n \right)^2 \right]^{\frac{1}{2}} \tag{4.11}$$

where R is a function of N independent variables $(x_1, x_2, ..., x_n)$. In executing Eq. 4.11, each term is calculated with only one variable augmented by its uncertainty interval, all others being at their recorded values.

Finally, uncertainty of distortion measurements depended on scanivalve pressure sensors and disposition of each probe in the total pressure rake. In this case, the readings from the scanivale provided the differential pressure of each probe in relation to the central total pressure probe, which was used to determine the standard deviation of reading. Thus, the values of the deviation from the average value were used to calculate the experimental error. The possible errors in each measurement were assumed normally distributed; so the error in each measurement was assumed independent of the error in any other measurement, and the error in every measurement was described at the same confidence level.

4.2.7 Repeatability

Repeatability refers to the agreement among repeated measurements, i.e., the spread of the collected data or how close they are together. The more precise a set of measurements, the closer together they are. In this study, several data sets related to the chosen experiment were repeated in order to assess the repeatability of the wind-tunnel observations. In particular, aerodynamic measurements were repeated five times per tunnel velocity and range of angle of attack; electrical power measurements were repeated 7 times per tunnel velocity and angular velocity of EDFs; flow mapping measurements were repeated two times per angular velocity of EDFs; and inlet pressure distortion measurements were repeated three times per tunnel velocity and range of angle of attack. The deviations of the measurements with respect to the mean value are computed per data set. These deviations were used to evaluate the confidence intervals using a Student's

Figure 38 – Alpha sweep of CFD and experimental results for unpowered configuration at $M = 0.089$ and $Re = 3.02 \times 10^5$. Repeatability is $\Delta C_L = 0.007$ and $\Delta C_D = 0.003$.

(a) Lift Coefficient. (b) Drag polar.

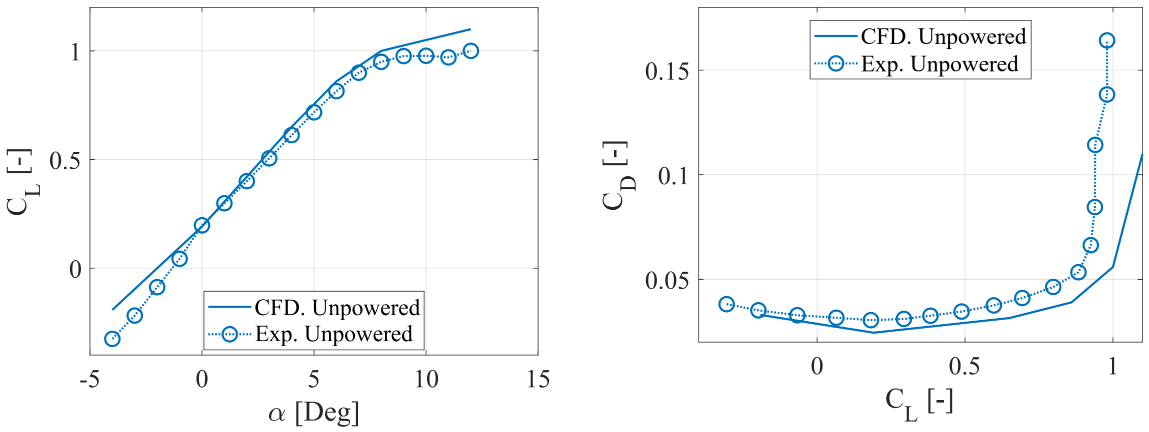

Source: The author

t-distribution. The data collected during a given run is fitted with a polynomial curve, indicating 95% of confidence intervals. Despite the fact that some angles of attack have a broader range of variation, the experiment is considered repeatable.

4.3 Results and Discussions

4.3.1 Aerodynamic Measurements

In this section, the experimental and CFD results for the unpowered configuration are first analyzed and compared (Fig. 38). Alpha sweeps (from $\alpha = -4°$ to $12°$ in $4°$ steps) using the converged grid were run to better understand the offset from experimental data. Experimental force measurements results of the three configurations in through-flow nacelle condition are also presented and discussed (Fig. 39). Lift and drag coefficients, drag polar, and aerodynamic efficiency are the variables evaluated. Table 29 shows a summary of the results from the experimental-numerical comparison of the unpowered configuration, as well as differences between the experimental curves of the configurations.

Figure 38a shows the comparison of lift coefficient in function of angle of attack. The lift curves show correlation for low to moderate angles of attack between the two methods, since the curves display a linear behavior with a similar slope ($\partial C_L/\partial\alpha$) from $\alpha = 0°$ to $5°$ (See Table 29). However, the CFD results over predict lift at negative angles. This could be explained by the fact that the wind tunnel models had strips on both sides of wing section, artificially increasing the boundary-layer thickness and reducing the model's effective curvature. Note that a greater dispersion (on the order of 11%) at high angles of attack is found due to the higher level of complexity in the flow pattern arising from the stall region, which is more difficult to be numerically simulated. Despite the $C_L - \alpha$ curve

Table 29 – Aerodynamic forces of the configurations in through-flow nacelle condition at $M = 0.089$ and $R_e = 3.02 \times 10^5$.

Configuration	**Unpowered**			**Non-BLI**		**BLI**	
Parameter	Exp	CFD	% error	Exp	Δ [%]	Exp	Δ [%]
C_L for zero α [-]	0.181 ± 0.0084	0.191	5.52	0.187 ± 0.0093	3.31 ± 0.11	0.184 ± 0.0097	1.65 ± 0.15
$\partial C_L/\partial\alpha$ [-]	0.102 ± 0.0118	0.111	8.82	0.102 ± 0.0106	0.0	0.102 ± 0.0113	0.0
C_{Lmax} [-]	$0.985_{\vert_{11^\circ}} \pm 0.0157$	$1.092_{\vert_{12^\circ}}$	10.86	$0.997_{\vert_{10^\circ}} \pm 0.0138$	1.21 ± 0.12	$1.004_{\vert_{10^\circ}} \pm 0.0149$	1.92 ± 0.10
C_D for zero α [-]	0.0304 ± 0.0042	0.0245	19.40	0.0338 ± 0.0064	11.18 ± 0.52	0.0319 ± 0.0051	4.93 ± 0.21
$\partial C_D/\partial {C_L}^2$ [-]	0.0217 ± 0.0107	0.018	14.28	0.0226 ± 0.0101	4.14 ± 0.05	0.0224 ± 0.0099	3.03 ± 0.07
$(L/D)_{max}$ [-]	$17.21_{\vert_{6^\circ}} \pm 0.0098$	$22.05_{\vert_{6^\circ}}$	28.12	$15.77_{\vert_{6^\circ}} \pm 0.0010$	8.36 ± 0.89	$16.67_{\vert_{6^\circ}} \pm 0.0088$	3.13 ± 0.10

Source: The author

matched well among all the simulations, there is an offset from the experimental data by approximately $-0.3°$ in angle of attack. This can be seen in Table 29 where the C_L for zero α has an error of 5.52%, which is explained by the calculated uncertainty of the pitch-strut system, i.e., the effective angle of attack of the wind-tunnel model might have been higher than the geometric angle of attack. At this point, additional investigations are needed to determine the reason of the shift.

Figure 38b depicts the complete drag polar chart for the unpowered configuration. The CFD results show under predictions with the experimental data in all evaluated angles of attack, where the values at zero angle of attack were 0.0245 and 0.0304, respectively (error rate of 19.4%). Although there is an offset in drag levels between the fully turbulent computation and the experimental data, the curves show relatively good agreement at low to moderate angles of attack. It should be noted that increasing grid density will result in a better approximation of numerical data in terms of C_D. On the other hand, the experimental curve showed larger drag values as the angle of attack increased. The reason of that difference is due to vibrations of the model under the effect of stall detachments, increasing the predicted drag values.

The experimental results of the unpowered configuration, as well as non-BLI and BLI configurations in through-flow nacelle condition are presented in Fig. 39. According to the lift coefficient results (Fig. 39a), the nacelle induces a gradually increasing amount of extra lift between $\alpha = 0°$ and $\alpha = 5°$; however, the change in lift is relatively small. At high angles of attack (i.e. from $\alpha = 8°$ to $\alpha = 12°$), the configurations exhibited a smooth stall behavior, which can be explained by the mutual interaction of the wings, in which the aft wing continues to provide lift, while the fore wing has already started the stall process. As a result, in the poststall regime, the lift coefficient does not drop rapidly, resulting in a nose pitch-down tendency. Such characteristic allows BW concepts to avoid risks due to stall effect when approaching stall angle, maximizing the total lift without creating adverse trim effects. This has a significant impact on safety, especially in commercial aircraft categories. This behavior was also observed in the IDINTOS project, where low-speed wind tunnel results showed the mutual interference between the wings, which changed at different angles of attack (FREDIANI; CIPOLLA; OLIVIERO, 2015). The mini-tuft flow visualization technique applied on the main box-wing surfaces near stall conditions also confirmed this behavior (Fig. 40). The mini-tufts indicated a region of blurred tufts flow on the fore wing, whereas the flow on the aft wing was completely unseparated.

The impact of through-flow nacelles on the overall aircraft drag was also evidenced by comparing the experimental curves (Fig. 39b). As expected, the non-BLI configuration showed an increase in total drag due to the contribution of pylons, as well as the contribution of nacelle drag. The mutual aerodynamic interference between the pylon and the nacelle

Figure 39 – Alpha sweep of wind tunnel configurations in through-flow nacelle condition at $M = 0.089$ and $R_e = 3.02 \times 10^5$ comparing free-air lift and drag with corrected experimental data. Repeatability is $\Delta C_L = 0.007,\ 0.009,\ 0.007$ for unpowered, non-BLI, and BLI configurations, respectively. Repeatability is $\Delta C_D = 0.003,\ 0.004,\ 0.004$ for unpowered, non-BLI, and BLI configurations, respectively.

(a) Lift Coefficient. (b) Drag Coefficient.

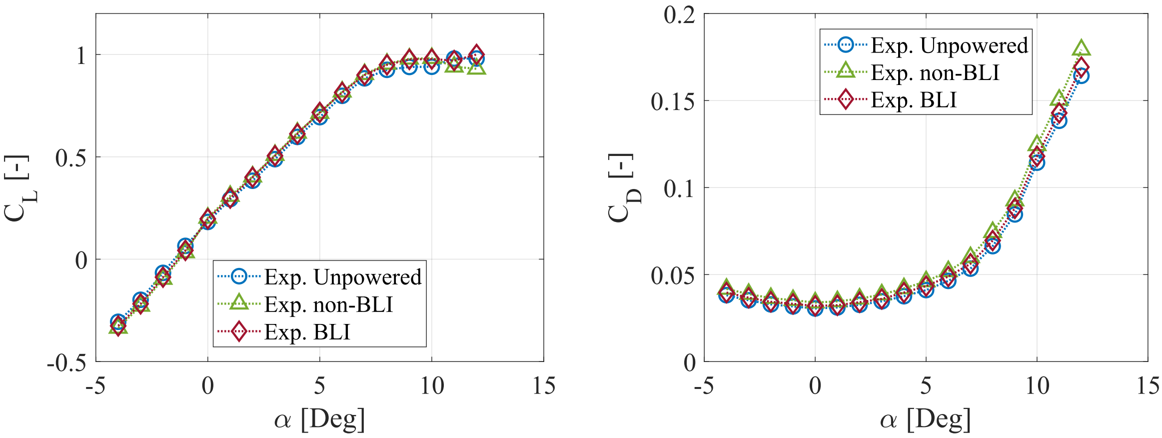

(c) Drag polar. (d) Lift-to-Drag ratio.

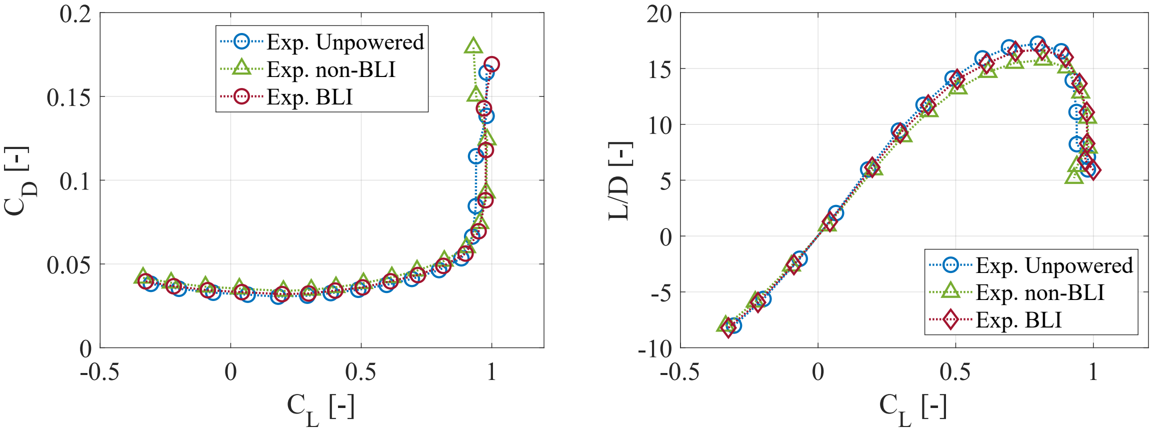

Source: The author

increased drag of about 11% in comparison with the unpowered configuration. In contrast, the BLI configuration increased drag on the order of 5% compared to the unpowered configuration, indicating that the magnitude of interference drag of the BLI model is lower than the non-BLI model, i.e., the BLI model allows for smaller nacelles and eliminates pylons, reducing the total wetted area, and consequently the surface dissipation.

Figure 39c illustrates the drag polar chart. Clearly, the through-flow nacelles can have a notable impact on the overall changes in C_D, but the three configurations exhibit nearly the same C_L over the operating range of α between 2° and 6°. This result is easier to understand in Table 29, where the variation of drag coefficient with the square of lift coefficient ($\partial C_D/\partial C_L^2$), is presented (induced drag parameter). The lift properties and spanwise load distributions are substantially identical for all the configurations, which

Figure 40 – Mini-tuft flow visualization on the wing surfaces at $M = 0.089$, $Re = 3.02 \times 10^5$, and $\alpha = 10°$.

Source: The author

means that the BLI and non-BLI configurations have the same vortex dissipation, implying that only propulsion aerodynamic factors contribute to the BLI benefit.

Figure 39d shows the aerodynamic efficiency curves versus lift coefficient. All configurations displayed a similar pattern, where the maximum values were obtained between the interval $0.5 \leq C_L \leq 0.8$, which corresponds to $4° \leq \alpha \leq 6°$. The efficiency curves showed the drag increase produced by the mounted nacelles. Note the aerodynamic performance of the non-BLI and BLI configurations decreased in 8.36% and 3.13%, respectively, when compared to the unpowered configuration. For the sake of argument, it can be concluded that all the aerodynamic measurements were performed successfully, since specific characteristics about the performance of this particular unconventional configuration were observed, such as the soft stall induced by the closed-wing system, and the viscous drag increase caused by the pylon/nacelle interference.

4.3.2 Power Balance and BLI Benefit

The outcomes of the integrated systems (non-BLI and BLI configurations) are provided in this section. At Reynolds numbers of 2.72×10^5 and 3.02×10^5, the wheel speed of the propulsors were varied and the net streamwise force and electrical power were measured. The results are shown in Fig. 41, where the net streamwise force coefficient (defined in eq. 4.2) is plotted against the electrical power coefficient (defined in eq. 4.5). The crosses represent the points for the seven different runs, and the lines are cubic splines curve-fit through the average of these points at each motor speed (Table 30). Across the entire range of power levels evaluated (Fig. 41a), the BLI configuration required less electrical power for a given net streamwise force than the non-BLI configuration. The BLI benefit (defined in eq. 4.8) at $C_X = 0$ was found to be $PSC = 7.41 \pm 2.5\%$. Such data were obtained by adjusting the electrical power of the EDFs until the net axial force on the apparatus was zero as measured by the load cell. The data were averaged to evaluate how engine thrust and nacelle installation affected power measurements in non-BLI and BLI

Figure 41 – Net streamwise force coefficient versus electrical power coefficient at $C_L = 0.51$. For each of the configurations, symbols are experimental measurements, and lines are curve fits to data points. Repeatability is $\Delta C_{P_E} = 0.003,\ 0.008$ or equivalently $\Delta C_X = 0.003,\ 0.007$ for non-BLI and BLI configurations, respectively.

(a) Full measured range.

(b) Close-up view on $C_X = 0$.

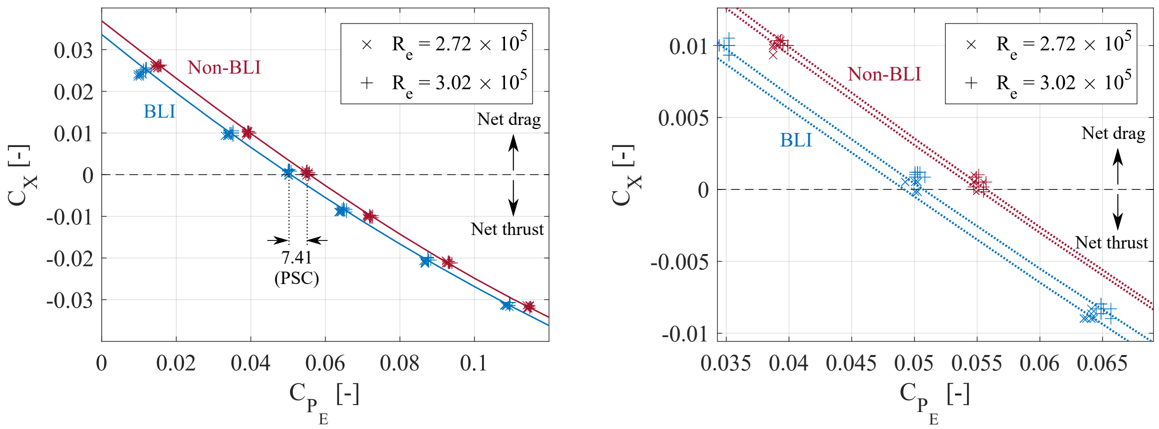

Source: The author

Table 30 – Cubic curve-fits of the C_{P_E} versus C_X data.

Tunnel condition	Configuration	Curve Fits and Confidence Interval
$R_e = 2.72 \times 10^5$	Non-BLI	$y = 2.6x^3 + 0.5574x^2 - 0.6947x + 0.03609$; $R^2 = 0.999$
$R_e = 3.02 \times 10^5$	Non-BLI	$y = 3.6x^3 + 0.4454x^2 - 0.6983x + 0.03689$; $R^2 = 0.999$
$R_e = 2.72 \times 10^5$	BLI	$y = 10.8x^3 - 0.989x^2 - 0.5878x + 0.03$; $R^2 = 0.997$
$R_e = 3.02 \times 10^5$	BLI	$y = -0.65x^3 + 1.292x^2 - 0.7276x + 0.03364$; $R^2 = 0.998$

Source: The author

configurations. These points can be seen in the zoomed-in view in Fig. 41b. The results are comparable to previous experimental studies that employed the electrical power coefficient instead of the mechanical flow power coefficient. For example, Uranga *et al.* (2014) reported preliminary experimental analyzes of the Double Bubble D8 aircraft with focus on the differences between the BLI and non-BLI configurations at Reynolds number of 3.6×10^5. The authors found a BLI benefit of about $6.85 \pm 2.3\%$. This result is highly comparable to subsequent experiments on this aircraft, in which measurements of pressure fields, velocity magnitudes, and flow directions are used to calculate the mechanical flow power of the propulsors (URANGA *et al.*, 2017). In the latter case, the measured BLI benefit was $8.6 \pm 1.8\%$ at simulated cruise. Given the experimental uncertainty, the application of the electrical power coefficient under the premise that the motor and fan work near peak efficiencies does not reveal substantial variance, as a positive advantage was found in both experimental campaigns.

On the other hand, CFD simulations using the actual scale and flight conditions of the INTI aircraft demonstrated a power saving coefficient of about 6.52%, as shown in

Chapter 3. This result is not plotted in Fig. 41, because it cannot be compared directly to the power extracted from the wind tunnel experiments. The CFD used an actuator disk model to characterize the propulsors, which does not considered fan rotation. Although the raw experimental data has some uncertainty due to the large degree of interference among the numerous competing effects, it was determined that the studied propulsion system has the potential to provide specific BLI benefits in the order of 5% to 7%.

4.3.3 Seven-Hole Probe Measurements

According to Uranga *et al.* (2018), three major parameters can influence the BLI benefit: the amount of dissipation ingested by the propulsors; the BLI installation efficiency in terms of surface dissipation reductions; and the propulsor jet velocity (typically set by the propulsor mass flow). As shown in Fig. 41, the variations in P_E between the configurations were derived from changes in the isolated airframe drag values, as well as the propulsion airframe integration effects. This confirms that the BLI benefit depends on the specifics of the integration between propulsor, fuselage, and vertical tail, achieving reduction in surface dissipation. However, the mechanical flow power, given by eq. 4.3, is dependent on the total pressure difference and the axial flow velocity, i.e., the streamwise velocity reflects the velocity deficit of the ingested boundary layer. In this context, seven hole probe surveys were conducted as close as possible to the propulsors to investigate the flow-field downstream the aircraft models. The axial velocity and streamwise vorticity were the most relevant flow parameters in the study of the flow-field. Contour maps of velocity (u^*), and streamwise vorticity (ω_x) are shown in Figs 42 and 43, respectively.

The velocity maps (Fig. 42) show the difference between through-flow nacelle condition (left) and powered configurations (right) for non-BLI (Fig. 42a) and BLI (Fig. 42b) configurations, respectively. The contour maps for the u^* component in through-flow nacelle condition revealed regions of reduced velocity, which correspond to the wake and velocity deficit of the airframe. The contour of the non-BLI configuration evidenced a clear aerodynamic interference between the pylon and nacelle, resulting in separation and increased drag on the nacelle's surfaces. At that region, the lowest velocity reached approximately $0.9V_\infty$. In contrast, the contour of the BLI configuration exhibited a larger region of low-velocity fluid due to the incoming boundary layer. In this case, the lowest velocity value reached $0.83V_\infty$. In both cases, the wake from the tail cone has most likely merged, creating a large momentum deficit. On the other hand, the contour maps for the u^* component in powered configurations perceived the reduction in kinetic energy dissipation due to the wake and the propulsive jet. Note that the BLI configuration achieved a lower jet velocity ($1.03V_\infty$) than the non-BLI configuration ($1.08V_\infty$), because the exhaust velocities of the BLI propulsor has lower stagnation pressure than the non-BLI propulsor. This result explains the smaller amount of energy (electrical power) of the BLI configuration to reach a certain net streamwise force.

Figure 42 – Axial velocity contours at $R_e = 3.02 \times 10^5$, $C_L = 0.51$, $U_{tip}/V_\infty = 1.96$. Through-flow nacelle condition (left) and powered configurations (right).

(a) Non-BLI configuration.

(b) BLI configuration.

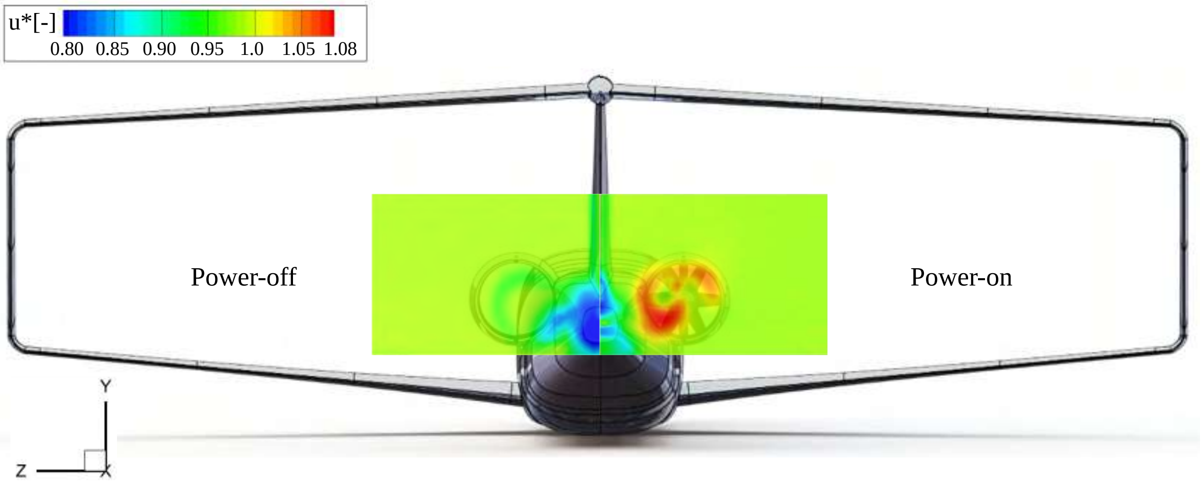

Source: The author

The distributions of axial vorticity along with velocity vectors for the non-BLI and BLI configurations are reported in Figs. 43a and 43b, respectively. Both configurations exhibited a region of negative (clockwise) vorticity at the center, and positive structures along the trailing edges of the nacelles. Such vortical structures also come from the secondary flow resulting of the cross-sectional changes of the different airframes. However, the presence of fans imposed additional complexities, and the vortical structures are the result of the mixing of secondary flows with fan rotational motion. Despite very similar patterns were observed with lower fan voltage inputs, the BLI configuration presented a lower velocity magnitude than the non-BLI configuration when viewed from downstream.

Figure 43 – Close-up views of streamwise vorticity contours and velocity vectors at $R_e = 3.02 \times 10^5$, $C_L = 0.51$, $U_{tip}/V_\infty = 1.96$.

(a) Non-BLI configuration.

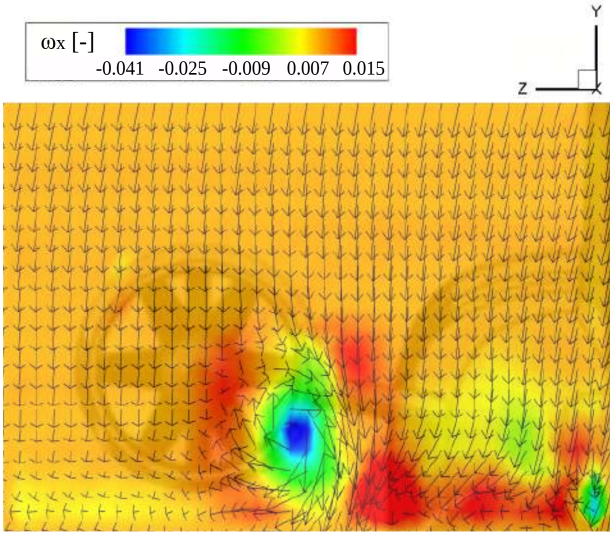

(b) BLI configuration.

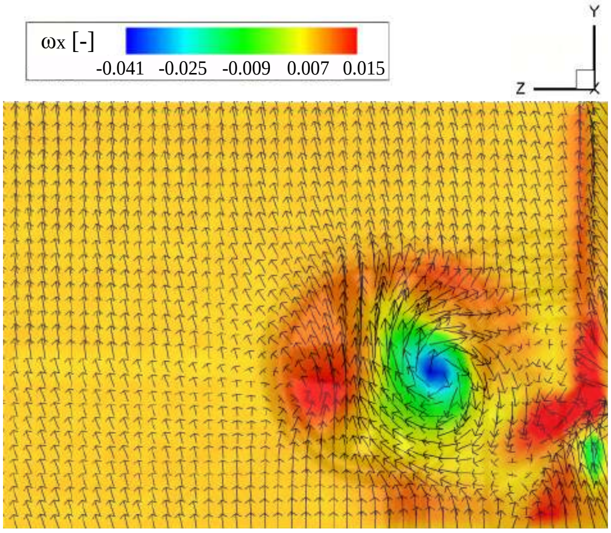

Source: The author

4.3.4 Inlet Efficiency

The inflow distortion associated with the fuselage boundary layer is ingested by the inlet duct and delivered to the engine. This fact imposes compatibility challenges due to the effect of the distorted propulsor inflow on fan performance, reducing the overall BLI benefit. To illustrate this issue, the total pressure coefficient contours as well as distortion analysis can be seen in Fig. 44. The grids for the total pressure survey were created using the locations of the probes mounted on the rake (Fig. 37). Therefore, the total pressure coefficient contours were obtained by linearly interpolating in the radial and circumferential directions for grid points between the innermost and outermost points on the survey grid. The values of DC_θ for both configurations and number of runs lie within

Figure 44 – DC_θ and C_{p_t} experimental results measured on the aerodynamic interface plane at $M = 0.089$, $Re = 3.02 \times 10^5$, and α from 0° to 8°.

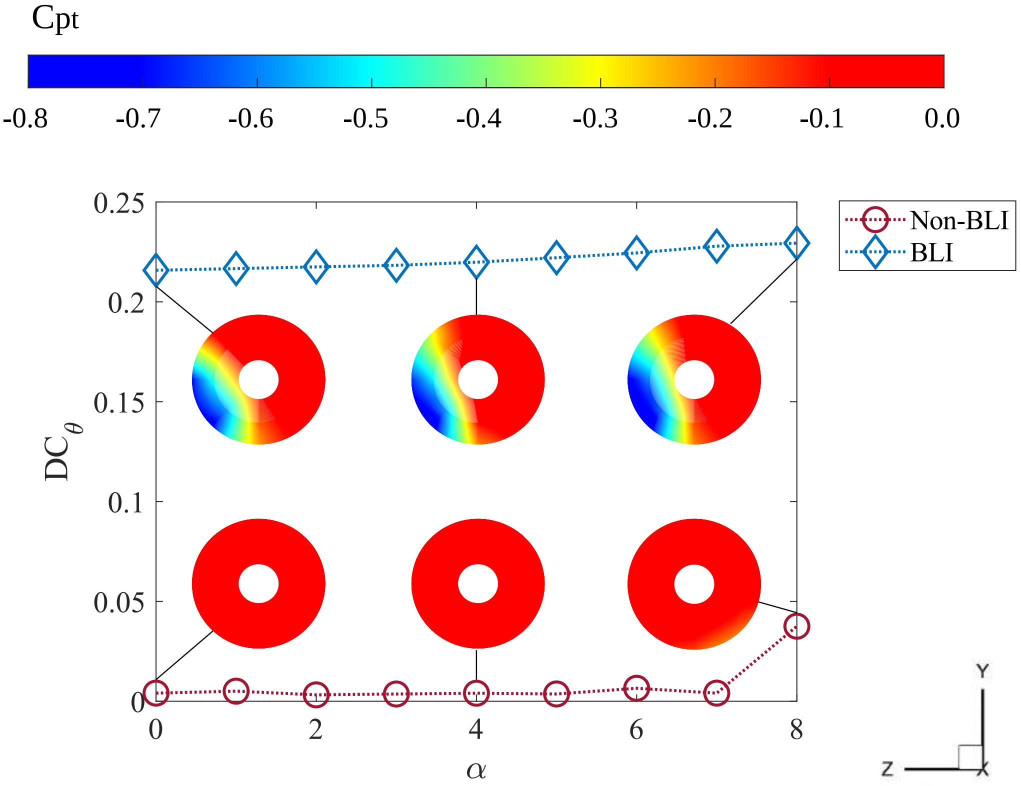

Source: The author

1% of each other, confirming the repeatability of the measurements.

The ingested boundary layer can be noted clearly, presenting high indices of distortion, as a consequence of the reduced low-pressure region. However, as the angle of attack increases until $\alpha = 8°$, the performance variation of the BLI configuration is relative low. Note that the pressure distribution seems similar, and the difference in distortion between $\alpha = 0°$ and $\alpha = 8°$ is 5.9%. This indicates that changing the angle of attack has no significant effect on cross-flow or separation in the current engine location, implying that fan performance should be unaffected under several flight conditions. In contrast, a clean airflow is evidenced for the non-BLI configuration until $\alpha = 7°$, however, at higher angles of attack, a small vortex is formed coming in from the side, creating distortion regions of lower total pressure in the aerodynamic interface plane. In sum, the non-BLI configuration presented distortion values of $DC_\theta \sim 0.004 - 0.007$ at low to moderate angles of attack, whereas the BLI configuration had distortion values of $DC_\theta \sim 0.021 - 0.023$, corresponding to total pressure recovery values of $\eta_R = 0.984 \sim 0.977$ and $\eta_R = 0.651 \sim 0.613$, respectively. This indicates that further research is needed to determine the fan response (aerodynamic and aeromechanic) to these higher distortion levels, as well as the influence on engine life cycle.

Finally, mini-tuft flow visualization have been performed upstream and downstream of the nacelles to visualize the flow entering the propulsors. The arrangement of the mini-

Figure 45 – Mini-tuft flow visualization on fuselage and nacelles upstream of propulsor inlets at $M = 0.089$, $Re = 3.02 \times 10^5$, and $\alpha = 3°$.

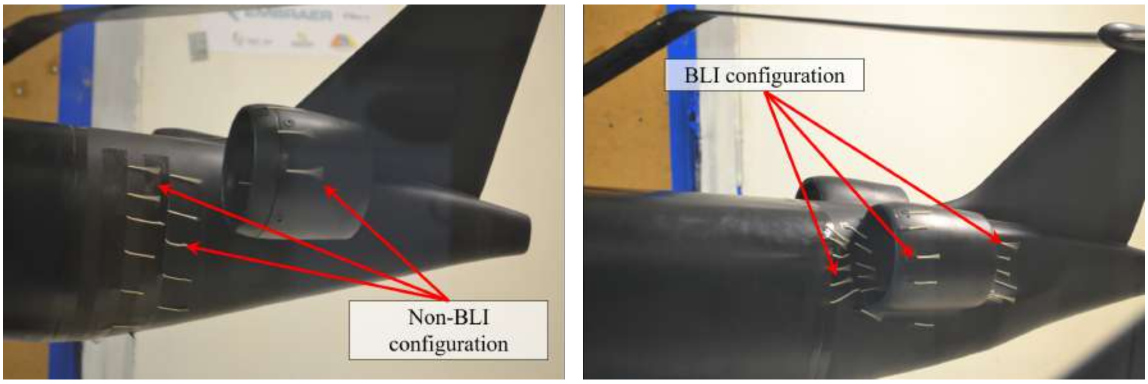

Source: The author

tufts at $\alpha = 3°$ is displayed in Fig. 45 for both configurations. Although no large-scale separation can be identified, cross-flow can be seen in both configurations. There are some blurred tufts around the nacelle lips of the non-BLI configuration, indicating a region of accelerated flow. However, the flow far from the propulsors is steady, with the tufts all pointing in the flow direction. In contrast, separated flow can be seen around the incoming flow of the BLI configuration, with tufts pointing in a random direction and continuing inwards and towards the propulsor inlet, i.e., indicating blockage and lower velocity flow entering to the propulsor, which caused high distortion levels. In this case, the overall flow over the nacelles remains aligned to the flow direction. In conclusion, inlet flow distortion is expected to play a major role in unconventional aircraft where complex air induction systems are required to couple the airframe with engines.

4.4 Summary of Key Findings

Wind-tunnel testing of a 3.5%-scale model of the INTI transport aircraft has been performed in the closed circuit wind tunnel at the Laboratory of Aerodynamics of the Aeronautical Engineering Department from São Carlos School of Engineering - University of São Paulo. The investigation presented the use of several methodologies to enable aerodynamic testing over a sub-scale model in order to determine the aerodynamic benefit owing to boundary layer ingestion (BLI). Therefore, it was possible to analyze and validate the main findings during the design process, which are summarized as follows:

- The analyses demonstrated a clear relation between the jet velocity and the power saving coefficient due to BLI, i.e., BLI allows for a lower jet velocity because the ingested flow is slower. As a result, there is a less momentum flow through the propulsor, as well as a more efficient use of power input. The measurements revealed that using BLI saved at least 7.41%±2.5% power in comparison with more conventional free-stream flow ingesting configurations, with a 99% confidence interval.

However, due to current scale model limitations, electrical power is used to quantify the BLI benefit, rather than more relevant mechanical flow power measurements of the propulsors. Therefore, subsequent experiments will convert the electrical power into mechanical flow cover by computing the shaft and fan efficiencies. Such experiments will not be difficult because one of the novel aspects of the current work lies in the use of an electrical driven fan, specifically adapted for the needs of the present tests, which allowed to control and measure precisely the power injected into the flow.

- Despite the fact that the current analysis does not explicitly evaluate the BLI benefit for an actual transonic transport aircraft, it does help to validate the processes needed to evaluate the potential of BLI on real aircraft geometries and thus enable their use in the design of novel propulsion technologies that are tightly integrated with the airframe. Indeed, the results of this experiment are similar to those obtained from steady CFD-RANS simulations of an actual scale and flight condition of the aircraft, although with a ±2.5% margin of error due to aerodynamic modeling uncertainties.

- The results are thought to be useful in understanding BLI aerodynamics for several reasons. First, the fan was scaled to match the full-scale fuselage boundary layer, due to differences in Reynolds and Mach numbers between the wind-tunnel scale and full-scale conditions. Second, the power balance method does not account for differences in Reynolds and Mach numbers, and the benefit of the BLI is mostly attributable to a lower jet to freestream velocity ratio (reduction of around 4.63%) and lower external losses due to the smaller nacelle wetted area (reduction of around 5.62%) compared to the non-BLI configuration. Third, previous research by many authors suggests that compressibility effects are unlikely to have a significant impact on the fuselage boundary layer. This demonstrates how the current aerodynamic model experiment may be used to appropriately assess the aero-propulsive efficiency of a BLI aircraft configuration.

- The aerodynamic flow measurements confirmed the existence of flow distortion which limits the aerodynamic performance of the BLI configuration. Therefore, the specific fan response to the distortion should be the subject of future investigations. This is mostly due to material restrictions, such as dealing with fan-blade stresses caused by the nonuniform incoming flow, which can result in noise or vibration problems.

- A seven-hole probe was used to take the flow measurements. The interference of this probe with the flow should be further investigated, and particle image velocimetry (PIV), a non-intrusive flow measurement technique, can offer a comprehensive assessment of the flow field. Although the findings of this research provide direct evidence for the benefits of boundary-layer ingestion, more research is needed to fully comprehend the influence on aircraft performance in detailed design phases.

4.5 Dissemination

The following article has been published as a result of this chapter:

- BRAVO-MOSQUERA, P; EGUEA, J; CERÓN-MUÑOZ, H; CATALANO, F. Experimental Investigation of a Next-Generation Airliner with Boundary Layer Ingestion. **In: International Congress of the Aeronautical Sciences (ICAS), Stockholm, Sweden**, 2022. (BRAVO-MOSQUERA *et al.*, 2022b).

5 EXPLORATION OF BOX-WING AIRCRAFT CONCEPT USING HIGH-FIDELITY AERODYNAMIC SHAPE OPTIMIZATION

5.1 Introduction

This chapter discusses a preliminary exploration on the application of aerodynamic shape optimization of a box-wing concept based on Reynolds-Averaged Navier-Stokes (RANS) equations. The optimization framework consists of B-spline parameterization surfaces, free-form and axial deformation geometry control, an integrated mesh-movement scheme based on the theory of linear elasticity, a Newton-Krylov-Schur flow solver for the Reynolds-averaged Navier-Stokes equations, a gradient-based optimizer, and the discrete-adjoint method for gradient evaluation. All these modules are integrated in an aerodynamic shape optimization framework called **Jetstream**. This chapter is divided into two main stages: (i) The application of a conceptual design environment called **Faber**, which allowed to expand the analysis of the box-wing concept with a finite-element based wing weight estimation method. (ii) The progress made on optimising a box-wing concept through aerodynamic shape optimization. The objective of the present study is therefore to further understand the aerodynamic design and performance potential of a BW configuration, including the fuselage geometry, in order to account for wing-body flow interactions and proper fuselage lift through aerodynamic shape optimization based on the RANS equations. In particular, drag minimization is applied to the aerodynamic design and performance evaluation of a BW aircraft based on the Airbus A320neo. The RANS-based aerodynamic shape optimization provides an accurate quantification of the trade-offs between induced drag and viscous drag for the BW aircraft concept, thus complementing previous low-fidelity conceptual design and optimization efforts, presented in Chapter 3.

The chapter is organized as follows. Section 5.2 provides a brief overview of the methodologies implemented to design and evaluate the proposed BW concept, including details of low-fidelity conceptual-level MDO frameworks that were used to evaluate different design alternatives at an early phase of the design process, as well as details of the high-fidelity aerodynamic shape optimization framework based on the RANS equations. Section 5.3 describes the problem setup for the aerodynamic shape optimization problem and includes details on aircraft size, initial geometry, computational mesh, and geometry control. Section 5.4 presents the results for the preliminary exploration of the lift-constrained drag minimization of the BW concept, as well as details of the performance analysis based on different mission profiles. Conclusions and suggestions for future work are given in Section 5.5 and Section 5.6, respectively.

5.2 Methodology

In this section, the computational tools that were used to design and assess the single-aisle medium-range BW aircraft are presented. The section is organised into subsections that describe how these tools were employed towards the development of a BW concept with reduced drag.

5.2.1 Conceptual-level Multidisciplinary Design Optimization

5.2.1.1 Faber

Faber is a mixed low- and medium-fidelity MDO tool that provides a means for the systems analysis, sizing, and optimization of transport aircraft, with a focus on developing aircraft that are representative of a given configuration and class (CHAU; ZINGG, 2021). Aircraft configurations include the CTW, as well as more unconventional aircraft configurations such as the BW. Given an initial concept and a set of design missions and top-level aircraft requirements, physics-based methods are used to iteratively size and analyze the aircraft components and subsystems. This iterative routine is further incorporated into a gradient-based optimization framework to refine the initial concept for minimum fuel burn.

In this work, **Faber** is primarily used to recompute the structural wing mass of the BW concept using its equivalent beam model. These results are then used to improve the weight estimate from **Paerom**, which uses a regression analysis based on finite element analysis data obtained from an idealized box wing structure (JEMITOLA; MONTERZINO; FIELDING, 2013). **Faber** also includes a global buckling detection method based on Euler-Bernoulli beam theory, currently not available in **Paerom**, which aids in sizing box wing structures subjected to compressive axial loads.

For this study, the objective is to minimize the block fuel consumption of the aircraft. In order to maintain the wing planforms obtained from **Paerom**, design variables only include thickness-to-chord ratio and chord degrees of freedom at major stations across the wing. Constraints include minimum wing volume, which ensures that there is enough space in the wing system to contain the fuel tanks; minimum tip chord lengths, which prevent the optimizer from creating a wing with unrealistic wing taper ratios; and buckling constraints, which ensure that each wing segment does not fail due to buckling. For structural sizing and analysis, the vertical wing segment is modeled as a series of bar elements, while rigid joints are used to define its connections with the fore and aft wings. Figure 46 shows details of the BW concept simulated in **Faber**. For a complete list of the modifications made to **Faber**, see Appendix J.

Figure 46 – Overview of the BW concept simulated in **Faber**.

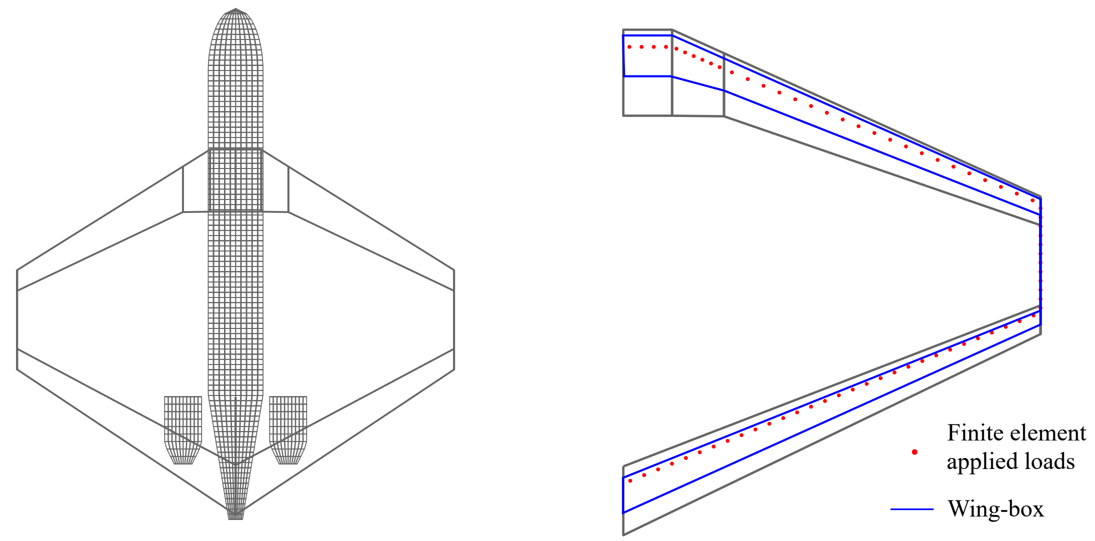
(a) Conceptual design - BW planform. (b) Beam element discretization.

Source: The author

5.2.2 High-Fidelity Aerodynamic Shape Optimization Framework - Jetstream

The multi-fidelity MDO framework with high-fidelity aerodynamic shape optimization suite used in this thesis is called **Jetstream**. The methodology for gradient-based aerodynamic shape optimization requires five main components: an integrated geometry parameterization, control, and mesh deformation scheme (HICKEN; ZINGG, 2010a), a free-form and axial deformation geometry control system (GAGNON; ZINGG, 2015), a Newton-Krylov-Schur RANS-based structured multi-block parallel implicit flow solver fully coupled with the Spalart-Allmaras turbulence model (OSUSKY *et al.*, 2015), the discrete-adjoint method for flow- and mesh-dependent gradient evaluation (PIRONNEAU, 1974; JAMESON, 1988), and SNOPT for gradient-based optimization (GILL; MURRAY; SAUNDERS, 2005). This framework has been used to explore several unconventional configurations, combining considerable geometric flexibility with frequently unknown design spaces in the pursuit of a viable solution for aviation sustainability. Some key examples include: Hybrid Wing–Body (HWB) geometries (REIST; ZINGG, 2016; REIST *et al.*, 2019) and Strut-Braced Wing (SBW) concepts (CHAU; ZINGG, 2021). An overview of the theoretical background for each component is briefly discussed in this chapter, whereas the optimization workflow can be seen in Fig. 47.

5.2.2.1 Geometry Parameterization, Control, and Mesh Movement

For geometry parameterization and control, a two-level B-spline system is used, in which B-spline surfaces with B-spline control points are used to parameterize the geometry. The control points of the Free-Form Deformation (FFD) volumes and axial curves are the

Figure 47 – Flowchart of **Jetstream**.

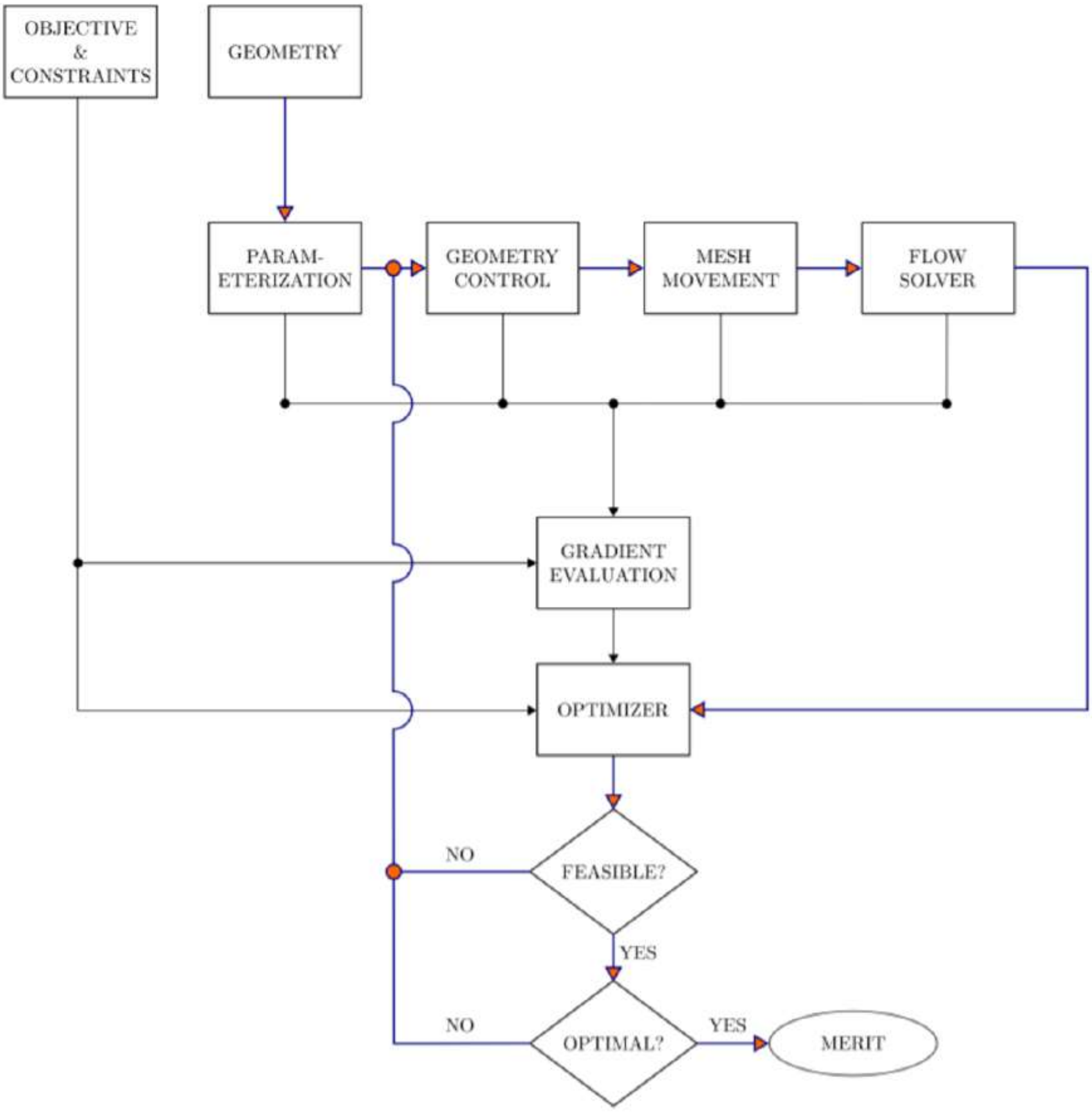

Source: Chau (2017)

used to control the location of the B-spline control points of the geometry parameterization, enabling an analytical geometry representation throughout the optimization process. Such an approach is integrated in a high-fidelity conceptual aircraft design tool called **Genair** (GAGNON; ZINGG, 2015). To propagate displacements on the B-spline surface to the rest of the control volume, the B-spline volume control mesh is deformed using a linear-elasticity model (HICKEN; ZINGG, 2010a). This section covers the fundamentals of B-splines, FFD control system, and mesh movement algorithm implemented in **Jetstream**:

- B-Spline representation: **Genair** parameterizes aircraft components with non-uniform rational B-splines (NURBS) (GAGNON; ZINGG, 2015). This is the most common method for modeling curves and surfaces in geometric computational design. **Genair** owns a NURBS library that allows to parameterize and automate aircraft design in a flexible and efficient manner while maintaining an accurate geometrical representation for optimization. Basically, the toolbox allows to generate and manipulate NURBS curves, surfaces, and volumes. Another interesting fact is that it offers excellent control for both smooth and sharp surfaces, allowing for a variety of resolutions depending on the application.

- Grid fitting: a grid fitting approach is used to parameterize the computational domain, in which each block of the multi-block mesh is parameterized with a cubic B-spline volume, i.e., the B-spline control volume replicates the spatial distribution of the computational mesh. Boundary layers in fluid flow require a grid that is very compressed normal to the flow direction. This creates a problem during the grid fitting procedure since the fitting error is bigger than the off-wall spacing (HICKEN; ZINGG, 2010a). Therefore, control point cross-over could occur, resulting in cells with negative Jacobians in the control grid and, ultimately, fitting or mesh-movement problems. According to Hicken and Zingg (2010a), the solution is to generate two computational meshes that fit together, which share the same structured blocking topology, number of nodes, and connectivity, but different distribution of nodes in the off-wall direction. Then, the first mesh contains off-wall spacings that are suited for RANS analysis of turbulent flows, whereas the second mesh uses coarsened off-wall spacings to recreate the original B-spline control volume.

- Free-Form Deformation control: FFD combines free-form surfaces and solid models into a single framework for deforming solid geometry in a free-form fashion, i.e., during optimization, an FFD control deforms the volume mesh to account for changes in the surface geometry while retaining its continuity and smoothness. As control points are moved, the embedded shape deforms in a continuous manner, giving the optimizer control over twist, taper, and cross-sectional shape design variables. Axial deformation is an extension of FFD that uses an axial curve (defined as a B-spline curve) that provides more degrees of freedom to the geometry. It can be defined as a polynomial curve of any order, and is usually located at either the leading edge, the trailing edge, or the quarter-chord of a wing geometry. In **Jetstream**, the degrees of freedom for a given axial curve controls span, sweep, and dihedral. Therefore, axial curves with more than two control points allows to design nonlinear planform designs (GAGNON; ZINGG, 2015).

- Mesh movement algorithm: in aerodynamic shape optimization problems, regenerating the mesh after each design iteration is computationally expensive. As a result, the most effective method for deforming a grid in **Jetstream** is to use a mesh movement algorithm based on a linear elasticity model (HICKEN; ZINGG, 2010a). This technique uses a B-spline volume to parameterize each block of the computational domain, and the mesh-movement approach can then be applied to a coarser grid of volume control points rather than directly to the computational mesh. This way, the number of B-spline volume control points is often two to three orders of magnitude fewer than the number of computational mesh nodes, preserving the analytical representation of the geometry while greatly reducing the computational cost. More details of the integrated mesh algorithm can be found in Hicken and Zingg (2010a).

5.2.2.2 Flow Solver

Jetstream uses a parallel, implicit, multi-block structured finite-difference solver called Diablo. This flow solver is capable of solving either Euler (HICKEN; ZINGG, 2008) or RANS (OSUSKY *et al.*, 2015) equations. Second-order summation-by-parts (SBP) operators with scalar or matrix numerical dissipation are used to discretize the equations, while boundary conditions and block interfaces are enforced using simultaneous approximation terms (SATs). The combination of SBP and SATs operators provides excellent numerical stability properties and efficient parallel performance (FERNÁNDEZ; HICKEN; ZINGG, 2014). For RANS analyses, the equations are closed with the Spalart-Allmaras one-equation turbulence model (SPALART; ALLMARAS, 1992).

The flow solver is based on a parallel Newton-Krylov-Schur algorithm that generates the initial iteration for the subsequent inexact-Newton phase using an approximate Newton start-up phase. As a result, the system of linear equations generated in both phases is solved using a flexible generalized minimal residual (GMRES) - a Krylov iterative solver with approximate-Schur parallel preconditioner. Additional details of the solver can be found in Osusky *et al.* (2015). Note that **Diablo** has been validated using the NASA Common Research Model wing-body configuration from the fifth Drag Prediction Workshop (OSUSKY; BOOM; ZINGG, 2013).

5.2.2.3 Optimization Algorithm and Gradient Evaluation

Numerical problems involving aerodynamic shape optimization, particularly in three dimensions, are typically associated with a large number of design variables (KENWAY *et al.*, 2019). This can result in large processing costs when using finite-difference methods to evaluate gradients. As solution, **Jetstream** uses the discrete adjoint method for computing objective function and constraint gradients that depend on the flow solution. The advantage of this approach is that the cost is almost independent of the number of design variables (PIRONNEAU, 1974; JAMESON, 1988). The main disadvantage of gradient-based algorithms is that they find a local rather than a global optimum. However, this is unlikely to be an issue, since experience has shown that some high-fidelity optimization problems have convex design spaces (CHERNUKHIN; ZINGG, 2013; STREUBER; ZINGG, 2021).

Table 31 – Geometric characteristics used for high-fidelity optimizations[1].

Parameter	Fore wing	Aft wing	Vertical wing
Planform area[2,3] $[m^2]$	51.8	36.5	9.3
Span $[m]$	16.1	16.1	5.7
Mean aerodynamic chord $[m]$	3.19	2.39	1.6
Aspect Ratio [-]	5.0	7.1	3.5
Taper Ratio [-]	0.31	0.54	1.0
Dihedral angle $[deg]$	$4°$	$-2°$	$90°$
Leading edge sweep angle $[deg]$	$32°$	$-28°$	$50°$

[1] Half-model dimensions.

[2] Portion inside the fuselage included for fore wing.

[3] Not including blended transitions.

Source: The author

In particular, **Jetstream** uses SNOPT (Sparse Nonlinear OPTimizer) (GILL; MURRAY; SAUNDERS, 2005) to solve aerodynamic shape optimization problems. This is a gradient-based optimizer that implements the sequential quadratic programming method. SNOPT is capable of handling large-scale nonlinear optimization problems with thousands of constraints and design variables, ensuring that mesh deformation, followed by flow, adjoint, and gradient evaluations, are all returned to SNOPT for the next design iteration. For gradient evaluation, the discrete-adjoint method is used for gradients that depend on the flow solution or mesh deformation scheme. For all other sensitivities, gradients are calculated analytically or approximated through the complex step method.

5.3 High-Fidelity Aerodynamic Shape Optimization Problem

In this work, the optimization objective is to minimize drag for the BW concept described above. An exploratory optimization is performed to investigate aerodynamic trends and trade-offs, and to refine the initial geometry using aerodynamic shape optimization. The problem is formulated for a given Mach number, lift coefficient, and wing planform. In this context, the focus in on modifications in airfoil shapes and spanwise twist distributions, whereas the taper, sweep, span, and dihedral of the closed-wing remain constant. This strategy is applied over the whole closed-wing system, including the blended transitions that join the fore and aft wings with the vertical wing.

5.3.1 The Baseline BW Concept

The geometry consists of two main components: fuselage and box-wing. The fuselage geometry is kept unchanged in this work, whereas the complete box-wing is optimized along with the patches of the fairing where the fore wing is attached. The length of the fuselage and its diameter are 37.57 m and 4.0 m, respectively. Patch topologies of the BW concept are illustrated in Fig. 48, and the main dimensions of each component are summarized in Table 31.

Figure 48 – Baseline BW configuration for high-fidelity aerodynamic shape optimization.

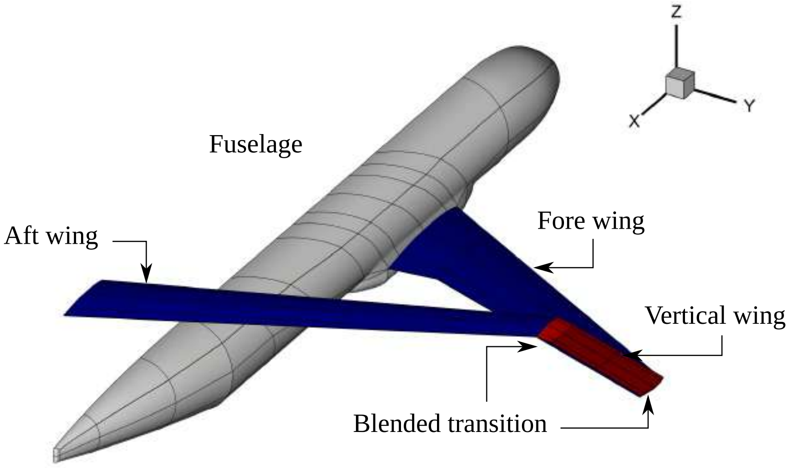

Source: The author

5.3.2 Computational Grid

The computational domain and aerodynamic geometries are discretized using a structured multiblock grid (O-O blocking topology), which is then fitted with B-spline volumes for mesh deformation and geometry control. ICEM-CFD software (FINLAYSON, 2013) was used to create the multiblock structured grid, which resulted in 970 blocks that are fitted together with some degree of grid continuity at their interfaces. The first step was to divide the physical region into sub-regions; each bounded by six faces in 3D. This step requires considerable user interaction in order to get a successful domain decomposition (e.g., with block edges aligned with complex geometric surfaces). The advantage of ICEM is the O-Grid functionality, which allowed to generate a good meshing around the aircraft and decrease the cell size up to the far field (FINLAYSON, 2013). However, the degree of grid point continuity that must be maintained among each block, particularly at the boundaries between sub-regions, is a significant drawback when dealing with complex geometries, because discontinuities cause poor flow solver convergence and can cause mesh deformation failure.

In this case, the grid topology required some kind of diagonal blocks in order to distribute uniformly the elements between the fore and aft wings, demanding a large deal of user effort. This fact introduced challenges to the generation of high-quality meshes since grid point continuity must be preserved among multiple geometry components. Figure 49 shows the structured surface mesh of the BW configuration along with close-up views of the O-grid in wing-fuselage intersection and symmetry plane, and details of elements distribution in diagonal blocks. Already at first sight, from Fig. 49a high quality meshes can be appreciated. In fact, the non-orthogonality quality metric has determinants larger than 0.6, indicating a good mesh orthogonality near the solid surfaces. However, the particular blocks decomposition of this model generated skewed cells, which was critic

Table 32 – BW grid information[1].

Refinement level	Number of nodes	Average Off-wall spacing[2]	Average y+
L0	21.18×10^{6}	1.17×10^{-6}	0.59
L1	40.73×10^{6}	8.79×10^{-7}	0.45
L2	81.46×10^{6}	6.79×10^{-7}	0.34

[1] Calculated for Reynolds number equal to 14.23×10^{6}.

[2] Off-wall spacings are in units of mean aerodynamic chord.

Source: The author

particularly in the blocks between the fore and aft wings in spanwise direction, as shown in Fig. 49b. Regardless this fact, and after improving the load balancing of the largest blocks, the mesh satisfied the relative residual drop criterion (approximately 1×10^{-11}), without any unsteadiness, or problems with the numerical convergence, mesh deformation, memory requirements, and solution time. Appendix K lists non-orthogonality and skewness quality metrics of the initial BW geometry.

In order to obtain performance estimates with reduced numerical error, a grid refinement study based on Richardson extrapolation is completed for the optimized geometry, using grids with roughly 40 (L1) and 80 (L2) million nodes. The grids were created using Jetstream's automatic grid refinement capabilities, which use grid node insertion and redistribution to keep the original mesh spacing functions while maintaining the analytical surface definition (OSUSKY *et al.*, 2015). Table 32 lists the numbers of cells in the three multi-block structured meshes. Note the optimization grid (L0) presented a reasonable balance between accuracy and computational cost. All performance results presented below are estimated grid-converged values obtained via Richardson extrapolation.

5.3.3 Geometry Parameterization and Control

Genair was used to parameterize and manipulate the box-wing shape using a FFD approach (GAGNON; ZINGG, 2015). This tool allowed to embed the wing surfaces in a grid of control points, and the modifications made to the control points are transferred to the embedded surface by using a B-spline mapping. The embedded shape deforms in a continuous manner as the control points are moved, allowing the optimizer to manage the twist and cross sectional shapes. The free-form and axial deformation geometry control system is shown in Fig. 50. The blue spheres are FFD control points, and the green spheres are axial control points. The aerodynamic surfaces are parameterized with B-splines, and the surface control points are embedded within 6 FFD volumes: two for the fore wing, one for the aft wing, one for the vertical tip fin, and one for each blended transition. The FFD volumes embedding the fore wing allow to propagate deformations from patches that are embedded within FFDs (i.e. wing patches adjacent to the fuselage) across those not within FFDs (i.e. the adjacent fuselage patches). The fore wing consist of 11 FFD-volume cross-sections, so those at the fore wing-fuselage junction allowed to modify the fuselage

Figure 49 – Visualization of O-grids for high-fidelity optimization.

(a) Structured surface meshes of the primary components of the aircraft.

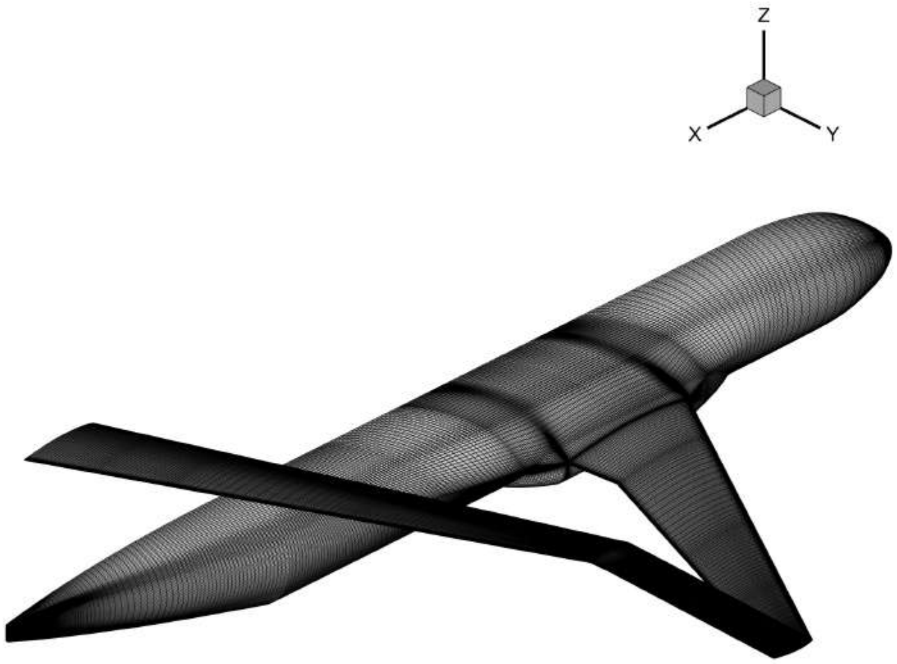

(b) Close-up view of wing-fuselage intersection and symmetry plane.

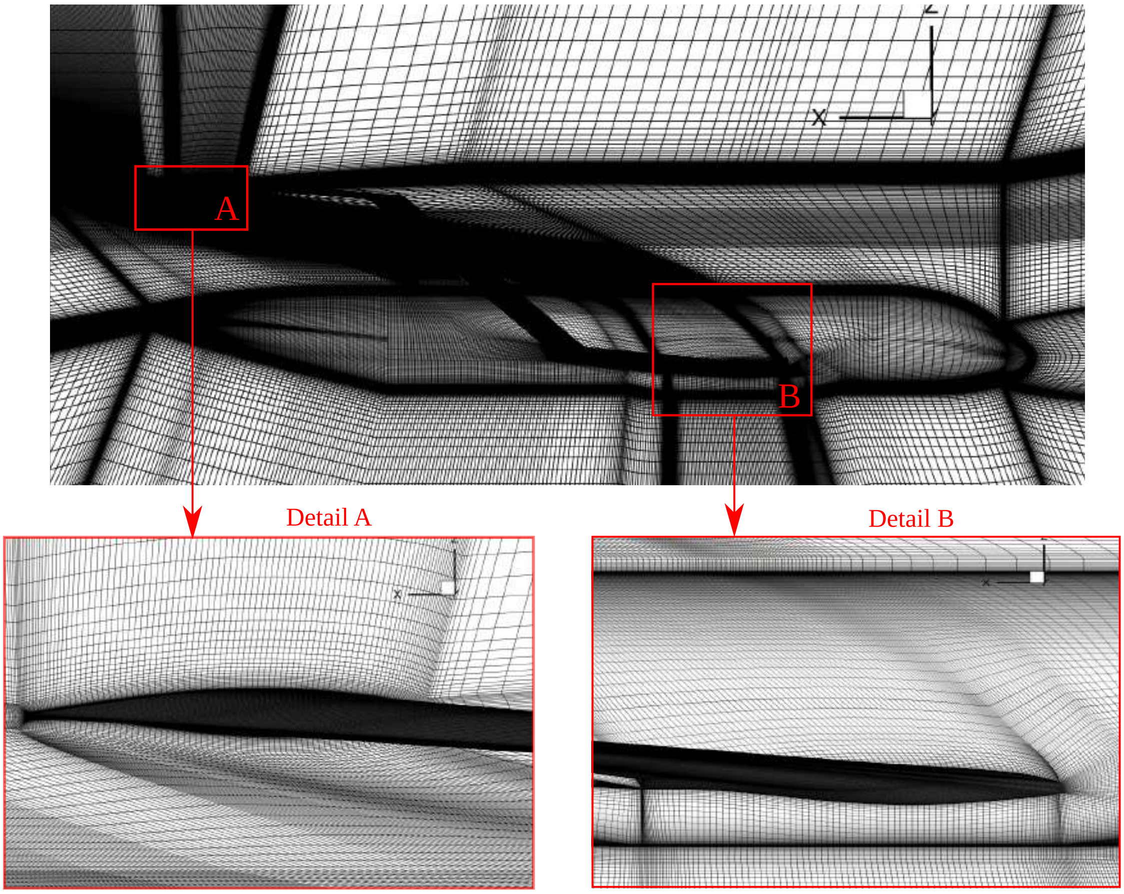

Source: The author

Figure 50 – Geometry control systems with FFD volume entities.

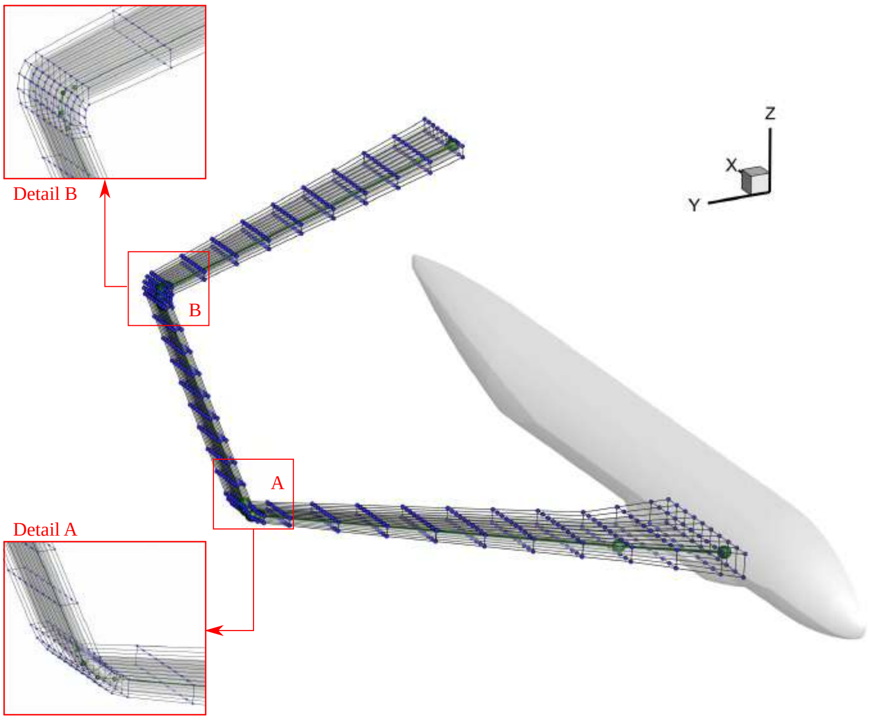

Source: The author

patches as the wing root deforms.

The aft wing and vertical tip fin each have 10 FFD-volume cross-sections, whereas both of the FFD volumes surrounding the blended transitions have 5 FFD-volume cross sections. This yields a total of 38 unique FFD-volume cross-sections, even accounting for overlaps. Each FFD-volume cross-section has 20 equally spaced FFD control points, 10 on each side of the aerodynamic surfaces. Linear axial curves are positioned at the quarter chord of the fore and aft wings and the vertical tip fin, whereas cubic axial curves are attached to the quarter chord of the two blended transitions, resulting in 11 axial curve control points. The axial curve is a nonuniform rational B-spline that determines the design variables that act on groups of FFD control points as well as the points of rotation for the twist design variables. In particular, the wing shape variables are defined by the movement of individual FFD control points in the z-direction, whereas the twist variables are defined by a rotation of the FFD-volume cross-section in the local xz-plane about the local origin. It is worth noting that FFD point coordinates are scaled to be on the same order of magnitude as axial curve control points. This preserves both the analytical representation of the geometry and the sensitivity of the aerodynamic surface with respect to the FFD control points, which is critical for calculating gradients.

5.3.4 Optimization Problem Formulation

The goal of this study is to minimize the drag coefficient for a certain flight condition, i.e., $C_L = 0.51$, Mach number of 0.78, altitude of 12500 m, which corresponds to

Table 33 – Design variables and constraints for high-fidelity aerodynamic shape optimization.

Optimization Problem	Function / Variable	Description	Lower Bound	Upper Bound
Minimize	C_D	Drag coefficient		
with respect to	Angle of attack (α)	The angle of attack is limited to ± 3°, based on deck angle requirements.	$-3°$	3°
	Twist (τ)	Twist of each FFD section.	$-10°$	10°
	Section Shape (Δ_z)	Vertical displacements of the FFD control points for airfoil-shape control.	0.5	2.0
Design variables	**799**			
	Constraint	Description		Value
subject to	Lift	Lift constraint at the start of cruise (nonlinear).		$C_L = 0.51$
	Trim	Aircraft pitching moment constraint equal to zero (nonlinear).		$C_M = 0$
	Wing volume	Minimum box-wing OML volume constraint based on fuel storage requirements (nonlinear).		$Vol = Vol_t$
	Wing thickness	Minimum thickness constraints between each pair of FFD-volume control points (linear).		$t/t_0 \geq 0.5$
	Linear twist	Links the twist design variables of the blended transition segments (linear).		-
Constraints	**1117**			

Source: The author

a Reynolds number of 16.57×10^6, based on a MAC of 2.55 m. The optimization problem can be stated as:

$$
\begin{aligned}
\text{min} \quad & \mathcal{J}(\mathbf{v}, \mathbf{q}, \mathbf{b}^{(m)}) \\
\text{with respect to} \quad & \mathbf{v} \\
\text{subject to} \quad & \begin{cases} \mathcal{M}^{(i)}(\mathbf{v}, \mathbf{b}^{(i)}, \mathbf{b}^{(i-1)}) = 0, \quad i = 1, 2, ..., m \\ \mathcal{R}(\mathbf{v}, \mathbf{q}, \mathbf{b}^{(m)}) = 0 \\ \mathcal{C}_e(\mathbf{v}, \mathbf{q}, \mathbf{b}^{(m)}) = 0 \\ \mathcal{C}_i(\mathbf{v}, \mathbf{q}, \mathbf{b}^{(m)}) \geq 0 \end{cases}
\end{aligned}
\tag{5.1}
$$

where $\mathcal{J}$ is the objective function, computed by $C_D S$, where S is the nondimensional planform area of the box-wing, which cannot be changed during optimization, $\mathbf{v}$ are the design variables, $\mathbf{q}$ are the flow variables, $\mathbf{b}^{(m)}$ are the control points of the B-spline volume in which the grid is embedded, $\{\mathcal{M}^{(i)}\}_{i=1}^{m}$ are the mesh movement equations, which are solved for $\mathbf{b}^{(i)}$, i.e. the B-spline volume control points at the ith increment, $\mathcal{R}$ is the flow residual, and $\mathcal{C}_e$ and $\mathcal{C}_i$ are additional equality and inequality constraints, respectively, which can be either linear or nonlinear. A summary of the design variables and their bounds, as well as a list of the linear and nonlinear constraints for this preliminary aerodynamic shape optimization study of a box-wing aircraft is presented in Table 33.

The objective of the optimization is to minimize drag subject to lift and pitching moment constraints, in addition to some geometric constraints described below. Lift is constrained to be equal to the weight at the start of cruise, and the pitching moment about the center of gravity must be zero. The wing volume is constrained to ensure that sufficient fuel can be stored in the fore and aft wings. The wing volume constraint largely drives the wing thickness, so thickness constraints are active at several locations along the chord, and are relative to the initial value. Finally, a linear twist interpolation over each blended transition is imposed in order to prevent the optimizer from designing blended transitions with large curvature, avoiding interference effects with the main wings. Such an approach makes for flexible design spaces that are well-suited for exploratory shape optimization. As far as the minimization of drag is concerned, this approach allows to optimize the twist of all wing segments, improving the performance in terms of induced and wave drag, whereas the optimizer looks for a shock free design at the main design point.

5.4 Results and Discussions

5.4.1 Weight Estimation Studies

The structural weight estimation (wings metallic structures) has been assessed by means of the FEM-based procedures described in Section 5.2.1.1. The non-structural components and fuselage weights have been assessed through statistical methods, as described in (TORENBEEK, 2013), whereas the payload weight has been evaluated considering the maximum number of passengers (165 pax) and a standard weight of 100 kg assigned to each passenger. The main mass breakdown for the BW configuration is reported in Table 34, which is compared with the initial mass estimation of the aircraft. Note the masses of the BW structure are very close to each other with a maximum difference of about 15% for the vertical wing structures. This result is highly dependent on the type of connection between the three wing elements, which determine how the loads are transferred through the statically indeterminate structure. In this case, it was found that a fixed joint led to the lowest structural weight for the wing, which is consistent with previous analyzes of box-wing structures (JEMITOLA; FIELDING; STOCKING, 2012). Overall, the Operational Empty Weight increased about 2.35%, which increased the Fuel Mass for the nominal mission of about 2.68%. It is possible to conclude that the aircraft mass estimation introduced by **Paerom** provided appropriate results at conceptual design level.

5.4.2 Optimization Convergence History

A gradient-based formulation is used for the aerodynamic shape optimization algorithm to minimize the objective function. For tracking convergence, SNOPT provides a

Table 34 – Mass breakdown of the BW concept in kilograms.

Parameter	**BW (Faber)**	**BW (Paerom)**	Δ [%]
MTOW	80335.1	78978.8	+1.7
OEW	46067.2	44982.1	+2.3
Total Wing	10070.1	9990.4	+0.8
Fore wing	5204.8	5095.1	+2.1
Aft wing	4527.8	4495.6	+0.7
Tip fin	337.3	399.6	-15.5
Fuselage	8041.5	8247.8	-2.5
Vertical tail	752.1	746.0	+0.8
Landing gear	3155.5	3160.5	-0.1
Propulsion[1]	9002.1	8946.9	+0.7
Systems	11739.8	11646.9	+0.8
Operational items	2291.6	2273.4	+0.8
FM[2]	8104.2	7886.7	+2.7

[1] Includes bare engines, nacelles, and pylons.
[2] For nominal range plus diversion range (single-aisle category).

Source: The author

Figure 51 – BW concept: Optimization history. The merit function represents C_D.

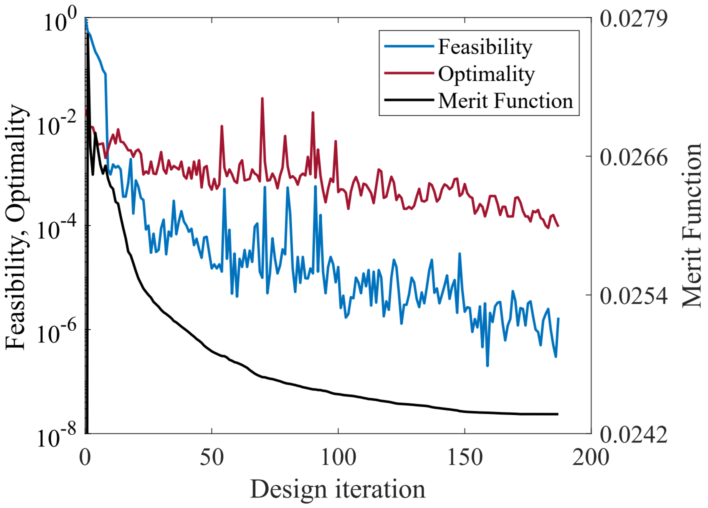

Source: The author

number of metrics: feasibility, optimality, and the merit function. The merit function is the objective when constraints are satisfied, whereas feasibility and optimality represent the constraint satisfaction and the gradient of the augmented objective function, respectively. The optimization convergence history for the Box-Wing optimization is shown in Fig. 51. After 187 iterations, the merit function is sufficiently converged to achieve engineering precision (asymptotic behavior), feasibility has been reduced to below 10^{-6}, and optimality has been reduced by at least two orders of magnitude. Deep convergence of optimality is preferable, although it is sometimes difficult to obtain in three-dimensional constrained optimization problems (OSUSKY *et al.*, 2015).

5.4.3 RANS-Based Aerodynamic Shape Optimization

This section describes the comparisons of aerodynamic characteristics between the baseline and optimized configurations under the cruise condition. For the baseline geometry, the selected airfoils are the NASA SC(2)-0412 (fore wing root), -0410 (fore wing crank and tip), -0410 (aft wing root to tip), and -0010 (vertical tip fin). These airfoils are characterized by a large leading-edge radius, and a reduced curvature over the middle region of the upper surface, which helps to delay the shock. The wing segments are initially untwisted and those intersecting the fuselage have angle of incidence equal to 1°. This provides a starting geometry for optimization and valid conceptual level estimates of various quantities. Fig. 52a shows the front views of the baseline and optimized geometries with shock surfaces highlighted in red. The shock surfaces over the upper surface of the fore wing have been mostly removed. A strong shock wave appearing close to the root of the baseline aft wing has also been largely eliminated following optimization. Likewise, Fig. 52b illustrates the surface pressure coefficient contours of the baseline and optimized configurations of the box-wing with L0 grid, clearly showing that the C_p lines are distributed more evenly in the optimized geometry. The baseline concept has an angle of attack of 3° at the initial cruise flight condition, where $C_L = 0.51$, and $C_D = 0.0269$. The optimized concept reached an angle of attack of 3°, $C_L = 0.51$, and $C_D = 0.0244$, meaning that the optimizer tends toward flying at the maximum angle of attack permitted. The reduction in the drag coefficient is over 10%.

The corresponding pressure coefficient distributions and section shapes of the fore wing and aft wing at various spanwise locations are given in Fig. 53a and Fig. 53b, respectively. For the baseline fore wing geometry, the sudden increase in pressure coefficient at about 50–60% of chord is due to the shock. However, the optimized section shapes greatly reduced shocks, demonstrating a reduction in wave drag. In this case, smooth pressure recoveries characterize the pressure coefficient distributions, which are beneficial for keeping attached boundary layers in viscous flow. In these results, the original volume is redistributed by thickening the wing sections near the root, which is typical for aerodynamic shape optimization problems where the minimum volume is a design constraint (CHAU; ZINGG, 2021). On the other hand, the baseline aft wing has weaker shocks than the fore wing. This is because the aft wing is more lightly loaded, i.e. has a lower C_L. Furthermore, its forward-swept wing shape and lower wing thickness-to-chord ratio distribution minimize structural weight and wave drag contribution. In this case, it can be seen that the optimizer has designed supercritical cambered airfoils with smoother pressure recoveries, especially along the trailing edge.

As far as the minimization of induced drag is concerned, acting on the twist distribution allows to modify the spanwise lift distribution to get it closer to the one of optimal solutions (DEMASI; MONEGATO; CAVALLARO, 2017). In this case, the fore

Figure 52 – Box-Wing configuration: Optimization results: $\alpha = 3.0°$, $C_L = 0.51$, $C_D = 0.0244$, $L/D = 20.9$.

(a) Shock surfaces for the baseline (left) and optimized (right) box-wing configuration.

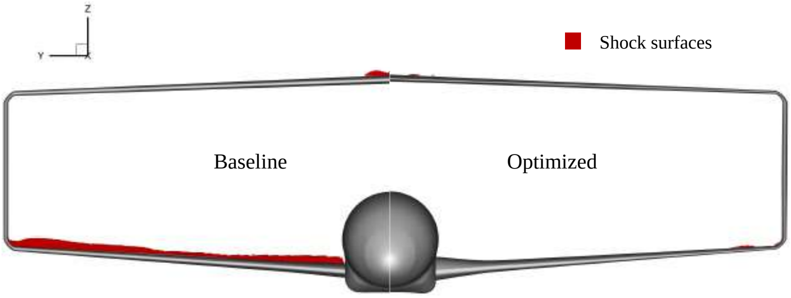

(b) Surface pressure coefficient contours for the baseline (left) and optimized (right) box-wing geometries (Top views of fore and aft wings. The red sphere represents the CG).

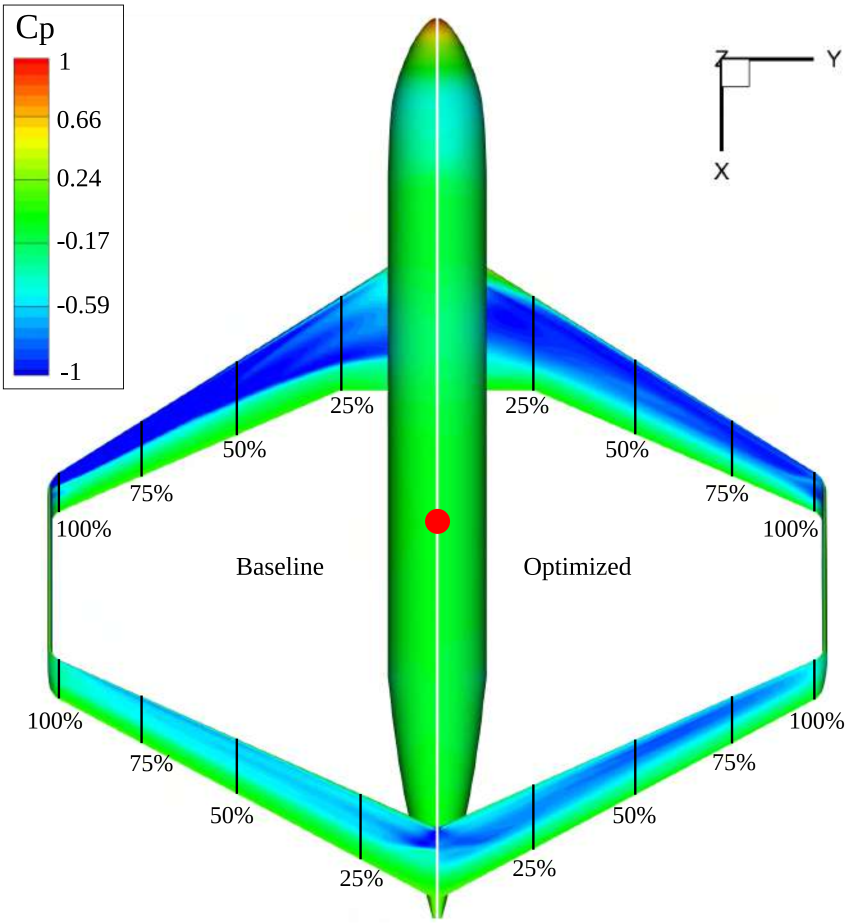

Source: The author

and aft wings are characterized by wash-out (i.e., decreasing the incidence angle from the wing root out to the wing tip) and wash-in (i.e., increasing the incidence angle from the root to the tip), respectively. The optimized results are consistent with those of past studies and with theoretical results, providing a reliable estimate of the performance of the BW aircraft (GAGNON; ZINGG, 2016a; CHAU; ZINGG, 2017). This suggest that the

Figure 53 – Pressure distributions on the baseline and optimized box-wing designs (fore and aft wings).

(a) Fore wing.

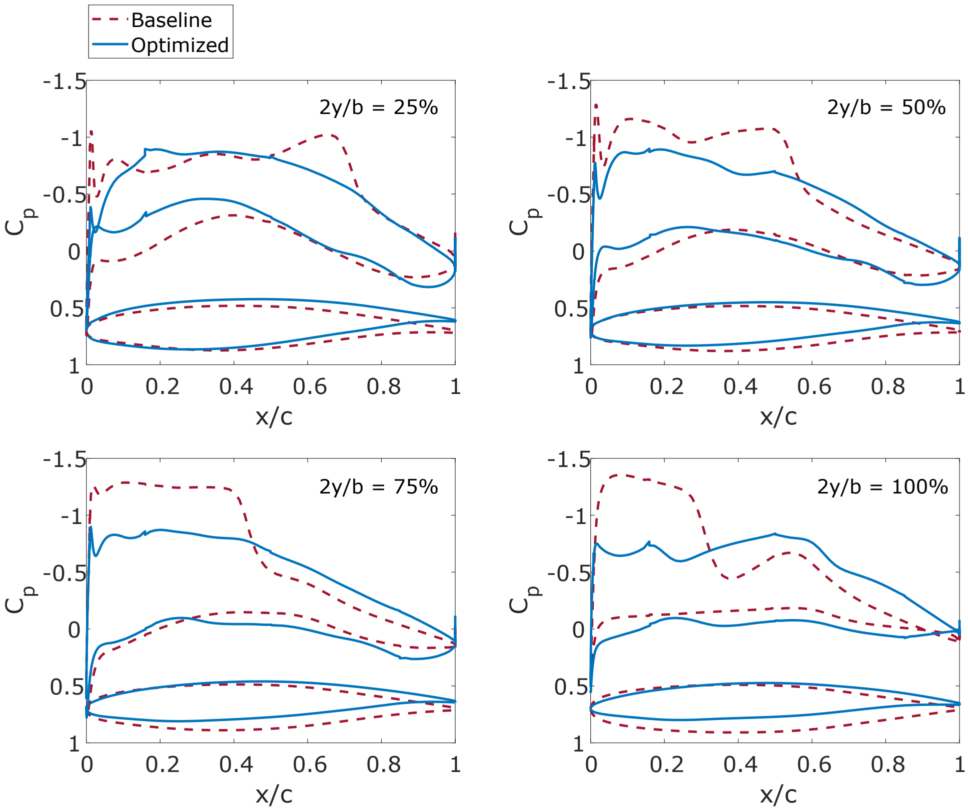

(b) Aft wing.

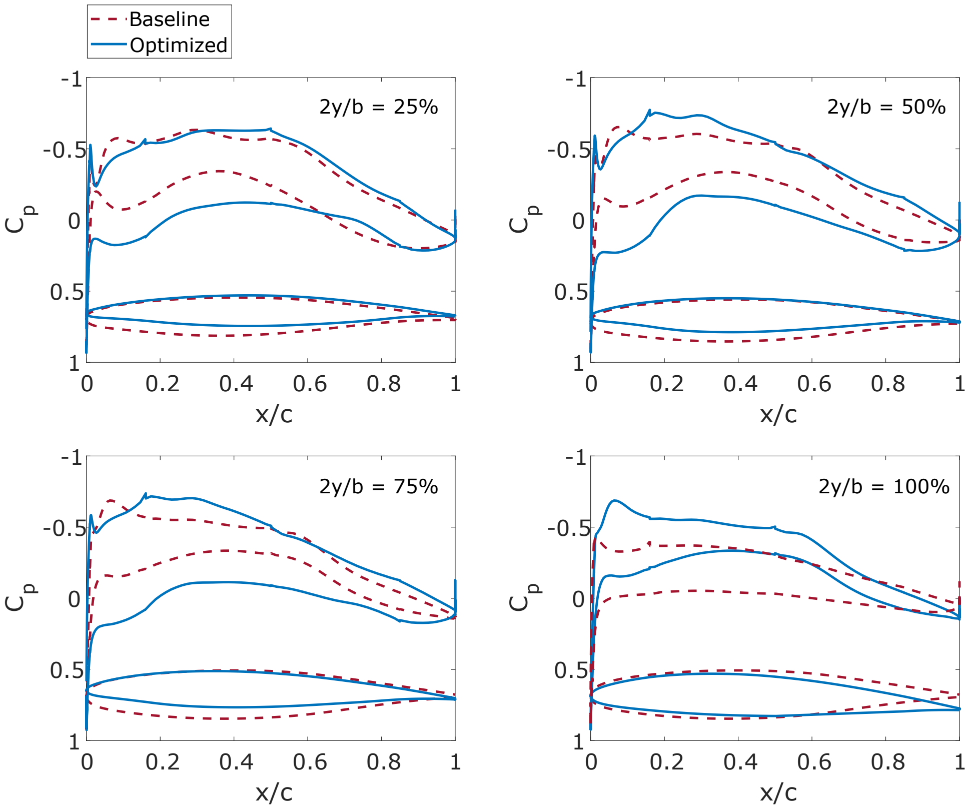

Source: The author

Figure 54 – Surface pressure coefficient contours for the baseline (left) and optimized (right) box-wing geometries (Lateral views of vertical wing).

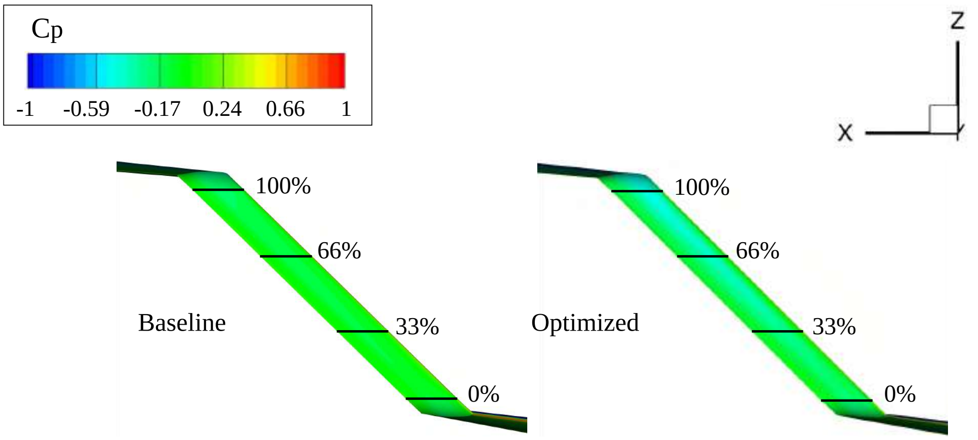

Source: The author

current methodology modify and optimize the twist of a box-wing aircraft and improve the performance in terms of induced and wave drag.

Figures 54 and 56 illustrate the surface pressure contours and pressure distributions, respectively, across the vertical wing. Note the baseline geometry presents an intense shock wave arise in the intersection with the blended transition of the fore wing ($x/h =\ 0\%$), which cause large areas of boundary layer separation. However, the optimizer handled this problem, and designed supercritical airfoils with a favorable pressure gradient that avoids premature separation on this region. The other sections of the vertical wing did not present a significant difference in the pressure distribution, despite their modification on the twist distribution that changed gradually from inboard to outboard from the bottom to the top of the vertical tip fin. This results in a wing design that is similar to those that can be found in the literature (SALEM *et al.*, 2021a; ANDREWS; PEREZ, 2018b), in which the side-force distribution over the vertical wing forms the signature closed-loop circulation pattern, as shown in Fig. 57. This result is also consistent with the incompressible Prandtl formula for the lift-induced drag of an elliptical wing, which has demonstrated very good agreement with the vortex-force-based definition of lift-induced drag, even in presence of shocks (PRANDTL, 1924; KROO, 2005; RUSSO; TOGNACCINI; DEMASI, 2020). This approach was used in the very initial stage of the aircraft design, which means that there is a solution of minimum induced drag for a fixed lift and height-to-span ratio before applying high-fidelity aerodynamic shape optimization.

Given that fully turbulent flow has been assumed and the box-wing area is highly constrained, the optimizer is not able to reduce the friction drag in this case, so the drag reduction on the BW concept is due to wave and induced drag reductions. Also visible in Fig. 57, the current optimization demonstrated the unique capability of the BW concept to redistribute its optimal lift distribution whereas trim and other constraints are satisfied. As a result, the condition of minimum induced drag of the box-wing configuration is valid

Figure 55 – A breakdown of the single-point optimized lifting forces computed on the L0 grid level.

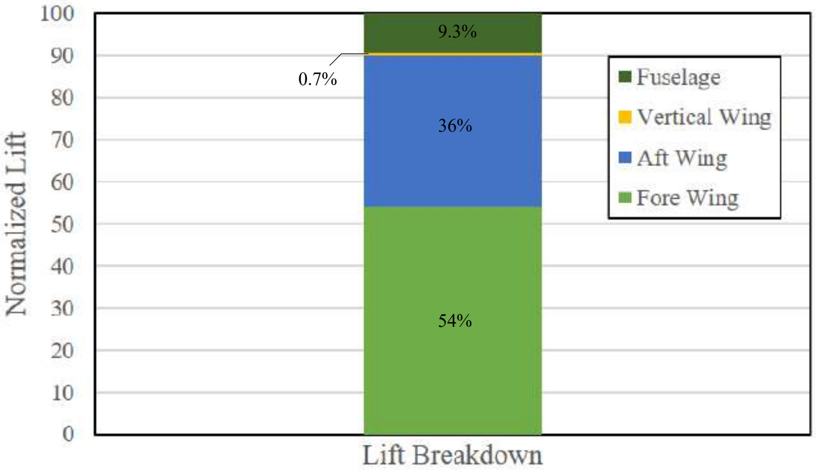

Source: The author

even though the lift on the fore and aft wings is different, and the lift across the vertical wings is distributed proportionally. Figure 55 presents the component breakdown of lift for the optimized BW concept. Note that the fore wing carries much more lift than the aft wing, as suggested by the optimized spanwise lift distributions.

Plane cuts of the normalized z-component of momentum are plotted one MAC length downstream of the baseline (Fig. 58a) and optimized (Fig. 58b) wing geometries. The figures clearly show that the optimized geometry reduced the strength and magnitude of the tip vortex. This result suggests that induced drag is minimized due to the smaller induced velocities.

5.4.4 Performance Studies

The flight simulation methods outlined in Chapter 3 were used to evaluate the mission performance of the BW configuration in terms of fuel burn. A standard nominal mission for the single-aisle medium range category was analyzed, in which the aircraft transports 160 passengers and 5 crew over a distance of 1852 km at a Mach number of 0.78, with a 805 km fuel reserve. Fuel weights are mostly computed using the fuel fractions method. For takeoff (including warm-up and taxi), climb, and landing, the fuel fractions were taken from historical data. For cruise and loiter segments, the fuel fractions are given by the Breguet-range equation. Results from high-fidelity optimization plus a 5% markup on the skin friction drag component to account for excrescence drag from the vertical tail, nacelles, and pylons, are used to compute the Breguet-range equation for the specified mission profile.

The overall mission performance estimates are reported in Table 35. The optimized BW concept reduced drag by about 10% in comparison with the baseline BW, which

Figure 56 – Pressure distributions on the baseline and optimized box-wing designs (vertical wing).

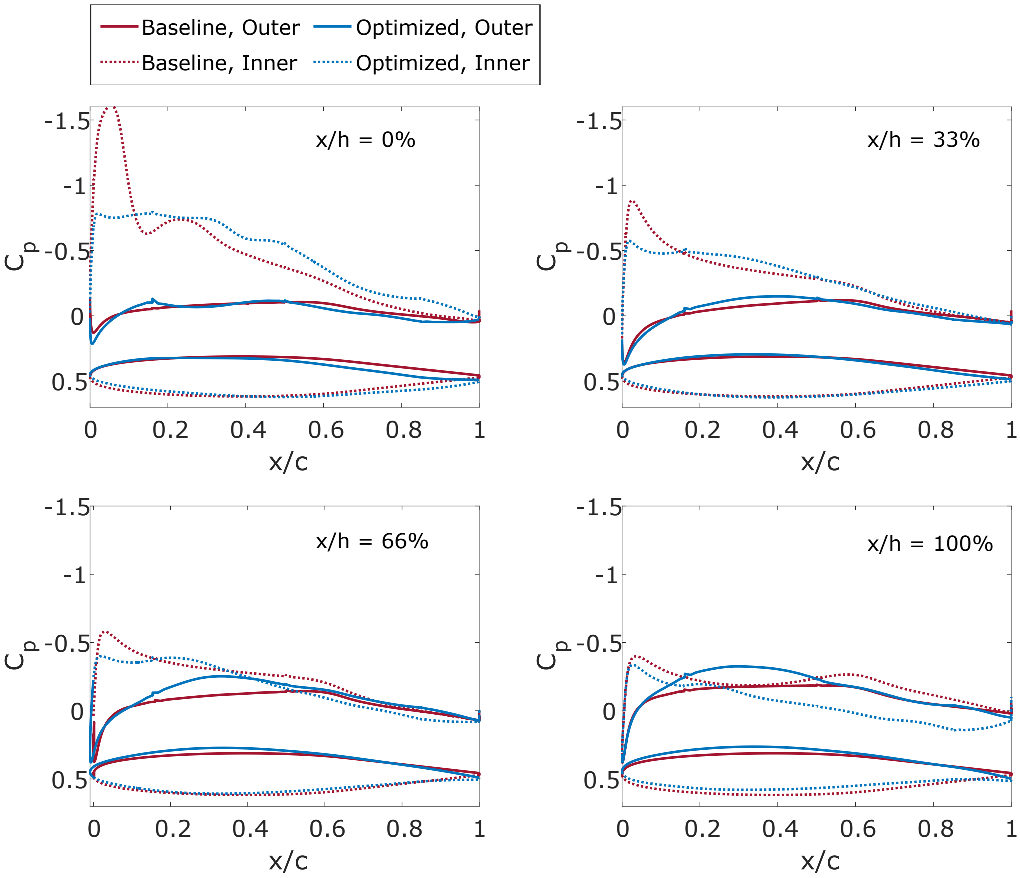

Source: The author

Table 35 – Aircraft performance comparison.

Parameter	CTW^{1,2}	BW^1 (Baseline)	BW^3 (Optimized)
L/D [-]	17.10	17.83	19.90
C_L [-]	0.59	0.51	0.51
C_D [-]	0.0344	0.0286	0.0256
Cruise Drag $[N]$	39634.8	38056.7	34064.7
Fuel Mass $[kg]$	8424.1	8287.5	7849.2

[1] Optimized using low-fidelity aerodynamics
[2] Aerodynamic data from CFD simulations.
[3] Optimized using high-fidelity aerodynamics.

Source: The author

reduced the fuel mass by about 5.3% for the specified mission profile. In contrast, a substantial drag reduction (about 14%) is obtained compared to the CTW aircraft. Note this conventional counterpart is not optimized from high-fidelity aerodynamics, but assuming that the wave drag contribution to pressure drag is similar to the one obtained for the BW concept, it can be concluded that the BW concept remains to be more fuel efficient than the CTW concept on the order of 8%.

Figure 57 – Optimized force coefficient distributions over the fore wing (left), the vertical tip wing (middle), and the aft wing (right).

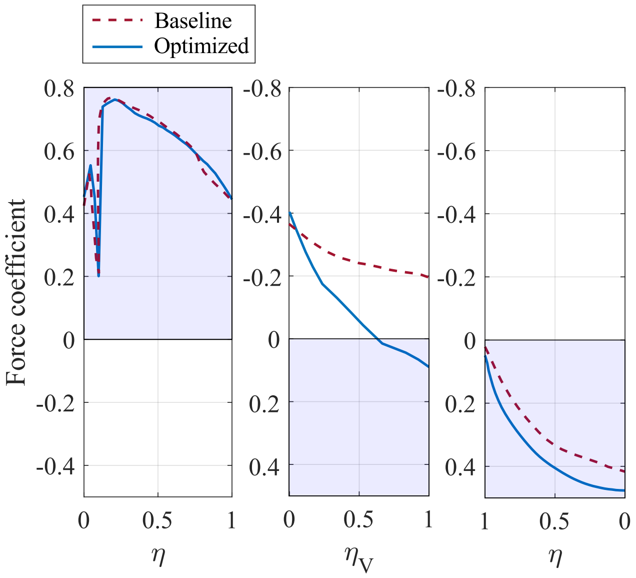

Source: The author

Figure 58 – Plane cuts of the vertical component of momentum taken at 1 root-chord length downstream of the baseline and optimized box-wing configurations.

(a) Baseline.

(b) Optimized.

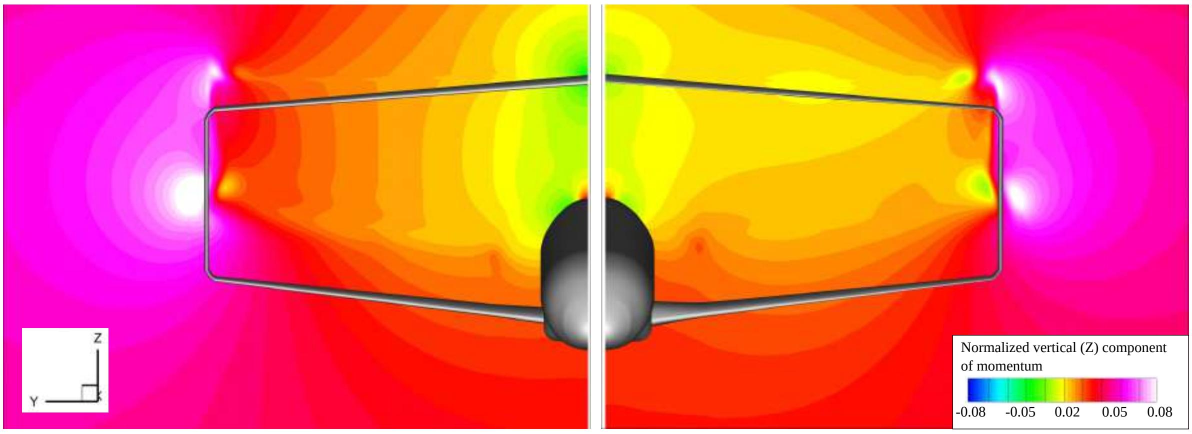

Source: The author

5.5 Concluding Remarks

The use of Computational Fluid Dynamics and numerical optimization has become prevalent in industry and academia for the analysis and design of unconventional aircraft. These methods were used in the present work to investigate the aerodynamic design and fuel burn performance of a box-wing aircraft in the single-aisle medium-range category. In particular, a RANS-based aerodynamic shape optimization framework was applied to minimize cruise drag, with respect to angle of attack, twist, and section shape variables. Results show that a box-wing aircraft can be designed for low cruise drag, while satisfying both constant lift and zero pitching moment constraints through an optimum twist distribution and the elimination of shocks.

With a height-to-span ratio of 0.244 and a stagger-to-span ratio of 0.7, the optimized box-wing aircraft was found to provide a 10.4% improvement in cruise lift-to-drag ratio over the baseline concept, indicating that the features of the lifting system enable benefits in terms of reduction in fuel consumption per passenger. Such results demonstrate the feasibility of high-fidelity modeling to quantify the benefits of a box-wing aircraft and address several issues identified during the conceptual design stage.

The amount of data and the experience during this research allowed to identify the most critical design parameters in transonic conditions and the potential strategies to improve the aerodynamic design of box-wing aircraft in cruise. To summarize, it is important to consider the twist distribution of the aft wing, in order to improve the lift distribution of a forward swept wing but also to avoid detrimental shock wave in the root region and the tip twist of the fore wing. These characteristics provide interesting trends and indicate that the further development of a box-wing configuration can be an important step in the improvement of next-generation transport aircraft.

5.6 Directions for Future Research

- To fully assess the performance of the box-wing concept and provide meaningful insights, this proof-of-concept must be presented in a multiple operating point optimization level. By investigating the cruise operating point in isolation, the impact of the box-wing configuration at other operating points such as take-off, climb and landing are ignored. Therefore, it is important to allow for realising optimum designs with better capabilities at varying conditions.

- For the case considered here, optimal aerodynamic design features were found but with permissive considerations toward structural integrity. Maintaining minimum thickness-to-chord ratios across each wing may help in producing more feasible structural designs.

- Only the box-wing system and fuselage geometries were part of the current high-fidelity aerodynamic shape optimization application. This geometry aided to account for wing-body flow interactions and to correct for the less efficient lift provided by the fuselage. However, the vertical tail contribution must be considered in the design space, because this aerodynamic surface dictates the lateral-directional stability behavior, as well as the structural feasibility of this unconventional aircraft. A single vertical tail solution reduces the empty weight and wetted area, but it can be prone to potential aeroelastic problems. In contrast, a twin vertical tail solution increases the structural weight, and can be prone to shock formation and separation, but it represents a solution to aeroelastic instabilities. The implementation of high-fidelity aerodynamic shape optimization to account for the vertical tail contribution remains to be an issue, since high-quality structured meshes for all the geometry components and intersections are required. Therefore, mesh generation and deformation approaches remains challenging for gradient-based aerodynamic shape optimization problems involving complex geometries with multiple components, such as the current box-wing with fuselage.

- Finally, due to the unique characteristics of the box-wing concept, an aerostructural optimization process shall be investigated using parametric geometry modeling as a first step, providing control on the aircraft surfaces of this closed wing-system. An aerostructural design takes into account both aerodynamic and structural coupling, and therefore involves iterative and successive reevaluation of both the aerodynamic loads and structural design to come up with a coupled design. This methodology represents an interesting opportunity to the progress of the box-wing concept, since there are still unknowns about structural weight, flutter, and the specific nonlinear structural response that necessitates an unique buckling treatment.

5.7 Dissemination

The following article has been published as a result of this chapter:

- BRAVO-MOSQUERA, P; CHAU, T; CATALANO, F; ZINGG, D. Exploration of Box-Wing Aircraft Concept Using High-Fidelity Aerodynamic Shape Optimization. **In: International Congress of the Aeronautical Sciencies (ICAS), Stockholm, Sweden**, 2022. (BRAVO-MOSQUERA *et al.*, 2022a).

6 THESIS CONCLUSIONS

The investigation covered in this thesis aimed to respond the following inquiries:

Which design variables and constraints allow to fully explore the potential of a given unconventional aircraft configuration in an optimization problem?

Which are the minimum fidelity levels required to design unconventional aircraft configurations and evaluate their performance?

Do all important design criteria and design variables have to be taken into account at once during optimization, or may a decoupled approach lead to the same findings at a reduced cost and complexity?

These concerns were the focus of several conceptual, numerical, and experimental investigations that were given in Chapters 2 to 5. Some of these studies were more theoretical, while others were more practical and concentrated on the design of a particular unconventional configuration that combines a box-wing layout with boundary layer ingestion propulsion engines, which served as a case study. I use this final chapter to summarize the key findings of these investigations and review major contributions. Furthermore, I identified numerous open issues and provide suggestions for further investigation.

6.1 A Review of Unconventional Configurations

A state-of-the-art literature review on the progress in unconventional aircraft towards the next-generation civil aviation is presented in Chapter 2. The aim of this review was to provide an objective account of the benefits and challenges of unconventional configurations from a design perspective. The references are divided into categories based on design and optimization methodologies, as well as performance comparisons between unconventional and conventional designs. Furthermore, benefits and drawbacks from older to more current design methods are presented and discussed.

Special attention was given to the flight altitude and the aerodynamic performance of each configuration over CTW aircraft. The comparisons suggest that unconventional configurations can provide energy savings due to their increased aerodynamic performance, which can be further improved through the application of disruptive technologies, or the combination of them. Moreover, this review pointed out the importance of expanding knowledge during the conceptual design of unconventional configurations, such as the requirement to fly at higher altitudes than CTW aircraft, which has structural, operational, and environmental penalties that must be carefully considered. That is the reason why, throughout the review presented in Chapter 2, special attention is given to the fidelity levels implemented in MDO formulations, which enable to address key complex aerodynamic design challenges of unconventional configurations.

Finally, the information contained in Chapter 2 can be used as a starting point for future projects on next-generation airliners. Aircraft designers recognize the importance of having rules of thumb during the initial conception of a new aircraft. This has always been a challenge when designing unconventional configurations, due to the little information available in the open literature, and the fact that no configuration has been certified by the aviation industry. For this reason, the integration of available data in a single report would aid to expedite the design process, ensuring that designers implement accurate information and appropriate objective functions and design constraints.

6.2 The Low-Fidelity Conceptual-Level MDO Tool

Conceptual design is an early phase of the design process and includes both design space exploration and evaluation of different design alternatives. This phase requires tools that are fast but accurate enough to evaluate different design alternatives and provide some initial estimations of system performance. In chapter 3, a conceptual-level MDO framework that was used to design and evaluate the BW concept is introduced.

This framework was used to define the main characteristics of the aircraft, such as its wingspan (32.2 m), height-to-span ratio (0.244), stagger-to-span ratio (0.7), among others, based on top-level requirements and user-defined parameters such as propulsion system type, configuration, and specific airframe elements. It features several analysis modules that help to estimate aircraft aerodynamics, weights, stability, and mission performance. After the initial sizing and sensitivity analyses, a single-objective optimization of the BW concept was performed to investigate the relationship between fuel burn per passenger-km as a function of aircraft size. The nominal range is 1852 km plus 805 km for reserve and the maximum number of passengers is set equal to 165. A Genetic Algorithm was used to perform the aircraft optimization. Design variables included wing geometric properties such as aspect ratio, height-to-span ratio, stagger-to-span ratio, among others, as well as performance characteristics such as initial cruise altitude, wing area, and maximum required thrust, while design constraints were set based on top-level requirements and operational characteristics such as the available wing fuel volume.

In this work, we confirmed that height-to-span ratio variable is important to reduce the induced drag. However, the performance of the current BW aircraft is comprised by the fact of considering the fuel to be stored in the wings. That is, if the fuel volume constraint is active in the optimization process, the thickness-to-chord ratio and wing area variables change in such a way that reduce the fuel consumption. This results in very thin wings with a large wing area, which increase the viscous drag as well as the empty weight. In contrast, if the fuel volume constraint is relaxed, the thickness-to-chord ratio of the wings remains constant, and the chord of a single main wing is divided in two to make a BW aircraft design of the same projected area. In this case, the resulting cross section available for fuel storage is divided in half, and a significant amount of fuel cannot be stored in the wings. The excess fuel could be stored in the fuselage, which would require considerable alterations to the cabin design, making certification more difficult. To verify that the method was correctly formulated and implemented, a verification study was performed by comparing the results to a CTW design. In this case, the BW concept presented an increase in OEW of rougly 4% due to the increased wing area. However, the cruise lift-to-drag ratio is 8% higher than the CTW due to the reduced induced drag. Thus, the BW aircraft has a 5.7% advantage over CTW aircraft in terms of total fuel consumed over the course of the mission. This research was complemented with high-fidelity aerodynamic shape optimization analyses to obtain more detailed information regarding the flow field of the box-wing aircraft and its performance, as shown in Chapter 5.

Finally, it should be noted that the efforts in developing box-wing concepts have received less attention in comparison to other concepts such as the Blended Wing Body or the Truss Braced Wing, as presented in Chapter 2. In fact, the PARSIFAL concept from Pisa University is the only ongoing project that has been funded in the last few years. This aircraft has been designed for different market sectors, which of course means different cruise ranges and design cruise altitudes for optimal mission performance. In general, this box-wing concept follows the ICAO “C” gate standard, i.e., wingspan lower than 36 m, which is a design constraint for an aircraft in the single-aisle category. However, due to its larger wing surface, this configuration can transport a greater number of passenger (similar to the twin-aisle long-range category) for the same mission range (around 4000 km), providing an optimistic reduction on the fuel burn per passenger metric relative to the conventional single-aisle concept. Despite such benefit, it is unclear how to effectively this concept can perform since there are still concerns about the aeroelastic behavior, the handling qualities, and the production costs in case this concept reaches subsequent design stages. It is then of paramount importance to choose appropriate design variables and constraints to realize the potential of the box-wing concept, avoiding unnecessary manufacturing challenges or impeding the convergence of the optimization problem.

6.3 Wind-tunnel Experimental Analysis of a Sub-scale prototype

Two experimental setups were employed to investigate the aerodynamic interaction of the box-wing layout with the propulsion system: one focusing on the effect of podded engines on the airframe, and one investigating boundary layer ingestion inlets. The experimental data were used to validate preliminary CFD studies, also presented in Chapter 3, which were in turn used to perform sensitivity studies and complement the low-fidelity design of the concept. The experimental study included force and electrical power measurements, flow mapping, and total pressure surveys.

The main results suggested that the BLI configuration enhances the propulsive efficiency by reducing both the electrical power coefficient and the kinetic energy waste due to lower jet velocities. Other benefits include reduced ram drag, lower structural weight, and less wetted area than the pylon-mounted engine configuration. However, the propulsion-airframe integration of BLI inlets introduces complicated aerodynamic interactions, causing high-levels of fan-face distortion that decrease engine performance and can lead to issues in the reliability of safe operation. Distortion further leads to additional vibration and noise; therefore, the optimum design of the airframe shape and the integration of distortion tolerant fan blades that adjust boundary-layer ingestion are key elements for improving inlet/engine compatibility. The experimental results also confirmed that the box-wing concept is attractive for security reasons. In particular, the concept has a favorable stall recovery, in which the downwash on the aft wing is alleviated, producing a soft stall, and inducing a nose-down pitching moment to restore the state of the aircraft.

Compared to a CTW concept, the combination of a box-wing layout with boundary layer ingestion inlets could reduce the fuel burn of about 12%. However, additional technological advances such as innovative materials and engine-core technologies expected to occur in the next 20 years, could yield to fuel burn savings close to 30% compared to a conventional configuration with 2020 technologies. Overall, this research highlights the importance of reducing wasted kinetic energy in the combined wake and jet flow, which leads to lower propulsive power, and whose benefits can be fully exploited if newer engine technologies are provided.

It should be noted that the experimental part of this thesis was conducted at lower Reynolds numbers and under subsonic conditions than those found in actual flight. The reader is therefore reminded that, even while Reynolds and Mach number effects will be taken into consideration to some extent during flight, the values of the performance coefficients will vary from a full-scale application. Thus, more detailed research into these flight conditions will provide a more accurate comparison of the different configurations.

6.4 Application of High-Fidelity Aerodynamic Shape Optimization

Since the introduction of Prandtl's "best wing system" in 1924, the particular layout of the BW concept, i.e., its closed nonplanar wing design, has allowed researchers to investigate its potential aerodynamic features using mainly low and medium fidelity tools by means of multidisciplinary approaches. Most of these investigations proved that an optimal distribution of total lift on the fore, aft, and vertical wings reduces induced drag by 40% compared to conventional cantilever wings. However, the application of high-fidelity aerodynamic shape optimization allowed to further understand different trade-offs on the design of the box-wing concept. Particularly, this is the first work that evaluates wing-body flow interactions and proper fuselage lift and drag through aerodynamic shape optimization based on the RANS equations. This method also allows to estimate the fuel-burn benefit of the concept at cruise condition, which can be applied to box-wing concepts of different categories.

A RANS-based approach has been implemented to minimize drag considering prescribed design variables and constraints. The box-wing was able to redistribute the total lift from one wing to the other, satisfying several design constraints, while simultaneously improving aerodynamic performance. It is worth mentioning that the optimizer designed supercritical cambered airfoils with very weak shocks, while introducing an optimal twist distribution that minimized induced drag. The drag of the optimized box-wing configuration is about 10% lower than the initial concept due to reduced wave drag from the removal of shocks, and reduced induced drag from an optimal spanwise lift distribution. The results presented in Chapter 5 demonstrate the potential aerodynamic advantages of the box-wing concept, and the importance of high-fidelity analysis and optimization tools towards the development and evaluation of novel configurations that can lead to reduced fuel burn and emissions.

Finally, the aircraft presented in this thesis is the subject of ongoing research on unconventional configurations for next-generation civil aviation. Subsequent works also include the evaluation of other objectives such as direct operating costs and appropriate environmental metrics. Trade-offs between those objectives would result in a different configuration to be compared with the current version towards expanding the possibilities for subsequent design phases.

Appendix

APPENDIX A – LITERATURE REVIEW PROTOCOL

First of all, we defined a set of "key-words", "search strings" and search limitations in order to classify each paper regarding the subjects under evaluation. Search strings were composed by combining key-words. Search limitations refer to the selection and rejection criteria. Once determined the aforementioned parameters, we selected the search sources for the review methodology, in this case, the ISI Web of Science database and Google scholar. The ISI Web of Science database includes peer reviewed papers from other databases (such as Scopus, AIAA and Wiley) that were published in indexed journals with a calculated impact factor in the JCR (Journal Citation Report). Google scholar aided to include "grey literature" such as reports arising from conferences and symposiums, as well as master's dissertations, Ph.D. theses, and technical reports. No limitation on year of publication was imposed on the database searches. The search criteria is provided in Fig. 59. In sum, the complete literature sample consisted of 203 journal articles, 88 conference papers, 36 technical reports, and 26 additional references (including thesis, books and websites). The search criteria is provided in Table 36.

Due to the great amount of bibliographic material on unconventional configurations, the second phase started by identifying the included and excluded reports. Selection and rejection criteria helped to identify the most relevant documents regarding the scope of the review. References suited for the review were retrieved as full papers for closer inspection of their introduction and conclusions.

A.0.1 Selection Criteria

- Reports describing design methodologies for developing unconventional configurations are included.
- Reports describing performance comparisons (in terms of fuel-burn benefits) between unconventional configurations and conventional aircraft are included.
- References of design and simulation tools used to create unconventional configurations are included.
- Literature reviews of related topics, such as state-of-the-art of Multidisciplinary Design Optimization (MDO) frameworks, Aerodynamic Shape Optimization, BWB configurations, non-planar wing configurations, distributed propulsion, electric aircraft, alternative fuels, noise prediction, evolutionary aircraft technologies, history and progress in aerodynamics are included.

Figure 59 – Synthesis of the state-of-the-art review.

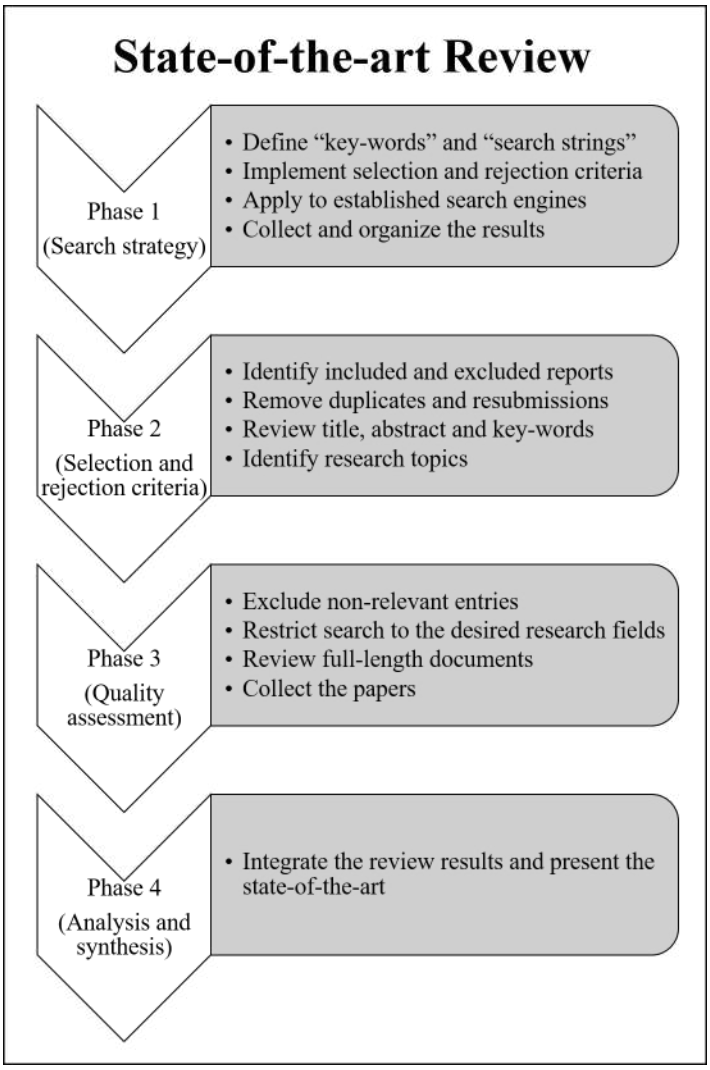

Source: The author

A.0.2 Exclusion Criteria

- Reports focused on aerodynamic, structural, stability, alternative fuels or aeroelasticity analysis without any reference to design of unconventional configurations are excluded.

- Reports focused on mathematical modeling of Multidisciplinary Design Optimization and Aerodynamic Shape Optimization frameworks without any reference to aircraft design are excluded.

- Reports focused on design processes for different aircraft categories such as military, commuter, agricultural, UAVs, etc, are excluded. However, some specific papers were included as literature promoting future implementations of unconventional configurations.

Table 36 – Search criteria applied for the revision process.

Objective	Review progress in unconventional aircraft for next-generation civil aviation, considering design, new aerodynamic technologies and optimization frameworks.
Key-Words	Blended Wing Body; Hybrid Wing Body; Box-wing; The prandtlplane; Truss-braced wing; Non-planar wings; Joined wings; Wingtip devices; Double Bubble D8; Open-rotor aircraft; Distributed propulsion; Non-conventional configurations; Future aircraft; Low-boom Supersonic jets; Electric aircraft; hybrid-electric transport aircraft; Alternative fuels; ACARE Vision 2020; ACARE FlightPath 2050; NASA N+2; NASA N+3; Direct Operational Cost; Aerodynamic drag reduction; Multidisciplinary Design Optimization; Aerodynamic Shape Optimization; Boundary layer ingestion; Green aviation; Sustainable aviation; fuel-burn reduction; High-fidelity codes; CFD; History of aviation; Progress in aerodynamics.
Search strings	Conceptual Design of BWB; Conceptual design of box-wing aircraft; Aerodynamic design of box-wing aircraft; fuel-burn reductions for future aircraft; Conceptual design of new aircraft concepts; Conceptual design of electric aircraft; Multidisciplinary design optimization of BWB; Multidisciplinary design optimization of truss-braced wing concepts; BWB and Boundary Layer Ingestion; Propulsion airframe integration of BLI concepts; Design of low-boom supersonic jets; Computational Fluid Dynamics for unconventional configurations; Aerodynamic Shape Optimization for future commercial airliners; Conceptual design of Double Bubble aircraft; Computational simulation for boundary layer ingestion; Distributed propulsion on BWB configurations; CFD-based for aircraft design; Review of BWB; Review of drag reduction technologies; Review of joined wing concepts; Review of electric/hybrid-electric aircraft; Progress in aerodynamic technologies.
Types of references	Quantitative, literature reviews of related topics, design and simulation.
Source engine	ISI Web of Science, Google Schoolar
Time span	Without restrictions

Source: The author

- Conference papers and thesis that were the basis for subsequent journal articles are excluded.

Once collected the main reports, a more in-depth review started by reading the full document. In this phase, we evaluated the quality of the chosen documents by adding some extra criteria which were appropriate for this review, for example:

- Did the study present an original configuration/unconventional analysis?
- Did the study accomplish a set of design requirements for next-generation airliners?
- Did the study present a benchmark for future works?
- Did the author(s) compare the results with those of others who have investigated a similar design approach?

APPENDIX B – MULTIDISCIPLINARY PROBLEM VARIABLES

Table 37 – Design variables and bounds for the BW conceptual-level MDO problems.

Variable	**Lower bound**	**Upper bound**	**Optimum values**
CTW configuration			
Aspect Ratio [-]	9	12	10.4
Wing sweep angle [DEG]	20°	30°	27°
Wing taper ratio [-]	0.2	0.6	0.25
Wing root thickness-to-chord ratio [-]	0.08	0.16	0.16
Wing tip thickness-to-chord ratio [-]	0.08	0.16	0.10
Wing area [m^2]	120	130	123.3
Maximum required thrust (per engine) [kN]	110	125	119.5
BW configuration			
Aspect Ratio [-]	5	8	5.92
Height-to-span ratio [-]	0.1	0.4	0.244
Stagger-to-span ratio [-]	0.5	1.5	0.70
Fore wing leading edge station[2] [-]	0.2	0.4	0.27
Fore wing taper ratio [-]	0.2	0.6	0.31
Aft wing taper ratio [-]	0.2	0.6	0.54
Fore wing root chord thickness-to-chord ratio [-]	0.08	0.16	0.12
Fore wing tip chord thickness-to-chord ratio [-]	0.08	0.16	0.10
Aft wing root chord thickness-to-chord ratio [-]	0.08	0.16	0.10
Aft wing tip chord thickness-to-chord ratio [-]	0.08	0.16	0.10
Nose gear axial location[1,2] [-]	0.05	0.15	0.10
Main gear axial location[1,2] [-]	0.5	0.7	0.61
Propulsion station[1,2,3] [-]	0.7	0.8	0.73/0.74
Initial cruise altitude [m]	11000	13000	12500
Wing area[4] [m^2]	120	180	174.9
Wing area ratio [-]	0.5	0.6	0.51
Maximum required thrust (per engine) [kN]	110	125	121.6

[1] Based on center of gravity limits between the fore and aft wings ($\Delta_{CG}/\bar{c}$).

[2] Normalized by fuselage length.

[3] For Non-BLI and BLI configurations.

[4] Portion inside the fuselage included.

Source: The author

APPENDIX C – MODULES IMPLEMENTED IN PAEROM

In this appendix, a detailed description of the modules implemented in **Paerom** is provided.

C.0.1 Inputs

- Top-level requirements: the design process begins with the definition of a set of top-level design requirements to create a balanced design. The objective here is to select design requirements that improve the aircraft performance in function of its mission. This section is based on traditional aircraft design methods where high-level design requirements must be defined, like the ones suggested by Raymer (2012) and Torenbeek (2013).
- Initial Geometry: This module includes geometric quantities related to the wing, fuselage, horizontal and vertical tails, nacelle and pylon, and propulsion systems, which are necessary for the disciplinary analyses that are described in the following sections.

C.0.2 Aerodynamic Module

This module uses low-fidelity methods for computing aerodynamic performance, which are inexpensive in terms of computational cost, making them attractive for Multidisciplinary Design Optimization (MDO) studies. The methods described below are capable of capturing dominate features related to parasitic drag (skin friction, interference, form, and excresence drag), induced drag, and wave drag.

- Profile Drag is calculated using the drag buildup method of Raymer (2012), which, for a given component, is given by:

$$C_{D_0} = \frac{C_f f_{\text{inter}} f_{\text{form}}\, f_{\text{excr}}\, S_{\text{wet}}}{S} \tag{C.1}$$

where C_f is the skin friction coefficient, f_{inter} is the interference drag factor, f_{form} is the form drag factor, f_{excr} is the excresence drag factor, S_{wet} is the wetted area, and S is the wing reference area. The skin friction coefficient is calculated using the Mach corrected Prandtl-Schlichting relation for turbulent flow:

$$C_f = \frac{0.455}{(\log_{10} Re)^{2.58}\,(1 + 0.144 M_\infty^2)^{0.65}} \tag{C.2}$$

where the Reynolds number is given by the following expression:

$$Re = \frac{\rho_\infty V_\infty l_\mathrm{c}}{\mu_\infty} \quad \text{or} \quad Re_\mathrm{cutoff} = 44.62 \left(\frac{l_\mathrm{c}}{k_\mathrm{cutoff}}\right)^{1.053} M_\infty^{1.16} \tag{C.3}$$

where l_c is the characteristic length (e.g. fuselage length, nacelle length, or mean aerodynamic chord), and $k_\mathrm{cutoff} = 1.33 \times 10^5$ for sheet metal. The interference drag factor (f_{inter}) is 1.0 for fuselage and cantilever wings, 1.03 for box-wings, 1.05 for vertical and horizontal tails, 1.2 for pylons, and 1.3 for nacelles. For wings, horizontal and vertical tails, and pylons, the form drag factor is given by:

$$f_\mathrm{form} = \left[1 + \frac{0.6}{(x/c)_{\mathrm{max}\,t/c}}\left(\frac{t}{c}\right) + 100\left(\frac{t}{c}\right)^4\right]\left[1.34 M_\infty^{0.18}\left(\cos\Lambda_{\mathrm{max}\,t/c}\right)^{0.28}\right] \tag{C.4}$$

where $(x/c)_{\mathrm{max}\,t/c}$ and $\Lambda_{\mathrm{max}\,t/c}$ is the location of and sweep angle at maximum thickness-to-chord ratio. For fuselages and nacelles, the form drag factor is given by:

$$f_\mathrm{form} = 1 + \frac{60}{FR^3} + \frac{FR}{400} \tag{C.5}$$

$$f_\mathrm{form} = 1 + \frac{0.35}{FR} \tag{C.6}$$

where FR is the fineness ratio for fuselages and nacelles, given by:

$$FR = \frac{l_\mathrm{c}}{d_\mathrm{max}} \tag{C.7}$$

$$FR = \frac{l_\mathrm{c} + d_\mathrm{inlet}}{\sqrt{d_\mathrm{max}^2 - 0.5\left(d_\mathrm{exit}^2 + 0.64 d_\mathrm{inlet}^2\right)}} \tag{C.8}$$

where d_max is the maximum diameter of the fuselage. With regard to excresence drag, which comes from leaks and protuberances, Raymer (2012) suggests a mark-up of 5% on the profile drag, namely:

$$f_{excr} = 0.05 \tag{C.9}$$

In addition to the drag contributions provided above, fuselage base drag is also included (TORENBEEK, 2013):

$$C_{D_\mathrm{base}} = 3.83\theta_\mathrm{upsweep}^{2.5}\left(\frac{\pi d_\mathrm{max}^2}{4}\right) \tag{C.10}$$

where θ_{upsweep} is the fuselage upsweep angle in radians. This angle is defined as the angle between the fuselage midline, and a line extending from the midpoints of the start and end of the fuselage tail section.

- Induced drag is calculated using a Vortex Lattice Method (VLM) algorithm, in which discrete vortices are positioned along the primary lifting surfaces, and are used to calculate transverse and vertical perturbations induced in the flow by the generation of lift. The lift distribution along the span, the C_p distribution, the wing circulation, the wake circulation, and other basic parameters are also determined.

  To apply the VLM code, it is necessary to discretize the finite wing into several panels, whose coordinates are distributed along the span and chord. To begin, $m+1$ point vortices are distributed based on a cosine spacing in the spanwise direction along the primary lifting surfaces. This function allows to determine the location of the start and end points of the vortices on the panels. The same function is used to calculate the control points, which are located at 3/4 chord and 1/2 of each panel.

  The induced velocities caused by the vortices on each of the panels can be calculated using the following expression:

$$\omega_i = \frac{\Gamma_i}{4\pi}[A(B-C)+D-E] \tag{C.11}$$

where the constants A, B, C, D, and E are used to calculate the circulation on each panel:

$$\begin{aligned}
A &= \frac{1}{(x_2-X)(y_1-Y)-(x_1-X)(y_2-Y)};\\
B &= \frac{(x_2-x_1)(x_1-X)+(y_2-y_1)(y_1-Y)}{\sqrt{(x_1-X)^2+(y_1-Y)^2}};\\
C &= \frac{(x_2-x_1)(x_2-X)+(y_2-y_1)(y_2-Y)}{\sqrt{(x_2-X)^2-(y_2-Y)^2}};\\
D &= \frac{1}{(y_1-Y)}\left[1-\frac{(x_1-X)}{\sqrt{(x_1-X)^2+(y_1-Y)^2}}\right];\\
E &= \frac{1}{(y_2-Y)}\left[1-\frac{(x_2-X)}{\sqrt{(x_2-X)^2+(y_2-Y)^2}}\right]
\end{aligned} \tag{C.12}$$

Once the circulation is determined, the lift of each panel can be easily determined by the following equation:

$$L_i = \rho V \Gamma_i \Delta y_i \tag{C.13}$$

where Δy_i is the span of each panel. The total lift of the wing system is approximated by the following sum:

$$L = \sum L_i = \sum \rho V \Gamma_i \Delta y_i \tag{C.14}$$

This is a reasonable approximation as long as the wing planform is designed based on practical values for wing loading, taper ratio, and aspect ratio. The induced drag can then be calculated through,

$$C_{D_i} = \frac{1}{V_\infty^2 S} \int \Gamma w_i \, \mathrm{d}s' \tag{C.15}$$

An advantage of this method is that it can handle any given spanwise lift distribution, which can be helpful in estimating the induced drag of unconventional wing systems. For a box-wing, the induced drag calculated with this assumption requires special treatment. In this case, the defined spanwise lift distribution represents that of an optimal biplane, which, according to Prandtl (1924) has an induced drag given by:

$$\frac{D_i^{\mathrm{bi}}}{D_i^{\mathrm{ctw}}} = 1.0 + \sigma \tag{C.16}$$

where D_i^{ctw} is the induced drag of a cantilever wing of the same span and lift:

$$\sigma = \frac{(1 - 0.66(h/b))}{(1.05 + 3.7(h/b))} \tag{C.17}$$

where h/b if the height-to-span ratio. Prandtl (1924) provides the relative induced drag for an optimal box-wing, namely,

$$\frac{D_i^{\mathrm{bw}}}{D_i^{\mathrm{ctw}}} = \frac{(1 + 0.45(h/b))}{(1.04 + 2.81(h/b))} \tag{C.18}$$

- Wave drag is calculated using the method of Malone and Mason (1995), in which the wave drag coefficient for a given wing strip is given by Lock's fourth power law:

$$C_{d_w} = 20 \left(M_\infty - M_{\mathrm{crit}}\right)^4 \tag{C.19}$$

if $M_\infty > M_{\mathrm{crit}}$, where M_{crit} is the critical Mach number. Taking the definition of drag divergence as $\mathrm{d}C_{d_w}/\,\mathrm{d}M|_{M=M_{DD}} = 0.1$, the critical Mach number is given by:

$$M_{\mathrm{crit}} = M_{DD} - \left(\frac{0.1}{80}\right)^{1/3} \tag{C.20}$$

The drag divergence Mach number, M_{DD} is calculated using the Korn equation corrected for swept wings (GUR; MASON; SCHETZ, 2010):

$$M_{DD} = \frac{f_{\text{Korn}}}{\cos\left(\Lambda_{0.50}\right)} - \frac{(t/c)}{\cos^2\left(\Lambda_{0.50}\right)} - \frac{C_l}{10\cos^3\left(\Lambda_{0.50}\right)} \tag{C.21}$$

where f_{Korn} is the Korn factor (equal to 0.95 for supercritical airfoils). The total wave drag is then given by summing the contributions across all wing strips, as follows:

$$C_{D_w} = \sum_{i=1}^{n} C_{d_{w_i}} \left(\frac{S_i}{S_{\text{ref}}}\right) \tag{C.22}$$

where S_i is the reference area of wing strip i.

C.0.3 Weight Module

The weight of the aircraft components is determined using empirical techniques that, when applied to components that are conventional, are sufficiently accurate. This includes specific modifications to take box-wing designs into consideration. These include the fuselage, wings, horizontal and vertical tail, propulsion, landing gear, systems, and operational items groups.

- Fuselage

$$W_{\text{f}} = k_{\text{f}} \sqrt{V_D \left(\frac{l_{\text{h}}}{b_{\text{f}} + h_{\text{f}}}\right)} S_{\text{wet}_\text{f}}^{1.2} \tag{C.23}$$

where $k_{\text{f}} = 0.021$, V_D is the design dive speed in EAS (knots), l_h is the horizontal tail arm, b_f and h_f are the maximum width and height of the fuselage, respectively, and S_{wet_f} is the wetted area of the fuselage with all excresences omitted. To this basic weight, 4% is added for rear fuselage mounted engines, 7% is added for fuselage-attached main landing gear, and 8% is added for pressurized cabins. For box-wing configurations, the fore and aft wings alleviate fuselage bending loads, resulting in a 7.5-10% reduction in fuselage structural weight (OLIVEIRO, 2015). In this case, a 7.5% discount is applied to the basic weight.

- Wings

$$W_W = W_{W_1} + W_{W_2} \tag{C.24}$$

where W_{W_1} and W_{W_2} are the primary and secondary wing weights, respectively. The primary wing weight is calculated by using an empirical wing mass estimation equation for the fore and aft wings of a medium range box-wing aircraft (JEMITOLA; MONTERZINO; FIELDING, 2013):

$$W_{W_1} = C_1 \left[\frac{bS}{\mathrm{Cos}\,\Lambda_{1/4}} \left(\frac{1+2\lambda}{3+3\lambda} \right) \left(\frac{(MTOW)(n)}{S} \right)^{0.3} \left(\frac{V_D}{\tau} \right)^{0.5} \right]^{0.9} \tag{C.25}$$

where b is the wingspan, λ is the taper ratio, n is the load factor, and τ is the maximum thickness-to-chord ratio. This equation is derived by computing the optimised minimum mass of the wing primary structure, based on the bending and torsional strengths. It represents a compromise between wing stiffness and lightness, based on the use of aluminium alloy construction. The equation also uses C_1 to account for different types of box-wing aircraft and layout details.

The weight of secondary items such as high lift devices and controls were estimated using statistical data (TORENBEEK, 2013). The weight of the flaps, slats, and spoilers are given by:

$$W_{\text{flaps}} = 100 \left(2.09 \times 10^{-2} \right) k_{\text{flaps}} \left(1 + \sqrt{\frac{\text{MTOW}}{0.225 \times 10^{6}}} \right) S_{\text{flaps}} \tag{C.26}$$

$$W_{\text{slats}} = 160 \left(2.09 \times 10^{-2} \right) \left(1 + 0.7 \sqrt{\frac{\text{MTOW}}{0.225 \times 10^{6}}} \right) S_{\text{slats}} \tag{C.27}$$

$$W_{\text{spoilers}} = 110 \left(2.09 \times 10^{-2} \right) S_{\text{spoilers}} \tag{C.28}$$

respectively, where W_{flaps}, W_{slats}, and W_{spoilers} are the projected areas of the flaps, slats, and spoilers in their nested positions, respectively, and k_{flaps} is a constant that depends on the type of flaps (e.g. 1.0 for single slotted flaps).

The weight of the ailerons is given by:

$$W_{\text{ailerons}} = 125 \left(2.09 \times 10^{-2} \right) \left[1 + 0.5 \left(\frac{\text{MTOW}}{0.225 \times 10^{6}} \right)^{0.25} \right] S_{\text{ailerons}} \tag{C.29}$$

where S_{ailerons} is the projected area of the ailerons.

The weights of the structures required to maintain fixed leading and trailing edge shapes against surface pressure are respectively given by:

$$W_{\text{fle}} = 75 \left(2.09 \times 10^{-2} \right) k_{\text{fle}} \left(1 + \sqrt{\frac{\text{MTOW}}{0.225 \times 10^{6}}} \right) S_{\text{fle}} \tag{C.30}$$

$$W_{\text{fte}} = \left(2.09 \times 10^{-2}\right) \left[60 \left(1 + 1.6\sqrt{\frac{\text{MTOW}}{0.225 \times 10^{6}}}\right) + \Delta\right] S_{\text{fte}} \tag{C.31}$$

where W_{fle} and W_{fte} are the projected areas of the leading and trailing edge sections, respectively (which are assumed to extend from the leading edge to the fore spar, and from the aft spar to the trailing edge, respectively), $k_{\text{fle}} = 1.4$ or 1.0 for wings with and without leading edge devices, respectively, and $\Delta = 0$ for single slotted flaps.

The weight of the ribs is given by:

$$W_{\text{rib}} = k_{\text{rib}} \rho_{\text{matl}} g S \left(t_{\text{ref}} + \frac{t_r + t_t}{2}\right) \tag{C.32}$$

where $k_{\text{rib}} = 0.5 \times 10^{-3}$, ρ_{matl} is the material density, g is the gravitational acceleration, $t_{\text{ref}} = 3.28$ ft, and t_r and t_t are the maximum thickness at the wing root and tip, respectively. Lastly, the weight penalty associated with non-optimum structures is given by:

$$W_{\text{NO}} = \rho_{\text{matl}}\, g S \left(1 + 2\left(\frac{t}{c}\right)_{\text{avg}}\right) \delta_{\text{NO}} \tag{C.33}$$

where $(t/c)_{\text{avg}}$ is the average thickness-to-chord ratio and $\delta_{\text{NO}} = 3.28 \times 10^{-3}$ ft is the nonoptimum extra thickness. Once each contribution has been computed, the secondary weight of the wing system is given by:

$$W_{\text{w}_2} = W_{\text{flaps}} + W_{\text{slats}} + W_{\text{spoilers}} + W_{\text{ailerons}} + W_{\text{fle}} + W_{\text{fte}} + W_{\text{rib}} + W_{\text{NO}} \tag{C.34}$$

Horizontal and Vertical Tail

$$W_{\text{h}} = k_{\text{h}} \left[2 + 4.15\,\text{erf}\left(\frac{S_{\text{h}}^{0.2} V_D}{10^3 \sqrt{\cos\left(\Lambda_{\text{h}}\right)}} - 0.65\right)\right] S_{\text{h}} \tag{C.35}$$

$$W_{\text{v}} = k_{\text{v}} \left[2 + 4.15\,\text{erf}\left(\frac{S_{\text{v}}^{0.2} V_D}{10^3 \sqrt{\cos\left(\Lambda_{\text{v}}\right)}} - 0.65\right)\right] S_{\text{v}} \tag{C.36}$$

where $erf(x)$ is the error function, S_h and S_v are the reference areas of the horizontal and vertical tails, respectively, and λ_h and λ_v are the sweep angles at 50% chord of the horizontal and vertical tails, respectively. For the horizontal tail, $k_h = 1.0$ for a fixed stabilizer. For the vertical tail, $k_v = 1.0$ for a horizontal tail mounted to the fuselage, and $k_v = 1 + 0.15(S_h h_h / S_v b_v)$ for a horizontal tail mounted to the vertical tail; h_h is the vertical distance between the roots of the horizontal and vertical tails, and b_v is the span of the vertical tail.

- Propulsion

$$W_{\text{propulsion}} = W_{\text{engines}} + W_{\text{nacpyl}} + W_{\text{ec}} + W_{\text{oilsys}} + W_{\text{fuelsys}} + W_{\text{reversers}} \tag{C.37}$$

The weight of the propulsion group consists of the weight of the dry engines, nacelles and pylons, engine controls, oil systems, fuel systems, and thrust reversers:

$$W_{\text{engines}} = N_{\text{e}} W_{\text{e}} \tag{C.38}$$

$$W_{\text{nacpyl}} = 0.055 T_{\text{max}} \tag{C.39}$$

$$W_{\text{ec}} = 36 N_{\text{e}} (\text{TSFC}) T_{\text{max}} \tag{C.40}$$

$$W_{\text{oilsys}} = 0.01 N_{\text{e}} W_{\text{e}} \tag{C.41}$$

$$W_{\text{fuelsys}} = 80 \left(N_{\text{e}} + N_{\text{tanks}} - 1 \right) + 15 \sqrt{N_{\text{tanks}}}\, V_{\text{tanks}}^{0.333} \tag{C.42}$$

$$W_{\text{reversers}} = 0.18 N_{\text{e}} W_{\text{e}}$$

(C.43)

where N_e is the number of engines, W_{ec} and T_{max} are the dry weight and maximum takeoff thrust of each engine, respectively, TSFC is the thrust specific fuel consumption, N_{tanks} is the number of fuel tanks, and V_{tanks} is the total fuel capacity in US gallons.

- Landing gear

$$W_{\text{lg}} = k_{\text{lg}} \left(80 + 0.26 \text{MTOW}^{0.75} + 0.019 \text{MTOW} + 3.5 \times 10^{-5} \text{MTOW}^{1.5} \right) \tag{C.44}$$

where $k_{lg} = 1.0$ or 1.08 for low and high wing configurations, respectively. This equation is largely a function of the maximum takeoff weight since it must be sized for heat dissipation requirements during an aborted takeoff, as well as maximum landing loads.

- Systems

$$W_{\text{systems}} = W_{\text{sc}} + W_{\text{APU}} + W_{\text{ieg}} + W_{\text{hydpneu}} + W_{\text{electrical}} + W_{\text{pressurization}} + W_{\text{furnishings}} \tag{C.45}$$

The weight of the systems group is calculated using the statistical correlations of Torenbeek (2013) and comprises contributions from the flight control systems, auxiliary power unit (APU), avionics (instruments, navigational equipment, and electronics), hydraulic and pneumatic systems, electrical systems, pressurization systems (air conditioning, oxygen, and deicing systems), and furnishings, as shown below:

$$W_{\text{sc}} = k_{\text{sc}}\text{MTOW}^{0.667} \tag{C.46}$$

$$W_{\text{APU}} = 32(1.1\text{PAX})^{0.6} \tag{C.47}$$

$$W_{\text{ieg}} = k_{\text{ieg}}\,\text{MEW}^{0.556}R_{\text{max}}^{0.25} \tag{C.48}$$

$$W_{\text{hydpneu}} = 0.011\text{MEW} + 400 \tag{C.49}$$

$$W_{\text{electrical}} = 9.72\ \text{V}_{\text{cabin}}^{0.7}\left(1 - 0.018\ \text{V}_{\text{cabin}}^{0.35}\right) \tag{C.50}$$

$$W_{\text{pressurization}} = 6.75L_{\text{cabin}}^{1.28} \tag{C.51}$$

$$W_{\text{furnishings}} = 0.211\text{MZFW}^{0.91} \tag{C.52}$$

where $k_{\text{sc}} = 2.14$ for powered controls and with slats, flaps, and spoilers included, $k_{\text{ieg}} = 0.575$, R_{max} is the maximum range in nautical miles, V_{cabin} and L_{cabin} are the cabin volume and length, respectively, and MEW and MZFW are the maximum empty weight and maximum zero fuel weight, respectively. The weight of the APU is based on an assumed bleed airflow requirement of 1.1 lb/min per PAX, where PAX is the maximum number of passengers.

- Operational Items

$$W_{\text{operational}} = W_{\text{consumables}} + W_{\text{safety}} + W_{\text{baggage}} + W_{\text{crew}} \tag{C.53}$$

The weight of the operational items group includes the weight of consumables, safety equipment, baggage containers, and crew with provisions:

$$W_{\text{consumables}} = 19\text{PAX}, \text{ for single-aisle aircraft} \tag{C.54}$$

$$W_{\text{safety}} = 7.5\text{PAX}, \text{ for single-aisle aircraft} \tag{C.55}$$

$$W_{\text{baggage}} = 1.6 \text{ V}_{\text{cargo}} \tag{C.56}$$

$$W_{\text{crew}} = 205 N_{\text{crew}} \tag{C.57}$$

where V_{cargo} is the cargo volume, and N_{crew} is the number of crew members.

C.0.4 Propulsion Module

The propulsion system is sized using rubber engine model for conventional installation (GUR *et al.*, 2011). This analytic approach provides a means for adjusting the propulsion system weight, nacelle drag, and rate of fuel consumption according to the maximum thrust parameter, T_{max} (sea-level, static). The dry engine weight, maximum length, and diameter of the propulsion system are recalculated from:

$$W_{\text{e}} = W_{\text{ref}} \left(\frac{T_{\text{max}}}{T_{\text{ref}}} \right) \tag{C.58}$$

$$l_{\text{nacelle}} = l_{\text{ref}} \sqrt{\frac{T_{\text{max}}}{T_{\text{ref}}}} \tag{C.59}$$

$$d_{\text{nacelle}} = d_{\text{ref}} \sqrt{\frac{T_{\text{max}}}{T_{\text{ref}}}} \tag{C.60}$$

where W_{ref}, l_{ref} , and d_{ref} are the dry engine weight, the maximum length, and the maximum diameter of the reference engine. The thrust specific fuel consumption is also recalculated, and is given by:

$$\text{TSFC}_{\text{SLS}} = k_1 T_{\text{max}}^2 - k_2 T_{\text{max}} + k_3 \tag{C.61}$$

$$\text{TSFC}_{\text{cr}} = (\text{TSFC}_{\text{SLS}} + 0.4021\text{M}_{\infty}) \left(\frac{\text{OAT}_{\text{cr}}}{\text{OAT}_{\text{SL}}} \right)^{0.4707} \tag{C.62}$$

where $k_1 = 2.472 \times 10^{-11}$, $k_2 = 4.851 \times 10^{-6}$, $k_3 = 0.5175$, and OAT is the operating air temperature. These equations are recalibrated to meet the reference $TSFC_{cr}$ at the reference maximum thrust, cruise Mach number, and initial cruise altitude through a constant shift in $TSFC_{SLS}$. The thrust available at a given Mach number and altitude can also be calculated, and is given by:

$$T_{\text{avail}} = T_{\max}\left[k_4 + k_5\left(k_6 - M_\infty\right)^{k_7}\right]\left(\frac{\rho}{\rho_{\text{SL}}}\right)^{k_8} \tag{C.63}$$

where $k_4 = 0.60685$, $k_5 = 0.5344216$, $k_6 = 0.9001142$, $k_7 = 2.7981$, and $k_8 = 0.8851778$.

The performance assessment of the BLI propulsion system is estimated based on Goldberg *et al.* (2017). Similar to a conventional propulsion system, the net thrust should counterbalance the aircraft drag in steady level flight. However, the control volume is defined to begin slightly ahead of the inlet at the interface point. Therefore, the net propulsive force may be defined as follows:

$$\text{NPF} = F_{G9} - F_{Gi} - \tau_w S_{\text{wet}} - D_{\text{nacelle}} = D_{\text{aircraft ,clean}} \tag{C.64}$$

where F_{G9} is the gross thrust, F_{Gi} is the momentum drag, $\tau_w S_{wet}$ is the skin friction of the surface from the interface point to the inlet, D_{nacelle} is the drag of the nacelle, and $D_{\text{aircraft,clean}}$ is the drag of the aircraft without the propulsion system. The difference between F_{G9} and F_{Gi} is analogous to the net thrust term used in conventional propulsion. Following this net propulsive force formulation, performance of a BLI propulsion system may be estimated in a similar manner to that of a conventional installation.

The boundary layer thickness for turbulent flows can be calculated as a function of the Reynolds number by:

$$\frac{\delta}{x} = \frac{0.382}{Re_x^{1/5}} \tag{C.65}$$

For turbulent flows, the boundary layer profile behave as the well known $1/7^{\text{th}}$ power law relation:

$$u(y) = u_\infty\left(\frac{y}{\delta}\right)^{1/7} \tag{C.66}$$

The flow average boundary layer velocity at the inlet can be calculated by integration of the velocity profile along the thickness, resulting in:

$$\bar{u} = \frac{7}{8}u_\infty\left(\frac{y}{\delta}\right)^{1/7} \tag{C.67}$$

The nacelle height can be higher than the boundary layer thickness ($h/\delta > 1$, where h is the height of the ingested streamtube, and δ is the fuselage boundary layer thickness), then the propulsor also ingest part of the free stream flow:

$$\bar{u} = -\frac{1}{8}u_\infty \left(\frac{1}{\frac{h}{\delta}} + 1 \right) \tag{C.68}$$

Lastly, the situation at the fan face in the presence of asymmetric BLI is designed according to Budziszewski and Friedrichs (2018). The extent of the low velocity region is determined by the boundary layer thickness (δ), computed for the substitution model, and the fan radius (r_{fan}), as follows:

$$A_{\text{dis}} = \frac{r_{\text{fan}}^2}{2} \cdot \left[\varepsilon \cdot \frac{\pi}{180^\circ} - \sin(\varepsilon) \right] \tag{C.69}$$

$$\varepsilon = 2 \cdot \arccos \left(1 - \frac{\delta}{r_{\text{fan}}} \right) \tag{C.70}$$

where A_{dis} is the distorted sector and ε is the angle of the distorted sector. Thus, it is possible to calculate the wetted area of an integrated engine, as follows:

$$A_{\text{wet, int}} = 2 \cdot \pi \cdot r_{\text{eng}} \cdot z \cdot \left(1 - \frac{\lambda}{360^\circ} \right) \tag{C.71}$$

where r_{eng} is the radius of the engine, z is the length of the engine, and λ is the angle which describes the embedded part of an engine, calculated by:

$$\lambda = 2 \cdot \arccos \left(1 - \frac{h}{r_{\text{eng}}} \right) \tag{C.72}$$

where h is the depth of embedment. The drag of the embedded engines can therefore be estimated with:

$$D_{\text{eng,int}} = \frac{A_{\text{wet,int}}}{A_{\text{wet}}} \cdot D_{\text{eng}} \tag{C.73}$$

where A_{wet} is the wetted area of a conventional aeroengine, and D_{eng} is the contribution of conventional to the total drag of an aircraft.

C.0.5 Center of Gravity Module

The center of gravity location affects trim drag and longitudinal static stability, and are calculated based on empirical relationships provided by Torenbeek (2013). For simplicity, the analysis of the fully loaded aircraft (MTOW) with its respective position of the gravity center is shown in Table 38.

Table 38 – Weight and balance analysis for fully loaded aircraft.

Group	**Description of center of gravity**
Fuselage	Located at 42% or 47% fuselage length for engines mounted to the wing and at the rear of the fuselage, respectively.
Wings	Located at 30% mean aerodynamic chord. For box-wings, the center of gravity is calculated for each wing, and a weighted average is considered.
Horizontal tail	Located at 30% chord and 35% semispan.
Vertical tail	Located at 30% chord and 35% semispan.
Propulsion system	Located at 50% nacelle length. The moment does not include the weight of the fuel systems.
Landing gear	Located at 50% fuselage length.
Flight control systems	Located at 100% mean aerodynamic chord. For box-wings, the center of gravity is calculated for each wing, and a weighted average is considered.
Auxiliary Power Unit	Located at 75% fuselage tail length.
Avionics	Located at 40% fuselage nose length.
Hydraulic and pneumatic systems	75% of the center of gravity is located at the wing center of gravity, and 25% is located at the horizontal and vertical tail center of gravity. This partitioning is considered to be 90% and 10% for a box-wings.
Electrical systems	75% of the center of gravity is located at 50% fuselage length, and 25% is located at the propulsion system center of gravity.
Furnishing	Located at 51% fuselage length.
Pressurization systems	Located at 100% fuselage nose length.
Consumables	Located at 51% fuselage length.
Safety equipment	Located at 51% fuselage length.
Baggage	Located at 51% fuselage length.
Crew	Flight crew is located at 45% fuselage nose length. Flight attendants located at 51% fuselage length.
Fuel systems	Calculated based on the distribution of fuel tank capacity.
Fuel	Calculated based on the distribution of fuel tank capacity, i.e., fuel consumption is assumed to be uniform across all fuel tanks, weighted by their volumes.
Payload	Located at 51% fuselage length.

Source: The author

C.0.6 Stability Module

- Longitudinal Stability: the static margin at the start and end of each cruise segment is calculated to ensure that the transport aircraft satisfies longitudinal static stability requirements for a significant portion of the mission profile. The static margin is given by:

$$K_{\mathrm{n}} = \tilde{x}_{\mathrm{n}} - \tilde{x}_{\mathrm{cg}} = -\frac{\partial C_M/\partial \alpha}{\partial C_L/\partial \alpha} \tag{C.74}$$

where $\tilde{x}_{\mathrm{n}} = x_n/\bar{c}$ and $\tilde{x}_{\mathrm{cg}} = x_{cg}/\bar{c}$ are the nondimensional neutral point and center of gravity, respectively. The stability derivatives are defined as follows:

$$\frac{\partial C_L}{\partial \alpha} = \frac{\partial C_{L_{\mathrm{wb}}}}{\partial \alpha}\left(1 - \frac{d\varepsilon_{\mathrm{w}}}{d\alpha}\right)\frac{S_{\mathrm{w}}}{S}\eta_{\mathrm{w}} + \frac{\partial C_{L_{\mathrm{h}}}}{\partial \alpha}\left(1 - \frac{d\varepsilon_{\mathrm{h}}}{d\alpha}\right)\frac{S_{\mathrm{h}}}{S}\eta_{\mathrm{h}} \tag{C.75}$$

$$\frac{\partial C_M}{\partial \alpha} = (\tilde{x}_{\mathrm{cg}} - \tilde{x}_{\mathrm{acwb}})\frac{\partial C_{L_{\mathrm{wb}}}}{\partial \alpha}\left(1 - \frac{d\varepsilon_{\mathrm{w}}}{d\alpha}\right)\frac{S_{\mathrm{w}}}{S}\eta_{\mathrm{w}} + \left(\tilde{x}_{\mathrm{cg}} - \tilde{x}_{\mathrm{ac_h}} - \frac{l_{\mathrm{h}}}{\bar{c}}\right)\frac{\partial C_{L_{\mathrm{h}}}}{\partial \alpha}\left(1 - \frac{d\varepsilon_{\mathrm{h}}}{d\alpha}\right)\frac{S_{\mathrm{h}}}{S}\eta_{\mathrm{h}} \tag{C.76}$$

where $\tilde{x}_{\mathrm{ac}}$ is the nondimensional aerodynamic center, $d\varepsilon/d\alpha$ is the downwash gradient, and η is the tail efficiency factor, representing the interference effect between the wing and tail. According to Torenbeek (2013), the downwash gradient can be approximated as:

$$\frac{d\varepsilon}{d\alpha} = 4.44\left[K_{Æ}K_{\lambda}K_{R}\sqrt{\cos\left(\Lambda_{c/4}\right)}\right]^{1.19} \tag{C.77}$$

where $K_{Æ}$, K_{λ}, and K_R are referred to the fore wing and are calculated as follows:

$$K_{Æ} = \frac{1}{Æ} - \frac{1}{1 + Æ^{1.7}} \tag{C.78}$$

$$K_{\lambda} = \frac{10 - 3\lambda}{7} \tag{C.79}$$

$$K_R = \frac{1 - h_R/b}{(2l_R/b)^{1/3}} \tag{C.80}$$

where h_R is the vertical distance between fore wing root chord and aft wing mean geometric chord, and l_R is the longitudinal distance between the points located at 1/4 of the mean aerodynamic chords of the two wings. As suggested by Torenbeek (2013), the downwash gradient is reduced by 10% for engines mounted to the rear of the fuselage.

For the wing, the airfoil efficiency factor is set to 0.95, while for the horizontal tail, a value of 0.85, 0.9, or 1 is considered for a horizontal tail mounted to the fuselage, a horizontal tail mounted to the vertical tail, and a T-tail, respectively. In the case of a box wing, the fore and aft wings are treated as the main wing and horizontal tail, respectively. For the aerodynamic derivatives, **Paerom** uses the DATCOM method, which estimates the lift-curve slope as:

$$\frac{\partial C_L}{\partial \alpha} = \frac{2\pi Æ}{2 + \sqrt{4 + \frac{Æ^2\beta^2}{\eta^2}\left(1 + \frac{\tan^2(\Lambda_{\max t/c})}{\beta^2}\right)}} \tag{C.81}$$

where $\beta = \sqrt{1 - M_{\infty}^2}$, and η is the airfoil efficiency factor (0.95). From this, Torenbeek (2013) provides the following equation for the lift-curve slope of the wing-body:

$$\frac{\partial C_{L_{\mathrm{wb}}}}{\partial \alpha} = k_{\mathrm{wb}} \left(\frac{\partial C_{L_{\mathrm{w}}}}{\partial \alpha} \right) \tag{C.82}$$

where k_{wb} is the wing-body interference factor, given by:

$$k_{\mathrm{wb}} = 1 - 0.25 \left(\frac{d_B}{b} \right)^2 + 0.025 \left(\frac{d_B}{b} \right) \tag{C.83}$$

where d_B is the fuselage diameter.

- Lateral-Directional Stability: the directional stability and the dihedral effect were evaluated at off-design condition based on the formulation proposed by Cipolla, Salem and Bachi (2019). The aircraft is directionally stable if the derivative of yawing moment coefficient with respect to the side-slip angle ($C_{n\beta}$) is positive. In contrast, to have a stable rolling mode, the aircraft's derivative of the rolling moment with respect to the side-slip angle ($C_{l\beta}$) must be negative. According to this approach, the sideslip angle derivative of lateral force for a single vertical surface on the plane of symmetry is given by:

$$C_{y\beta_V} = -kC_{L\alpha_V} \left(1 + \frac{d\sigma}{d\beta} \right) \eta_V \frac{S_V}{S} \tag{C.84}$$

where k is an empirical factor depending on vertical surface span and fuselage geometry $(1.0 \leq\ k\ lgeq\ 2.2)$, $C_{L\alpha_V}$ is the vertical surface lift coefficient, S_V is the area of the vertical surface, and $\eta_V(1 + d\sigma/s\beta)$ is the sidewash parameter by dynamic pressure ratio at the vertical surface, which can be estimated by:

$$\eta_V \left(1 + \frac{d\sigma}{d\beta} \right) = 0.724 + 3.06 \left(\frac{S_V S_W}{1 + cos\Lambda_{(c/4)}} \right) + 0.4 \frac{Z_W}{d_F} + 0.009 \text{Æ}_W \tag{C.85}$$

where Z_W is the parallel distance to axis 'z' measured from 25% chord and fuselage centerline, d_F is the maximum fuselage diameter. The β-derivatives of yaw moment and roll moment can be calculated after evaluating $C_{y\beta_V}$ and the position of its aerodynamic centre:

$$C_{n\beta}\big|_v = -\ C_{y\beta}\big|_v \left(\frac{z_v \sin\alpha + l_v \cos\alpha}{b} \right) \tag{C.86}$$

$$C_{l\beta}\big|_v = C_{y\beta}\big|_v \left(\frac{z_v \cos\alpha - l_v \sin\alpha}{b} \right) \tag{C.87}$$

where z_v and l_v identify the position of the vertical tail aerodynamic center from the aircraft center of gravity. The dihedral effect can be calculated through the following equation:

$$\begin{aligned} C_{l\beta_{FB}} =& 57.3 \left\{ C_L \left[\left(\frac{C_{l_\beta}}{C_L} \right)_{\Lambda_{c/2}} K_{M_\Lambda} K_B + \left(\frac{C_{l_\beta}}{C_L} \right)_{\text{Æ}} \right] \right. \\ & + \Gamma \left(\frac{C_{l_\beta}}{\Gamma} K_{M_\Gamma} + \frac{\Delta C_{l_\beta}}{\Gamma} \right) + \left(\Delta C_{l_\beta} \right)_{Z_F} \\ & \left. + \theta \tan \Lambda_{c/4} \left(\frac{\Delta C_{l_\beta}}{\theta \tan \Lambda_{c/4}} \right) \right\} \end{aligned} \tag{C.88}$$

where Γ is the wing geometric dihedral angle, θ is the wing twist between root and tip sections of the wing, $(C_{l_\beta}/C_L)_{\Lambda_{c/2}}$ is the wing sweep contribution depending on λ, Æ, $\Lambda_{c/2}$, K_{M_Λ} is the compressibility correction sweep depending on M, $\Lambda_{c/2}$, K_B is a fuselage correction factor depending on Æ, $\Lambda_{c/2}$, $(C_{l_\beta}/C_L)_{\text{Æ}}$ is the aspect ratio contribution depending on Æ, λ, C_{l_β}/Γ is the wing dihedral effect depending on , Æ, $\Lambda_{c/2}$, K_{M_Γ} is the compressibility correction to dihedral depending on Æ, M, $\Lambda_{c/2}$, $\Delta C_{l_\beta}/\Gamma$ and $\Delta C_{l_\beta Z_F}$ are body induced effects on the wing height depending on fuselage geometry, and $\Delta C_{l_\beta}/\theta \tan \Lambda_{c/4}$ is a wing twist correction factor depending on Æ. From the standpoint of the assessment of flight mechanic requirements, in this case dihedral effect and stability margin are well estimated. In contrast, the directional stability is significantly overestimated.

C.0.7 Performance Module

The conventional methodology for estimation of fuel weight is the application of fuel weight fractions. In this case, the fuel consumption estimations are based either on statistical data or on analytical calculations, depending on the flight segment. For takeoff (including warmup and taxi) and landing, the spreadsheet methods described by Raymer (2012) were used:

$$F_{\text{to}} = 0.995 \tag{C.89}$$

$$F_{\text{l}} = 0.998 \tag{C.90}$$

The fuel consumption during climb is calculated by:

$$F_c = 1 - 0.013 \left(\frac{ICA}{30000} \right) \tag{C.91}$$

where ICA is the initial cruise altitude. In this case, the aircraft climbs at a maximum calibrated airspeed (CAS) of 250 knots from a specified initial climb altitude until 10000 ft.

The aircraft then accelerates at 270 knots CAS until the cruise Mach number is reached, and performs a constant Mach number climb until the initial cruise altitude is reached.

The Breguet equation is used to estimate the required fuel for the loiter and cruise segments:

$$R = E \cdot V = \int_{W_{i+1}}^{W_i} \frac{V}{c_t} \frac{L}{D} \frac{dW}{W} \tag{C.92}$$

where R and E are the cruise range and loiter endurance respectively, V is the respective flight velocity and c_t is the specific fuel consumption, whereas W_i refers to the weight of the aircraft at the end of the mission segment i. The fuel fraction for the descent segment is also determined by the Breguet range equation, and a reduction in cruise range for the cruise segment calculation is not needed (TORENBEEK, 2013). Once the fuel fractions have been determined, the total fuel burn for a given mission profile is given by:

$$W_{\text{fuel}} = \frac{1 - \Pi_i F_i}{\Pi_i F_i} (\text{OEM} + \text{DPLM}) \tag{C.93}$$

where i is the segment index, OEM is the operational empty mass, and DPLM is the design payload mass. The OEM is calculated as follows:

$$\begin{aligned} \text{OEM} =& 1.01 \left(W_f + W_W + W_h + W_v + W_{propulsion} + W_{lg} + W_{systems} \right) \\ & + W_{operational} \ + \ 0.05\text{FM} \end{aligned} \tag{C.94}$$

where FM is the fuel mass, which is calculated for a given design mission and accounts a 6% for trapped fuel. The sum of the fuel mass, the operational empty mass, and the design payload mass results in the takeoff weight.

C.0.8 Optimization Module

The sizing and optimization of transport aircraft is performed by ‘*optimoptions*’ (mode ‘*ga*’) from Matlab coded environment. The Matlab Genetic Algorithm (GA) toolbox allows the retention of existing modelling and simulation tools for building objective functions, allowing the user to make direct comparisons between genetic methods and traditional procedures.

The main concept of GA is to mimic the natural selection and the survival of the fittest (WHITLEY, 1994). The algorithm begins by initializing a population of solution, then, the GA can combine the components of a solution that are required to create a globally optimal solution by repeatedly using genetic operators, such as selection, crossover, and mutation. In this project, a real-coded GA was implemented as recommended by (CHUANG; CHEN; HWANG, 2015). The real-coded GA selection seems particularly natural when optimization problems with variables in continuous search spaces are tackled (CHUANG; CHEN; HWANG, 2016).

C.0.8.1 Data structures

Matlab supports only one type of data, which is a rectangular matrix of real or complex numeric elements. The main data structures in the GA toolbox are chromosomes, phenotypes, fitness functions, and objective function. The chromosome structure stores an entire population in a single matrix of size $N_{ind} \times L_{ind}$, where N_{ind} is the number of individuals and L_{ind} is the length of the chromosome structure. Phenotypes are stored in a matrix of dimensions $N_{ind} \times N_{var}$, where N_{var} is the number of decision variables. The fitness functions are stored in a vector of length (N_{ind}), and an $N_{ind} \times N_{obj}$ matrix stores the objective function values, where N_{obj} is the number of objectives. Note that each row of these data structures corresponds to a particular individual.

C.0.8.2 Toolbox structure

The GA toolbox uses matrix functions to create a set of routines for implementing a wide range of GA methods. In this section, the major procedures of the GA Toolbox are outlined:

- The first step is to define a population. The function '$PopulationSize$' specifies how many individuals there are in each generation. Real-valued populations can be initialised using ('$crtrp$').

- The ranking selection ('$fitscalingprop$') scales the raw scores based on the rank of each individual. This proportional scaling makes the scaled value of an individual proportional to its raw fitness score. Subsequently, uniform selection ('$selectionuniform$') chooses parents using the expectations and number of parents, which is fast to estimate, and preserves the best chromosomes for the subsequent evolution.

- The crossover routines recombine pairs of individuals with given probability to produce offspring. To support real-valued chromosome representations, a Direction-Based crossover (DBX) operator is provided. The method uses the fitness information of the paired parents ('$pop\_crossover$'). In this case, the crossover probability range from 0 to 1.0, which is generally set at higher value as in the range 0.7 to 1.0. The variable-wise crossover probability (theoretical range: 0 to 1.0) is generally set at higher value like in the range 0.7 to 1.0. The directional probability is generally set in the range 0.5 to 1.0, and the multiplying factor is generally set in the range 0.5 to 2.5.

- The Dynamic Random Mutation (DRM) was adopted to enhance population diversity (‘$mutationadaptfeasible$’), which aids to prevent population convergence to a suboptimal solution. It randomly generates directions that are adaptive with respect to the last successful or unsuccessful generation. As a result of this variability, the search technique provides a higher probability to elude local traps. The mutation probability is set between 0 and 1.0, and the second operator is a random disruption vector in n-dimensional cube that range from 0 to 1.0.

C.0.9 Validation

The conceptual design tool was validated by comparing the aircraft characteristics of the Airbus A320neo against a reference CTW aircraft designed with the framework, which follows the geometric characteristics of the actual A320neo (A320. . . , 2005). Table 39 shows the main results including the design weight errors.

Table 39 – Validation of conceptual-level design tool.

Parameter	**Airbus 320neo**	**CTW**	**error [%]**
MTOW [kg]	77400	77067.4	0.43
MZFW [kg]	62800	62450.8	0.55
OEW [kg]	44315.9	44251.1	0.14
MFW [kg]	20554.3	20332.9	1.07

Source: The author

APPENDIX D – TEST MATRIX FOR THE INTI AIRCRAFT EXPERIMENTS

This appendix shows the test matrix implemented in the experimental campaign.

Figure 60 – Test matrix of force measurements.

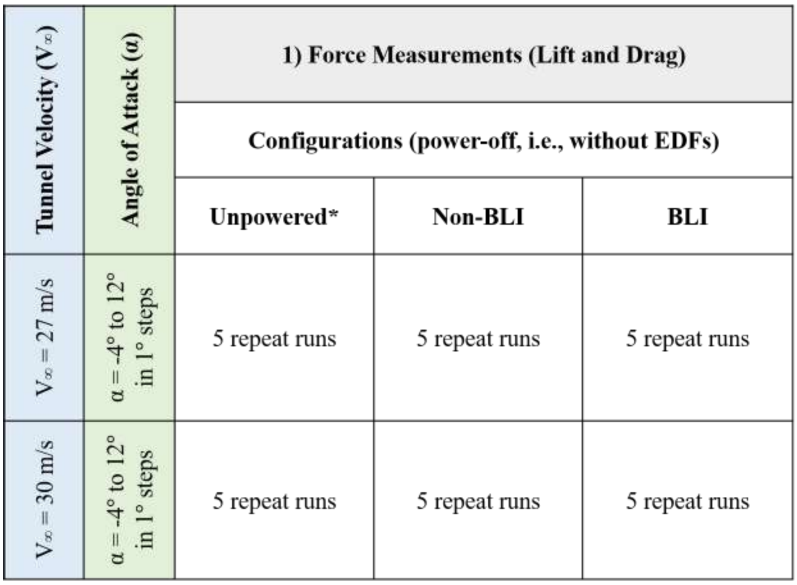

Tunnel Velocity (V∞)	Angle of Attack (α)	1) Force Measurements (Lift and Drag)		
		Configurations (power-off, i.e., without EDFs)		
		Unpowered*	Non-BLI	BLI
V∞ = 27 m/s	α = -4° to 12° in 1° steps	5 repeat runs	5 repeat runs	5 repeat runs
V∞ = 30 m/s	α = -4° to 12° in 1° steps	5 repeat runs	5 repeat runs	5 repeat runs

* Validation using CFD

Source: The author

Figure 61 – Test matrix of electrical power measurements.

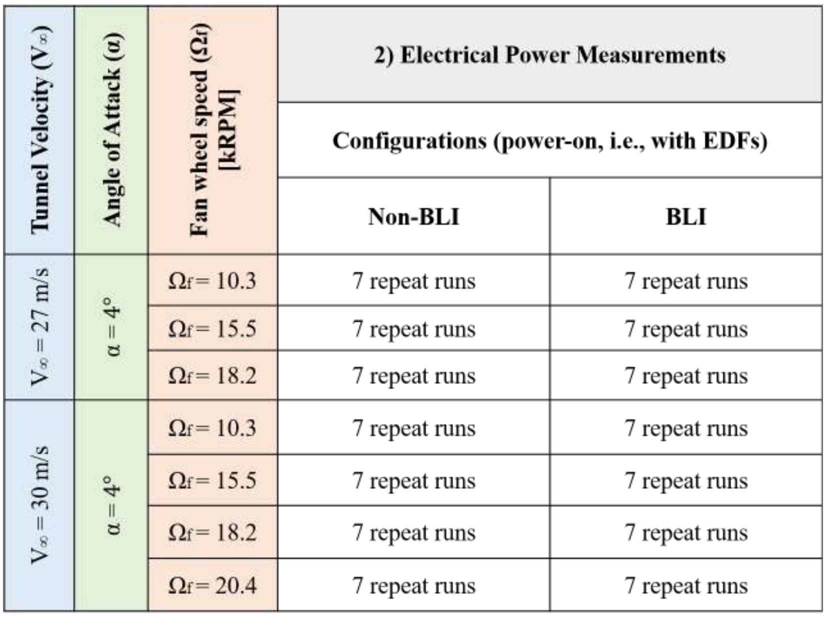

Tunnel Velocity (V∞)	Angle of Attack (α)	Fan wheel speed (Ω_f) [kRPM]	2) Electrical Power Measurements	
			Configurations (power-on, i.e., with EDFs)	
			Non-BLI	BLI
V∞ = 27 m/s	α = 4°	$\Omega_f = 10.3$	7 repeat runs	7 repeat runs
		$\Omega_f = 15.5$	7 repeat runs	7 repeat runs
		$\Omega_f = 18.2$	7 repeat runs	7 repeat runs
V∞ = 30 m/s	α = 4°	$\Omega_f = 10.3$	7 repeat runs	7 repeat runs
		$\Omega_f = 15.5$	7 repeat runs	7 repeat runs
		$\Omega_f = 18.2$	7 repeat runs	7 repeat runs
		$\Omega_f = 20.4$	7 repeat runs	7 repeat runs

Source: The author

Figure 62 – Test matrix of flow field measurements.

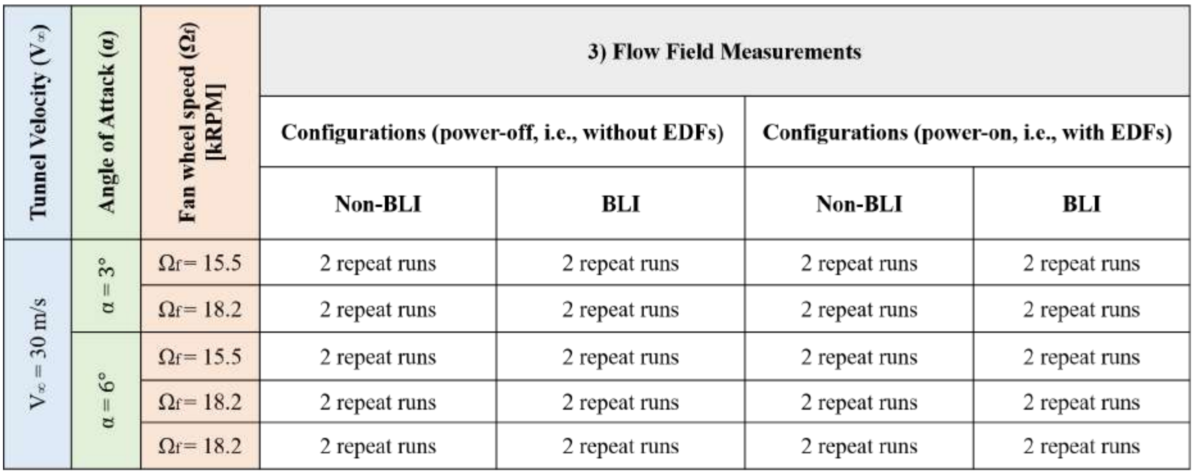

Tunnel Velocity (V_∞)	Angle of Attack (α)	Fan wheel speed (Ω_f) [kRPM]	3) Flow Field Measurements			
			Configurations (power-off, i.e., without EDFs)		Configurations (power-on, i.e., with EDFs)	
			Non-BLI	BLI	Non-BLI	BLI
$V_\infty = 30$ m/s	$\alpha = 3°$	$\Omega_f = 15.5$	2 repeat runs	2 repeat runs	2 repeat runs	2 repeat runs
		$\Omega_f = 18.2$	2 repeat runs	2 repeat runs	2 repeat runs	2 repeat runs
	$\alpha = 6°$	$\Omega_f = 15.5$	2 repeat runs	2 repeat runs	2 repeat runs	2 repeat runs
		$\Omega_f = 18.2$	2 repeat runs	2 repeat runs	2 repeat runs	2 repeat runs
		$\Omega_f = 18.2$	2 repeat runs	2 repeat runs	2 repeat runs	2 repeat runs

Source: The author

Figure 63 – Test matrix of inlet pressure distortion measurements.

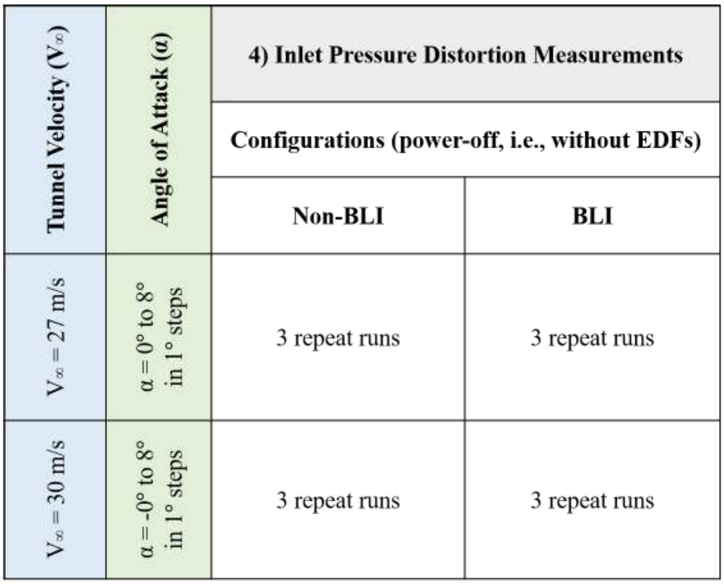

Tunnel Velocity (V_∞)	Angle of Attack (α)	4) Inlet Pressure Distortion Measurements	
		Configurations (power-off, i.e., without EDFs)	
		Non-BLI	BLI
$V_\infty = 27$ m/s	$\alpha = 0°$ to $8°$ in 1° steps	3 repeat runs	3 repeat runs
$V_\infty = 30$ m/s	$\alpha = -0°$ to $8°$ in 1° steps	3 repeat runs	3 repeat runs

Source: The author

APPENDIX E – CALIBRATION OF PITCH-STRUT SYSTEM AND ELECTRIC DUCTED FAN CONTROL

E.0.1 Pitch-Strut System Calibration

The calibration technique for determining the angle-of-attack of the wind-tunnel model using the pitch-strut system is described in this appendix. Figure 64 shows the BLI configuration in the wind tunnel section, highlighting the pitch-strut system. Basically, a first-order polynomial equation determined the relation between the motor's total amount of steps and the model's angle of attack (Fig. 65). Note the motor needed around four complete turns from a reference point to move the model one degree. From the linear equation shown in Fig. 65, the next step was to create a code that allows to activate the motor by repeatedly moving the threaded bar until the desired angle of attack is attained, as well as return information on the modifications performed. In this way, the models were tested for several angles of attack, ranging from −4° to 12° with angle variations of 1°. After every run, the pitch-strut system returned the model to its initial position.

E.0.2 Electronic Circuit for EDF's Control

The electronic circuit shown in Fig. 66 was assembled to control the brushless motor's speed. The potentiometer is connected to the Arduino so that its output channel

Figure 64 – BLI configuration installed in LAE-1 wind-tunnel.

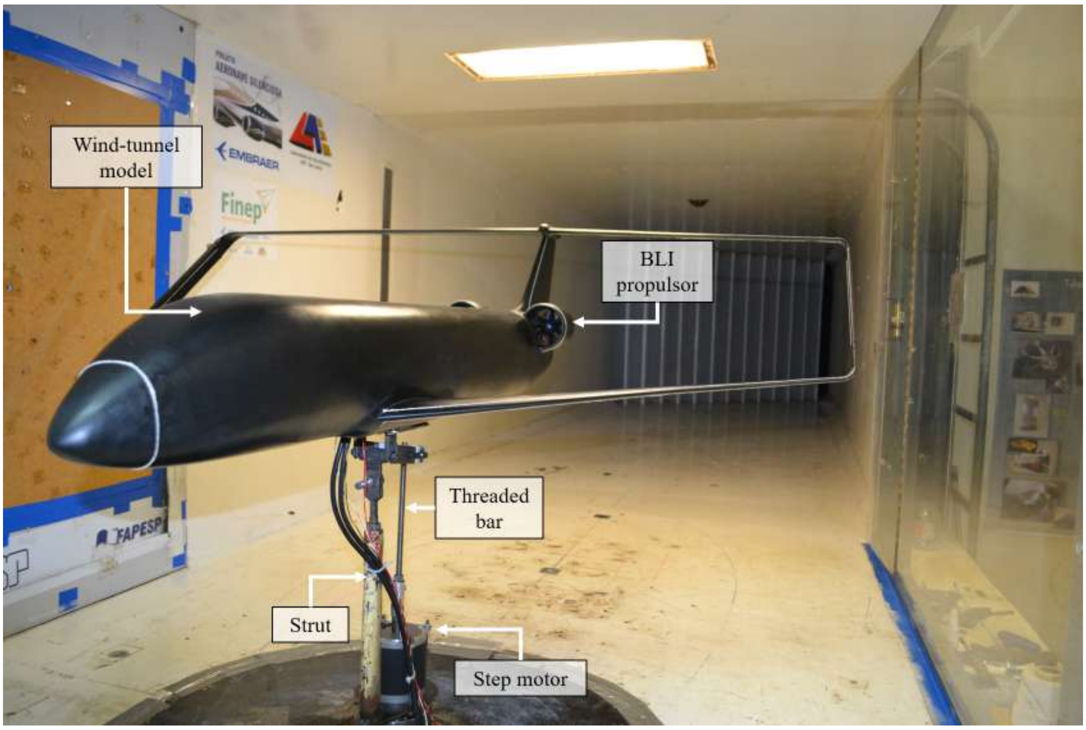

Source: The author

Figure 65 – Relation between motor's number of steps and model's angle of attack.

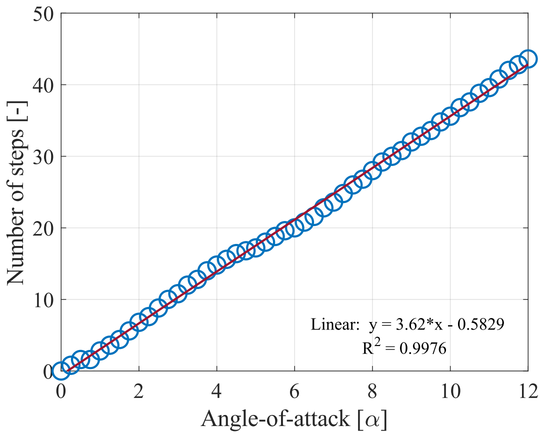

Source: The author

Figure 66 – Electronic circuit for measuring engine speed.

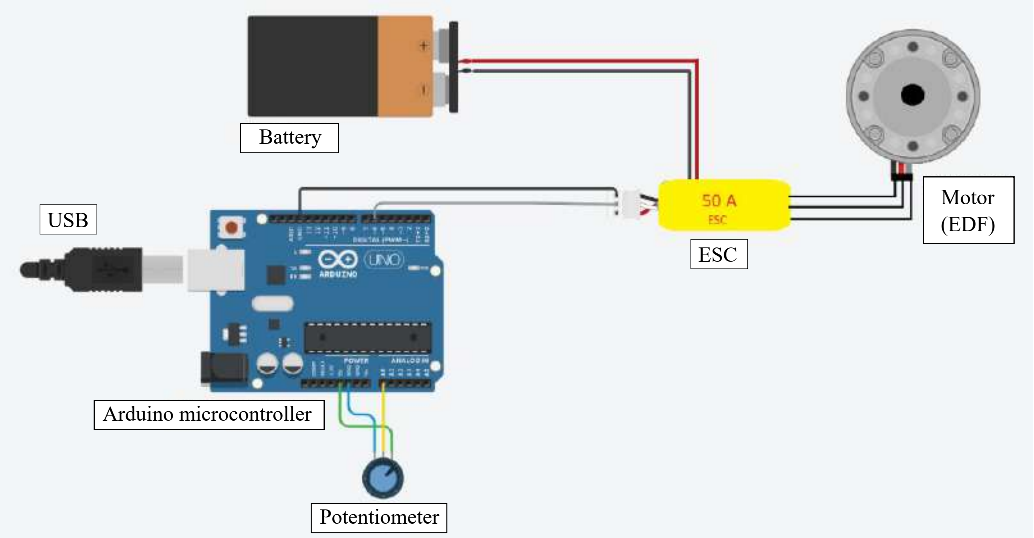

Source: The author

has been connected to the analog output (A0) of the Arduino (yellow wire in the diagram). The voltage output (+) was connected to the (5V) output of the Arduino (green wire of the circuit). The output (-) was connected to the (GND) of the Arduino (blue wire of the circuit). The ESC has three sets of wires, the first set corresponding to the set of three black wires that was directly connected to the motor so that, depending on the order of this connection, the motor could rotate clockwise or counterclockwise. The second set of wires are thicker in terms of gauge and were connected directly to the battery (positive terminal in red and negative terminal in black). Finally, the last set of wires having the smallest gauge was responsible for communicating with the Arduino board where the white wire was connected to the Arduino channel (6) located at the PMW outputs which is digital and the black wire was connected to the (GND). In this case, the white wire was not used because the Arduino board was powered directly via USB with the computer.

APPENDIX F – SCALE INTI MODEL BREAKDOWN AND DETAILS

The complex geometry and the small scale of the wind tunnel model made difficult to perform direct comparison between sub-scale and full-scale conditions. To overcome this challenge, the wing and tail airfoils on the model deviate from full-scale transonic airfoils, which is required for optimal behavior at low test Reynolds numbers. Therefore, the choice of the box-wing airfoil was emphasized to obtain a sufficient lift coefficient. Several airfoils were analyzed using two-dimensional simulations performed in XFLR5 free code (DEPERROIS, 2009). Different levels of turbulence (critical N-values) were studied in order to enable efficient modification of the sub-scale model design and test conditions to achieve the highest similarity with the prototype. The Eppler 222 low Reynolds number airfoil presented the best results for $R_e = 3.02 \times 10^5$. The NACA 0010 and NACA 0012 airfoils were used on the vertical tip fin and vertical tail, respectively. Strips (grit size) were added at specific chord length percentage in order to eliminate a detrimental laminar separation bubble. Figure 67 illustrates details of strips location and size, which is useful to relate the values provided in Figs. 68, 69, and 70.

Figure 67 – Detail of strips location and size for wind-tunnel experiments.

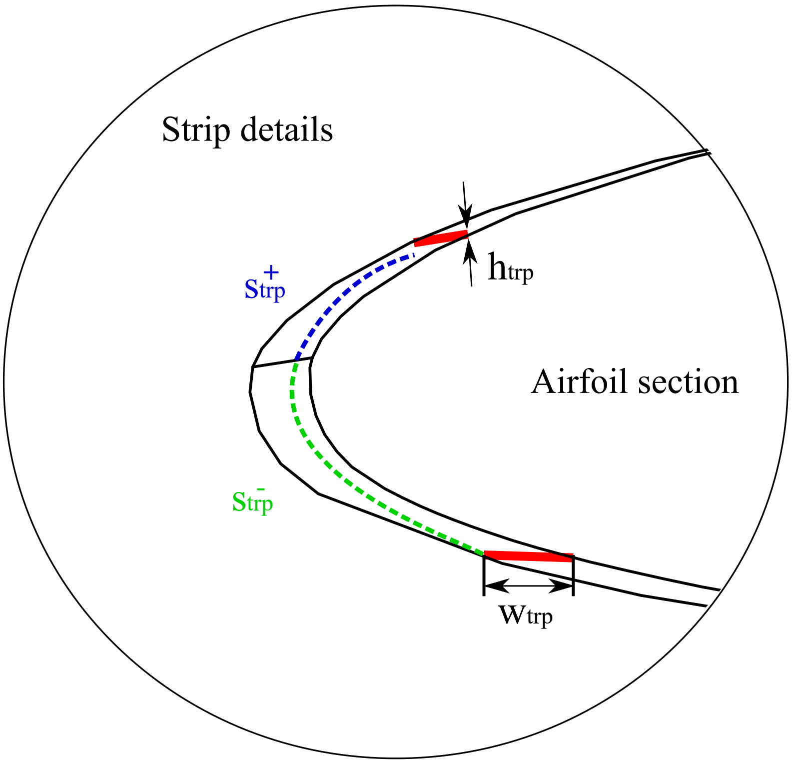

Source: The author

Figure 68 – Box-wing strips.

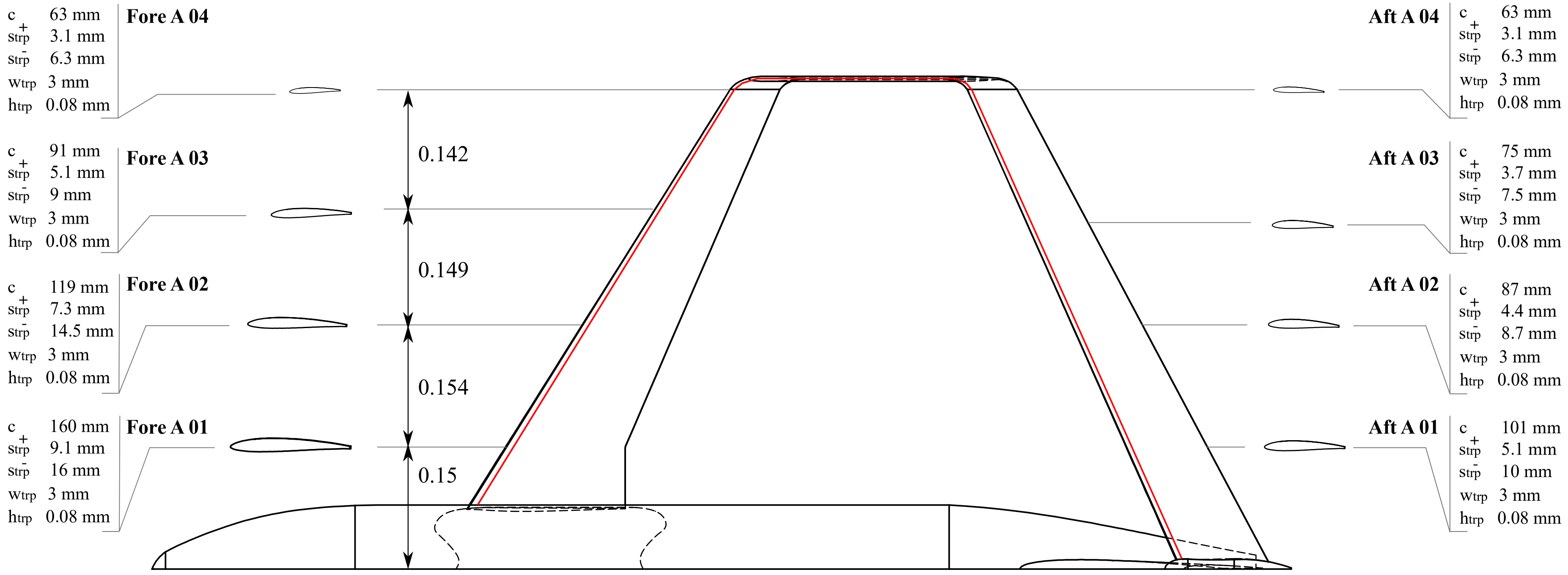

Source: The author
]

Figure 69 – Fuselage, Vertical Tip, and Vertical Tail strips.

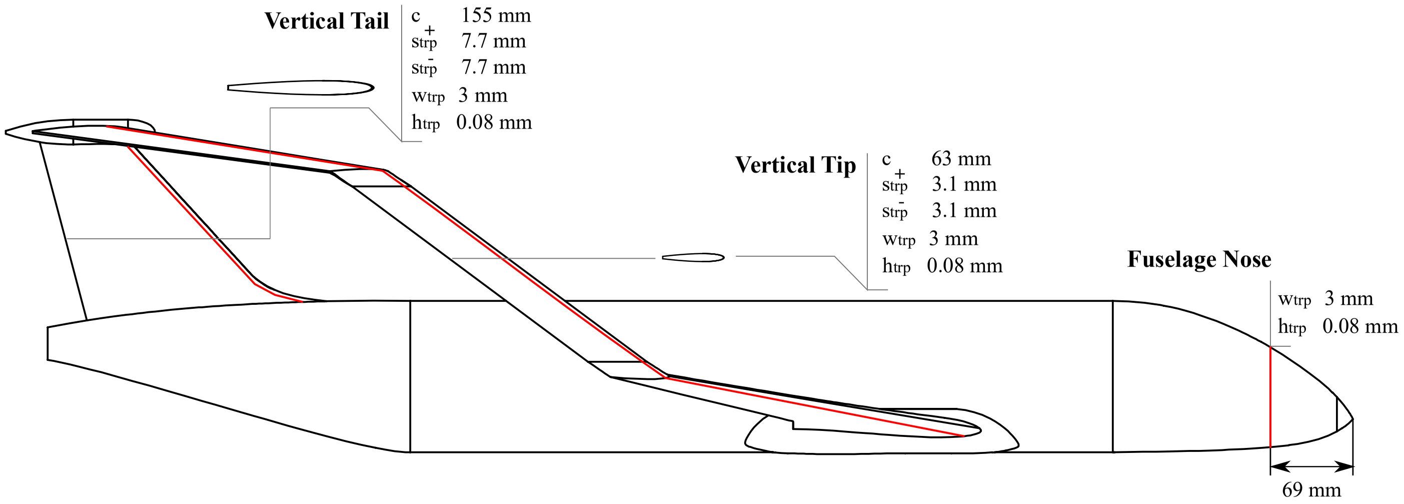

Source: The author

Figure 70 – Nacelle strips.

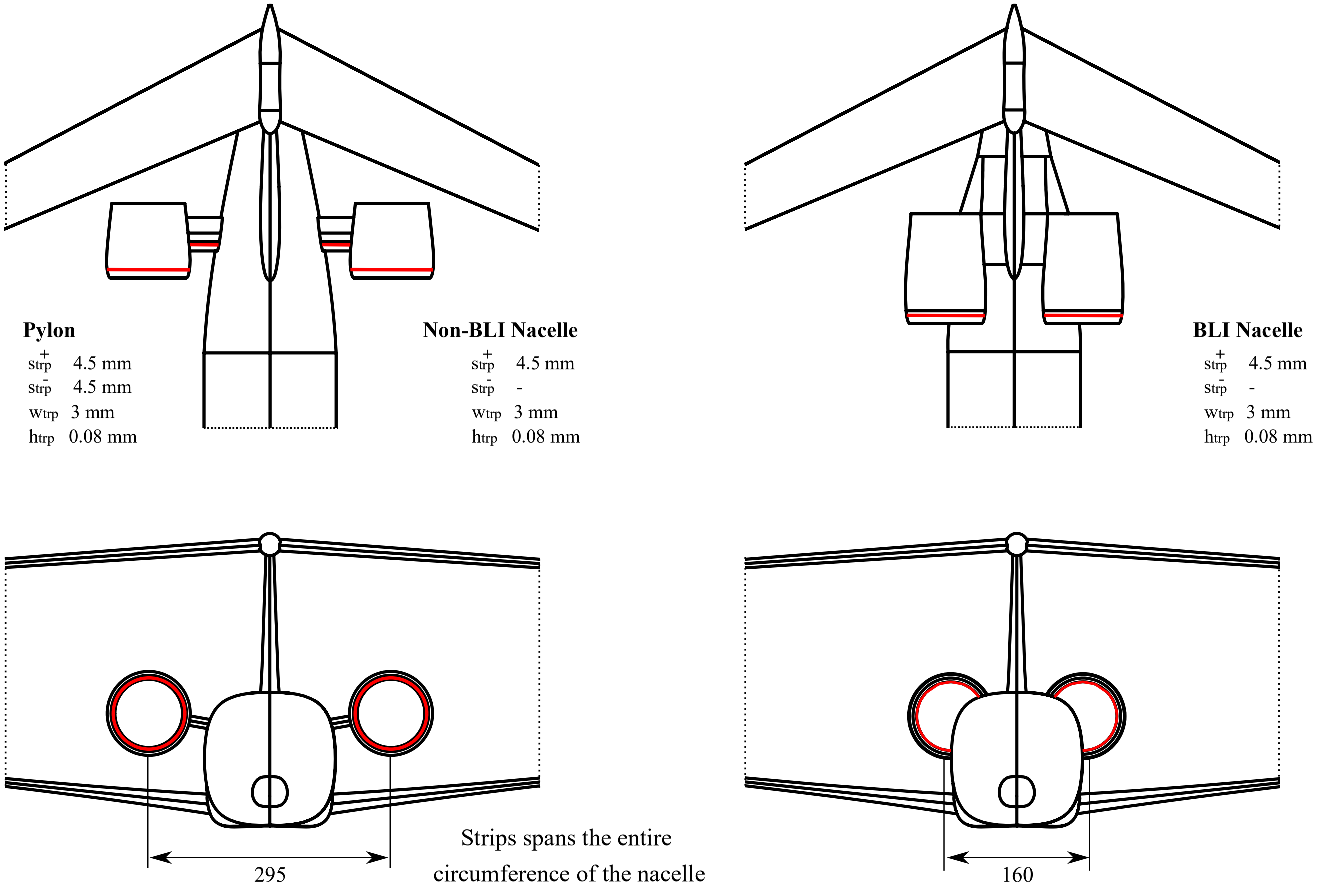

Source: The author

APPENDIX G – CALIBRATION AND CORRECTION OF AERODYNAMIC FORCES

G.0.1 Calibration of Aerodynamic Balances

The load cells calibration procedure is explained in this section. The drag balance load cells were tested by attaching a rope to the wind tunnel model and connecting it to a set of weights. In contrast, the lift balance was calibrated by adding weights on the top of the fuselage model. The weights were added and removed consecutively, reading the voltage output on the acquisition board and relating the force and voltage output data. This approach allowed to avoid any type of bias or hysteresis effect with the load cells. The linear regression from Matlab is used to find the relation between applied forces and voltage output. Figure 71 shows the calibration for lift and drag forces.

Figure 71 – Calibration of aerodynamic forces.

(a) Lift force balance calibration.

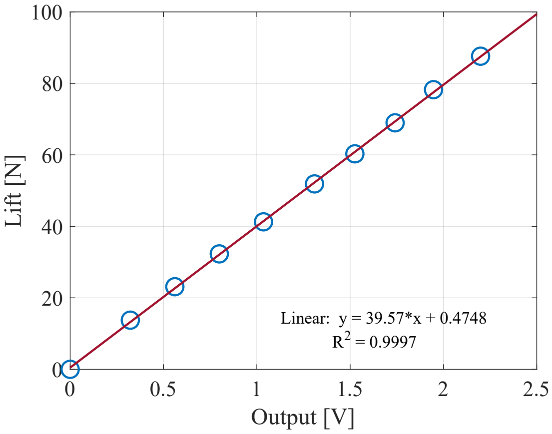

(b) Drag force balance calibration.

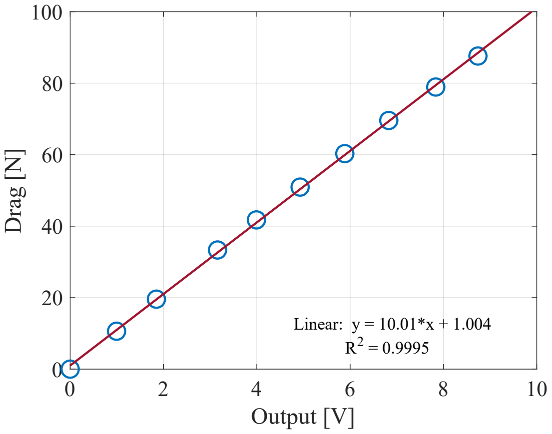

Source: The author

G.0.2 Evaluation of Tare

This section describes the process to evaluate the drag generated by the pitch-strut system. Basically, the aerodynamic forces acting on the model support were recorded at different tunnel speeds. Then, regression statistical analysis is performed to obtain an equation to relate the drag of the support for each value of dynamic pressure (see Fig. 72). The drag generated by the support is calculated by replacing the values of the dynamic pressure for each type of experiment, whose results are simply subtracted from the total drag of the experiment to obtain the model's drag.

Figure 72 – Pitch-strut system drag correction.

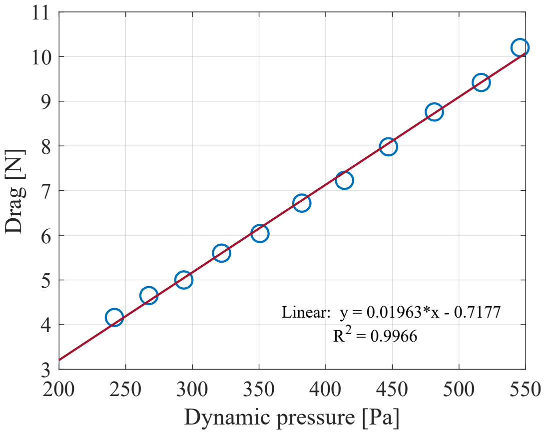

Source: The author

Note that the effect of the pitch-strut system appeared to be largely linear in this case, suggesting limited aerodynamic interaction between the model and the support. In contrast, the strut has no substantial effect on the lift coefficient, since its apparent effect does not change for different dynamic pressure runs, and its magnitude is comparable to the balance repeatability.

APPENDIX H – SEVEN-HOLE PROBE CALIBRATION

This appendix describes the procedure for 7-hole probe calibration and post-processing at LAE-1. The 7-hole probe used in the presented work was calibrated at flow angles between −30° and +30°. A neural network was used to calibrate the probe, in which values for pitch (α_p) and yaw (β_p) flow angles, and total and static pressures are correlated to coefficients based on the pressure differentials of the different holes. This network achieves errors of less than 1.5° and is used to avoid extrapolations when flow angles are less than the calibration maximum (30°). A close-up view of the installation of the probe at LAE-1 and a schematic of the probe are shown in Fig. 73 and Fig. 74, respectively.

Figure 73 – Close-up view of the installation of the probe for the non-BLI experiments at LAE-1.

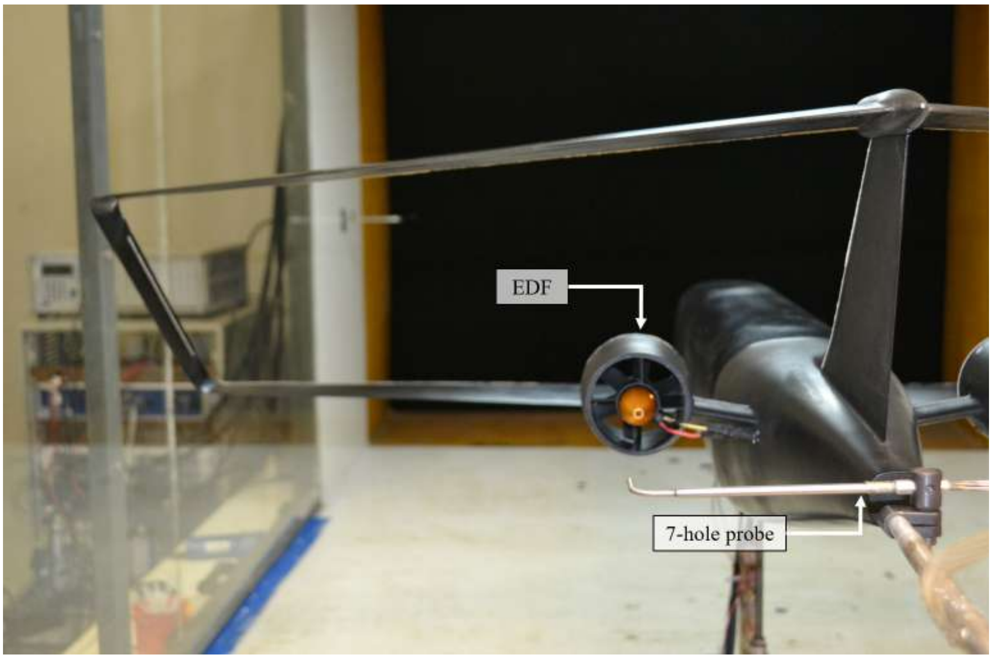

Source: The author

Three pressure coefficients are calculated as shown in Eq. H.1:

$$C_{p_i} = \frac{p_{total_i} - p_{total_{i+3}}}{p_{total_7} - p_{total_m}} \tag{H.1}$$

where p_{total_m} is the mean of all pressures measured by all probe holes, and the holes numbers (i) are referred to the probe presented in Fig. 74. The velocity components intensity is calculated using Eq. H.3, based on correlations among the flow angle and the pressure of the probe holes.

Figure 74 – Front view of the probe, pressure port numbering.

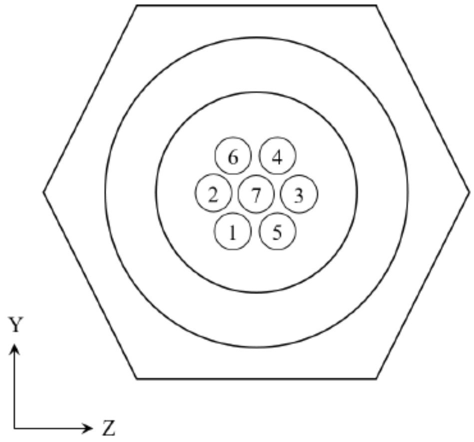

Source: The author

$$[u^*, v^*, w^*] = [cos(\alpha_p) \times cos(\beta_p), -sin(\alpha_p), sin(\beta_p)] \times \frac{V}{V_\infty} \tag{H.2}$$

where V/V_∞ is the velocity ratio, given by the following expression:

$$\frac{V}{V_\infty} = \sqrt{max\left(\frac{p_{total_i} - p_{total_\infty}}{q_\infty}\right) + 1} = \sqrt{C_{p_{max}+1}} \tag{H.3}$$

APPENDIX I – UNCERTAINTY ANALYSIS

In this section, the calculations used to determine the experimental uncertainties are presented.

I.0.1 Freestream Condition Uncertainty

The precision of tunnel instrumentation determined the level of uncertainty in tunnel operating conditions (Table 40).

Table 40 – Instrument precision and uncertainty.

Uncertainty in	Value
Atmospheric pressure	$\Delta p \pm 1 mmHg$
Dynamic pressure	$\Delta q_\infty \pm 0.1\ Pa$
Temperature	$\Delta T \pm 0.1°C$

Source: The author

The uncertainty of tunnel velocity was calculated by:

$$\Delta V_\infty = \left[\left(\frac{\partial V_\infty}{\partial q_\infty}\Delta q_\infty\right)^2 + \left(\frac{\partial V_\infty}{\partial p}\Delta p\right)^2 + \left(\frac{\partial V_\infty}{\partial T}\Delta T\right)^2\right]^{1/2} \tag{I.1}$$

where the uncertainty for each variable is determined by the following equations:

$$\left(\frac{\partial V_\infty}{\partial q_\infty}\Delta q_\infty\right)^2 = \left[\frac{\partial\left(\sqrt{\frac{2q_\infty RT}{p}}\right)}{\partial q_\infty}(\Delta q_\infty)\right]^2 \tag{I.2}$$

$$\left(\frac{\partial V_\infty}{\partial p}\Delta p\right)^2 = \left[\frac{\partial\left(\sqrt{\frac{2q_\infty RT}{p}}\right)}{\partial p}(\Delta p)\right]^2 \tag{I.3}$$

$$\left(\frac{\partial V_\infty}{\partial T}\Delta T\right)^2 = \left[\frac{\partial\left(\sqrt{\frac{2q_\infty RT}{p}}\right)}{\partial T}(\Delta T)\right]^2 \tag{I.4}$$

I.0.2 Aerodynamic Forces Uncertainty

The uncertainty of lift and drag coefficients, and lift-to-drag ratio, was calculated using the pressure and area readings, as well as the voltage output measurement variance from the lift and drag bridges:

$$C_L = \Delta C_L = \frac{39.57 \times \left[O_L(V) \pm \frac{\sigma}{\sqrt{n_{sample}}}\right]}{(q_\infty \pm \Delta q_\infty)(S \pm \Delta S)} \tag{I.5}$$

$$C_D = \Delta C_D = \frac{10.01 \times \left[O_D(V) \pm \frac{\sigma}{\sqrt{n_{sample}}}\right]}{(q_\infty \pm \Delta q_\infty)(S \pm \Delta S)} \tag{I.6}$$

$$\frac{C_L}{C_D} = \Delta \frac{C_L}{C_D} = \frac{39.57 \times \left[O_L(V) \pm \frac{\sigma}{\sqrt{n_{sample}}}\right]}{10.02 \times \left[O_D(V) \pm \frac{\sigma}{\sqrt{n_{sample}}}\right]} \tag{I.7}$$

Propagation of uncertainty is performed using multiplication and division equations:

$$(A \pm \Delta A) \times (B \pm \Delta B) = AB \pm A\Delta B \pm B\Delta A \tag{I.8}$$

$$\frac{A \pm \Delta A}{B \pm \Delta B} = \frac{A}{B} \pm \frac{A\Delta B + B\Delta A}{B^2} \tag{I.9}$$

I.0.3 BLI Benefit Uncertainty (from electrical power measurements)

The metric of interest for this study is the power saving coefficient (PSC), which determines the BLI benefit considering the electrical power coefficient (C_{P_E}) at zero net streamwise force ($C_X = 0$). As a result, uncertainty in both measured power and measured net streamwise force contributes to the uncertainty in BLI benefit. Assuming that all uncertainties are statistically independent, the instrumentation uncertainties are propagated to the quantities of interest as follows:

$$\sigma_{C_X} = \left[\left(\frac{\sigma_{F_X}}{F_X}\right)^2 + \left(\frac{\sigma_{q_\infty}}{q_\infty}\right)^2\right]^{\frac{1}{2}} C_X \tag{I.10}$$

$$\sigma_{P_E|C_X=0} = \left[\left(\frac{\sigma_{P_E}}{P_E}\right)^2 + \left(\frac{\sigma_{F_X}}{P_E}\frac{dP_E}{dF_X}\right)^2\right]^{\frac{1}{2}} P_E \tag{I.11}$$

$$\sigma_{C_{P_E}} = \left[\left(\frac{\sigma_{P_E}}{P_E}\right)^2 + \left(\frac{\sigma_{q_\infty}}{q_\infty}\right)^2 + \left(\frac{\sigma_{V_\infty}}{V_\infty}\right)^2\right]^{\frac{1}{2}} C_{P_E} \tag{I.12}$$

I.0.4 Details of the Distortion Rake and Scanivalve Uncertainty

The distortion rake is a standard eight-arm design that measures total pressure, and correlates the data according to the DC_θ distortion parameters. A schematic of the distortion rake is shown in Fig. 75. The 40 pitot tubes were cut from 0.028" outer diameter and 0.0035" wall stainless steel hypodermic tubing stock. Each tube was attached at the back end with pneumatic tubing to connect with the scanivalve transducers. The main

Figure 75 – Eight-arm total pressure distortion rake, dimensions in mm.

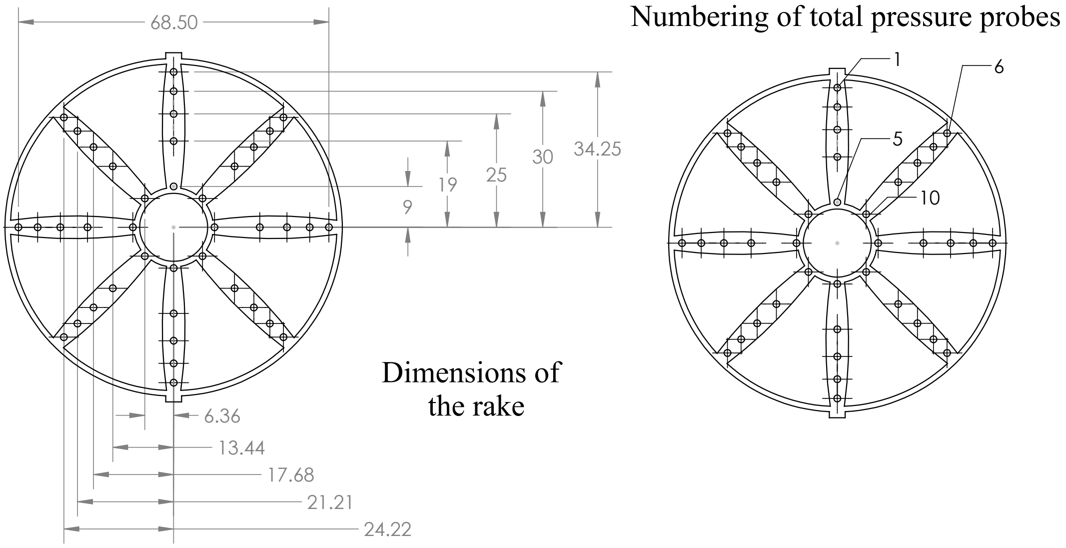

Source: The author

structure of the rake was 3D printed, and soft solder and acid flux were used to connect all of the components.

The output values from the scanivalve are given in Volts, corresponding to the differential pressure of each probe in relation to the central total pressure transducer. Hence, it is possible to compare the dynamic pressure connected, for example, at probe 1 with the dynamic pressure read by the micromanometer, to find the approximate calibration of the scanivalve.

The uncertainties in total pressure fields were calculated using the standard deviation of the reading. In particular, the error of each reading in Volts for a given number of samples was calculated by the Student's t inverse cumulative distribution function from Matlab. The overall total pressure uncertainty was determined from the contributions of the errors using the root-sum-square combination.

$$\sigma_{p_t} = \left[\left(\frac{\partial p_t}{\partial X_1} \sigma_{X_1} \right)^2 + \left(\frac{\partial p_t}{\partial X_2} \sigma_{X_2} \right)^2 + ... + \left(\frac{\partial p_t}{\partial X_n} \sigma_{X_n} \right)^2 \right]^{\frac{1}{2}} \tag{I.13}$$

where X is the error of each of the samples.

APPENDIX J – MODIFICATIONS TO THE ORIGINAL FABER PROGRAM

In this appendix, modifications made to the original **Faber** program are described. Faber's optimizer was set to minimize the block fuel consumption of the aircraft. There are a total of 14 design variables available for optimization, however, only 2 design variables were evaluated; in this case, the thickness-to-chord ratio and the chord length. The other geometric design variables were omitted and their values remain constant throughout the optimization process because of their impacts on the main wing planform as well as the computation speed and stability. Design constraints included: minimum wing volume, ensuring enough space in the wing to store the fuel required for the mission; minimum chord length at the tips, preventing the optimizer from creating a wing with unrealistically wing tips; buffet constraint to prevent the development of significant shock waves over the surfaces of the wings; and buckling constraint (based on Euler-Bernoulli beam theory), ensuring that the compressive stress in the BW structure is not high enough to produce buckling. For this constraint, the boundary conditions governing the joints among the vertical wing and the horizontal wings were modified using the structural module. In particular, a beam element type for vertical wing segment was imposed, whereas rigid joints characterized the fore wing and aft wing segments. Such configuration improved buckling performance, evaluating internal forces and stresses as a function of the section properties (boom areas and skin thicknesses).

The load cases include (i) a $2.5g$ symmetric maneuver load at MTOW, and (ii) a $-1g$ dive load at MTOW. Inertial loads from the weight of the aircraft components and fuel (100% mission) are also included in each load condition. Together, these two conditions ensure that statically indeterminate structures are sufficiently sized against buckling in both out-of-plane directions. Below is a list of piece of code modifications implemented in **Faber** in order to optimize BW configurations:

1. Buckling constraint.

File name: Faber Optimization.m
Function name: *calcConstrPrimitive*

```
if      (beam.Pavg(i,j)<0 && (strcmp(topo,‘bw’) && j==3))
        numConstr = numConstr + 1;
        C(numConstr) = abs(beam.Pavg(i,j))/beam.Pcr(i,j) - 1;
else
        numConstr = numConstr + 1;
        C(numConstr) = 0;
end
```

Note: The constraint ‘optim.constraint.nonlinear.buckling’ gave error message as the size of the constraint matrix kept changing after each iteration. The new constraint will now have a fix size.

2. Box-wing structural boundary conditions.

```
File name: weight_calcPrimaryWingWeight.m
Function name: setBoundaryConditions
elseif   strcmp(beam.joint,‘Mix’) % Fore-fin = universal, aft-fin = rigid
         bc_indx = [bc_indx, dof_elem(indx_elem_cll{3}(N_elem_vec(3)), ...
         [7 8 9])];
% Set boundary condition for fore wing to vertical fin connection
         bc_indx = [bc_indx, dof_elem(indx_elem_cll{5}(N_elem_vec(5)), ...
         [10 11 12])];
elseif   strcmp(beam.joint,‘Mix2’) % Fore-fin = universal, aft-fin = rigid
         bc_indx = [bc_indx, dof_elem(indx_elem_cll{3}(N_elem_vec(3)), ...
         [9 10 11 12])]; % custom 1
% Set boundary condition for aft wing to vertical fin connection
         bc_indx = [bc_indx, dof_elem(indx_elem_cll{5}(N_elem_vec(5)), ...
         [7 8 10 11 12])]; % custom 2
```

Note: This modification adds the new boundary condition settings for the wing joints between the vertical wing segment and the horizontal wing segments, which allows to add the new input options for the ‘beam.joint’ variable, as follows:

```
File name: Input_Mod.m
field_options =   {‘Free’, ‘Universal’, ‘Rigid’, ‘Pinned’, ‘Mix’, ‘Mix2’ };
```

3. Box-wing induced drag calculation and load distribution modification.

```
File name: Aerodynamic_Mod.m
Function name: calcWingInducedDrag
CDi =   (aero_basic.wing.CL + aero_basic.tail.CL)^2 ...
        / (pi*wing.aspect_ratio)*D_rel_bw
```

Note: This modification calculates induced drag for an optimal box-wing using Prandtl's empirical equation. The total lift was equally divided between the fore and aft wings according to Prandtl's induced drag calculation, as follows:

```
File name: Aerodynamic_Mod.m
Function name: defLoadDistribution
A_ell_f =    n_aero*(0.5)*(0.5*F_lift);
A_ell_a =    n_aero*(0.5)*(0.5*F_lift);
```

4. Total lift distribution calculation.

File name: Aerodynamic_Mod.m

Function name: *calcLift*

```
        Lf = 0*lift;
        Lw = 0*lift;
        Lt = 0;
else
        Lf = 0*lift;
        Lw = 0.5*lift;
        Lt = 0.5*lift;
```

Note: This modification assumed that the fuselage does not generate any lift.

5. Wing height modification.

File name: Faber_Optimization.m

Function name: *transDesignVariables*

```
if      strcmp(topo,'bw')
% align the x coordinate of the aft wing root and the fin tip
        partial_stagger = 0;
        N_segment = max(size(wing.segment));
        wingXlocation = wing.location(1)*fuselage.length;
        for  i1 = 1:N_segment
              if i1 = 4
              partial_stagger = partial_stagger + wing.segment(i1).span*...
              tan(abs(wing.segment(i1).sweep_le));
              end
        end
        wing.segment(4).sweep_le = atan((fin.location(1)*fuselage.length ...
        wingXlocation + fin.span*tan(fin.sweep_le) - partial_stagger) ...
        /wing.height);
% align the z coordinate of the aft wing root and the fin tip
        finZlocation = fin.location(3)*fuselage.height - 0.5*fuselage.height;
        wing.height = fin.span + 2*finZlocation;
end
```

Note: This modification ensured that when changing the vertical tail span, the wing height is also updated accordingly, so that the tip of the vertical tail is aligned to the aft wing root. When changing the wing sweep or the vertical tail streamwise location, the sweep angle of the vertical wing segment (segment 4) is also updated automatically, so that the tip of the vertical tail is aligned to the aft wing root.

Figure 76 – Planform views from **Faber**.

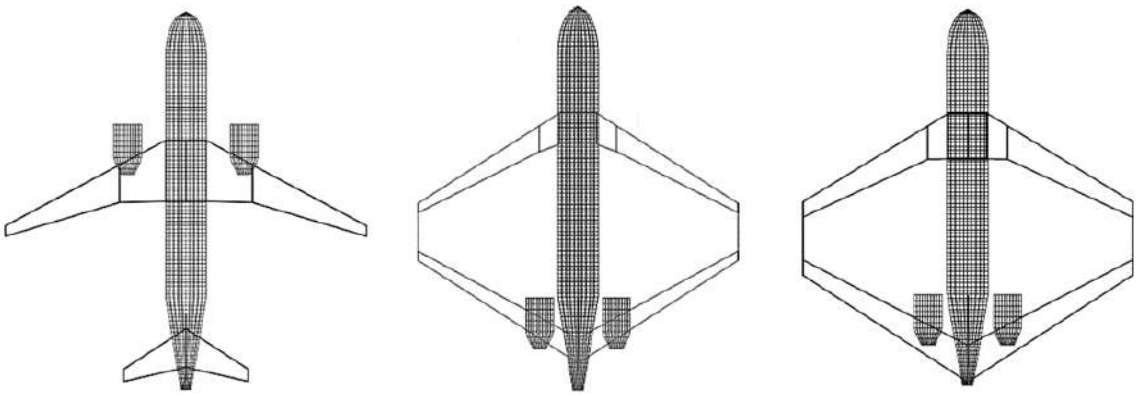
(a) CTW.

(b) BW v. 1.

(c) BW v. 2.

Source: The author

Table 41 – Conceptual design results from **Faber**[1].

Parameter	**CTW**	**BW v. 1**	Δ [%]	**BW v. 2**	Δ [%]
MTOW [kg]	79052.1	74544.3	-5.7	80334.8	+1.6
OEW [kg]	44447.5	41520.9	-7.0	46066.8	+3.5
Total Wing [kg]	8486.7	7099.6	-16.3	10069.9	+15.7
MZFW [kg]	63947.5	61020.9	-4.57	65566.8	+2.53
MFW [kg]	20851.6	18547.8	-11.0	19136.6	-8.9
Wingspan [m]	35.9	32.2	-10.5	32.2	-10.5
Wing area [m^2] -	123.7	123.7	0	174.9	+29
Aspect Ratio [-]	10.45	8.3	-20.5	5.9	-43.5
Wetted Aspect Ratio [-]	1.60	1.51	-5.6	1.29	-19.3
Wing fuel volume [lt]	29659	16425	-44	29569	0
Cruise altitude [m]	11200	11200	0	12500	+19.5
Cruise L/D [-]	17.9	18.5	+3.4	19.3	+7.2
Cruise C_L [-]	0.55	0.51	-5.4	0.51	-7.2
Cruise C_D [-]	0.0307	0.0277	-9.5	0.0264	-14
Cruise C_{D0} [-]	0.0201	0.0213	+5.3	0.0179	-12.4
Cruise C_{Di} [-]	0.0101	0.0063	-37	0.0061	-39
Cruise drag [N]	37142	33624	-9.5	34074	-8.2
Block Fuel [kg]	8424.1	7767.1	-7.8	7943.9	-5.7

[1] Aerodynamic data obtained from cruise condition, and operating data for nominal range plus diversion range, based on requirements given in Table 13.

Source: The author

Figure 76 and Table 41 present the conceptual design results using **Faber**. Two BW concepts (BW v. 1. and BW v. 2.) were designed in order to compare their performance against a CTW. There are important trade-offs to be considered for future design phases. For example, if the aircraft stores the fuel inside the wings, a larger wing surface is required, as shown in Fig. 76c. This increases viscous drag and reduce the benefit of the configuration that comes from the induced drag reduction, so the total cruise drag is increased. In contrast, box-wings could be designed with a reduced wing surface (see Fig. 76b), which also reduce weight, but leads to certification challenges due to the need to store fuel inside the fuselage.

APPENDIX K – MESH QUALITY METRICS

Figure 77 shows non-orthogonality (determinant 3x3x3) and skewness metrics for the mesh of the initial geometry. The multiblock mesh was created manually using ICEM-CFD (FINLAYSON, 2013). The non-orthogonality is defined as the angle between the line joining the cell centers of two cells with the normal of their common face. This metric computes the normalized determinant of the Jacobian for a mesh cell. A determinant of 1.0 corresponds to a perfect hexahedral cube, whereas a determinant of 0.0 corresponds to an inverted cube with a negative volume (FINLAYSON, 2013). As shown in Fig. 77a, the mesh cells have mesh quality larger than 0.6. In contrast, the skewness is defined as the ratio of the distance between the intersection point of the line joining two cell centers with the plane of their common face. Highly skewed cells can decrease accuracy and destabilize the solution. The mean skewness values vary ranging from 0.0 to 1.0, where skewness close to 1.0 is good for a hexahedral element mesh. A general rule is that the maximum skewness for a hexahedral mesh in most flows must be kept between 0.6 up to 0.95 (FINLAYSON, 2013). The high complexity of the mesh structure due to the diagonal blocks required to connect the fore and aft wings led to obtain high skewed cells, as shown in Fig. 77b. Overall, the mean non-orthogonality values are high, which is favorable for accuracy, and the mesh was robust enough to enable large range of valid mesh deformations.

Figure 77 – Quality metrics for the mesh of the initial geometry.

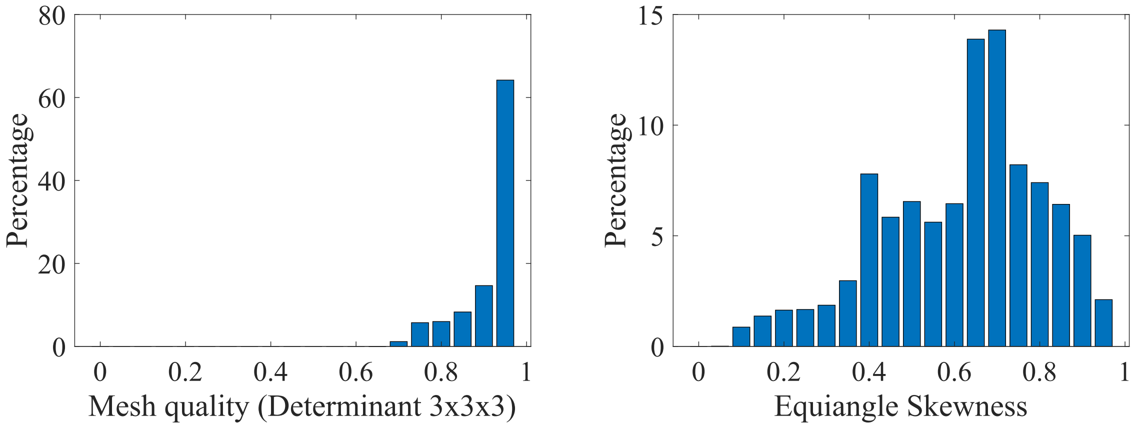

(a) Non-orthogonality.

(b) Skewness.

Source: The author

BIBLIOGRAPHY

A320 - Aircraft characteristics airport and maintenance planning. 2005. Accessed in 05/03/2021. Available from Internet: <https://www.airbus.com/aircraft/support-services/airport-operations-and-technical-data/aircraft-characteristics.html>.

ABBAS, A.; VICENTE, J. D.; VALERO, E. Aerodynamic technologies to improve aircraft performance. **Aerospace Science and Technology**, Elsevier, v. 28, n. 1, p. 100–132, 2013.

AEROPROBE L-Shaped Probe. 2018. Accessed in 23/03/2022. Available from Internet: https://www.aeroprobe.com.

AHUJA, J.; MAVRIS, D. N. A method for modeling the aero-propulsive coupling characteristics of bli aircraft in conceptual design. *In*: **AIAA Scitech 2021 Forum, AIAA 2021-0112. Virtual event**. [*S.l.: s.n.*], 2021.

ALMEIDA, O. de; CATALANO, F. M.; PEREIRA, L. T. Improvements of a hard-wall closed test-section of a subsonic wind tunnel for aeroacoustic testing. **International Journal of Acoustics and Vibration**, INT INST ACOUSTICS & VIBRATION AUBURN UNIV, MECHANICAL ENGINEERING DEPT, 270 . . . , v. 26, n. 3, p. 248–258, 2021.

AMMAR, S. *et al.* Conceptual design, performance and stability analysis of a 200 passengers blended wing body aircraft. **Aerospace Science and Technology**, Elsevier, v. 71, p. 325–336, 2017.

ANDERSON, J. D.; JR, J. D. A. **A history of aerodynamics: and its impact on flying machines**. [*S.l.: s.n.*]: Cambridge University Press, 1998. v. 8.

ANDREWS, S. A.; PEREZ, R. E. Analytic study of the conditions required for longitudinal stability of dual-wing aircraft. **Proceedings of the Institution of Mechanical Engineers, Part G: Journal of Aerospace Engineering**, SAGE Publications Sage UK: London, England, v. 232, n. 5, p. 958–972, 2018.

ANDREWS, S. A.; PEREZ, R. E. Comparison of box-wing and conventional aircraft mission performance using multidisciplinary analysis and optimization. **Aerospace Science and Technology**, Elsevier, v. 79, p. 336–351, 2018.

ANDREWS, S. A.; PEREZ, R. E.; WOWK, D. Wing weight model for conceptual design of nonplanar configurations. **Aerospace Science and Technology**, Elsevier, v. 43, p. 51–62, 2015.

ARMSTRONG, M. J. *et al.* Propulsion system component considerations for NASA N3-X turboelectric distributed propulsion system. **SAE International Journal of Aerospace**, v. 5, n. 2012-01-2165, p. 344–353, 2012.

ASHCRAFT, S. W. *et al.* Review of propulsion technologies for n + 3 subsonic vehicle concepts. **NASA Technical Report**, NASA/TM-2011-217239, 2011.

AURORA Flight Science - Double bubble D8. 2017. Accessed in 23/03/2021. Available from Internet: https://www.nasa.gov/content/the-double-bubble-d8-0/.

BARBARINO, S. *et al.* A review of morphing aircraft. **Journal of intelligent material systems and structures**, Sage Publications Sage UK: London, England, v. 22, n. 9, p. 823–877, 2011.

BARLOW, J. B.; RAE, W. H.; POPE, A. **Low-speed wind tunnel testing**. [*S.l.: s.n.*]: John wiley & sons, 1999.

BECCASIO, N.; TESCONI, M.; FREDIANI, A. Prandtlplane propelled with liquid hydrogen: a preliminary study. *In*: **Variational Analysis and Aerospace Engineering: Mathematical Challenges for Aerospace Design**. [*S.l.: s.n.*]: Springer, 2012. p. 1–25.

BEJAN, A.; CHARLES, J.; LORENTE, S. The evolution of airplanes. **Journal of Applied Physics**, AIP, v. 116, n. 4, p. 044901, 2014.

BERTON, J. J.; HALLER, W. J. A noise and emissions assessment of the N3-X transport. *In*: **52nd Aerospace Sciences Meeting, AIAA 2014-0594. National Harbor, Maryland**. [*S.l.: s.n.*], 2014.

BHATIA, M.; KAPANIA, R. K.; HAFTKA, R. T. Structural and aeroelastic characteristics of truss-braced wings: A parametric study. **Journal of Aircraft**, v. 49, n. 1, p. 302–310, 2012.

BIELER, H. *et al.* **A Common Platform for Validation of Aircraft Drag Reduction Technologies, URL http://congress.cimne.com/padri-2017/frontal/default. asp**. 2018. Cited: 07 Mar. 2021.

BIJEWITZ, J. *et al.* A review of recent aircraft concepts employing synergistic propulsion-airframe integration. *In*: **30th Congress of the International Council of the Aeronautical Sciences, Daejeon, Korea**. [*S.l.: s.n.*], 2016.

BIJEWITZ, J. *et al.* Progress in optimizing the propulsive fuselage aircraft concept. **Journal of Aircraft**, American Institute of Aeronautics and Astronautics, v. 54, n. 5, p. 1979–1989, 2017.

BIJEWITZ, J. *et al.* Multi-disciplinary design investigation of propulsive fuselage aircraft concepts. **Aircraft Engineering and Aerospace Technology: An International Journal**, Emerald Group Publishing Limited, 2016.

BINANTE, V. *et al.* Prandtlplane performance analysis and scaling procedures, PARSIFAL project deliverable, d 3.4; European commission: Luxembourg, cordis website. 2020.

BINITHA, S.; SATHYA, S. S. *et al.* A survey of bio inspired optimization algorithms. **International Journal of Soft Computing and Engineering**, v. 2, n. 2, p. 137–151, 2012.

BLAKEY, S.; RYE, L.; WILSON, C. W. Aviation gas turbine alternative fuels: A review. **Proceedings of the combustion institute**, Elsevier, v. 33, n. 2, p. 2863–2885, 2011.

BLUMENTHAL, B. T. *et al.* Computational investigation of a boundary-layer-ingestion propulsion system. **Journal of aircraft**, American Institute of Aeronautics and Astronautics, v. 55, n. 3, p. 1141–1153, https://doi.org/10.2514/1.C034454, 2018.

BOLSUNOVSKY, A. *et al.* Flying wing—problems and decisions. **Aircraft design**, Elsevier, v. 4, n. 4, p. 193–219, 2001.

BOMBARDIERI, R. *et al.* On the dynamic fluid-structure stability response of an innovative airplane configuration. **Journal of Fluids and Structures**, Elsevier, v. 105, p. 103347, 2021.

BONET, J. T. *et al.* **Environmentally Responsible Aviation (ERA) Project-N+ 2 Advanced Vehicle Concepts Study and Conceptual Design of Subscale Test Vehicle (STV) Final Report**. [*S.l.*], 2011. NASA/CR-2011-216519.

BOTERO, E. M. *et al.* SUAVE: An open-source environment for conceptual vehicle design and optimization. *In*: **54th AIAA Aerospace Sciences Meeting, AIAA 2016-1275. San Diego, California**. [*S.l.: s.n.*], 2016.

BRADLEY, K. R. **A sizing methodology for the conceptual design of blended-wing-body transports**. [*S.l.*], 2004. NASA/CR-2004-213016.

BRADLEY, M. K.; DRONEY, C. K. **Subsonic ultra green aircraft research**. [*S.l.*], 2011. NASA/CR-2011-216847.

BRADLEY, M. K.; DRONEY, C. K. **Subsonic ultra green aircraft research phase II: N+ 4 advanced concept development**. [*S.l.*], 2011. NASA/CR-2012-217556.

BRADLEY, M. K.; DRONEY, C. K. **Subsonic ultra green aircraft research: Phase 2. Volume 2; Hybrid electric design exploration**. [*S.l.*], 2015. NASA/CR–2015-218704/Volume II.

BRADLEY, M. K.; DRONEY, C. K. **Subsonic ultra green aircraft research: Phase II. Volume 2; Hybrid electric design exploration**. [*S.l.*], 2015. NASA/CR–2015-218704/Volume II.

BRADLEY, M. K.; DRONEY, C. K.; ALLEN, T. J. **Subsonic ultra green aircraft research: Phase II. Volume 1; truss braced wing design exploration**. [*S.l.*], 2015. NASA/CR–2015-218704/Volume I.

BRAVO-MOSQUERA, P. D. *et al.* Integration assessment of conceptual design and intake aerodynamics of a non-conventional air-to-ground fighter aircraft. **Aerospace Science and Technology**, Elsevier, v. 86, p. 497–519, 2019.

BRAVO-MOSQUERA, P. D. *et al.* Aerodynamic design analysis of a UAV for superficial research of volcanic environments. **Aerospace Science and Technology**, Elsevier, v. 70, p. 600–614, 2017.

BRAVO-MOSQUERA, P. D.; CATALANO, F. M.; ZINGG, D. W. Unconventional aircraft for civil aviation: A review of concepts and design methodologies. **Progress in Aerospace Sciences**, v. 131, p. 100813, 2022. ISSN 0376-0421.

BRAVO-MOSQUERA, P. D.; CERÓN-MUÑOZ, H. D.; CATALANO, F. Design and computational analysis of a closed non-planar wing aircraft coupled to a boundary layer ingestion propulsion system. *In*: **AIAA Propulsion and Energy 2019 Forum, AIAA 2019-3850. Indianapolis, Indiana**. [*S.l.: s.n.*], 2019.

BRAVO-MOSQUERA, P. D.; CERÓN-MUÑOZ, H. D.; CATALANO, F. M. Design, aerodynamic analysis and optimization of a next-generation commercial airliner. **Journal of the Brazilian Society of Mechanical Sciences and Engineering**, Springer Nature, v. 44, n. 609, 2022.

BRAVO-MOSQUERA, P. D. *et al.* Conceptual design and CFD analysis of a new prototype of agricultural aircraft. **Aerospace Science and Technology**, Elsevier, v. 80, p. 156–176, 2018.

BRAVO-MOSQUERA, P. D. *et al.* Exploration of box-wing aircraft concept using high-fidelity aerodynamic shape optimization. *In*: **33th Congress of the International Council of the Aeronautical Sciences, Stockholm, Sweden**. [*S.l.: s.n.*], 2022.

BRAVO-MOSQUERA, P. D. *et al.* Experimental investigation of a next-generation airliner with boundary layer ingestion. *In*: **33th Congress of the International Council of the Aeronautical Sciences, Stockholm, Sweden**. [*S.l.: s.n.*], 2022.

BRAVO-MOSQUERA, P. D. *et al.* Design and aerodynamic evaluation of a medium short takeoff and landing tactical transport aircraft. **Proceedings of the Institution of Mechanical Engineers, Part G: Journal of Aerospace Engineering**, SAGE Publications Sage UK: London, England, v. 236, n. 5, p. 825–841, 2022.

BRELJE, B. J.; MARTINS, J. R. Electric, hybrid, and turboelectric fixed-wing aircraft: A review of concepts, models, and design approaches. **Progress in Aerospace Sciences**, Elsevier, 2018.

BRELJE, B. J.; MARTINS, J. R. Aerostructural wing optimization for a hydrogen fuel cell aircraft. *In*: **AIAA Scitech 2021 Forum, AIAA 2021-1132. Virtual event**. [*S.l.: s.n.*], 2021.

BROUCKAERT, J.-F. *et al.* Clean sky research and demonstration programmes for next-generation aircraft engines. **The Aeronautical Journal**, Cambridge University Press, v. 122, n. 1254, p. 1163–1175, 2018.

BROWN, G. Weights and efficiencies of electric components of a turboelectric aircraft propulsion system. *In*: **49th AIAA aerospace sciences meeting including the new horizons forum and aerospace exposition, AIAA 2011-225. Orlando, Florida**. [*S.l.: s.n.*], 2011.

BROWN, M.; VOS, R. Conceptual design and evaluation of blended-wing body aircraft. *In*: **2018 AIAA Aerospace Sciences Meeting, AIAA 2018-0522. Kissimmee, Florida**. [*S.l.: s.n.*], 2018.

BRUNET, M.; AUBRY, S.; LAFAGE, R. The clean sky programme: environmental benefits at aircraft level. *In*: **15th AIAA Aviation Technology, Integration, and Operations Conference, AIAA 2015-2390. Dallas, Texas**. [*S.l.: s.n.*], 2015.

BUDZISZEWSKI, N.; FRIEDRICHS, J. Modelling of a boundary layer ingesting propulsor. **Energies**, MDPI, v. 11, n. 4, p. 708, 2018.

BUSEMANN, A. Compressible flow in the thirties. **Annual Review of Fluid Mechanics**, Annual Reviews 4139 El Camino Way, PO Box 10139, Palo Alto, CA 94303-0139, USA, v. 3, n. 1, p. 1–12, 1971.

BUSHNELL, D. Aircraft drag reduction—a review. **Proceedings of the Institution of Mechanical Engineers, Part G: Journal of Aerospace Engineering**, SAGE Publications Sage UK: London, England, v. 217, n. 1, p. 1–18, 2003.

BUSHNELL, D. M. **Enabling Electric Aircraft_Applications and Approaches**. [*S.l.*], 2018. NASA/TM–2018-220088.

BUSHNELL, D. M. **Ultra-Low to Emissionless Air Transport Design**. [*S.l.*], 2021. NASA/TM–20210021985.

BUTTAZZO, G.; FREDIANI, A. **Variational analysis and aerospace engineering: mathematical challenges for aerospace design**. [*S.l.: s.n.*]: Springer Science & Business Media, 2009. v. 66.

CAMBIER, L.; HEIB, S.; PLOT, S. The onera elsa CFD software: input from research and feedback from industry. **Mechanics & Industry**, EDP Sciences, v. 14, n. 3, p. 159–174, 2013.

CANTO, D. D. *et al.* The lifting system of a prandtlplane, part 1: design and analysis of a light alloy structural solution. *In*: **Variational analysis and aerospace engineering: mathematical challenges for aerospace design**. [*S.l.: s.n.*]: Springer, 2012. p. 211–234.

CARINI, M. *et al.* Aerodynamic analysis and optimization of a boxwing architecture for commercial airplanes. *In*: **AIAA Scitech 2020 Forum, AIAA 2020-1285. Orlando, Florida**. [*S.l.: s.n.*], 2020.

CARRIER, G. *et al.* Investigation of a strut-braced wing configuration for future commercial transport. *In*: **28th Congress of the International Council of the Aeronautical Sciences**. [*S.l.: s.n.*], 2012.

CARRIER, G. G. *et al.* Multidisciplinary analysis and design of strut-braced wing concept for medium range aircraft. *In*: **AIAA SCITECH 2022 Forum, AIAA 2022-0726. San Diego, CA and Virtual**. [*S.l.: s.n.*], 2022.

CARTER, M. B. *et al.* Designing and testing a blended wing body with boundary-layer ingestion nacelles. **Journal of aircraft**, v. 43, n. 5, p. 1479–1489, 2006.

CASALINO, D. *et al.* Aircraft noise reduction technologies: a bibliographic review. **Aerospace Science and Technology**, Elsevier, v. 12, n. 1, p. 1–17, 2008.

CATALANO, F. The new closed circuit wind tunnel of the aircraft laboratory of university of sao paulo, brazil. *In*: **24TH International Congress of the Aeronautical Sciencies**. [*S.l.: s.n.*], 2004.

CAVALLARO, R. *et al.* Prandtlplane joined wing: Body freedom flutter, limit cycle oscillation and freeplay studies. **Journal of Fluids and Structures**, Elsevier, v. 59, p. 57–84, 2015.

CAVALLARO, R.; DEMASI, L. Challenges, ideas, and innovations of joined-wing configurations: a concept from the past, an opportunity for the future. **Progress in Aerospace Sciences**, Elsevier, v. 87, p. 1–93, 2016.

CECERE, D.; GIACOMAZZI, E.; INGENITO, A. A review on hydrogen industrial aerospace applications. **International journal of hydrogen energy**, Elsevier, v. 39, n. 20, p. 10731–10747, 2014.

CENTRACCHIO, F.; ROSSETTI, M.; IEMMA, U. Approach to the weight estimation in the conceptual design of hybrid-electric-powered unconventional regional aircraft. **Journal of Advanced Transportation**, Hindawi, v. 2018, 2018.

CERÓN-MUÑOZ, H. Estudo da interferência aerodinâmica do sistema motopropulsor em uma aeronave do tipo BLENDED WING BODY. **São Carlos School of Engineering - University of São Paulo, PhD Thesis, Brazil**, 2009.

CERÓN-MUÑOZ, H.; CATALANO, F. Aerodynamic interference of power-plant system on a Blended Wing Body. *In*: **27TH International Congress of the Aeronautical Sciences, Nice, France**. [*S.l.: s.n.*], 2010.

CERÓN-MUÑOZ, H. *et al.* Experimental analyses of droop, wingtips and fences on a BWB model. *In*: **30th International Congress of the Aeronautical Sciences, Daejeon, Korea**. [*S.l.: s.n.*], 2016.

CHAKRABORTY, I. *et al.* Comparative assessment of strut-braced and truss-braced wing configurations using multidisciplinary design optimization. **Journal of Aircraft**, American Institute of Aeronautics and Astronautics, v. 52, n. 6, p. 2009–2020, 2015.

CHAU, T. Aerodynamic shape optimization of a box-wing regional aircraft based on the Reynolds-Averaged Navier-Stokes equations. **University of Toronto, Master Thesis, Canada**, 2017.

CHAU, T.; KENWAY, G.; KIRIS, C. C. Conceptual exploration of aircraft configurations for the SUSAN electrofan. *In*: **AIAA SCITECH 2022 Forum, AIAA 2022-2181. San Diego, CA and Virtual**. [*S.l.: s.n.*], 2022.

CHAU, T.; ZINGG, D. W. Aerodynamic shape optimization of a box-wing regional aircraft based on the Reynolds-Averaged Navier-Stokes equations. *In*: **35th AIAA Applied Aerodynamics Conference, AIAA 2017-3258. Denver, Colorado**. [*S.l.: s.n.*], 2017.

CHAU, T.; ZINGG, D. W. Aerodynamic design optimization of a transonic strut-braced-wing regional aircraft. **Journal of Aircraft**, American Institute of Aeronautics and Astronautics, p. 1–19, 2021.

CHAUHAN, S. S.; MARTINS, J. R. RANS-based aerodynamic shape optimization of a wing considering propeller–wing interaction. **Journal of Aircraft**, American Institute of Aeronautics and Astronautics, v. 58, n. 3, p. 497–513, 2021.

CHERNUKHIN, O.; ZINGG, D. W. Multimodality and global optimization in aerodynamic design. **AIAA journal**, American Institute of Aeronautics and Astronautics, v. 51, n. 6, p. 1342–1354, 2013.

CHIESA, S.; SCIUVA, M. D.; MAGGIORE, P. The double-fuselage layout: A preliminary case study of a possible way of reducing the development costs for new high-capacity aircraft. **Proceedings of the Institution of Mechanical Engineers, Part G: Journal of Aerospace Engineering**, SAGE Publications Sage UK: London, England, v. 214, n. 2, p. 85–95, 2000.

CHRISTOPHER, D. *et al.* **Subsonic Ultra Green Aircraft Research: Phase III – Mach 0.75 Transonic Truss-Braced Wing Design**. [*S.l.*], 2020. NASA/CR–20205005698.

CHUANG, Y.-C.; CHEN, C.-T.; HWANG, C. A real-coded genetic algorithm with a direction-based crossover operator. **Information Sciences**, Elsevier, v. 305, p. 320–348, 2015.

CHUANG, Y.-C.; CHEN, C.-T.; HWANG, C. A simple and efficient real-coded genetic algorithm for constrained optimization. **Applied Soft Computing**, Elsevier, v. 38, p. 87–105, 2016.

CIAMPA, P. D.; NAGEL, B. AGILE paradigm: the next generation collaborative MDO for the development of aeronautical systems. **Progress in Aerospace Sciences**, Elsevier, v. 119, p. 100643, 2020.

CIAMPA, P. D. *et al.* Streamlining cross-organizational aircraft development: results from the AGILE project. *In*: **AIAA Aviation 2019 Forum, AIAA 2019-3454. Dallas, Texas**. [*S.l.: s.n.*], 2019.

CIPOLLA, V. *et al.* A DoE-based approach for the implementation of structural surrogate models in the early stage design of box-wing aircraft. **Aerospace Science and Technology**, p. 106968, 2021. ISSN 1270-9638.

CIPOLLA, V. *et al.* Ultralight amphibious prandtlplane: the final design. **Aerotecnica Missili & Spazio**, Springer, v. 95, n. 3, p. 125–135, 2016.

CIPOLLA, V.; SALEM, K. A.; BACHI, F. Preliminary stability analysis methods for prandtlplane aircraft in subsonic conditions. **Aircraft Engineering and Aerospace Technology**, Emerald Publishing Limited, v. 91, n. 3, p. 525–537, 2019.

CIPOLLA, V. *et al.* Preliminary design and performance analysis of a box-wing transport aircraft. *In*: **AIAA Scitech 2020 Forum, AIAA 2020-0267. Orlando, Florida**. [*S.l.: s.n.*], 2020.

COELLO, C. A. C. Theoretical and numerical constraint-handling techniques used with evolutionary algorithms: a survey of the state of the art. **Computer methods in applied mechanics and engineering**, Elsevier, v. 191, n. 11-12, p. 1245–1287, 2002.

CORTE, B. D. *et al.* Aerodynamic performance of an aircraft with aft-fuselage boundary-layer-ingestion propulsion. **Journal of Aircraft**, American Institute of Aeronautics and Astronautics, p. 1–17, 2022.

CORTE, B. D. *et al.* Power balance analysis experiments on an axisymmetric fuselage with an integrated boundary-layer-ingesting fan. **AIAA Journal**, American Institute of Aeronautics and Astronautics, p. 1–14, 2021.

CUMPSTY, N. *et al.* Report of the independent experts integrated technology goals assessment and review for engines engines and aircraft. **ICAO Report**, 2017.

DAGGETT, D.; HENDRICKS, R.; WALTHER, R. **Alternative fuels and their potential impact on aviation**. [*S.l.*], 2006. NASA/TM-2006-214365.

DAGGETT, D. L. *et al.* **Alternate fuels for use in commercial aircraft**. [*S.l.*], 2008. NASA/TM–2008-214833.

DAGGETT, D. L. *et al.* **Blended wing body systems studies: boundary layer ingestion inlets with active flow control**. [*S.l.*], 2003. NASA/CR-2003-212670.

DEMASI, L.; MONEGATO, G.; CAVALLARO, R. Minimum induced drag theorems for nonplanar systems and closed wings. *In*: **Variational Analysis and Aerospace Engineering**. [*S.l.: s.n.*]: Springer, 2016. p. 191–217.

DEMASI, L.; MONEGATO, G.; CAVALLARO, R. Minimum induced drag theorems for multiwing systems. **AIAA Journal**, American Institute of Aeronautics and Astronautics, v. 55, n. 10, p. 3266–3287, 2017.

DEMASI, L. *et al.* Optimum induced drag of wingtip devices: the concept of best winglet design. **Aerotecnica Missili & Spazio**, Springer, p. 1–33, 2022.

DEMASI, L. *et al.* Minimum induced drag theorems for joined wings, closed systems, and generic biwings: Applications. **Journal of Optimization Theory and Applications**, Springer, v. 169, n. 1, p. 236–261, 2016.

DEPERROIS, A. Xflr5 analysis of foils and wings operating at low reynolds numbers. **Guidelines for XFLR5**, v. 142, 2009.

DIAMANTIDOU, D. E.; HOSAIN, M. L.; KYPRIANIDIS, K. G. Recent advances in boundary layer ingestion technology of evolving powertrain systems. **Sustainability**, Multidisciplinary Digital Publishing Institute, v. 14, n. 3, p. 1731, 2022.

DIAZ, P.; YOON, S.; THEODORE, C. High-fidelity computational aerodynamics of the elytron 4S UAV. *In*: **AHS Technical Conference on Aeromechanics Design for Transformative Vertical Flight, No. sm_aeromech_2018_02, American Helicopter Socety International**. [*S.l.: s.n.*], 2018.

DOMMELEN, J. van; VOS, R. Conceptual design and analysis of blended-wing-body aircraft. **Proceedings of the Institution of Mechanical Engineers, Part G: Journal of Aerospace Engineering**, SAGE Publications Sage UK: London, England, v. 228, n. 13, p. 2452–2474, 2014.

DORSEY, A.; URANGA, A. Design space exploration of future open rotor configurations. *In*: **AIAA Propulsion and Energy 2020 Forum, AIAA 2020-3680. Virtual event**. [*S.l.: s.n.*], 2020.

DORSEY, A.; URANGA, A. Design space exploration of blended wing bodies. *In*: **AIAA AVIATION 2021 FORUM, AIAA 2021-2422. Virtual event**. [*S.l.: s.n.*], 2021.

DRELA, M. Power balance in aerodynamic flows. **AIAA journal**, v. 47, n. 7, p. 1761–1771, 2009.

DRELA, M. **TASOPT 2.00**. 2010. Accessed in 28/05/2019. Available from Internet: http://web.mit.edu/drela/Public/N+3/TASOPT_doc.pdf.

DRELA, M. Development of the D8 transport configuration. *In*: **29th AIAA Applied Aerodynamics Conference, AIAA 2011-3970. Honolulu, Hawaii**. [*S.l.: s.n.*], 2011.

DRONEY, C. *et al.* **Subsonic Ultra Green Aircraft Research: Phase III – Mach 0.75 Transonic Truss-Braced Wing Design**. [*S.l.*], 2020. NASA/CR–2015-20205005698.

DRUOT, T. Y. *et al.* Hydrogen powered airplanes, an exploration of possible architectures leveraging boundary layer ingestion and hybridization. *In*: **AIAA SCITECH 2022 Forum, AIAA 2022-1025. San Diego, CA and Virtual**. [*S.l.: s.n.*], 2022.

DURAND, W. F. **Aerodynamic Theory: A General Review of Progress Under a Grant of the Guggenheim Fund for the Promotion of Aeronautics**. [*S.l.: s.n.*]: Springer-Verlag, 2013.

EARLY, K. Propulsion airframe integration design, analysis and challenges going into the 21st century. **Aeronautical Journal**, London, Royal Aeronautical Society., v. 104, n. 1038, p. 375–381, 2000.

ECONOMON, T. D. *et al.* SU2: An open-source suite for multiphysics simulation and design. **AIAA Journal**, American Institute of Aeronautics and Astronautics, v. 54, n. 3, p. 828–846, 2015.

EGUEA, J. P.; BRAVO-MOSQUERA, P. D.; CATALANO, F. M. Camber morphing winglet influence on aircraft drag breakdown and tip vortex structure. **Aerospace Science and Technology**, Elsevier, v. 119, p. 107148, 2021.

EGUEA, J. P.; SILVA, G. P. G. da; CATALANO, F. M. Fuel efficiency improvement on a business jet using a camber morphing winglet concept. **Aerospace Science and Technology**, Elsevier, v. 96, p. 105542, 2020.

ELMENDORP, R.; VOS, R.; ROCCA, G. L. A conceptual design and analysis method for conventional and unconventional airplanes. *In*: **29th Congress of the International Council of the Aeronautical Sciences, St. Petersburg, Russia**. [*S.l.: s.n.*], 2014.

EPSTEIN, A. H.; O'FLARITY, S. M. Considerations for reducing aviation's co 2 with aircraft electric propulsion. **Journal of Propulsion and Power**, American Institute of Aeronautics and Astronautics, v. 35, n. 3, p. 572–582, 2019.

FAGGIANO, F. *et al.* Aerodynamic design of a flying V aircraft. *In*: **17th AIAA Aviation Technology, Integration, and Operations Conference, AIAA 2017-3589. Denver, Colorado**. [*S.l.: s.n.*], 2017.

FARASSAT, F. *et al.* Open rotor noise prediction methods at NASA langley: A technology review. *In*: **15th AIAA/CEAS Aeroacoustics Conference (30th AIAA Aeroacoustics Conference), AIAA 2009-3133. Miami, Florida**. [*S.l.: s.n.*], 2009.

FELDER, J.; KIM, H.; BROWN, G. Turboelectric distributed propulsion engine cycle analysis for hybrid-wing-body aircraft. *In*: **47th AIAA aerospace sciences meeting including the new horizons forum and aerospace exposition, AIAA 2009-1132. Orlando, Florida**. [*S.l.: s.n.*], 2009.

FELDER, J. *et al.* An examination of the effect of boundary layer ingestion on turboelectric distributed propulsion systems. *In*: **49th AIAA aerospace sciences meeting including the new horizons forum and aerospace exposition, AIAA 2011-300. Orlando, Florida**. [*S.l.: s.n.*], 2011.

FERNÁNDEZ, A. M.; SMITH, H. Effect of a fuselage boundary layer ingesting propulsor on airframe forces and moments. **Aerospace Science and Technology**, Elsevier, v. 100, p. 105808, 2020.

FERNÁNDEZ, D. C. D. R.; HICKEN, J. E.; ZINGG, D. W. Review of summation-by-parts operators with simultaneous approximation terms for the numerical solution of partial differential equations. **Computers & Fluids**, Elsevier, v. 95, p. 171–196, 2014.

FILIPPONE, A. Aircraft noise prediction. **Progress in Aerospace Sciences**, Elsevier, v. 68, p. 27–63, 2014.

FINLAYSON, M. A. Ansys ICEM CFD user's manual. *In*: **ANSYS, Inc. Canonsburg, PA, Nov**. [*S.l.: s.n.*], 2013.

FLYING-V. 2021. Accessed in 23/03/2021. Available from Internet: https://www.tudelft.nl/lr/flying-v.

FREDIANI, A.; CIPOLLA, V.; OLIVIERO, F. IDINTOS: the first prototype of an amphibious prandtlplane-shaped aircraft. **Aerotecnica Missili & Spazio**, Springer, v. 94, n. 3, p. 195–209, 2015.

FREDIANI, A.; CIPOLLA, V.; RIZZO, E. The prandtlplane configuration: overview on possible applications to civil aviation. *In*: **Variational Analysis and Aerospace Engineering: Mathematical Challenges for Aerospace Design**. [*S.l.: s.n.*]: Springer, 2012. p. 179–210.

FREDIANI, A. *et al.* Conceptual design of prandtlplane civil transport aircraft. **Proceedings of the Institution of Mechanical Engineers, Part G: Journal of Aerospace Engineering**, SAGE Publications Sage UK: London, England, p. 0954410019826435, 2019.

FREDIANI, A.; MONTANARI, G. Best wing system: an exact solution of the prandtl's problem. *In*: **Variational Analysis and Aerospace Engineering**. [*S.l.: s.n.*]: Springer, 2009. p. 183–211.

FRENKEN, K.; LEYDESDORFF, L. Scaling trajectories in civil aircraft (1913–1997). **Research Policy**, Elsevier, v. 29, n. 3, p. 331–348, 2000.

FRIEDRICHS, J. *et al.* Vehicle technologies towards sustainable and energy efficient aviation. *In*: **AIAA SCITECH 2022 Forum, AIAA 2022-0685. San Diego, CA and Virtual**. [*S.l.: s.n.*], 2022.

FROTA, J. Nacre novel aircraft concepts. **The Aeronautical Journal**, Cambridge University Press, v. 114, n. 1156, p. 399–404, 2010.

GAGNON, H.; ZINGG, D. W. High-fidelity aerodynamic shape optimization of unconventional aircraft through axial deformation. *In*: **52nd Aerospace Sciences Meeting, AIAA 2014-0908. National Harbor, Maryland**. [*S.l.: s.n.*], 2014.

GAGNON, H.; ZINGG, D. W. Two-level free-form and axial deformation for exploratory aerodynamic shape optimization. **Aiaa Journal**, American Institute of Aeronautics and Astronautics, v. 53, n. 7, p. 2015–2026, 2015.

GAGNON, H.; ZINGG, D. W. Aerodynamic optimization trade study of a box-wing aircraft configuration. **Journal of Aircraft**, American Institute of Aeronautics and Astronautics, v. 53, n. 4, p. 971–981, 2016.

GAGNON, H.; ZINGG, D. W. Euler-equation-based drag minimization of unconventional aircraft configurations. **Journal of Aircraft**, American Institute of Aeronautics and Astronautics, v. 53, n. 5, p. 1361–1371, 2016.

GARCIA-BENITEZ, J. *et al.* Conceptual design of a nonplanar wing airliner. **Aircraft Engineering and Aerospace Technology: An International Journal**, Emerald Group Publishing Limited, v. 88, n. 4, p. 561–571, 2016.

GENT, I. van; ROCCA, G. L. Formulation and integration of MDAO systems for collaborative design: A graph-based methodological approach. **Aerospace Science and Technology**, Elsevier, v. 90, p. 410–433, 2019.

GERN, F. H. Conceptual design and structural analysis of an open rotor hybrid wing body aircraft. *In*: **54th AIAA/ASME/ASCE/AHS/ASC Structures, Structural Dynamics, and Materials Conference, AIAA 2013-1688. Boston, Massachusetts**. [*S.l.: s.n.*], 2013.

GERN, F. H. *et al.* Multidisciplinary design optimization of a transonic commercial transport with strut-braced wing. **Journal of aircraft**, v. 38, n. 6, p. 1006–1014, 2001.

GILL, P. E.; MURRAY, W.; SAUNDERS, M. A. Snopt: An sqp algorithm for large-scale constrained optimization. **SIAM review**, SIAM, v. 47, n. 1, p. 99–131, 2005.

GNADT, A. R. *et al.* Technical and environmental assessment of all-electric 180-passenger commercial aircraft. **Progress in Aerospace Sciences**, Elsevier, 2018.

GOHARDANI, A. S. A synergistic glance at the prospects of distributed propulsion technology and the electric aircraft concept for future unmanned air vehicles and commercial/military aviation. **Progress in Aerospace Sciences**, Elsevier, v. 57, p. 25–70, 2013.

GOHARDANI, A. S.; DOULGERIS, G.; SINGH, R. Challenges of future aircraft propulsion: A review of distributed propulsion technology and its potential application for the all electric commercial aircraft. **Progress in Aerospace Sciences**, Elsevier, v. 47, n. 5, p. 369–391, 2011.

GOLDBERG, C. *et al.* Performance assessment of a boundary layer ingesting distributed propulsion system at off-design. *In*: **53rd AIAA/SAE/ASEE Joint Propulsion Conference, AIAA 2017-5055. Atlanta, GA**. [*S.l.: s.n.*], 2017.

GRAHAM, W. R.; HALL, C. A.; MORALES, M. V. The potential of future aircraft technology for noise and pollutant emissions reduction. **Transport Policy**, Elsevier, v. 34, p. 36–51, 2014.

GRANT, R. G. Flight–100 years of aviation. **Aircraft Engineering and Aerospace Technology**, Emerald Group Publishing Limited, v. 75, n. 2, 2003.

GRASMEYER, J. Multidisciplinary design optimization of a transonic strut-braced wing aircraft. *In*: **37th Aerospace Sciences Meeting and Exhibit, AIAA 1999-10. Reno, Nevada**. [*S.l.: s.n.*], 1999.

GRAY, A.; REIST, T.; ZINGG, D. W. Further exploration of regional-class hybrid wing-body aircraft through multifidelity optimization. *In*: **AIAA Scitech 2021 Forum, AIAA 2021-0014. Virtual event**. [*S.l.: s.n.*], 2021.

GRAY, J. S. *et al.* Openmdao: An open-source framework for multidisciplinary design, analysis, and optimization. **Structural and Multidisciplinary Optimization**, Springer, p. 1–30, 2019.

GRAY, J. S. *et al.* Modeling boundary layer ingestion using a coupled aeropropulsive analysis. **Journal of Aircraft**, American Institute of Aeronautics and Astronautics, v. 55, n. 3, p. 1191–1199, 2018.

GRAY, J. S. *et al.* Coupled aeropropulsive optimization of a three-dimensional boundary-layer ingestion propulsor considering inlet distortion. **Journal of Aircraft**, American Institute of Aeronautics and Astronautics, v. 57, n. 6, p. 1014–1025, 2020.

GRAY, J. S.; MARTINS, J. R. Coupled aeropropulsive design optimisation of a boundary-layer ingestion propulsor. **The Aeronautical Journal**, Cambridge University Press, v. 123, n. 1259, p. 121–137, 2019.

GREEN, J. Greener by design—the technology challenge. **The Aeronautical Journal**, Cambridge University Press, v. 106, n. 1056, p. 57–113, 2002.

GREEN, J. *et al.* Air travel-greener by design. mitigating the environmental impact of aviation: opportunities and priorities. **The Aeronautical Journal**, v. 109, n. 1099, p. 361–418, 2005.

GREITZER, E. M. *et al.* N+3 aircraft concept designs and trade studies, final report. **NASA CR-2010-216794/vol2, NASA Glenn Research Center, Cleveland, Ohio**, v. 44135, 2010.

GUNDLACH, J. F. *et al.* Conceptual design studies of a strut-braced wing transonic transport. **Journal of Aircraft**, v. 37, n. 6, p. 976–983, 2000.

GUPTA, K. K.; REHMAN, A.; SARVIYA, R. Bio-fuels for the gas turbine: A review. **Renewable and Sustainable Energy Reviews**, Elsevier, v. 14, n. 9, p. 2946–2955, 2010.

GUR, O. *et al.* Development of a framework for truss-braced wing conceptual MDO. **Structural and Multidisciplinary Optimization**, Springer, v. 44, n. 2, p. 277–298, 2011.

GUR, O. *et al.* Design optimization of a truss-braced-wing transonic transport aircraft. **Journal of aircraft**, v. 47, n. 6, p. 1907–1917, 2010.

GUR, O.; MASON, W. H.; SCHETZ, J. A. Full-configuration drag estimation. **Journal of Aircraft**, v. 47, n. 4, p. 1356–1367, 2010.

GUR, O.; SCHETZ, J. A.; MASON, W. H. Aerodynamic considerations in the design of truss-braced-wing aircraft. **Journal of Aircraft**, v. 48, n. 3, p. 919–939, 2011.

GUYNN, M. *et al.* Analysis of turbofan design options for an advanced single-aisle transport aircraft. *In*: **9th AIAA Aviation Technology, Integration, and Operations Conference (ATIO) and Aircraft Noise and Emissions Reduction Symposium (ANERS), AIAA 2009-6942. Hilton Head, South Carolina**. [*S.l.: s.n.*], 2009.

GUYNN, M. *et al.* Initial assessment of open rotor propulsion applied to an advanced single-aisle aircraft. *In*: **11th AIAA Aviation Technology, Integration, and Operations (ATIO) Conference, including the AIAA Balloon Systems Conference and 19th AIAA Lighter-Than, AIAA 2011-7058. Virginia Beach, Virginia**. [*S.l.: s.n.*], 2011.

GUYNN, M. D. *et al.* **Performance and environmental assessment of an advanced aircraft with open rotor propulsion**. [*S.l.*], 2012. NASA/TM-2012-217772.

HABERMANN, A. *et al.* Performance bookkeeping for aircraft configurations with fuselage wake-filling propulsion integration. **CEAS Aeronautical Journal**, Springer, p. 1–23, 2019.

HALL, D. *et al.* **Feasibility of Electrified Propulsion for Ultra-Efficient Commercial Aircraft Final Report**. [*S.l.*], 2019. NASA/CR—2019-220382.

HALL, D. K. *et al.* Boundary layer ingestion propulsion benefit for transport aircraft. **Journal of Propulsion and Power**, American Institute of Aeronautics and Astronautics, v. 33, n. 5, p. 1118–1129, 2017.

HALL, D. K.; LIEU, M. Propulsor models for computational analysis of aircraft aerodynamic performance with boundary layer ingestion. *In*: **AIAA Scitech 2021 Forum, AIAA 2021-0991. Virtual event**. [*S.l.: s.n.*], 2021.

HANSEN, L. *et al.* Representation of structural solutions in blended wing body preliminary design. **Paper ICAS**, v. 1, n. 4, p. 2006, 2006.

HANTRAIS-GERVOIS, J.-L.; PIAT, J.-F.; HANTRAIS, J.-L. A methodology to derive wind tunnel wall corrections from rans simulations. **Integration**, 2012.

HARRISON, N. A. *et al.* Development of an efficient M= 0.80 transonic truss-braced wing aircraft. *In*: **AIAA Scitech 2020 Forum, AIAA 2020-0011. Orlando, Florida**. [*S.l.: s.n.*], 2020.

HASSAN, M.; MAVRIS, D. Impact of vehicle technologies and operational improvements on aviation system fuel burn. **Journal of Aircraft**, American Institute of Aeronautics and Astronautics, p. 1–10, 2019.

HE, P. *et al.* Dafoam: An open-source adjoint framework for multidisciplinary design optimization with openfoam. **AIAA Journal**, American Institute of Aeronautics and Astronautics, p. 1–16, 2020.

HEERDEN, A. S. van; GUENOV, M. D.; MOLINA-CRISTÓBAL, A. Evolvability and design reuse in civil jet transport aircraft. **Progress in Aerospace Sciences**, Elsevier, 2019.

HEFNER, J. N.; BUSHNELL, D. M. An overview of concepts for aircraft drag reductions. n. 77N32092, 1977.

HENDRICKS, E. S. **A review of boundary layer ingestion modeling approaches for use in conceptual design**. [*S.l.*], 2018. NASA/TM—2018-219926.

HEPPERLE, M. Electric flight-potential and limitations. **AVT-209 Workshop on Energy Efficient Technologies and Concepts Operation**, 2012.

HICKEN, J. E.; ZINGG, D. W. Parallel newton-krylov solver for the euler equations discretized using simultaneous approximation terms. **AIAA journal**, v. 46, n. 11, p. 2773–2786, 2008.

HICKEN, J. E.; ZINGG, D. W. Aerodynamic optimization algorithm with integrated geometry parameterization and mesh movement. **AIAA journal**, v. 48, n. 2, p. 400–413, 2010.

HICKEN, J. E.; ZINGG, D. W. Induced-drag minimization of nonplanar geometries based on the euler equations. **AIAA journal**, v. 48, n. 11, p. 2564–2575, 2010.

HILEMAN, J. *et al.* Airframe design for silent fuel-efficient aircraft. **Journal of aircraft**, v. 47, n. 3, p. 956–969, 2010.

HILEMAN, J. I. *et al.* The carbon dioxide challenge facing aviation. **Progress in Aerospace Sciences**, Elsevier, v. 63, p. 84–95, 2013.

HOOGREEF, M. *et al.* Conceptual assessment of hybrid electric aircraft with distributed propulsion and boosted turbofans. *In*: **AIAA Scitech 2019 Forum, AIAA 2019-1807. San Diego, California**. [*S.l.: s.n.*], 2019.

HORNUNG, M. *et al.* Ce-liner-case study for emobility in air transportation. *In*: **2013 Aviation Technology, Integration, and Operations Conference, AIAA 2013-4302. Los Angeles, California**. [*S.l.: s.n.*], 2013.

HOSSEINI, S. *et al.* Conceptual design and analysis of an affordable truss-braced wing regional jet aircraft. **Proceedings of the Institution of Mechanical Engineers, Part G: Journal of Aerospace Engineering**, SAGE Publications Sage UK: London, England, p. 0954410020923060, 2020.

HUETE, J.; PILIDIS, P. Parametric study on tank integration for hydrogen civil aviation propulsion. **International Journal of Hydrogen Energy**, Elsevier, 2021.

IATA - Aircraft Technology Roadmap to 2050. 2021. Accessed in 23/03/2021. Available from Internet: https://www.iata.org/en/programs/environment/technology-roadmap/.

ICAO - Effects of Novel Coronavirus (COVID-19) on Civil Aviation: Economic Impact Analysis, International Civil Aviation Organization. 2021. Accessed in 05/03/2021. Available from Internet: http://www.asma.org.

IEMMA, U.; VITAGLIANO, F. P.; CENTRACCHIO, F. Multi-objective design optimization of sustainable commercial a-ircraft: performance and costs. **International Journal of Sustainable Engineering**, Taylor & Francis, v. 10, n. 3, p. 147–157, 2017.

ISIKVEREN, A. T. *et al.* Distributed propulsion and ultra-high by-pass rotor study at aircraft level. **The Aeronautical Journal**, Cambridge University Press, v. 119, n. 1221, p. 1327–1376, 2015.

IWANIZKI, M. *et al.* Conceptual design studies of unconventional configurations. *In*: **3AF Aerospace Europe Conference 2020, hal-02907205f**. [*S.l.: s.n.*], 2020.

JAMESON, A. Aerodynamic design via control theory. **Journal of scientific computing**, Springer, v. 3, n. 3, p. 233–260, 1988.

JANSEN, R. *et al.* Overview of NASA electrified aircraft propulsion (EAP) research for large subsonic transports. *In*: **53rd AIAA/SAE/ASEE Joint Propulsion Conference, AIAA 2017-4701. Atlanta, Georgia**. [*S.l.: s.n.*], 2017.

JANSEN, R. *et al.* Subsonic single aft engine (SUSAN) transport aircraft concept and trade space exploration. *In*: **AIAA SCITECH 2022 Forum, AIAA 2022-2179. San Diego, CA and Virtual**. [*S.l.: s.n.*], 2022.

JEMITOLA, P.; FIELDING, J.; STOCKING, P. Joint fixity effect on structural design of a box wing aircraft. **The Aeronautical Journal**, Cambridge University Press, v. 116, n. 1178, p. 363–372, 2012.

JEMITOLA, P.; MONTERZINO, G.; FIELDING, J. Wing mass estimation algorithm for medium range box wing aircraft. **The Aeronautical Journal**, Cambridge University Press, v. 117, n. 1189, p. 329–340, 2013.

JEMITOLA, P. O. Conceptual design and optimization methodology for box wing aircraft. **Cranfield University, PhD Thesis, England**, 2012.

JOHNSON, M. E.; GONZALEZ, A. Estimating cost savings for aviation fuel and CO2 emission reductions strategies. **The Collegiate Aviation Review International**, v. 31, n. 2, 2018.

JONES, R. T. **Wing planforms for high-speed flight**. [*S.l.*], 1946. Technical Note 1033.

JONES, R. T. **Theory of wing-body drag at supersonic speeds**. [*S.l.*], 1956. NACA-TR-1284.

JONSSON, E. *et al.* Flutter and post-flutter constraints in aircraft design optimization. **Progress in Aerospace Sciences**, Elsevier, v. 109, p. 100537, 2019.

JOSLIN, R. D. Aircraft laminar flow control. **Annual review of fluid mechanics**, Annual Reviews 4139 El Camino Way, PO Box 10139, Palo Alto, CA 94303-0139, USA, v. 30, n. 1, p. 1–29, 1998.

JOSLIN, R. D. **Overview of laminar flow control**. [*S.l.*], 1998. NASA/TP-1998-208705.

JUPP, J. The design of future passenger aircraft–the environmental and fuel price challenges. **The Aeronautical Journal**, Cambridge University Press, v. 120, n. 1223, p. 37–60, 2016.

KAPAROS, P. *et al.* Conceptual design methodology of a box wing aircraft: A novel commercial airliner. **Proceedings of the Institution of Mechanical Engineers, Part G: Journal of Aerospace Engineering**, SAGE Publications Sage UK: London, England, v. 232, n. 14, p. 2651–2662, 2018.

KARPUK, S.; ELHAM, A. Conceptual design trade study for an energy-efficient mid-range aircraft with novel technologies. *In*: **AIAA Scitech 2021 Forum, AIAA 2021-0013. Virtual event**. [*S.l.: s.n.*], 2021.

KARPUK, S.; LIU, Y.; ELHAM, A. Multi-fidelity design optimization of a long-range blended wing body aircraft with new airframe technologies. **Aerospace**, Multidisciplinary Digital Publishing Institute, v. 7, n. 7, p. 87, 2020.

KARPUK, S. *et al.* Development of a multi-fidelity design, analysis, and optimization environment for future transport aircraft. *In*: **AIAA SCITECH 2022 Forum, AIAA 2022-0686. San Diego, CA and Virtual**. [*S.l.: s.n.*], 2022.

KAWAI, R. T. **Acoustic prediction methodology and test validation for an efficient low-noise hybrid wing body subsonic transport**. [*S.l.*], 2011. NASA/NF1676L-14465.

KEHAYAS, N. Aeronautical technology for future subsonic civil transport aircraft. **Aircraft Engineering and Aerospace Technology**, Emerald Group Publishing Limited, v. 79, n. 6, p. 600–610, 2007.

KELLARI, D.; CRAWLEY, E. F.; CAMERON, B. G. Influence of technology trends on future aircraft architecture. **Journal of Aircraft**, American Institute of Aeronautics and Astronautics, v. 54, n. 6, p. 2213–2227, 2017.

KELLARI, D.; CRAWLEY, E. F.; CAMERON, B. G. Architectural decisions in commercial aircraft from the dc-3 to the 787. **Journal of Aircraft**, American Institute of Aeronautics and Astronautics, v. 55, n. 2, p. 792–804, 2018.

KENWAY, G. K. *et al.* Effective adjoint approaches for computational fluid dynamics. **Progress in Aerospace Sciences**, Elsevier, p. 100542, 2019.

KHAN, F. A. **Preliminary aerodynamic investigation of box-wing configurations using low fidelity codes**. [*S.l.: s.n.*], 2010.

KHANDELWAL, B. *et al.* Hydrogen powered aircraft: The future of air transport. **Progress in Aerospace Sciences**, Elsevier, v. 60, p. 45–59, 2013.

KIM, H.; LIOU, M.-F. Flow simulation and drag decomposition study of n3-x hybrid wing-body configuration. **Aerospace Science and Technology**, Elsevier, v. 85, p. 24–39, 2019.

KIM, H.; LIOU, M.-S. Shape design optimization of embedded engine inlets for N2B hybrid wing-body configuration. **Aerospace Science and Technology**, Elsevier, v. 30, n. 1, p. 128–149, 2013.

KIM, H.; LIOU, M.-S. Flow simulation and optimal shape design of n3-x hybrid wing body configuration using a body force method. **Aerospace Science and Technology**, Elsevier, v. 71, p. 661–674, 2017.

KIM, H. D.; BROWN, G. V.; FELDER, J. L. **Distributed turboelectric propulsion for hybrid wing body aircraft**. [*S.l.*], 2008. WBS 561581.02.08.03.13.03.

KIM, H. D.; PERRY, A. T.; ANSELL, P. J. A review of distributed electric propulsion concepts for air vehicle technology. *In*: **2018 AIAA/IEEE Electric Aircraft Technologies Symposium (EATS), AIAA 2018-4998. Cincinnati, Ohio**. [*S.l.: s.n.*], 2018. p. 1–21.

KIRACI, K.; AKAN, E. Aircraft selection by applying AHP and TOPSIS in interval type-2 fuzzy sets. **Journal of Air Transport Management**, Elsevier, v. 89, p. 101924, 2020.

KIRBY, M.; BARROS, P.; MAVRIS, D. Enhancing the environmnetal policy making process with the FAA's EDS analysis tool. *In*: **47th AIAA Aerospace Sciences Meeting including The New Horizons Forum and Aerospace Exposition, AIAA 2009-1262. Orlando, Florida**. [*S.l.: s.n.*], 2009.

KNOBLOCH, K. *et al.* Future aircraft and the future of aircraft noise. *In*: **Leylekian L., Covrig A., Maximova A. (eds) Aviation Noise Impact Management**. [*S.l.: s.n.*]: Springer, Cham, 2022. p. 117–139.

KO, A. *et al.* MDO of a blended-wing-body transport aircraft with distributed propulsion. *In*: **AIAA's 3rd Annual Aviation Technology, Integration, and Operations (ATIO) Forum, AIAA 2003-6732. Denver, Colorado**. [*S.l.: s.n.*], 2003.

KONING, W. J. *et al.* **Mid-Fidelity Computational Fluid Dynamics Analysis of the Elytron 4S UAV Concept**. [*S.l.*], 2018. NASA/TM-2018y219788.

KRAMER, D. Hydrogen-powered aircraft may be getting a lift. **Physics today**, American Institute of Physics, v. 73, n. 12, p. 27–31, 2020.

KRISHNAN, K.; BERTRAM, O.; SEIBEL, O. Review of hybrid laminar flow control systems. **Progress in Aerospace Sciences**, Elsevier, v. 93, p. 24–52, 2017.

KROO, I. Drag due to lift: concepts for prediction and reduction. **Annual review of fluid mechanics**, Annual Reviews 4139 El Camino Way, PO Box 10139, Palo Alto, CA 94303-0139, USA, v. 33, n. 1, p. 587–617, 2001.

KROO, I. Nonplanar wing concepts for increased aircraft efficiency. **VKI lecture series on innovative configurations and advanced concepts for future civil aircraft**, VKI, p. 6–10, 2005.

KRUSE, M.; WUNDERLICH, T.; HEINRICH, L. A conceptual study of a transonic NLF transport aircraft with forward swept wings. *In*: **30th AIAA Applied Aerodynamics Conference, AIAA 2012-3208. New Orleans, Louisiana**. [*S.l.: s.n.*], 2012.

KUSUNOSE, K.; MATSUSHIMA, K.; MARUYAMA, D. Supersonic biplane—a review. **Progress in Aerospace Sciences**, Elsevier, v. 47, n. 1, p. 53–87, 2011.

LANGE, R. *et al.* **Feasibility study of the transonic biplane concept for transport aircraft application**. [*S.l.*], 1974. NASA-CR-132462.

LANGE, R. H. Review of unconventional aircraft design concepts. **Journal of Aircraft**, v. 25, n. 5, p. 385–392, 1988.

LARSSON, L.; NSTEDT, T. G.; KYPRIANIDIS, K. G. Conceptual design and mission analysis for a geared turbofan and an open rotor configuration. *In*: **Turbo Expo: Power for Land, Sea, and Air, GT2011-46451. Vancouver, British Columbia**. [*S.l.: s.n.*], 2011. v. 54617, p. 359–370.

LEE, J. J. *et al.* Historical and future trends in aircraft performance, cost, and emissions. **Annual Review of Energy and the Environment**, Annual Reviews 4139 El Camino Way, PO Box 10139, Palo Alto, CA 94303-0139, USA, v. 26, n. 1, p. 167–200, 2001.

LEIFSSON, L. *et al.* Multidisciplinary design optimization of blended-wing-body transport aircraft with distributed propulsion. **Aerospace Science and Technology**, Elsevier, v. 25, n. 1, p. 16–28, 2013.

LEQUEU, P. *et al.* Engineering for the future: weight saving and cost reduction initiatives. **Aircraft Engineering and Aerospace Technology**, MCB UP Ltd, v. 73, n. 2, p. 147–159, 2001.

LIEBECK, R. Blended wing body design challenges. *In*: **AIAA International Air and Space Symposium and Exposition: The Next 100 Years, AIAA 2003-2659. Dayton, Ohio**. [*S.l.: s.n.*], 2003.

LIEBECK, R. H. Design of the blended wing body subsonic transport. **Journal of aircraft**, v. 41, n. 1, p. 10–25, 2004.

LIOU, M.-S.; KIM, H.; LIOU, M.-F. **Challenges and progress in aerodynamic design of hybrid wingbody aircraft with embedded engines**. [*S.l.*], 2016. NASA/TM-2016-218309.

LOCKHEED-MARTIN-BOX-WING. **Lockheed Martin's box-wing concept for the N+2 study**. 2017. Accessed in 31/05/2019. Available from Internet: https://www.nasa.gov/topics/aeronautics/features/greener_aircraft.html.

LUKACZYK, T. W. *et al.* SUAVE: an open-source environment for multi-fidelity conceptual vehicle design. *In*: **16th AIAA/ISSMO Multidisciplinary Analysis and Optimization Conference, AIAA 2015-3087. Dallas, Texas**. [*S.l.: s.n.*], 2015.

LV, P. *et al.* Performance analysis of wake and boundary-layer ingestion for aircraft design. **Journal of Aircraft**, American Institute of Aeronautics and Astronautics, v. 53, n. 5, p. 1517–1526, 2016.

LYU, Z.; MARTINS, J. R. Aerodynamic design optimization studies of a blended-wing-body aircraft. **Journal of Aircraft**, American Institute of Aeronautics and Astronautics, v. 51, n. 5, p. 1604–1617, 2014.

MA, Y.; ELHAM, A. Twin-fuselage configuration for improving fuel efficiency of passenger aircraft. **Aerospace Science and Technology**, Elsevier, v. 118, p. 107000, 2021.

MA, Y.; KARPUK, S.; ELHAM, A. Conceptual design and comparative study of strut-braced wing and twin-fuselage aircraft configurations with ultra-high aspect ratio wings. **Aerospace Science and Technology**, v. 121, p. 107395, 2022. ISSN 1270-9638.

MACHADO, L. M. *et al.* High-fidelity aerodynamic analysis and optimization of the SUSAN electrofan concept. *In*: **AIAA SCITECH 2022 Forum, AIAA 2022-2304. San Diego, CA and Virtual**. [*S.l.: s.n.*], 2022.

MACINTOSH, A.; WALLACE, L. International aviation emissions to 2025: Can emissions be stabilised without restricting demand? **Energy Policy**, Elsevier, v. 37, n. 1, p. 264–273, 2009.

MADER, C. *et al.* Adflow—–an open-source computational fluid dynamics solver for aerodynamic and multidisciplinary optimization. **Journal of Aerospace Information Systems**, 2020.

MADONNA, V.; GIANGRANDE, P.; GALEA, M. Electrical power generation in aircraft: Review, challenges, and opportunities. **IEEE Transactions on Transportation Electrification**, IEEE, v. 4, n. 3, p. 646–659, 2018.

MAHASHABDE, A. *et al.* Assessing the environmental impacts of aircraft noise and emissions. **Progress in Aerospace Sciences**, Elsevier, v. 47, n. 1, p. 15–52, 2011.

MALDONADO, D. *et al.* Computational simulations of a mach 0.745\transonic truss-braced wing design. *In*: **AIAA Scitech 2020 Forum, AIAA 2020-1649. Orlando, Florida**. [*S.l.: s.n.*], 2020.

MALLIK, W. *et al.* Effect of flutter on the multidisciplinary design optimization of truss-braced-wing aircraft. **Journal of Aircraft**, American Institute of Aeronautics and Astronautics, v. 52, n. 6, p. 1858–1872, 2015.

MALONE, B.; MASON, W. H. Multidisciplinary optimization in aircraft design using analytic technology models. **Journal of Aircraft**, v. 32, n. 2, p. 431–438, 1995.

MANGALGIRI, P. Composite materials for aerospace applications. **Bulletin of Materials Science**, Springer, v. 22, n. 3, p. 657–664, 1999.

MANKINS, J. C. Technology readiness assessments: A retrospective. **Acta Astronautica**, Elsevier, v. 65, n. 9-10, p. 1216–1223, 2009.

MAREC, J.-P. Drag reduction: a major task for research. *In*: **Aerodynamic Drag Reduction Technologies**. [*S.l.: s.n.*]: Springer, 2001. p. 17–27.

MARINO, M.; SABATINI, R. *et al.* Advanced lightweight aircraft design configurations for green operations. *In*: ENGINEERS AUSTRALIA. **Practical Responses to Climate Change Conference 2014, Paper 207**. [*S.l.: s.n.*], 2014.

MARTINEZ-VAL, R. Flying wings. a new paradigm for civil aviation? **Acta Polytechnica**, v. 47, n. 1, 2007.

MARTÍNEZ-VAL, R. *et al.* Potential effects of blended wing bodies on the air transportation system. **Journal of Aircraft**, v. 47, n. 5, p. 1599–1604, 2010.

MARTINEZ-VAL, R.; PEREZ, E. Aeronautics and astronautics: recent progress and future trends. **Proceedings of the Institution of Mechanical Engineers, Part C: Journal of Mechanical Engineering Science**, SAGE Publications Sage UK: London, England, v. 223, n. 12, p. 2767–2820, 2009.

MARTINEZ-VAL, R. *et al.* Conceptual design of a medium size flying wing. **Proceedings of the Institution of Mechanical Engineers, Part G: Journal of Aerospace Engineering**, SAGE Publications Sage UK: London, England, v. 221, n. 1, p. 57–66, 2007.

MARTINS, J.; NING, A. **Engineering design optimization**. [*S.l.: s.n.*]: Cambridge University Press, 2021.

MARTINS, J. R.; HWANG, J. T. Review and unification of methods for computing derivatives of multidisciplinary computational models. **AIAA journal**, American Institute of Aeronautics and Astronautics, v. 51, n. 11, p. 2582–2599, 2013.

MARTINS, J. R.; LAMBE, A. B. Multidisciplinary design optimization: a survey of architectures. **AIAA journal**, American Institute of Aeronautics and Astronautics, v. 51, n. 9, p. 2049–2075, 2013.

MATSSON, J. **An Introduction to ANSYS Fluent 2020**. [*S.l.: s.n.*]: SDC Publications, 2020.

MATTINGLY, J. D.; HEISER, W. H.; PRATT, D. T. **Aircraft engine design**. [*S.l.: s.n.*]: American Institute of Aeronautics and Astronautics, 2002.

MAVERIC. **AIRBUS - Imagine travelling in this blended wing body aircraft**. 2020. Accessed in 05/03/2020. Available from Internet: https://www.airbus.com/newsroom/stories/Imagine-travelling-in-this-blended-wing-body-aircraft.html.

MCMASTERS, J. H.; CUMMINGS, R. M. Airplane design-past, present, and future. **Journal of Aircraft**, v. 39, n. 1, p. 10–17, 2002.

MCMASTERS, J. H.; CUMMINGS, R. M. From farther, faster, higher to leaner, meaner, greener: Future directions in aeronautics. **Journal of aircraft**, v. 41, n. 1, p. 51–61, 2004.

MEADOWS, N. A. *et al.* Multidisciplinary design optimization of medium-range transonic truss-braced wing transport aircraft. **Journal of Aircraft**, v. 49, n. 6, p. 1844–1856, 2012.

MENEGOZZO, L.; BENINI, E. Boundary layer ingestion propulsion: A review on numerical modeling. **Journal of Engineering for Gas Turbines and Power**, American Society of Mechanical Engineers Digital Collection, v. 142, n. 12, 2020.

MENTER, F. R.; KUNTZ, M.; LANGTRY, R. Ten years of industrial experience with the SST turbulence model. **Turbulence, heat and mass transfer**, v. 4, n. 1, p. 625–632, 2003.

MOERLAND, E. *et al.* On the design of a strut-braced wing configuration in a collaborative design environment. *In*: **17th AIAA Aviation Technology, Integration, and Operations Conference, AIAA 2017-4397. Denver, Colorado**. [*S.l.: s.n.*], 2017.

MOORE, J.; MADDALON, D. Multibody transport concept. *In*: **2nd International Very Large Vehicles Conference, Paper 810. Washington, DC**. [*S.l.: s.n.*], 1982.

NAKAMURA, H.; KAJIKAWA, Y.; SUZUKI, S. Multi-level perspectives with technology readiness measures for aviation innovation. **Sustainability science**, Springer, v. 8, n. 1, p. 87–101, 2013.

NANGIA, R.; PALMER, M.; TILMANN, C. Unconventional high aspect ratio joined-wing aircraft with aft-and forward-swept wing-tips. *In*: **41st Aerospace Sciences Meeting and Exhibit, AIAA 2003-0506. Reno, Nevada**. [*S.l.: s.n.*], 2003.

NASA. **Industry Provides NASA with Ideas for Next X-Plane**. 2017. Accessed in 06/03/2020. Available from Internet: https://www.nasa.gov/aero/industry-provides-nasa-with-ideas-for-next-x-plane.

NEITTAANMÄKI, P. *et al.* Overview on drag reduction technologies for civil transport aircraft. *In*: **European Congress on Computational Methods in Applied Sciences and Engineering (ECCOMAS)**. [*S.l.: s.n.*], 2004. p. 24–28.

NELSON, T. E.; ZINGG, D. W. Fifty years of aerodynamics: successes, challenges, and opportunities. **Canadian Aeronautics and Space Journal**, NRC Research Press Ottawa, Canada, v. 50, n. 1, p. 61–84, 2004.

NICKOL, C. Hybrid wing body configuration scaling study. *In*: **50th AIAA aerospace sciences meeting including the new horizons forum and aerospace exposition, AIAA 2012-0337. Nashville, Tennessee**. [*S.l.: s.n.*], 2012.

NICKOL, C. L.; HALLER, W. J. Assessment of the performance potential of advanced subsonic transport concepts for NASA's environmentally responsible aviation project. *In*: **54th AIAA Aerospace Sciences Meeting, AIAA 2016-1030. San Diego, California**. [*S.l.: s.n.*], 2016.

NICOLOSI, F. *et al.* Design and optimization of a large turboprop aircraft. **Aerospace**, Multidisciplinary Digital Publishing Institute, v. 8, n. 5, p. 132, 2021.

NORTON, D.; OLASON, M. Aerodynamic design philosophy of the boeing 737. **Journal of Aircraft**, v. 3, n. 6, p. 524–528, 1966.

OKONKWO, P.; SMITH, H. Review of evolving trends in blended wing body aircraft design. **Progress in Aerospace Sciences**, Elsevier, v. 82, p. 1–23, 2016.

OKONKWO, P. P. C. Conceptual design methodology for blended wing body aircraft. **Cranfield University, PhD Thesis, England**, 2016.

OLIVEIRO, F. Preliminary design of a very large prandlplane freighter and airport network analysis. **Universita di Pisa, PhD Thesis, Italy**, 2015.

OSUSKY, L. *et al.* Drag minimization based on the Navier-Stokes equations using a Newton-Krylov approach. **AIAA Journal**, American Institute of Aeronautics and Astronautics, v. 53, n. 6, p. 1555–1577, 2015.

OSUSKY, M.; BOOM, P. D.; ZINGG, D. W. Results from the fifth aiaa drag prediction workshop obtained with a parallel newton-krylov-schur flow solver discretized using summation-by-parts operators. *In*: **31st AIAA Applied Aerodynamics Conference, AIAA 2013-2511. San Diego, CA**. [*S.l.: s.n.*], 2013.

OWEN, B.; LEE, D. S.; LIM, L. Flying into the future: aviation emissions scenarios to 2050. **Environmental Science and Technology**, ACS Publications, v. 44, n. 7, p. 2255–2260, 2010.

PAGE, M.; SMETAK, E.; YANG, S. Single-aisle airliner disruption with a single-deck blended wing-body. *In*: **31st Congress of the International Council of the Aeronautical Sciences. Belo Horizonte, Minas Gerais**. [*S.l.: s.n.*], 2018.

PALERMO, M.; VOS, R. Experimental aerodynamic analysis of a 4.6%-scale flying-V subsonic transport. *In*: **AIAA Scitech 2020 Forum, AIAA 2020-2228. Orlando, Florida**. [*S.l.: s.n.*], 2020.

PANDYA, S. A. *et al.* Computational assessment of the boundary layer ingesting nacelle design of the D8 aircraft. *In*: **52nd Aerospace Sciences Meeting, AIAA 2014-0907. National Harbor, Maryland**. [*S.l.: s.n.*], 2014.

PAPAGEORGIOU, A. *et al.* Multidisciplinary design optimization of aerial vehicles: A review of recent advancements. **International Journal of Aerospace Engineering**, Hindawi, v. 2018, 2018.

PASCUAL, B. R.; VOS, R. The effect of engine location on the aerodynamic efficiency of a flying-V aircraft. *In*: **AIAA Scitech 2020 Forum, AIAA 2020-1954. Orlando, Florida**. [*S.l.: s.n.*], 2020.

PEIFENG, L. *et al.* Aerodynamic design methodology for blended wing body transport. **Chinese Journal of Aeronautics**, Elsevier, v. 25, n. 4, p. 508–516, 2012.

PELZ, P. F.; LEISE, P.; MECK, M. Sustainable aircraft design—a review on optimization methods for electric propulsion with derived optimal number of propulsors. **Progress in Aerospace Sciences**, Elsevier, p. 100714, 2021.

PEREZ, R. E.; JANSEN, P. W.; MARTINS, J. R. pyopt: a python-based object-oriented framework for nonlinear constrained optimization. **Structural and Multidisciplinary Optimization**, Springer, v. 45, n. 1, p. 101–118, 2012.

PERULLO, C. A. *et al.* Effects of advanced engine technology on open rotor cycle selection and performance. **Journal of engineering for gas turbines and power**, American Society of Mechanical Engineers Digital Collection, v. 135, n. 7, 2013.

PETERS, A. *et al.* Ultrashort nacelles for low fan pressure ratio propulsors. **Journal of Turbomachinery**, American Society of Mechanical Engineers Digital Collection, v. 137, n. 2, 2015.

PETRESCU, R. V. *et al.* History of aviation-a short review. **Journal of Aircraft and Spacecraft Technology**, Elsevier, v. 1, n. 1, 2017.

PFENNINGER, W. Design considerations of large subsonic long range transport airplanes with low drag boundary layer suction. **Northrop Aircraft, Inc., Report NAI-54-800 (BLC-67)**, 1954.

PIRONNEAU, O. On optimum design in fluid mechanics. **Journal of fluid mechanics**, Cambridge University Press, v. 64, n. 1, p. 97–110, 1974.

PLAS, A. *et al.* Performance of a boundary layer ingesting (bli) propulsion system. *In*: **45th AIAA aerospace sciences meeting and exhibit, AIAA 2007-450. Reno, Nevada**. [*S.l.: s.n.*], 2007.

PORNET, C.; ISIKVEREN, A. T. Conceptual design of hybrid-electric transport aircraft. **Progress in Aerospace Sciences**, Elsevier, v. 79, p. 114–135, 2015.

PRAKASHA, P. *et al.* Multidisciplinary design analysis of blended wing body through collaborative design approach: AGILE EU project. *In*: **ICAS Conference Proceedings, Belo Horizonte, Brazil**. [*S.l.: s.n.*], 2018.

PRAKASHA, P. S. *et al.* Model based collaborative design & optimization of blended wing body aircraft configuration: AGILE EU project. *In*: **2018 Aviation Technology, Integration, and Operations Conference, AIAA 2018-4006. Atlanta, Georgia**. [*S.l.: s.n.*], 2018.

PRANDTL, L. **Induced drag of multiplanes**. [*S.l.*], 1924. Technical note NO. 182.

PW1100G-JM Series Engines Type-Certificate Data Sheet, https://www.easa.europa.eu/. 2019. Accessed in 05/03/2021. Available from Internet: Type-CertificateDataSheet.

QIN, N. *et al.* Aerodynamic considerations of blended wing body aircraft. **Progress in Aerospace Sciences**, Elsevier, v. 40, n. 6, p. 321–343, 2004.

RAO, A. G.; YIN, F.; WERIJ, H. G. Energy transition in aviation: The role of cryogenic fuels. **Aerospace**, Multidisciplinary Digital Publishing Institute, v. 7, n. 12, p. 181, 2020.

RAYMER, D. Enhancing aircraft conceptual design using multidisciplinary optimization. **Royal Institute of Technology, PhD Thesis, Sweden**, 2002.

RAYMER, D. **Aircraft Design: A Conceptual Approach 5e and RDSWin student**. [*S.l.: s.n.*]: American Institute of Aeronautics and Astronautics, Inc., 2012.

RAYMER, D. P. *et al.* **Advanced technology subsonic transport study: N+ 3 technologies and design concepts**. [*S.l.*], 2011. NASA/TM-2011-217130.

RECKZEH, D. Multifunctional wing moveables design of the A350XWB and the way to future concepts. *In*: **29th Congress of the International Council of the Aeronautical Sciences, St. Petersburg, Russia**. [*S.l.: s.n.*], 2014.

REIST, T. A.; ZINGG, D. W. Optimization of the aerodynamic performance of regional and wide-body-class blended wing-body aircraft. *In*: **33rd AIAA applied aerodynamics conference, AIAA 2015-3292. Dallas, Texas**. [*S.l.: s.n.*], 2015.

REIST, T. A.; ZINGG, D. W. High-fidelity aerodynamic shape optimization of a lifting-fuselage concept for regional aircraft. **Journal of Aircraft**, American Institute of Aeronautics and Astronautics, v. 54, n. 3, p. 1085–1097, 2016.

REIST, T. A. *et al.* Multifidelity optimization of hybrid wing–body aircraft with stability and control requirements. **Journal of Aircraft**, American Institute of Aeronautics and Astronautics, v. 56, n. 2, p. 442–456, 2019.

RISCH, T. *et al.* X-48b flight test progress overview. *In*: **47th AIAA Aerospace Sciences Meeting including The New Horizons Forum and Aerospace Exposition, AIAA 2009-934. Orlando, Florida**. [*S.l.: s.n.*], 2009.

ROCCA, G. L. Knowledge based engineering: Between ai and cad. review of a language based technology to support engineering design. **Advanced engineering informatics**, Elsevier, v. 26, n. 2, p. 159–179, 2012.

RODRIGUEZ, D. L. Multidisciplinary optimization method for designing boundary-layer-ingesting inlets. **Journal of Aircraft**, v. 46, n. 3, p. 883–894, 2009.

ROMPOKOS, P. *et al.* Synergistic technology combinations for future commercial aircraft using liquid hydrogen. **Journal of Engineering for Gas Turbines and Power**, American Society of Mechanical Engineers, v. 143, n. 7, p. 071017, 2021.

RUSSO, L.; TOGNACCINI, R.; DEMASI, L. Box wing and induced drag: Compressibility effect in subsonic and transonic regimes. *In*: **AIAA Scitech 2020 Forum, AIAA 2020-0447. Orlando, Florida**. [*S.l.: s.n.*], 2020.

RYE, L.; BLAKEY, S.; WILSON, C. W. Sustainability of supply or the planet: a review of potential drop-in alternative aviation fuels. **Energy & Environmental Science**, Royal Society of Chemistry, v. 3, n. 1, p. 17–27, 2010.

SAHOO, S.; ZHAO, X.; KYPRIANIDIS, K. A review of concepts, benefits, and challenges for future electrical propulsion-based aircraft. **Aerospace**, Multidisciplinary Digital Publishing Institute, v. 7, n. 4, p. 44, 2020.

SALAM, I. R.; BIL, C. Multi-disciplinary analysis and optimisation methodology for conceptual design of a box-wing aircraft. **The Aeronautical Journal**, Cambridge University Press, v. 120, n. 1230, p. 1315–1333, 2016.

SALEM, K. A. *et al.* A physics-based multidisciplinary approach for the preliminary design and performance analysis of a medium range aircraft with box-wing architecture. **Aerospace**, Multidisciplinary Digital Publishing Institute, v. 8, n. 10, p. 292, 2021.

SALEM, K. A. *et al.* Tools and methodologies for box-wing aircraft conceptual aerodynamic design and aeromechanic analysis. **Mechanics & Industry**, EDP Sciences, v. 22, p. 39, 2021.

SALEM, K. A. *et al.* Preliminary take-off analysis and simulation of prandtlplane commercial aircraft. **Aerotecnica Missili & Spazio**, Springer, v. 99, n. 3, p. 203–216, 2020.

SAMUELSSON, S. *et al.* Performance analysis of turbo-electric propulsion system with fuselage boundary layer ingestion. **Aerospace Science and Technology**, Elsevier, v. 109, p. 106412, 2021.

SANTANA, L. D. *et al.* The update of an aerodynamic wind-tunnel for aeroacoustics testing. **Journal of Aerospace Technology and Management**, SciELO Brasil, v. 6, p. 111–118, 2014.

SARLIOGLU, B.; MORRIS, C. T. More electric aircraft: Review, challenges, and opportunities for commercial transport aircraft. **IEEE transactions on Transportation Electrification**, IEEE, v. 1, n. 1, p. 54–64, 2015.

SCANIVALVE DS4-48 - pressure scanner module, instruction and service manual - by Scanivalve Corp. 1975.

SCARDAONI, M. P.; MONTEMURRO, M.; PANETTIERI, E. Prandtlplane wing-box least-weight design: a multi-scale optimisation approach. **Aerospace Science and Technology**, Elsevier, v. 106, p. 106156, 2020.

SCHIKTANZ, D. Conceptual design of a medium range box wing aircraft. **Department Fahrzeug technik und Flugzeugbau, Master Thesis, Hamburg, HAW Hamburg**, 2011.

SCHILTGEN, B. T.; FREEMAN, J. Eco-150-300 design and performance: a tube-and-wing distributed electric propulsion airliner. *In*: **AIAA Scitech 2019 Forum, AIAA 2019-1808. San Diego, California**. [*S.l.: s.n.*], 2019.

SCHMIDT, M. *et al.* Challenges for ground operations arising from aircraft concepts using alternative energy. **Journal of Air Transport Management**, Elsevier, v. 56, p. 107–117, 2016.

SCHMITT, D. Challenges for unconventional transport aircraft configurations. **Air & Space Europe**, Elsevier, v. 3, n. 3-4, p. 67–72, 2001.

SCHMOLLGRUBER, P. *et al.* Multidisciplinary exploration of dragon: an onera hybrid electric distributed propulsion concept. *In*: **AIAA Scitech 2019 Forum, AIAA 2020-0501. Orlando, Florida**. [*S.l.: s.n.*], 2019.

SCHRAUF, G. Status and perspectives of laminar flow. **The aeronautical journal**, Cambridge University Press, v. 109, n. 1102, p. 639–644, 2005.

SECCHI, M. *et al.* Evaluation of a regional aircraft with boundary layer ingestion and electric-fan propulsor. **Journal of Aircraft**, American Institute of Aeronautics and Astronautics, p. 1–12, 2021.

SECCO, N. R.; MARTINS, J. R. RANS-based aerodynamic shape optimization of a strut-braced wing with overset meshes. **Journal of Aircraft**, American Institute of Aeronautics and Astronautics, v. 56, n. 1, p. 217–227, 2019.

SEHRA, A. K.; JR, W. W. Propulsion and power for 21st century aviation. **Progress in aerospace sciences**, Elsevier, v. 40, n. 4-5, p. 199–235, 2004.

SEITZ, A. *et al.* Proof of concept study for fuselage boundary layer ingesting propulsion. **Aerospace**, Multidisciplinary Digital Publishing Institute, v. 8, n. 1, p. 16, 2021.

SEITZ, A.; HÜBNER, A.; RISSE, K. The DLR TuLam project: design of a short and medium range transport aircraft with forward swept NLF wing. **CEAS Aeronautical Journal**, Springer, v. 11, n. 2, p. 449–459, 2020.

SGUEGLIA, A. Methodology for sizing and optimising a blended wing-body with distributed electric ducted fans. **ISAE-SUPAERO, PhD Thesis, France**, 2019.

SGUEGLIA, A. *et al.* Multidisciplinary design optimization framework with coupled derivative computation for hybrid aircraft. **Journal of Aircraft**, American Institute of Aeronautics and Astronautics, v. 57, n. 4, p. 715–729, 2020.

SHAW, R. **Boeing 737-300 to 800**. [*S.l.: s.n.*]: Zenith Press, 1999.

SILVA, G. P. G. da *et al.* Slat aerodynamic noise reduction using dielectric barrier discharge plasma actuators. **Aerospace Science and Technology**, Elsevier, v. 97, p. 105642, 2020.

SINGH, R.; NALIANDA, D. Turbo-electric distributed propulsion–opportunities, benefits and challenges. **Aircraft Engineering and Aerospace Technology: An International Journal**, Emerald Group Publishing Limited, 2014.

SINGH, R. *et al.* Conceptual investigation of a propulsive fuselage aircraft layout. **Aircraft Engineering and Aerospace Technology: An International Journal**, Emerald Group Publishing Limited, 2014.

SINGH, V. Fuel consumption minimization of transport aircraft using real-coded genetic algorithm. **Proceedings of the Institution of Mechanical Engineers, Part G: Journal of Aerospace Engineering**, SAGE Publications Sage UK: London, England, v. 232, n. 10, p. 1925–1943, 2018.

SINGH, V.; SHARMA, S. K.; VAIBHAV, S. Transport aircraft conceptual design optimization using real coded genetic algorithm. **International Journal of Aerospace Engineering**, Hindawi, v. 2016, p. 2813541, 2016.

SKOWRON, A. *et al.* Greater fuel efficiency is potentially preferable to reducing nox emissions for aviation's climate impacts. **Nature Communications**, Nature Research (part of Springer Nature), 2020.

SLOTNICK, J. *et al.* **CFD vision 2030 study: a path to revolutionary computational aerosciences**. [*S.l.*], 2014. NASA/CR-2014-218178, NF1676L-18332.

SMITH, H. A review of supersonic business jet design issues. **The Aeronautical Journal**, Cambridge University Press, v. 111, n. 1126, p. 761–776, 2007.

SMITH, H. *et al.* The genus aircraft conceptual design environment. **Proceedings of the Institution of Mechanical Engineers, Part G: Journal of Aerospace Engineering**, SAGE Publications Sage UK: London, England, v. 233, n. 8, p. 2932–2947, 2019.

SMITH, P. M. *et al.* A study of high-altitude manned research aircraft employing strut-braced wings of high-aspect-ratio. **NASA. Report NASA-CR-159262**, 1981.

SOBIESZCZANSKI-SOBIESKI, J.; HAFTKA, R. T. Multidisciplinary aerospace design optimization: survey of recent developments. **Structural optimization**, Springer, v. 14, n. 1, p. 1–23, 1997.

SOUTIS, C. Carbon fiber reinforced plastics in aircraft construction. **Materials Science and Engineering: A**, Elsevier, v. 412, n. 1-2, p. 171–176, 2005.

SOUTIS, C. Fibre reinforced composites in aircraft construction. **Progress in aerospace sciences**, Elsevier, v. 41, n. 2, p. 143–151, 2005.

SPACHT, G. The forward swept wing-a unique design challenge. *In*: **Aircraft Systems Meeting, AIAA 1980-1885. Anaheim, California**. [*S.l.: s.n.*], 1980.

SPALART, P.; ALLMARAS, S. A one-equation turbulence model for aerodynamic flows. *In*: **30th aerospace sciences meeting and exhibit**. [*S.l.: s.n.*], 1992. p. 439.

SPEARMAN, M. L. The evolution of the high-speed civil transport. **NASA Technical Memorandum, USA**, TM-109089, 1994.

STRACK, M. *et al.* Conceptual design assessment of advanced hybrid electric turboprop aircraft configurations. *In*: **17th AIAA Aviation Technology, Integration, and Operations Conference, AIAA 2017-3068. Denver, Colorado**. [*S.l.: s.n.*], 2017.

STREUBER, G. M.; ZINGG, D. W. Evaluating the risk of local optima in aerodynamic shape optimization. **AIAA Journal**, American Institute of Aeronautics and Astronautics, v. 59, n. 1, p. 75–87, 2021.

STÜRMER, A.; YIN, J.; AKKERMANS, R. Progress in aerodynamic and aeroacoustic integration of cror propulsion systems. **The Aeronautical Journal**, Cambridge University Press, v. 118, n. 1208, p. 1137–1158, 2014.

SUGAR. The Subsonic Ultra Green Aircraft Research. 2017. Accessed in 23/03/2021. Available from Internet: https://www1.grc.nasa.gov/aeronautics/hep/airplane-concepts/.

SUN, Y.; SMITH, H. Review and prospect of supersonic business jet design. **Progress in Aerospace Sciences**, Elsevier, v. 90, p. 12–38, 2017.

TASCA, A. *et al.* Innovative box-wing aircraft: Emissions and climate change. **Sustainability**, MDPI, v. 13, n. 6, p. 3282, 2021.

THIBERT, J.; ARNAL, D. A review of onera aerodynamic research in support of a future supersonic transport aircraft. **Progress in Aerospace Sciences**, Elsevier, v. 36, n. 8, p. 581–627, 2000.

TIMMIS, A. J. *et al.* Environmental impact assessment of aviation emission reduction through the implementation of composite materials. **The International Journal of Life Cycle Assessment**, Springer, v. 20, n. 2, p. 233–243, 2015.

TORENBEEK, E. Cruise performance and range prediction reconsidered. **Progress in Aerospace Sciences**, Elsevier, v. 33, n. 5-6, p. 285–321, 1997.

TORENBEEK, E. **Advanced aircraft design: conceptual design, analysis and optimization of subsonic civil airplanes**. [*S.l.: s.n.*]: John Wiley & Sons, 2013.

TORRIGIANI, F. *et al.* Design of the strut braced wing aircraft in the AGILE collaborative MDO framework. **Belo Horizonte, Brazil**, 2018.

TRAINELLI, L. *et al.* Optimal sizing and operation of airport infrastructures in support of electric-powered aviation. **Aerospace**, Multidisciplinary Digital Publishing Institute, v. 8, n. 2, p. 40, 2021.

TURRIZIANI, R. *et al.* Preliminary design characteristics of a subsonic business jet concept employing an aspect ratio 25 strut braced wing. **NASA. Report NASA CR-159361,**, 1980.

URANGA, A. *et al.* Preliminary experimental assessment of the boundary layer ingestion benefit for the d8 aircraft. *In*: **52nd Aerospace Sciences Meeting, AIAA 2014-0906. National Harbor, Maryland**. [*S.l.: s.n.*], 2014.

URANGA, A. *et al.* Boundary layer ingestion benefit of the D8 transport aircraft. **AIAA Journal**, American Institute of Aeronautics and Astronautics, p. 3693–3708, 2017.

URANGA, A. *et al.* Analysis of the aerodynamic benefit from boundary layer ingestion for transport aircraft. **AIAA Journal**, American Institute of Aeronautics and Astronautics, v. 56, n. 11, p. 4271–4281, 2018.

VALENCIA, E. *et al.* Novel fan configuration for distributed propulsion systems with boundary layer ingestion on an hybrid wing body airframe. **Thermal Science and Engineering Progress**, Elsevier, v. 18, p. 100515, 2020.

VINK, P. *et al.* Towards a hybrid comfortable passenger cabin interior for the flying v aircraft. **International Journal of Aviation, Aeronautics, and Aerospace**, v. 7, n. 1, p. 1, 2020.

VOS, J. *et al.* Navier-Stokes solvers in european aircraft design. **Progress in Aerospace Sciences**, Elsevier, v. 38, n. 8, p. 601–697, 2002.

VOSKUIJL, M. *et al.* Analysis and design of hybrid electric regional turboprop aircraft. **CEAS Aeronautical Journal**, Springer, v. 9, n. 1, p. 15–25, 2018.

VRIES, R. D.; BROWN, M.; VOS, R. Preliminary sizing method for hybrid-electric distributed-propulsion aircraft. **Journal of Aircraft**, American Institute of Aeronautics and Astronautics, v. 56, n. 6, p. 2172–2188, 2019.

VRIES, R. de; VOS, R. Aerodynamic performance benefits of over-the-wing distributed propulsion for hybrid-electric transport aircraft. *In*: **AIAA SCITECH 2022 Forum, AIAA 2022-0128. San Diego, CA and Virtual**. [*S.l.: s.n.*], 2022.

WAKAYAMA, S.; KROO, I. The challenge and promise of blended-wing-body optimization. *In*: **7th AIAA/USAF/NASA/ISSMO Symposium on Multidisciplinary Analysis and Optimization, AIAA 98-4736. St. Louis, Missouri**. [*S.l.: s.n.*], 1998.

WALSH, P. P.; FLETCHER, P. **Gas turbine performance**. [*S.l.: s.n.*]: John Wiley & Sons, 2004.

WELLS, D. P.; HORVATH, B. L.; MCCULLERS, L. A. **The flight optimization system weights estimation method**. [*S.l.*], 2017. NASA/TM-2017-219627.

WELSTEAD, J.; FELDER, J. L. Conceptual design of a single-aisle turboelectric commercial transport with fuselage boundary layer ingestion. *In*: **54th AIAA Aerospace Sciences Meeting, AIAA 2016-1027. San Diego, California**. [*S.l.: s.n.*], 2016.

WERNER-WESTPHAL, C.; HEINZE, W.; HORST, P. Multidisciplinary integrated preliminary design applied to unconventional aircraft configurations. **Journal of aircraft**, v. 45, n. 2, p. 581–590, 2008.

WHITCOMB, R. T.; CLARK, L. R. **An airfoil shape for efficient flight at supercritical mach numbers**. [*S.l.*], 1965. NASA TM X-1109.

WHITCOMB, R. T.; SEVIER, J. R. **A supersonic area rule and an application to the design of a wing-body combination with high lift-drag ratios**. [*S.l.: s.n.*]: US Government Printing Office, 1960. v. 72.

WHITLEY, D. A genetic algorithm tutorial. **Statistics and computing**, Springer, v. 4, n. 2, p. 65–85, 1994.

WIART, L. *et al.* Development of nova aircraft configurations for large engine integration studies. *In*: **33rd AIAA Applied Aerodynamics Conference, AIAA 2015-2254. Dallas, Texas**. [*S.l.: s.n.*], 2015.

WILLIAMS, J. E.; VUKELICH, S. R. **The USAF stability and control digital dATCOM. Volume I. Users manual**. [*S.l.*], 1979.

WITHERS, M. R. *et al.* Economic and environmental assessment of liquefied natural gas as a supplemental aircraft fuel. **Progress in Aerospace Sciences**, Elsevier, v. 66, p. 17–36, 2014.

WOLKOVITCH, J. The joined wing-an overview. **Journal of Aircraft**, v. 23, n. 3, p. 161–178, 1986.

WUNDERLICH, T. *et al.* Multidisciplinary optimization of an NLF forward swept wing in combination with aeroelastic tailoring using cfrp. **CEAS Aeronautical Journal**, Springer, v. 8, n. 4, p. 673–690, 2017.

X-48B. **NASA - X-48B**. 2017. Accessed in 23/05/2019. Available from Internet: https://www.nasa.gov/centers/armstrong/multimedia/imagegallery/X-48B/index.html.

XU, J.; KROO, I. Aircraft design with active load alleviation and natural laminar flow. **Journal of Aircraft**, American Institute of Aeronautics and Astronautics, v. 51, n. 5, p. 1532–1545, 2014.

YANG, S.; PAGE, M.; SMETAK, E. J. Achievement of NASA new aviation horizons n+ 2 goals with a blended-wing-body x-plane designed for the regional jet and single-aisle jet markets. *In*: **2018 AIAA Aerospace Sciences Meeting, AIAA 2018-0521. Kissimmee, Florida**. [*S.l.: s.n.*], 2018.

YE, L. *et al.* Functionalized composite structures for new generation airframes: a review. **Composites science and technology**, Elsevier, v. 65, n. 9, p. 1436–1446, 2005.

YENIAY, Ö. Penalty function methods for constrained optimization with genetic algorithms. **Mathematical and computational Applications**, Association for Scientific Research, v. 10, n. 1, p. 45–56, 2005.

YILDIRIM, A. *et al.* Performance analysis of optimized STARC-ABL designs across the entire mission profile. *In*: **AIAA Scitech 2021 Forum, AIAA 2021-0891. Virtual event**. [*S.l.: s.n.*], 2021.

YILDIRIM, A. *et al.* Boundary-layer ingestion benefit for the STARC-ABL concept. **Journal of Aircraft**, v. 0, n. 0, p. 1–16, 2022.

YILMAZ, N.; ATMANLI, A. Sustainable alternative fuels in aviation. **Energy**, Elsevier, v. 140, p. 1378–1386, 2017.

ZANTE, D. E. V. Progress in open rotor research: A US perspective. *In*: **ASME Turbo Expo 2015: Turbine Technical Conference and Exposition, GT2015-42203. Montreal, Quebec**. [*S.l.: s.n.*], 2015.

ZHANG, G. *et al.* Aerodynamic characteristics of canard-forward swept wing aircraft configurations. **Journal of aircraft**, American Institute of Aeronautics and Astronautics, v. 50, n. 2, p. 378–387, 2013.

ZHANG, X.; CHEN, Y.; HU, J. Recent advances in the development of aerospace materials. **Progress in Aerospace Sciences**, Elsevier, v. 97, p. 22–34, 2018.

ZHENLI, C. *et al.* Assessment on critical technologies for conceptual design of blended-wing-body civil aircraft. **Chinese Journal of Aeronautics**, Elsevier, v. 32, n. 8, p. 1797–1827, 2019.

ZHENQING, X. *et al.* Nacelle-airframe integration design method for blended-wing-body transport with podded engines. **Chinese Journal of Aeronautics**, Elsevier, v. 32, n. 8, p. 1860–1868, 2019.

ZINGG, D. W.; GÜLDER, Ö. L. Technology developments and renewable fuels for sustainable aviation. **In A. De Mestral, P. Fitzgerald, M. Ahmad (Eds.), Sustainable Development, International Aviation, and Treaty Implementation (Treaty Implementation for Sustainable Development**, v. 21, n. 2, p. 17–31, 2018.

ZOHLANDT, C. Conceptual design of high subsonic prandtl planes-analysis and performance comparison with conventional configurations in the high subsonic transport category. **Delft University, Master Thesis, The Netherlands**, 2016.